Spin-transfer effects in spin-valves for CPP-GMR heads: A static and dynamic investigation

Alina Deac

Spin-transfer effects in spin-valves for CPP-GMR heads: A static and dynamic investigation

by

Alina Maria Deac

Thesis submitted to the Joseph Fourier University (Grenoble)
for the degree of Doctor of Philosophy

June 2005

Thesis advisors:
Jean-Pierre Nozières
Bernard Dieny
Olivier Redon

Defence jury:
Jacques Miltat (referee)
Alain Schuhl (referee)
Peter Levy
Henri Jaffrès
Joël Cibert

Laboratoire de Spintronique et Technologie des Composants (Spintec), and
Laboratoire d'Electronique de Technologie de L'Information (Léti)
Commissariat à l'Energie Atomique, Grenoble, France

To the memory of my father,
who showed me how to make strawberry ice-cream with liquid nitrogen
when I was still in kindergarten,

and to my mother,
who taught me to never give up.

Acknowledgements

I would like to express my gratitude to all the people who helped me during my thesis:

My three PhD advisors, for everything I learned from them, scientifically but not only, and for letting me do things my way:

- *Jean-Pierre Nozières, my official PhD advisor, for his diplomatic touch, his optimism and energy and all the problems he has solved;*

- *Olivier Redon, my other PhD advisor, for having accepted me as his first PhD student (hopefully the experience didn't prove completely discouraging for the future…though one never knows), for introducing me to thin layers magnetism and measurements, for motivating me and reading my "chef d'oeuvre" through and through;*

- *Bernard Dieny, my un-official PhD advisor, for having always been there for me – for scientific discussions and more. Merci, Bernard, for all the things you taught me, for your constant interest in my work, for your moral support during conferences and other difficult times, and for many the other things, including a beautiful drive on the 101 and showing me San Francisco.*

Jacques Miltat and Alain Schuhl for having accepted to referee my thesis (all 200 pages of it!), and Peter Levy, Henri Jaffres and Joel Cibert, for taking part in the defense jury;

The people from Headway for making (and sending me) the samples: Yue Liu, Min Li, Pokang Wang;

Pierre Gaud, director of LCMI, the group where I started my thesis and which has since split in several laboratories (among which LMNO), for being such a good mediator; Xavier Hugon, director of LMNO, for his constant support;

Jean-Eric Wegrowe, for his hospitality at the Ecole Polytechnique in Paris, for his honesty, humor and good will, for all his efforts in helping me with the experiments and for unforgettable dinners at the 'Crocodile';

Claude Chappert and Thibault Devolder, for offering me the chance of measuring at the Institut D'Electronique Fondamentale in Paris;

All the people at Spintec who helped me in various ways:

- *Kyung-Jin Lee for spin-torque micromagnetic simulations;*
- *Anatoly Vedyaev (quit smoking, Anatoly!), Natalia Ryzhanova and Nikita Strelkov for discussions on spin-torque theory and CPP-GMR calculations;*

- *Sebastien Petit (Seb, if you're the one to inherit my beloved samples, I'll sleep easily knowing they are in good hands…), Dana Stanescu, Ricardo Sousa, Stephane Auffret, Christophe Tirion and Ursula Ebels for helping me with the experiments;*
- *Catherine Broisin, the super-secretary who always finds a way;*
- *all my other colleagues for their moral support, interesting and enlightening discussions on unspeakable topics, coffee breaks, dining out, going dancing (for the braver ones…) and so on.*

People from the old LCMI:

- *Monique Drevon, the other super-secretary;*
- *Marie-Helene Vaudaine, for introducing me to clean-room techniques;*
- *Bernard Viala, Marcel Audoin, Line Vieux-Rochaz and Venceslass Rat for their friendship;*

All my friends, for still being my friends after various horrible times;

All the people I forgot but should have mentioned;

My family, for love and understanding;

And, finally, Frank, for having seen me through my highs and lows and still being here.

Foreword

The research related to spin-torque phenomena is one of the "hottest" topics in magnetism these days, at least going by the number of publications and international conferences on the subject. Although the physics of these effects is still not completely understood, it is already clear that the applications would be of major importance. The first studies have investigated current induced magnetization switching, motivated by the perspective of using it as a new writing scheme for MRAMs. Precessional states induced by the current, demonstrated less than two years ago, may constitute the working principle for new RF oscillators, interesting for telecom applications. Consequently, though the research in this field remains pretty fundamental, all the big microelectronics companies (such as Sony, Toshiba, Hitachi, IBM, Seagate…) are getting involved in this topic, considering the foreseen applications of spin-transfer in computer industry, wireless communication and so on.

To-date, spin-transfer phenomena have been analysed in detail in simple Co/Cu/Co multilayers. Studying spin-transfer in very complicated spin-valves, containing exchanged biased synthetic antiferromagnetic laminated reference layers and laminated free layers of considerable thickness, has brought another point of view on the matter and put forward several interesting new observations.

On the other hand, this study was particularly timely not only for applications such as MRAM or RF components, but also considering the importance of spin-transfer effects in CPP-GMR heads for hard disk drives. The magnetic read-head industry expects to be able to push forward the CIP head technology for about two years longer, after which it should probably move on to the CPP geometry. By then, parasitic effects induced by spin-transfer must be under control in these devices.

This thesis is divided into two main parts: part A gives an introduction to CPP-GMR and spin-transfer (through theoretical models, simulation results and experimental studies); part B presents spin-transfer in spin-valves for CPP-GMR heads, including a

brief motivation, descriptions of the experimental setups and sample fabrication procedure, results of static and dynamic measurements and an analysis of the influence of the laminating material on the CPP-GMR and the switching currents. A possible structure for microwave oscillators devices based on spin-current induced effects is proposed in the last chapter.

Avant-propos

En considérant le nombre de publication et de conférences internationales sur le sujet, le transfert de spin est aujourd'hui une des thématiques les plus florissantes et probablement les plus porteuses aussi.

Même si on ne comprend toujours pas complètement la physique de ces effets, il est déjà évident que leurs applications seront de première importance. En effet, la plus part des études antérieures concernaient le renversement par courant polarisé, qui pourrait être utilisé comme nouvelle méthode d'écriture dans les mémoires magnétiques (MRAM). Plus récemment, la precession entretenue induite par le transfert de spin a été proposé comme principe de fonctionnement pour un nouveau type d'oscillateur RF pour les télécommunications mobiles. Vu l'importance que ces applications pourraient avoir dans l'industrie des ordinateurs, télécommunications sans fil, etc., toutes les grandes compagnies en microélectronique (Sony, Toshiba, Hitachi, IBM, Seagate, Freescale…) financent des études sur les effets de transfert de spin. Néanmoins, la recherche dans le domaine reste en général assez fondamentale.

Jusqu'à présent, les phénomènes induits par le transfert de spin ont été analysés en détail dans de multicouches simples de type Co/Cu/Co. L'étude (présenté ici) de ces effets dans des vannes de spin complexes, contenant des couches de référence synthétiques laminées et piégées par échange et des couches libres laminées aussi et d'épaisseur considérable a amené un point de vue différent sur le sujet et a permis de mettre en évidence plusieurs aspects inattendus.

Cette étude a été particulièrement opportune considérant l'évolution du marché des têtes de lecture magnétorésistives : on s'attend à pouvoir exploiter la technologie actuelle (basée sur des vannes de spin dans lesquelles on applique un courant dans le plan des couches) jusqu'à 2007. Ensuite, on prévoit de passer en géométrie CPP (où le courant est perpendiculaire aux interfaces). Il est donc souhaitable de trouver des moyens de contrôler le bruit induit par le transfert de spin dans ces structures avant cette date.

Ce mémoire de thèse est divisé en deux grandes parties : la première (A) est une introduction sur le sujet (à travers des études théoriques, simulations micromagnétiques

et résultats expérimentaux principalement dans des échantillons Co/Cu/Co) ; la deuxième partie (B) concerne le transfert de spin dans les vannes de spin pour têtes CPP-GMR. Elle inclut des descriptions des échantillons, du banc de mesure et de la procédure de fabrication, des résultats des mesures statiques et dynamiques et une analyse de l'influence du matériau de lamination sur la GMR et les courants de renversement. Finalement, une structure possible des oscillateurs RF basés sur le transfert de spin est proposée dans le dernier chapitre.

Part A :
Spin-transfer in CPP spin-valves: an introduction

Chapter 1. Current - perpendicular - to - plane giant magnetoresistance

The results presented in this thesis have been obtained studying metallic pillars, explicitly spin-valves developed for current-perpendicular-to-plane (CPP) giant magnetoresistance (GMR) heads. Spin-transfer effects are usually studied in metallic multilayers containing two ferromagnetic films, one fixed, and the second free to be oriented parallel or antiparallel to the first one. The orientation of the free layer's magnetization can be changed either under the effect of a magnetic field, or by applying a spin-polarized current. The resistance of the multilayer in the two states is different, which is the essence of the GMR phenomenon. Therefore, the GMR signal can be used to probe the switching of the free layer. Moreover, CPP-GMR and spin-transfer effects are strongly related through current polarization and spin accumulation effects. A good understanding of GMR mechanisms is therefore essential for the analysis of spin-torque induced effects.

A.1.1. Simple intuitive GMR model

In ferromagnetic transition metals (such as Co, Fe, Ni or their alloys) the electrons which participate to the conduction of the current are *s*, *d* and hybridized *sd*. According to the orientation of the projection of their spin along the magnetization of the layer (parallel / antiparallel), two types of conduction electrons can be distinguished: spin up ($\uparrow$) and spin down ($\downarrow$), also called "majority" and "minority" carriers.

A characteristic of these metals is the *d*-band exchange splitting [1]. For a hard ferromagnetic material such as cobalt, for example, the spin up *d* sub-band is completely filled, and the *d* states at the Fermi level contain only spin down electrons (Fig. A.1.1). The main consequence of the exchange splitting is that the majority and minority carriers have very different scattering rates, regardless of the nature of the scattering centres (magnetic impurities, phonons, structural defects…), because the densities of available states into which the electrons can be scattered are very different.

In the case of cobalt, scattering will affect more the spin down electrons, while the spin up electrons see a very low resistivity and carry most of the electrical current. **This implies that an electrical current crossing a ferromagnetic material can gain a spin polarization.**

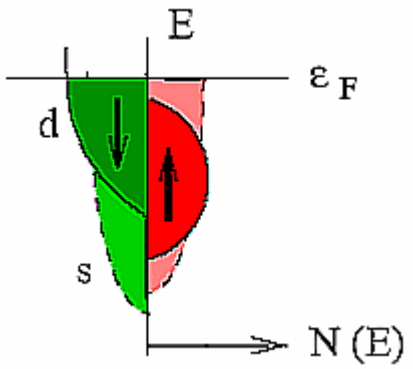

Fig. A.1 - 1 Schematic representation of the electronic structure in the case of cobalt. *N(E)* is the density of states for the *s* and *d* majority and minority electrons. The d states at the Fermi energy ε_F contain only spin down electrons.

At temperatures considerably lower than the Curie temperature, spin-flip scattering events are negligible and spin up and spin down electrons carry the electrical current in parallel. This is the so-called "two-current model" [2]. For ferromagnetic transition metals at low temperature this hypothesis is justified, since the spin-orbit coupling is weak and magnon scattering is negligible under these conditions. Therefore, if $\rho_\uparrow$ and $\rho_\downarrow$ are the resistivities seen by the two currents, the resistivity of the ferromagnetic material can be written:

$$\rho = \frac{\rho_\uparrow \cdot \rho_\downarrow}{\rho_\uparrow + \rho_\downarrow} \qquad (1)$$

At higher temperatures, however, spin-flip scattering must be considered. When electrons pass from one conduction channel to the other, the resistivity of the material can be determined as [3]:

$$\rho = \frac{\rho_\uparrow \cdot \rho_\downarrow + \rho_{\uparrow\downarrow} \cdot (\rho_\uparrow + \rho_\downarrow)}{\rho_\uparrow + \rho_\downarrow + 4\rho_{\uparrow\downarrow}} \qquad (2)$$

The GMR effect can be easily understood using the two-current model described above. Consider the simplest structure where this effect is present - a trilayer containing

two magnetic layers (like cobalt) separated by a non-magnetic spacer (like copper). In the parallel configuration, spin up electrons are weakly scattered in both magnetic layers, and can carry a lot of current (Fig. A.1 - 2). Similarly, spin down electrons are strongly scattered, and participate less to the conduction. In the antiparallel configuration, the majority spins in one layer become minority spins in the second, and vice-versa. If r (R) is the resistance of a magnetic layer for majority (minority) spins, and neglecting the resistance of the non-magnetic spacer, as well as spin-flip scattering, the equivalent resistance of the multilayer in the two configurations can be written (see Fig. A.1 - 2):

$$\begin{cases} R_P = \dfrac{1}{\dfrac{1}{2r} + \dfrac{1}{2R}} \\ R_{AP} = \dfrac{r+R}{2} \end{cases} \qquad (3)$$

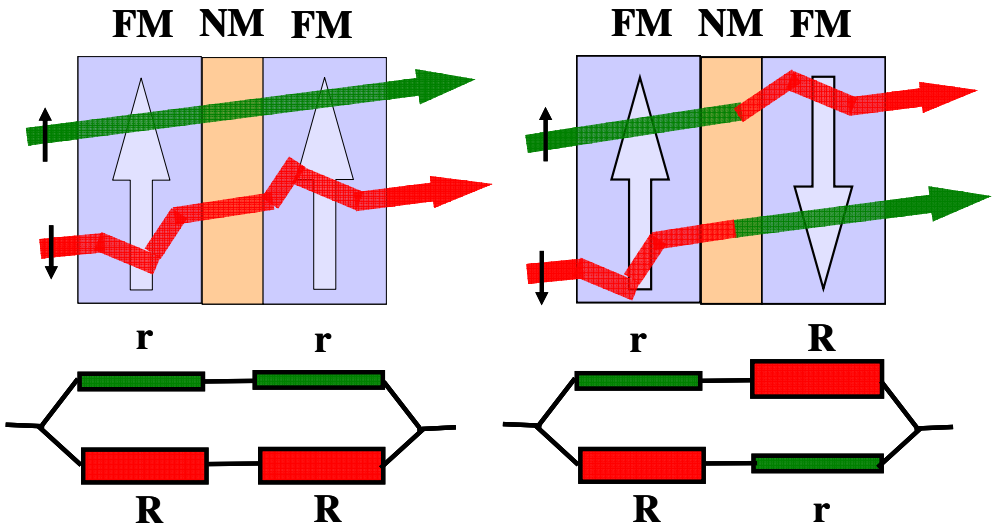

Fig. A.1 - 2 Two-current model in a Co/Cu/Co multilayer, for the parallel (**left**) and antiparallel (**right**) alignment between the magnetizations of the two layers. If *r (R)* is the resistance of a Co layer for the spin up (spin down) electrons, the resistance of the multilayer in each configuration can be calculated using the equivalent circuit below.

The GMR amplitude is defined as the variation of the resistance between the two configurations, normalized by the resistance of one of the states, for example P:

$$GMR = \frac{R_{AP} - R_P}{R_P} \tag{4}$$

Introducing $\alpha = \rho_{\uparrow}/\rho_{\downarrow} = r/R$, it can be shown that:

$$GMR = \frac{\Delta R}{R_P} = \frac{(1-\alpha)^2}{4\alpha} \tag{5}$$

Although the above formula (5) is valid both for CIP (current in plane) and CPP-GMR, the scaling lengths in the two geometries are very different. For the CIP configuration, classical [4] as well as quantum models [5] showed that electrons average the properties of the multilayers in the perpendicular-to-plane direction on the length scale of the electron mean free path (MFP) λ. The CIP-GMR vanishes when the period of the multilayer (i.e. the thickness of the layers) becomes much larger than MFP, since electrons see each magnetic layer independently. In the CPP configuration, electrons cross all layers and thus the relevant scaling parameter is the spin diffusion length (SDL) l_{sf}. For layers thinner than SDL, spin-flip scattering is negligible and the spin up and spin down conduction channels can be regarded as independent [6]. In most cases, l_{sf} is much larger than λ.

In addition to spin-dependent scattering phenomena previously discussed, the lattice potential modulation plays an important role for the GMR effect [7]. The potential seen by the electrons includes an intrinsic part due to the spin-dependent modulation of the potential in the multilayer, and an extrinsic contribution caused by interface or bulk defects which induce spin-dependent scattering (Fig. A.1 - 3).

The spin-dependent modulation of the lattice potential is the result of the difference in the positions of the bottoms of the conduction bands with respect to the Fermi energy in neighboring layers. In the case of Co/Cu multilayers, for instance, the matching of the conduction bands is very good for the majority electrons, so that spin up carriers encounter a nearly flat potential through the whole structure. On the other hand, a strong mismatch exists in the case of spin down electrons, resulting in large potential steps at the interfaces. Lattice potential modulations cause spin-dependent reflection and refraction of the electrons at the interfaces.

Although this image is valid both for CIP and CPP geometries, the roles played by lattice modulations in the two cases are very different [8]. For CIP, in the P configuration, minority electrons which propagate within the Cu layers bounce back and

forth between the two Co/Cu interfaces and remain confined in these layers, while flowing along the electric field. In the CPP geometry, the field is perpendicular to the interfaces and electrons are forced to pass the potential steps, resulting in additional spin-dependent interfacial resistance [9].

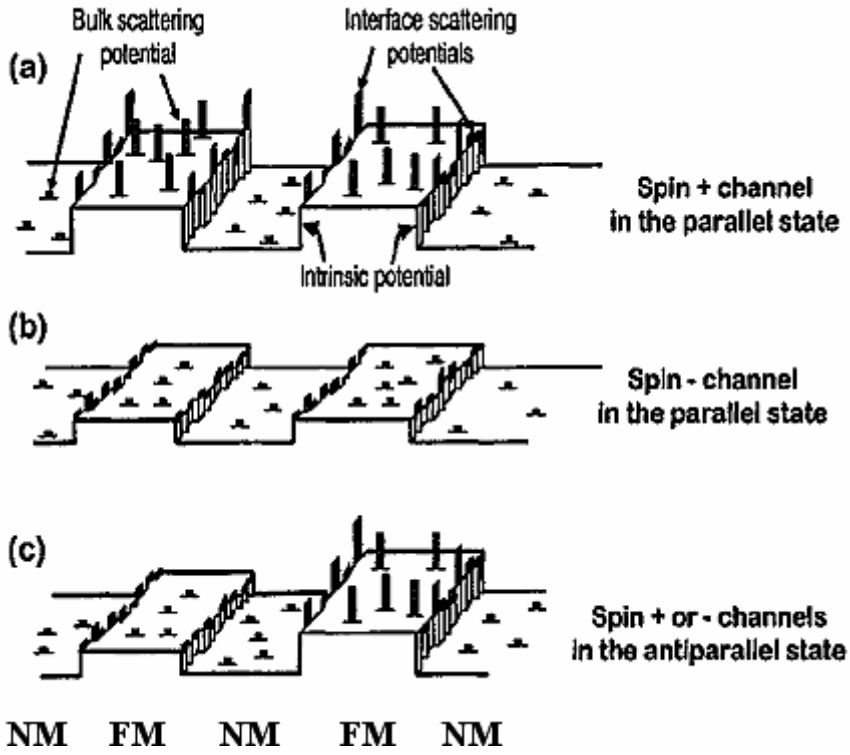

Fig. A.1 - 3 Potential landscape seen by the majority and the minority electrons in a Co/Cu multilayer. The intrinsic potential is represented by a periodic array of barriers; the extrinsic bulk and interface spin-dependent scattering potentials are represented by spikes. (Extracted from ref. 7)

The following paragraph concentrates on describing the specific mechanisms of CPP-GMR, since this is the important geometry for spin-transfer.

A.1.2. CPP-GMR and Valet-Fert theory for metallic multilayers

As mentioned before, in the absence of spin-flip mechanisms, the transport properties of magnetic multilayers in the CPP configuration can be described through a

very simple two-channel resistor model. For each channel, the various layers are considered as carrying the current in series, and interfaces are taken into account as additional spin-dependent resistances. In a FM/NM/FM multilayer, the resistivity for the spin up and spin down channels in the bulk of the layers can be written as:

$$\begin{cases} \rho_{FM}^{\uparrow(\downarrow)} = 2\rho_{FM}^{*}\left[1-(+)\beta\right] \\ \rho_{NM}^{\uparrow(\downarrow)} = 2\rho_{NM}^{*} \end{cases} \quad (6)$$

where β is a coefficient describing the bulk spin scattering asymmetry in the FM layer. ρ_{FM}^{*} and ρ_{NM}^{*} are related to the measurable resistivities ρ_{FM} and ρ_{NM} trough the following expressions:

$$\begin{cases} \rho_{FN} = \rho_{FN}^{*}\left(1-\beta^{2}\right) \\ \rho_{NM} = \rho_{NM}^{*} \end{cases} \quad (7)$$

Similarly, if $R_{FM/NM}$ is the resistance of an interface (which can be determined experimentally) the interfaces can be described using an interfacial spin scattering asymmetry coefficient γ:

$$\begin{cases} R_{F/NM}^{\uparrow(\downarrow)} = 2R_{F/NM}^{*}\left[1-(+)\gamma\right] \\ R_{F/NM} = R_{F/NM}^{*}\left(1-\gamma^{2}\right) \end{cases} \quad (8)$$

Both β and γ take values between -1 and 1, depending on the material. Since the resistance of a homogeneous pillar of section A varies as the resistivity times the thickness of the pillar divided by A, it is common to express the CPP resistance in terms of resistance×area product. This allows for the description of the intrinsic properties of the material independently of geometrical considerations.

Table A. 1-1 gives an overview of the values obtained for CPP parameters to-date. A wide spread is observed in the results published by different groups, since they used different deposition techniques and therefore obtained layers with different microstructures and defects. However, some general trends can still be deduced. For example, scattering asymmetry at the Co/Cu interface ($\gamma_{Co/Cu}$) is larger than in than in bulk Co (β_{Co}). In contrast, NiFe seems to have comparable scattering asymmetry in the bulk and at NiFe/Cu interfaces.

The serial resistance network model has been successfully used to explain a large number of results, obtained mainly at low temperature, in Co based multilayers with relatively thin layers [10]. However, strong deviations from this model were observed in NiFe based systems. Moreover, this model cannot explain the different magnetoresistive properties of multilayers in which the ordering of the layers was changed, for example interleaved $(Co1nm/Cu2nm/Co6nm/Cu2nm)_4$ and separated $(Co1nm/Cu2nm)_4/(Co6nm/Cu2nm)_4$. In the resistor model, the resistances of layers and interfaces are additive, so changing the order of the layers should not alter the result.

	Sputtered multilayers 4.2K (MSU) Bass, 1999 4.2K	MBE grown multilayers List, 1995 4.2K	Grooved substrates Oepts, 1996 4.2K	Electrodeposited nanowires Piraux, 1996 77K	Electrodeposited nanowires Doudin, 1996 20K
$\rho^*_{Cu}(\mu\Omega cm)$	0.6 ± 0.1	1.3 ± 0.3	0.39 ± 0.07	3.1	1.3-3.3
$\rho^*_{Co}(\mu\Omega cm)$	6.6 ± 0.5	3.0 ± 0.6	4.2 ± 0.7	18 ± 2	51-57
β_{Co}	0.38 ± 0.6	0.48 ± 0.04	0.27 ± 0.03	0.36 ± 0.04	0.46 ± 0.05
$AR^*_{Co/Cu}(m\Omega\mu m^2)$	0.38 ± 0.03	0.43 ± 0.04	0.25 ± 0.04	0.30 ± 0.05	0.3-1.1
$\gamma_{Co/Cu}$	0.71 ± 0.05	0.71 ± 0.02	0.50 ± 0.09	0.85 ± 0.10	0.55 ± 0.07
$\rho^*_{NiFe}(\mu\Omega cm)$	15.9			26.3	
β_{NiFe}	0.73			0.8 ± 0.1	
$AR^*_{NiFe/Cu}(m\Omega\mu m^2)$	0.54				
$\gamma_{NiFe/Cu}$	0.70			0.8 ± 0.1	
$l^{sf}_{Cu}(nm)$				140 ± 20	
$l^{sf}_{Co}(nm)$				59 ± 18	
$l^{sf}_{NiFe}(nm)$	5.5			4.3 ± 1	

Table A.1 - 1 CPP-GMR parameters determined experimentally by different groups using different deposition techniques [11]. All the experiments have been performed at low temperature. (Extracted from ref. 8).

It has been demonstrated that the different behavior of the interleaved and separated Co/Cu multilayers is due to the fact that in the AP configuration, the up and down orientations of the magnetizations alternate for interleaved stacks, while separated

multilayers organize so that half of the stack is up and the other half is down, neighboring layers being oriented in the same direction within each half of the stack. The deviations from the simple resistor network model can be explained by taking into account spin accumulation and spin relaxation effects [6].

Spin accumulation can be understood considering an interface separating two magnetic semi-infinite layers oriented antiparallel to each other. Suppose a current is flowing from right to left (i.e. electrons are drifting from left to right), and that spin ↑ electrons are less scattered than spin ↓ (β>0). For simplicity, the magnetization is assumed parallel to the spin of the majority electrons. In the left ferromagnetic layer, far from the interface, the current is mainly carried by spin ↑ electrons. If *J* is the total current density through the multilayer, the currents carried by the two spin channels are:

$$\begin{cases} j^{\uparrow} = \dfrac{J}{2}(1+\beta) \\ j^{\downarrow} = \dfrac{J}{2}(1-\beta) \end{cases} \qquad (9)$$

In the right ferromagnetic layer, the magnetization is oriented in the opposite direction and the roles of spin ↑ and spin ↓ electrons are inverted. More spin ↓ electrons flow away from the interface than spin ↑. Therefore, within each spin channel, there is a clear unbalance between the numbers of electrons moving towards the interface in the left layer and away from the interface in the right layer, per unit time (Fig. A.1 - 4). Consequently, there will be a local excess of spin ↑ electrons and a correlated local deficit in spin ↓ carriers around the interface.

In steady state, spin accumulation does not increase with time, being counterbalanced by spin flip processes, such as spin orbit and magnon scattering. The characteristic length scale over which spins maintain their orientation in a given material is the spin diffusion length l_{sf} , related to the spin-flip relaxation time τ_{sf} via :

$$\frac{1}{(l_{sf})^2} = \frac{1}{(l_{\uparrow})^2} + \frac{1}{(l_{\downarrow})^2} \qquad (10)$$

where the $l_{\uparrow(\downarrow)}$ are given by :

$$l_{\uparrow(\downarrow)} = \left[\frac{1}{3} \left(v_F \lambda_{\uparrow(\downarrow)} \right) \tau_{sf} \right]^{1/2} \qquad (11)$$

In equation (11), v_F is the Fermi velocity, and $\lambda_{\uparrow(\downarrow)}$ are the elastic MFP. Low temperature values of SDL in commonly used materials are given in Table A.1-1.

The equilibrium between spin accumulation and spin relaxation leads to local variations in the difference $\Delta\mu$ between the electrochemical potential of spin up and spin down electrons (Fig. A.1 - 4). Therefore, a small non equilibrium local magnetization, proportional to the current, appears near the interface.

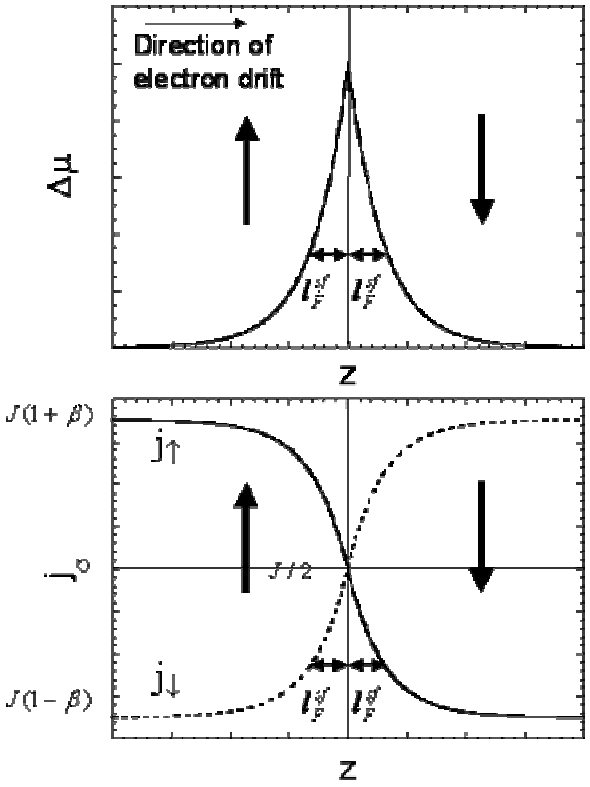

Fig. A.1 - 4 Electrochemical potential (top) and spin current densities (bottom) versus z for an isolated interface separating two semi-infinite domains with opposite magnetizations. The arrows represent the magnetization of the layers and z is the direction of the current (perpendicular to the plane of the layers). It is assumed that for both layers spin up electrons are less scattered than spin down ($\beta > 0$). $\Delta\mu > 0$ implies an accumulation of spin up electrons at the interface. The gradient of the spin current expresses the spin relaxation which takes place on the scale of the SDL on each side of the interface. Spin accumulation reduces the current asymmetry and increases the electric field over a length of the order of SDL on both sides of the interface, which adds an interface resistance of the order of $\rho^* l_{sf}$. (Extracted from ref. 6 and 8).

Starting with a Boltzmann equation model, Valet and Fert calculated the transport properties of magnetic multilayers for the CPP configuration, taking into account both volume and interface spin-dependent scattering. When SDL >> MFP, this model can be reduced to a macrospin approach, based on two basic equations:

$$\begin{cases} 2e\rho^{*}\dfrac{\partial j^{\sigma}}{\partial z} = -\dfrac{\left(\mu^{\sigma} - \mu^{-\sigma}\right)}{\left(l_{sf}\right)^{2}} \\ j^{\sigma} = \dfrac{1}{e\rho^{\sigma}}\dfrac{\partial \mu^{\sigma}}{\partial z} \end{cases} \qquad (12)$$

where e is the absolute value of the electron charge, σ is the spin ($\uparrow$, $\downarrow$) and the resistivities ρ^{*} and ρ^{σ} are given by eq. (6) and (7). The first equation describes spin relaxation effects, whereas the second is a generalized form of Ohm's law.

It can be shown that $\Delta\mu$ obeys a simple diffusion equation within each layer. The general solution of this equation is of the type:

$$\Delta\mu = A\exp\left(\frac{z}{l_{sf}}\right) + B\exp\left(-\frac{z}{l_{sf}}\right) \qquad (13)$$

The coefficients A and B can be determined from boundary conditions at the interfaces, which impose the continuity of the current for each spin channel, in the presence of spin-dependent interfacial resistance:

$$j^{\sigma}(z = z_0^{+}) - j^{\sigma}(z = z_0^{-}) = 0 \qquad (14)$$

(The interface is considered to be located at $z = z_0$.) Moreover, if significant spin scattering occurs in an interfacial zone of surface A which is considered to be infinitesimal thin, the electrochemical potential must fulfill the equation:

$$\mu^{\sigma}(z = z_0^{+}) - \mu^{\sigma}(z = z_0^{-}) = AR^{\sigma}ej^{\sigma}(z = z_0) \qquad (15)$$

Using these formulae, it is possible to calculate the spin accumulation, spin currents, CPP resistance and magnetoresistance of any magnetic multilayered stack, taking into account spin-flip processes [13]. Fig. A.1 – 5 shows the calculated spin accumulation and spin currents for a multilayer containing two ferromagnetic layers alternating with nonmagnetic layers, for both configurations possible (P and AP). The thickness of the magnetic (nonmagnetic) layers is t_{FM} (t_{NM}).

Considering the model of Valet and Fert, the failure of the simple resistor network to explain the CPP-GMR of NiFe based multilayers and the different behavior of separated and interleaved multilayers can be understood in terms of spin relaxation effects. In both types of systems, the length scale over which electrons propagating perpendicular to the plane experience a change from up magnetization to down magnetization is of the order of SDL, which is not longer than the thickness of the layers. Therefore, the assumption of simply additive resistances is incorrect.

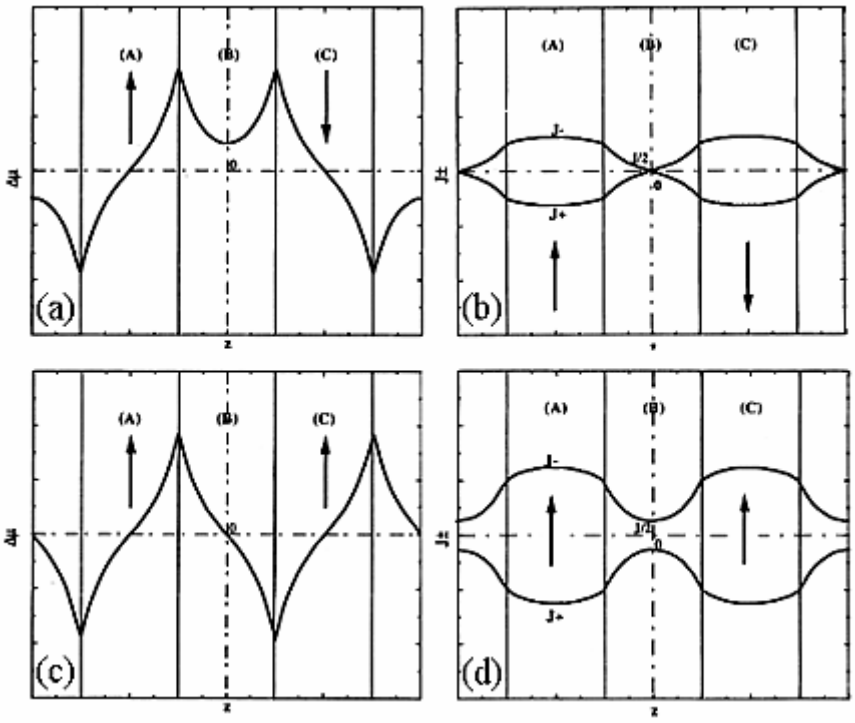

Fig. A.1 - 5 Spin accumulation $\Delta\mu$ (a, c) and spin up and spin down current densities for a magnetic multilayer (F t_{FN} / NM t_{NM}) with an infinite number of repeats, for the case $\beta > 0$. (a) and (b) are calculated for the antiparallel alignment between the two magnetizations, (c) and (d) for the parallel geometry. (Extracted from ref. 6).

It is important to note that the Valet and Fert model only takes into consideration the case of collinear magnetizations in the multilayer. When that is not the case, non-diagonal terms have to be considered in the spin tensors, giving rise to new phenomena.

Resumé :

Généralement, les effets de transfert de spin sont étudiés dans des multicouches métalliques dans lesquelles le courant est appliqué dans la direction perpendiculaire au plan des couches. Dans ces structures, l'aimantation d'une première couche (nommée 'couche libre') peut être orientée parallèlement ou antiparallèlement par rapport au moment magnétique d'une deuxième (appelée 'couche piégée'), considéré comme fixe. L'orientation de l'aimantation de la couche libre peut être changée en appliquant soit un champ magnétique, soit un courant à travers la structure. La résistance de l'empilement est différente dans le deux états : ce phénomène est connu sous le nom de 'magnétorésistance géante' (GMR). La GMR peut dont être utilisée comme sonde pour connaître l'état de la couche libre. En plus, ce phénomène et le transfert de spin sont corrélés à travers la polarisation du courant et les effets d'accumulation de spin. En conséquence, une bonne compréhension des mécanismes de la GMR est nécessaire pour l'analyse des effets induits par le transfert de spin.

Ce chapitre offre une courte description de la magnétoresistance géante. Un premier modèle, simple et intuitif, décrit le multicouche métallique comme un réseau de résistances connectées en série, à travers lesquelles les deux types d'électrons (spin up et spin down) transportent le courant en parallèle. Dans toute couche magnétique, les résistances vues par les électrons spin up et spin down sont différentes.

Un deuxième modèle plus élaboré, introduit par Valet et Fert, permet d'expliquer les détails de ce phénomène en prenant en compte des effets d'accumulation et relaxation de spin.

References :

[1] E.C. Stoner, Proc. Royal Soc. **A165**, 372 (1938)

[2] N.F. Mott and H.H Wills, Proc. Royal Soc. **A156**, 368 (1936)

[3] A. Fert and I.A. Campbell, J. Phys. F **6**, 849 (1976)

[4] R.E. Camley and J. Barnas, Phys. Rev. Lett. **63**, 664 (1989)
J. Barnas et al., Phys. Rev. B **42**, 8110 (1990)

[5] P.M. Levy et al., Phys. Rev. Lett. **65**, 1643 (1990)
A. Vedyaev et al., Phys. Lett. A **198**, 267 (1995)

[6] T. Valet and A. Fert, Phys. Rev. B **48**, 7099 (1993)

[7] C. Vouille et al., Phys. Rev. B **60**, 6710 (1999)

[8] "Spin electronics", edited by M. Johnson

[9] A. Vedyaev et al., Phys. Lett. A **198**, 267 (1995)
J. Barnas and A. Fert, J. Magn. Magn. Mat. **136**, 260 (1994)

[10] W.P. Pratt Jr. et al., Phys. Rev. Lett. **66**, 3060 (1991)
S.F. Lee et al., Phys. Rev. B **46**, 548 (1992)
S.F. Lee et al., J. Magn. Magn. Mat. **118**, L1 (1993)

[11] J. Bass and W.P. Pratt Jr., J. Magn. Magn. Mat. **200**, 274 (1999)
W. Oepts et al., Phys. Rev. B **53**, 14024 (1996)
N.J. List et al., J. Magn. Magn. Mat. **148**, 342 (1995)
L. Piraux et al., J. Magn. Magn. Mat. **159**, L.287 (1996)
B. Doudin et al., J. Appl. Phys. **79**, 6090 (1996)

[12] S. Zhang and P.M. Levy, J. Appl. Phys. 69, **4786** (1991)

[13] N. Strelkov et al., J. Appl. Phys. **94**, 3278 (2003)

Chapter 2. (Some) Spin-transfer theory

As explained before, the GMR effect illustrates the fact that the different relative orientations of the magnetic layers affect the electrical current, so that different configurations correspond to different measured resistances of the multilayer. The reciprocal phenomenon, that a spin-polarized current can transfer spin angular momentum to the magnetization of a layer and therefore alter its magnetic state, has also been demonstrated. This effect has been the object of intense study during the last few years, both theoretically and experimentally. Several numerical simulations have also been published. This chapter aims at an introduction to the theory of spin-transfer. The next chapters give an overview of numerical simulations and experimental studies in this field.

Theoretical works on spin-transfer can be divided in three categories [1]:

1. Models focusing on deriving and solving classical equations of motion for the magnetization under the effect of spin polarized current [2]. These studies generalize and solve the Landau-Lifshitz-Gilbert equation to take into account spin currents, spin accumulation and the mechanical torques generated by the transfer of spin angular momentum between current and magnetization.
2. Models generalizing charge transport theory to take account of spin currents and spin relaxation effects [3]. Using phenomenological methods or quantum mechanical formalisms (Boltzmann, Kubo or Landauer), these theories determine the spin-transfer torques that serve as input to the magnetization calculations.
3. Models which compute from quantum mechanical considerations various parameters that are used by the transport theories [4].

On the other hand, the early theories considered transport through the multilayer either as a purely ballistic [5] (A.1.2) or purely diffusive [6] problem (A.1.3). More recent models [7] regard transport as diffusive in the bulk of the layers and diffusive and / or ballistic at the interfaces.

A.2.1. Model structure

The essence of spin-transfer induced effects is that a spin polarized current entering a ferromagnetic layer exerts a torque on its magnetization. Consequently, it can generate magnetic excitations, and even flip the magnetization of a given domain under certain conditions.

The model structure used to study this effect contains two magnetic layers, separated by a non-magnetic spacer (Fig. A.2 – 1). Both magnetic layers are considered as single domains. Their moments are supposed to be oriented at an angle θ relative to each other (where $\theta \neq 0, \pi$, or else, no torque is exerted).

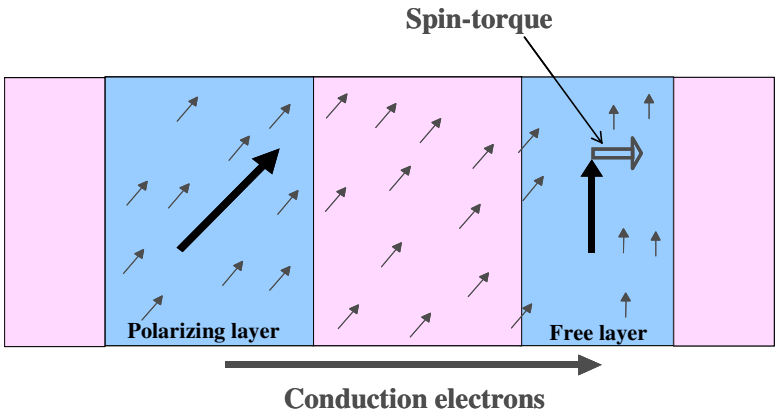

Fig. A.2 - 1 Model structure for the study of spin-transfer. The spin-torque exerted on the magnetization of the free layer is drawn for the case when the current is applied so that the electrons flow from the polarizing to the free layer. On the left and the right part of the stack there are two non-magnetic conducting leads.

One of the magnetic layers should be thicker than the other, for two reasons:

1. This layer should be thick enough to induce a considerable spin polarization of the current;
2. Since spin-transfer is essentially an interfacial effect, occurring mainly on a characteristic length scale of about 1 nm from the interface, spin-transfer effects are more important in a thin layer than in a thick one. Consequently, by associating a thin and a thick layer, the latter can be considered as a reference layer with fixed magnetization, whereas the orientation of the moment of the thinner layer will be influenced by spin-transfer.

The role of the spacer is to decouple the ferromagnetic layers. Its thickness should be small compared to SDL, so that the spin polarization gained by the current while crossing the polarizing layer is mostly transmitted to the free layer.

The current is applied perpendicular to the plane of the layers. On each side of the magnetic multilayer there is a non-magnetic conducting lead.

A.2.2. Mechanisms of spin-transfer

Inside a bulk ferromagnetic metal, Ohm's law guarantees that the current is naturally polarized, the conductivities of majority and minority spin electrons being different. By the same argument, the current is obviously non-polarized in a non-magnetic metal, since spin up and spin down electrons have the same conductivities.

Suppose a current is applied through the model structure in fig. A.2 – 1 so that the electrons flow from the thick to the free layer. While crossing the thick magnetic layer, the current will acquire a spin polarization. When the spin polarized current reaches the interface between the non-magnetic spacer and the second magnetic layer, three different processes occur [8]:

1. **Spin filtering**: The reflection and transmission probabilities for up and down electrons are spin dependent. The wave function for an electron with a non-zero spin component transverse to the magnetization can always be written as a linear combination of spin up and spin down components. The reflected and transmitted wave functions differ both from each other and from the incident state. This unavoidably leads to different transverse spin components and thus to a **discontinuity in the transverse spin current**. This is a one-electron effect that operates independently for each carrier.
2. **Differential spin reflection**: The spin of an electron generally rotates when it is reflected or transmitted at the interface between a non-magnetic material and a ferromagnetic layer. The rotation is non-classical and its amount differs considerably for electrons with wave vectors from different portions of the Fermi surface. While summing over all conduction electrons, **very little remains of the reflected transverse spin current**. The cancellation effect on the transmitted spin current is less dramatic.

3. **Differential spin precession**: Due to exchange splitting, the electrons transmitted into the ferromagnetic layer possess spin up and spin down components with the same total energy (Fermi energy), but with different kinetic energy and therefore different wave vectors. Consequently, each spin precesses in space as it propagates from the interface. The precession frequency varies noticeably over the Fermi surface. As they propagate into the ferromagnetic layer, a rapid dephasing of the transverse spin components of individual electrons occurs. Averaging on all the conduction electrons, **the precessing spin current cancels within few lattice constants from the interface**.

Through all the three processes mentioned above, the electrons lose transverse spin angular momentum. From the conservation law, it follows that the transverse angular momentum lost by the current is transmitted to the magnetic moment of the free layer. This can be expressed in terms of a torque acting on its magnetization. **In other words, the origin of the torque is the angular momentum transfer and the origin of angular momentum transfer is the absorption of transverse spin current at the interface. Therefore, to a good approximation, the torque is proportional to the transverse component of the spin current.** This assumption is generally accepted to-date, and agrees with most models published, whether they consider purely ballistic or purely diffusive transport in the multilayer – or a mixture of the two.

A.2.3. Ballistic theory: Slonczewski's original model

In 1996, Slonczewski introduced the term "spin-transfer", defining the interaction between a spin polarized current and a magnetic layer [9]. He calculated that for layers with a lateral size of the order of 100 nm, spin-transfer can dominate the Oersted field induced effects. In the same article, Slonczewski predicted that: **"two new phenomena become possible: a steady precession driven by a constant current, and alternatively a novel form of switching driven by a pulsed current"**. Needless to say, both predictions have since been demonstrated experimentally.

Slonczewski appreciated that in magnetic multilayers incorporating very thin metallic spacers spin-transfer effects would be more easily measurable than in magnetic tunnel junctions, for two reasons:

1. A metallic spacer implies low resistance and therefore low Ohmic dissipation for a given current; since spin-transfer effects are proportional to the current, they would become detectable for current densities above 10^6 A/cm². In contrast, the current densities which can be applied through magnetic tunnel junctions are most often too low to allow the observation of such phenomena.

2. The fundamental interlayer exchange coupling of RKKY type diminishes in strength and varies in sign as spacer thicknesses increases. Therefore, it is possible to find spacers which are thick enough (~ 4 nm) for the exchange coupling to be negligible, even though spin relaxation is too weak to significantly diminish the GMR. (In consequence, one can consider that no spin polarization is lost in the spacer).

Slonczewski considered a structure similar to the one in Fig. A.2 – 1, so that the conduction electrons flow from the polarizing to the free layer for the positive sense of the current, and in the opposite direction for the negative sense. He used the method of spin currents and momentum conservation widely employed in deriving the conventional exchange coupling, and made the following assumptions:

1. By conservation of angular momentum, the free magnetic layer reacts to the passage of the spin current by acquiring a change of classical momentum equal to the sum of the inward spin fluxes from both sides of the free layer;

2. The mean of spin-transfer averaged with respect to the direction of electron motion is equal to the total absorption of the expectation value of the transverse spin component of the electron incident on the free layer;

3. The thickness of the free layer is too great for appreciable tunneling of minority spins electrons; majority electrons are totally transmitted and the transport is considered to be ballistic;

4. The magnetic layers have the same band structure, but different thickness.

With these assumptions, it is possible to describe mathematically the complete transfer of the transverse component of the incident electron spin to the local magnetization. **As such, an electric current composed of preferentially polarized incident electrons generally induces a well-defined motion of the free layer's magnetization.**

The equations are solved in the WKB limit for a general value of θ. The off-diagonal nature of the spin wave matrix dictates that scattering from a ferromagnetic layer completely annihilates the component of the spin current perpendicular to its magnetization. **Therefore, the transverse component of the angular momentum of**

the spin current is transmitted to the magnetic moment of the layer. This can be expressed in terms of a mechanical torque acting on the moment of the ferromagnet. When the magnetizations of the two layers are collinear, the transverse component is zero and the torque is zero.

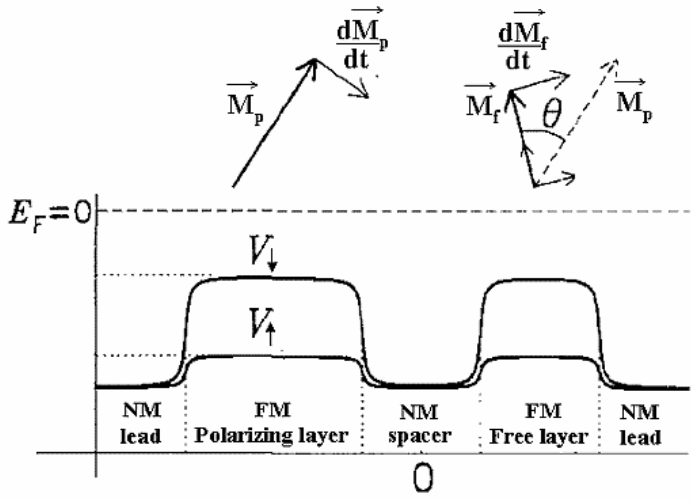

Fig. A.2 - 2 Bottom: Coulomb plus locally diagonalized exchange potential $V_{\uparrow(\downarrow)}$ versus position in the direction perpendicular to the plane of the layers in a multilayer including two ferromagnetic and three non-magnetic layers. **Top:** Vector diagram for the magnetizations of the two layers and their current-driven velocities. (Extracted from ref. 9.)

If n_+ (n_-) are the majority (minority) spin densities in the ferromagnetic material, the polarizing factor P can be defined as:

$$P = \frac{n_+ - n_-}{n_+ + n_-} \tag{16}$$

The spin-transfer torque can be written:

$$\vec{\Gamma}_{st} = -\frac{\hbar}{2e} \cdot \frac{\gamma}{M_s A t} \cdot g(\theta) \cdot I \cdot \vec{m} \times \left[\vec{m} \times \left(-\vec{u}_x\right)\right] \tag{17}$$

where: e is the electron charge in absolute value;

γ is the gyromagnetic ratio;

M_s is the saturation magnetization of the free layer;

A is the surface of the layer, perpendicular to the direction of the current;

t is the thickness of the free layer;

I is the applied current;

$\vec{m}$ is the unit vector parallel to the magnetization of the free layer;

$-\vec{u}_x$ is the unit vector parallel to the magnetization of the pinned layer.

$g(\theta)$ is a function of the polarization of the current and of the angle between the magnetizations of the two layers. In his initial article published in 1996, Slonczewski calculates $g(\theta)$ as:

$$g(\theta) = \frac{1}{-4 + \frac{(1+P)^3 (3+\cos\theta)}{4P^{3/2}}} \tag{18}$$

It is important to note that the dynamics is reversible with respect to the sign of the current. At the same time, the absolute value of the torque acting on the magnetization of the free layer is equal to that acting on the magnetization on the pinned layer. (The reflected minority electrons transfer back the spin to the thick layer.)

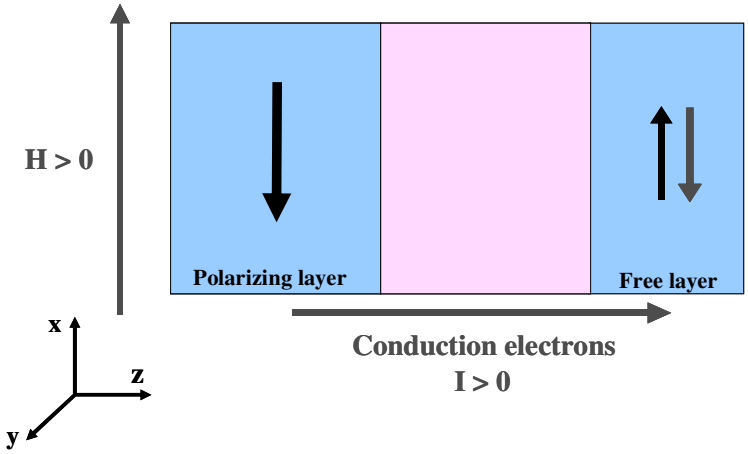

Fig. A.2 - 3 Coordinates system used: the magnetization of the polarizing layer is considered to be oriented along $-x$; the positive sense of the current is defined so that the electrons flow from the thick to the thin layer, along the z axis. This definition of positive field and current corresponds to the one used in Part B: Spin-transfer effects in spin-valves developed for CPP-GMR heads.

Equation (17) can be deduced from geometrical considerations. The counter-intuitive tendency for the magnetizations of the two layers to rotate in the same direction results from the angular momentum conservation in the pinned and free layers. It is this unique property of current-driven exchange that generates the novel magnetic dynamics.

The dynamics of the free layer's magnetization under the effect of a magnetic field H_{res} (which includes external, anisotropy and Oersted fields and dipolar coupling) and a current I can be described using a Landau-Lifshitz-Gilbert equation with a supplementary spin-torque term:

$$\frac{\partial \vec{m}}{\partial t} = -\gamma\, \vec{m}\times\left[\left(H_{res} \mp H_k\right)\cdot\vec{u}_x - H_d\left(\vec{m}\cdot\vec{u}_z\right)\cdot\vec{u}_z\right] + \alpha\cdot\left(\vec{m}\times\frac{\partial \vec{m}}{\partial t}\right) - \frac{\hbar}{2e}\cdot\frac{\gamma}{M_s At}\cdot g(\theta)\cdot I\cdot\vec{m}\times\left[\vec{m}\times\left(-\vec{u}_x\right)\right] \tag{19}$$

where $H_d = 4\pi M_s$ is the demagnetizing field (in the direction perpendicular to the plane of the layers),

H_k is the uniaxial anisotropy, and

α is the Gilbert damping parameter.

The positive sense of the field is considered to be along $-\vec{u}_x$. From eq. (19), it is possible to determine the instability currents, that is, the currents that drive the magnetization out of a given stable state:

$$\begin{cases} I^{P-AP} = \dfrac{2e}{\hbar}\dfrac{\alpha M_s At}{g(0)}\left(-\dfrac{Hd}{2} + H_{res} - H_k\right) \\ I^{AP-P} = \dfrac{2e}{\hbar}\dfrac{\alpha M_s At}{g(\pi)}\left(\dfrac{Hd}{2} + H_{res} + H_k\right) \end{cases} \tag{20}$$

Slonczewski calculated that magnetization precession with frequencies around 10 GHz can be induced by current around 10^6 A/cm². The switching currents were predicted to be of the order of 10^7 A/cm².

This theory has been extended [10] to combine ballistic and diffusive features (and take into account spin accumulation). The main difference from the fully ballistic model lies in the dependence of the torque on the entire structure of the multilayer, including the magnets and the non-magnetic leads.

A.2.4. Diffusive theory: the model of Zhang, Levy and Fert

Among others [for example ref. 7] Zhang, Levy and Fert introduced a model including spin diffusion effects in the study of spin-transfer [11]. They solved the equation of motion of the spin accumulation in order to derive the torque acting on the

background magnetization. Spin dependent scattering (both bulk and interfacial) and spin accumulation have proved to be necessary for understanding the CPP-GMR (see Chapter 1). The main achievement of this model was to express spin torques in terms of the same parameters as used for interpreting giant magnetoresistance in the CPP geometry. Following the conventional treatment of CPP transport in magnetic multilayers, it can be assumed that the magnetization is uniform within each layer and changes discontinuously at the interfaces. The boundary conditions at the diffusive interfaces between two layers with noncollinear magnetizations impose that the spin accumulation experiences a jump proportional to the interface resistance. The spin currents are either continuous, if no interfacial spin-flip is considered, or discontinuous in the opposite case. Specular reflection at the interfaces can also be taken into account.

Considering a multilayer such as the model structure in fig. A.2 – 1, with the current flowing uniformly along the z direction, the linear response of the multilayer to an electrical field can be written as a spinor form:

$$\hat{j} = \hat{C} \cdot E(z) - \hat{D} \frac{\partial \hat{n}}{\partial z} \tag{21}$$

where $E(z)$ is the electrical field, and $\hat{j}$, $\hat{C}$, $\hat{D}$, and $\hat{n}$ are 2×2 matrices representing the current, conductivity, diffusion constant, and accumulation at a given point. They can be written in terms of Pauli spin matrices:

$$\begin{cases} \hat{C} = C_0 \hat{I} + \boldsymbol{\sigma} \cdot \vec{C} \\ \hat{D} = D_0 \hat{I} + \boldsymbol{\sigma} \cdot \vec{D} \\ \hat{n} = n_0 \hat{I} + \boldsymbol{\sigma} \cdot \vec{n}_m \end{cases} \tag{22}$$

where $2n_0$ is the charge accumulation and $\vec{n}_m$ is the spin accumulation. If $\vec{m}$ is the unit vector of the local magnetization, the spin polarization parameter β is defined as:

$$\vec{C} = \beta \cdot C_0 \cdot \vec{m} \tag{23}$$

A similar spin polarization constant β' can be introduced for the diffusion constant:

$$\vec{D} = \beta' \cdot D_0 \cdot \vec{m} \tag{24}$$

If the densities of states are different for the spin up and spin down electrons, β and β' are different. For a degenerate metal with $\hat{N}(\varepsilon_F)$ the density of states at the Fermi level, conductivity and diffusion constants are related through the Einstein relation:

$$\hat{C} = e^2 \hat{N}(\varepsilon_F)\hat{D} \tag{25}$$

The interaction between the spin accumulation and the local magnetic moment is described as an exchange interaction:

$$H_{\text{int}} = -J \cdot \vec{n}_m \cdot \vec{m} \tag{26}$$

With these definitions, and bearing in mind that only the component of the spin accumulation transverse to the local magnetization will influence the local moment, it is possible to show that the equation of motion of the magnetization under the effect of a spin polarized current can be written as:

$$\frac{\partial \vec{m}}{\partial t} = -\gamma\ \vec{m} \times \left(\vec{H}_{res} - b\vec{m}_p\right) + \alpha \cdot \vec{m} \times \frac{\partial \vec{m}}{\partial t} - \gamma \cdot a \cdot \vec{m} \times \left(\vec{m} \times \vec{m}_p\right) \tag{27}$$

where $\vec{m}_p$ is the unit vector parallel to the magnetization of the pinned layer and *a* and *b* are coefficients determined by geometric and structural details of the multilayer.

Eq. (27) expresses the fact that the transverse spin accumulation produces two effects simultaneously:

1. Depending on the sense of the current, the **spin-torque** term $a \cdot \vec{m} \times \left(\vec{m} \times \vec{m}_p\right)$, first introduced by Slonczewski, acts so as to increase or decrease the angle between the magnetizations of the two layers (in other words, depending on the sign of the current, the spin-torque acts as damping or antidamping);
2. The term $b \cdot \left(\vec{m} \times \vec{m}_p\right)$ is the torque due to an **effective field** $b \cdot \vec{m}_p$, which produces a precessional motion around the magnetization of the polarizing layer, acting as if spin-transfer created an equivalent magnetic field on the free layer.

It is important to note that in eq. (27) the two terms appear on equal footing. Indeed, it has been estimated that although the effective field decreases much faster than the spin torque as the thickness of the layers is increased, both have the same magnitude at their maximum [12]. The coefficients *a* and *b* have to be calculated for each system in particular. To derive the effective field and the spin torque analytically, an oversimplified case has to be considered.

The following assumptions are made:

1. The thick ferromagnetic layer is assumed to be pinned and half metallic, so that the current is fully polarized (spin accumulation is neglected in the pinned layer);
2. The spacer is infinitely thin and no spin-flip scattering occurs in this region, so that the spin current is conserved across this layer; the leads are perfect paramagnets;

3. The characteristic times of transport phenomena are much shorter (fs to ps) than the characteristic time of magnetization motion (ns); therefore, the background magnetization can be assumed to be fixed on the transport time scale, so that the equations for magnetization dynamics and for spin accumulation can be decoupled;

4. Spin-dependent reflection at the interfaces can be neglected;

5. SDL is the same in both magnetic layers; one can introduce:

$$\lambda_{sf} = \sqrt{2D_0\tau_{sf}} \tag{28}$$

$$l_{sf} = \sqrt{1-\beta\beta'}\cdot\lambda_{sf} \tag{29}$$

a and b are determined by first calculating the spin accumulation at a position z in the free layer and then averaging it over $0 \le x \le t$ (where t is the thickness of the free layer):

$$\begin{cases} a = -\dfrac{hja_0^3}{\sqrt{2}e\mu_B\lambda_J}\left(\dfrac{1-\cos\dfrac{t}{\sqrt{2}\lambda_J}\cdot e^{-\frac{t}{\sqrt{2}\lambda_J}}}{\dfrac{t}{\sqrt{2}\lambda_J}}\right) \\ b = \dfrac{hja_0^3}{\sqrt{2}e\mu_B\lambda_J}\left(\dfrac{\sin\dfrac{t}{\sqrt{2}\lambda_J}\cdot e^{-\frac{t}{\sqrt{2}\lambda_J}}}{\dfrac{t}{\sqrt{2}\lambda_J}}\right) \end{cases} \tag{30}$$

where j is the current density in the pillar, $j = I/A$,

a_0 is the lattice constant,

μ_B is the Bohr magneton.

The characteristic decay length for the spin accumulation is defined as:

$$\lambda_J = \sqrt{\frac{2hD_0}{J}} \tag{31}$$

The above expressions for a and b are only valid in the limit $\lambda_{sf} >> \lambda_J$. This condition holds in the case of cobalt, for example, where λ_J is of the order of 1 nm. λ_J is the characteristic length scale for spin accumulation in the direction perpendicular to the plane of the layers. At the interface, the spin accumulation has to adjust to the new magnetization direction. Both the longitudinal and the transverse components of the spin accumulation experience changes of the same order of magnitude; however, the distance over which the transverse component is absorbed, λ_J (~ 1 nm) is much smaller

than that for the longitudinal spin accumulation l_{sf} (~ 60 nm). Far from the interfaces, at $z >> \lambda_J$ and $z << -\lambda_J$, the spin current is collinear with either the magnetization of the free layer or that of the polarizing layer, approaching the bulk values in the respective materials; for $-\lambda_J < z < \lambda_J$, a strong gradient is found in the transverse spin accumulation, and it is this gradient that contributes to the spin-transfer. As a consequence, λ_J is also the characteristic length scale for spin momentum transfer.

Similar calculations can be also performed if the approximation $\lambda_{sf} >> \lambda_J$ is no longer valid, or for the more general case when the polarizing layer is not half metallic and taking into consideration spin-dependent reflection at the interfaces. Also, a more realistic analysis should treat the spin accumulation in the polarizing and the free layer in a self consistent manner. However, although the expressions for the two coefficients are more complicated in the general case, the oversimplified example above conveys the physical result of the diffusive model.

Different authors have applied this formalism to interfacial [13] ($\lambda_J \approx 1$ nm) and non-interfacial [14] ($\lambda_J = 4$ nm, for example) spin-transfer. The main difference between the two limits is that in the case when purely interfacial spin-transfer is considered, the effective field term becomes much less important than the spin torque term. Experimental results have been interpreted as agreeing with one concept [12] or the other [15].

Whether considering the interfacial or the non-interfacial approach, when calculations are carried out taking into account the entire structure (including the current leads), it turns out that the spin angular momentum transferred from the polarized current to the background magnetization of the free layer far exceeds the transverse component of the bare portion of the incoming spin polarized current (Fig. A.2 – 4). This amplification is due to the large gradient of the transverse spin accumulation at the interface between the spacer and the free layer, which generates very strong local diffusion transverse spin currents. Fert et al. estimate this enhancement to be of the order of the mean value of SDL divided by MFP in all the structure, including the leads ($\langle l_{sf} / \lambda_{sdl} \rangle$) [13]. Shpiro et al. evaluate the amplification to be proportional to the ratio of SDL to the characteristic length scale of the spin accumulation (l_{sf} / λ_J). Slonczewski found a similar effect in his “diffusive” model [9]. It was pointed out that

this amplification effect might be used in order to reduce the switching currents in view of spintronics applications.

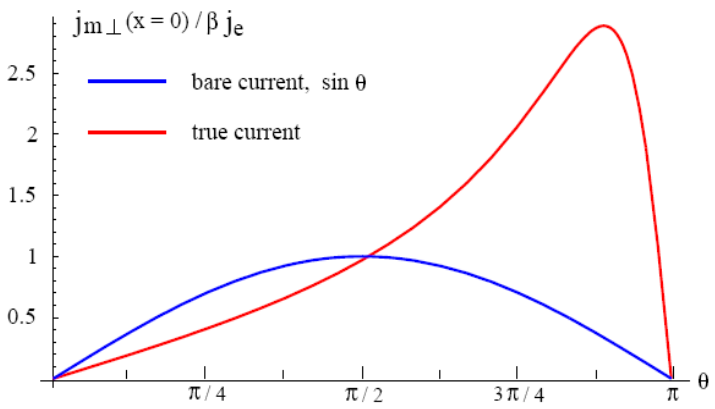

Fig. A.2 - 4 True spin current at the interface between the spacer and the free layer (red line) in comparison with the bare transverse current (blue line) as a function of the angle between the magnetizations of the two layers, for $\lambda_J = 4$ nm and $l_{sf} = 60$ nm. (Extracted from ref. 10).

It is important to note that calculations considering diffusive transport find that there is a strong asymmetry between the spin-torque exerted on the free layer's magnetization close to the P or AP configurations, similar to the ballistic model of Slonczewski. While in Slonczewski's case the asymmetry was expressed through the dependence of the spin-torque on the function $g(\theta)$, in the diffusive limit the asymmetry is the result of the different values taken by transverse spin accumulation for different configurations.

A.2.5. Magnetic temperature model

In order to account for the strongly incoherent dynamics observed experimentally at finite field when studying spin-transfer effects, S. Urazhdin [16] introduced a quantum model which describes the effect of a spin polarized current on the magnetization of a layer in terms of an effective magnetic temperature rather than a spin-torque. This model portrays current induced magnetization reversal as thermally

activated switching over a one-dimensional potential barrier, with an effective temperature $T_m(I)$ which depends on the current. It was argued that T_m can differ from the lattice temperature T_{ph} in confined geometry, where the magnetic energy relaxes significantly more slowly than the highly excited individual magnetic modes.

For a current I flowing through the pillar, $T_m^P(I) \neq T_m^{AP}(I)$. (The positive sense of the current is defined so that the electrons flow from the polarizing to the free layer.) In the P state, for negative currents higher than a threshold value, magnetic excitations lead to an increase of T_m^P so that a thermally activated transition to AP occurs. For this direction of the current, the conditions for magnetic excitations are not satisfied for the AP state, so the magnetic system cools back to the lattice temperature, and the AP state is stable. If then, for the same current, a field higher than the coercivity of the free layer is applied so that it favors the P state, the transition from the antiparallel to the parallel orientation can also be thermally activated, leading to telegraph noise. Similar behavior is expected when the current and the field are reversed.

Although the mechanisms are different for magnetic temperature and spin-torque models, the stability phase diagrams are very similar. Also, the actual switching dynamics may be the same, since thermally activated switching occurs through an almost deterministic optimal path, which can be very close to a coherent rotation.

A.2.6. Important parameters

While several details concerning spin-transfer effects remain controversial and nut fully understood, the scientific community seems to have reached a consensus over several aspects of the problem:

A.2.6.a. Sign of the torque

The torque is proportional to the current density flowing through the multilayer, and it changes sign when the current is reversed. When the current is applied so that the

electrons flow from the polarizing to the free layer, the resulting torque tends to align the magnetization of the latter parallel to that of the former. If the current direction is reversed, the torque acts so as to bring the two magnetizations in the antiparallel state.

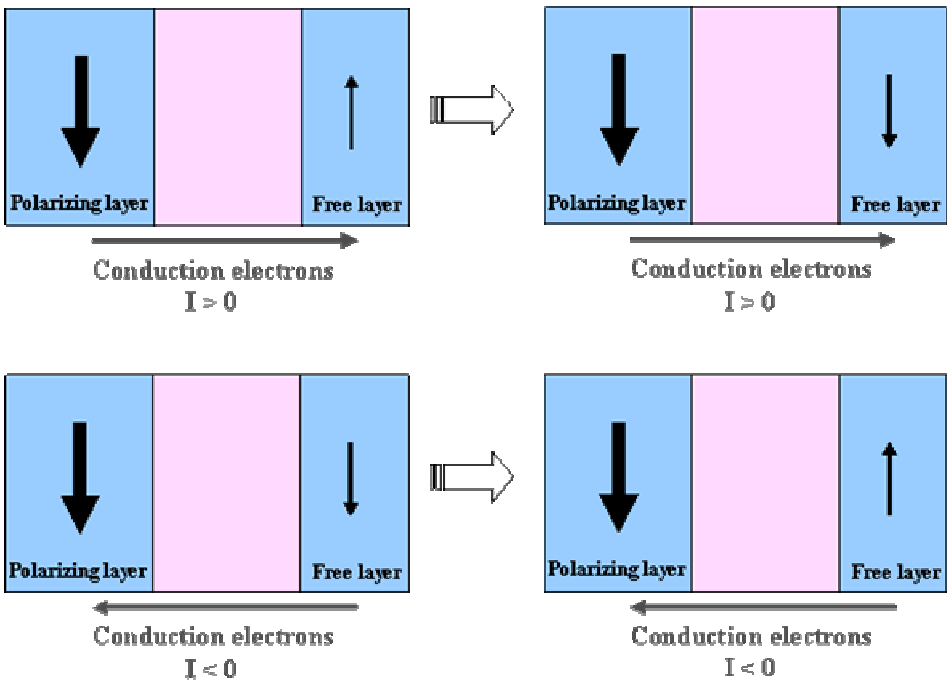

Fig. A.2 - 5 Top: When a positive current is applied, the electrons flow from the pinned to the free layer and the torque favors the parallel alignment between the magnetizations of the two layers. **Bottom:** The opposite sense of the current generates a torque that tends to bring the magnetization of the free layer to the direction antiparallel with respect to the moment of the thick layer.

A.2.6.b. The decay length

It is mostly accepted that the transverse component of the spin polarized current is absorbed in a few atomic layers from the interface. The quantum mechanical analysis of Stiles and Zangwill [8], for example, finds that in general the spin-transfer takes place in the first nanometer of the free layer. Their calculations are restricted to Ohmic transport but should be valid for most metallic multilayers where layer thicknesses are less than the relevant mean-free paths. Shpiro, Levy and Zhang consider, however, that the decay length can be much longer (~ 5 nm) [14].

A.2.6.c. Instability and switching currents

The instability currents are the currents that drive the magnetization out of a given stable state

$$j^{\mp} = \frac{I^{\mp}}{A} \sim \alpha \cdot M_s \cdot t \cdot f(\theta) \cdot \left(\mp \frac{Hd}{2} + Hres \mp H_k \right) \qquad (32)$$

The instability current densities depend on the free layer's thickness and structure (they are proportional to the Gilbert damping constant, the anisotropy fields and saturation magnetization) and on the applied field. They decrease as the thickness of the polarizing layer increases, saturating at a minimum level when the thickness exceeds the SDL (and the polarization of the current reaches its maximum). The instability currents increase with the spacer thickness (at the scale of the mean free path), because this implies a decrease of the polarization.

The instability currents depend on the angle θ between the two magnetizations, though the expression of the angle dependence depends on the theory considered. Different calculations find that one or the other of the two currents should be higher. Stiles and Zangwill, for example, calculated that the $g(\theta)$ function from Slonczewki's ballistic theory should vary between ~ 0.2 for $\theta = 0$ and ~ 0.58 for $\theta = \pi$. (In Sloczewski's ballistic theory, the instability currents are inversely proportional to $g(\theta)$, see eq. (20)).

The switching (critical) currents are the smallest currents which can actually induce the switching of the free layer's magnetization from one orientation to the other (from parallel to antiparallel, and back). They are usually found to be slightly higher than the instability currents. It is possible to deduce analytic formulae for the critical currents starting from the Landau-Lifshitz-Gilbert equation with a spin-torque term and by means of bifurcation theory [19]. However, the expressions thus obtained are fairly complicated. In most cases, in order to compare experimental results and theory, the formulae for the instability currents are used to fit the measured values for the switching currents.

A.2.6.d. Amplification factor and non-magnetic lead influence

Recent theories seem to agree that the diffusion currents generated by transverse spin accumulation discontinuities can be much higher than the charge currents. The value of the amplification factor differs in various models, but it seems to depend (among others) on the properties of the non-magnetic leads at the extremities of the multilayer. Recent experimental results apparently support this finding [17].

A.2.6.e. Effective field

No consensus has been reached to-date on the question whether the spin polarized current produces an effective field as well as a spin-torque. Different groups (dealing either with the theoretical or experimental aspects of the problem) have argued that the current generates only a spin torque, that it generates both spin-torque and effective field but the effective field term is an order of magnitude lower than the spin torque, or that it generates both and they are equally important. However, from an experimental point of view, it is generally difficult to distinguish between an effective field generated by the spin current and any other fields that may arise in the system (especially current-induced fields related to a non-uniform flow of the current through the pillar).

A.2.6.f. Presence of a polarizing layer

It has been lately suggested that the presence of a polarizing layer is not necessary to observe spin-transfer induced precession [18]. In a non-magnetic lead / ferromagnetic film / non-magnetic lead geometry, with a magnetic field applied perpendicular to the plane of the layers, an unpolarized current can still generate magnetic excitations. Two sources for spin-transfer torque can be identified: longitudinal asymmetry of the magnetization and longitudinal asymmetry of the leads.

Indeed, when a non-polarized current approaches the interface with the ferromagnetic film, continuity of spin currents induces spin accumulation. This can be

expressed in terms of a flow of spins parallel to the magnetization in the ferromagnet, superimposed with a flow of antiparallel spins away from the interface, into the non-magnetic layer. If the magnetization is uniform, the 'imprinted' spins only encounter spins parallel to themselves, because all the imprinting was done by ferromagnetic moments that are parallel. When the magnetization varies along the interface, the imprinting ferromagnetic moments differ in their transverse directions, so that spins diffusing back into the non-magnetic lead typically encounter spins whose transverse components are different than their own. When summing up over all conduction electrons, the outcome is a net reduction of the transverse spin accumulation, which increases with the distance from the interface, as the transverse and longitudinal diffusion superimpose. This results in a corresponding increase in the transverse spin current near the interface, and therefore a torque which tends to rotate the local moments away from the normal to the interface. In other words, when the current flows from a paramagnetic to a ferromagnetic layer, it gains a spin polarization that acts on the non-uniform magnetization of the ferromagnet so as to generate an increasing precessional instability. Through a similar reasoning, it is found that when the current flows from the ferromagnet to a non-magnetic layer, it generates a torque that tends to suppress a precessional instability. In a paramagnetic / ferromagnetic / paramagnetic multilayer with two identical interfaces, the torque generated at one end of the ferromagnetic layer should cancel the one generated at the other end. However, in a real system interfaces are different and the two torques do not cancel.

The presence of a second polarizing layer tends to enhance the precessional instability. As a practical matter, this means that the critical current for the onset of precession is lower when two ferromagnets are present than in the case of a single ferromagnetic layer.

Resumé :

Ce deuxième chapitre de la partie du mémoire qui traite de l'état de l'art a pour but de constituer une introduction dans la théorie des effets de transfert de spin. Etant donné le grand nombre de modèles qui ont été publiés les dernières années, seulement les plus représentatifs sont mentionnés ici.

Les premiers modèles sur le transfert de spin décrivait le transport du courant à travers le multicouche soit en tant que purement balistique (comme la théorie de Slonczewski), soit en tant que diffusif (par exemple, la théorie de Zhang, Levy et Fert). Plus récemment, ces modèles ont été revus pour prendre en compte un transport diffusif à l'intérieur des couches et diffusif et/ou balistique aux interfaces. Un troisième modèle, celui de la température magnétique, propose une approche différente, qui a néanmoins été invalidée par des résultats récents.

References:

[1] M.D. Stiles and A. Zangwill, Phys. Rev. B **66**, 014407 (2002)

[2] Ya.B. Bazaliy et al., Phys. Rev. B **57**, R3213 (1998); J. Appl. Phys. **89**, 6793 (2001)
J.Z. Sun, Phys. Rev. B **62**, 570 (2000)
C. Heide, Phys. Rev. Lett. **87**, 197201 (2001)
J. Miltat et al., J. Appl. Phys. **89**, 6982 (2001)
S. Zhang and P.M. Levy, Phys. Rev. B. **65**, 052409 (2002)
Ya. Tserkovnyak et al., Phys. Rev. Lett. **88**, 119601 (2002)

[3] J.-E. Wegrowe, Phys. Rev. B **62**, 1067 (2000)
A. Brataas et al., Phys. Rev. Lett **84**, 2481 (2000); Eur. Phys. J. B **22**, 99 (2001)
X. Waintal et al., Phys. Rev. B **62**, 12317 (2000)
D.H. Hernando et al., Phys. Rev. B **62**, 5700 (2000)
M.D. Stiles and A. Zangwill, J. Appl. Phys. **91**, 6812 (2002); Phys. Rev. B **66**, 014407 (2002)

[4] J.C. Slonzewski, J. Magn. Magn. Mater. **159**, L1 (1996); **195,** L261 (1999); **247**, 324 (2002)
L. Berger, Phys. Rev. B **54**, 9359 (1996); J. Appl. Phys. **81**, 4880 (1997); Phys. Rev. B **59**, 11465 (1999); J. Appl. Phys. **89**, 5521 (2001); J. Appl. Phys. **91**, 6795 (2002)
K. Xia et al., Phys. Rev. B **65**, 220401 (2002)

[5] J.C. Slonzewski, J. Magn. Magn. Mat. **159**, L1 (1996)
L. Berger, Phys. Rev. B **54**, 9353 (1996)
Ya.B. Bazaliy et al., Phys. Rev. B **57**, R3213 (1998)
X. Waintal et al., Phys. Rev. B **62**, 12317 (2000)

[6] S. Zhang et al., Phys. Rev. Lett. **88**, 236601 (2002)

[7] M.D. Stiles and A. Zangwill, J. Appl. Phys. **91**, 6812 (2002); Phys. Rev. B **66**, 014407 (2002)
Ya. Tserkovnyak et al., Phys. Rev. B **66**, 224403 (2002)
A. Brataas et al., Phys. Rev. Lett **66**, 060404R (2000)
A. Fert et al., J. Magn. Magn. Mater. **272-276**, 1706 (2003)
A. Shpiro, "Two problems in spin-dependent transport in metallic magnetic multilayers", PhD thesis, New-York University (2004)

[8] M.D. Stiles and A. Zangwill, J. Appl. Phys. **91**, 6812 (2002); Phys. Rev. B **66**, 014407 (2002)

[9] J.C. Slonzewski, J. Magn. Magn. Mater. **159**, L1 (1996)

[10] J.C. Slonzewski, J. Magn. Magn. Mater. **247**, 324 (2002)

[11] S. Zhang et al., Phys. Rev. Lett. **88**, 236601 (2002)

[12] A. Shpiro, "Two problems in spin-dependent transport in metallic magnetic multilayers", PhD thesis, New-York University (2004)

[13] A. Fert et al., J. Magn. Magn. Mater. **272-276**, 1706 (2003)

[14] A. Shpiro et al., Phys. Rev. B 67, 104430 (2003)

[15] M.A. Zimmler et al., Phys. Rev. B **70**, 184438 (2004)

[16] S. Urazhdin, J. Appl. Phys. **95**, 7429 (2004); Phys. Rev. B **69**, 134430 (2004)

[17] Y. Jiang et al., Phys. Rev. Lett. **92**, 167204-1 (2004)

[18] M.D. Stiles et al., Phys. Rev. B **69**, 054408 (2004)

[19] T. Valet, unpublished.

Chapter 3. Current induced magnetization precession: numerical simulations

The interaction between a spin polarized current and a thin magnetic layer brings about a whole new concept of magnetization dynamics, the details of which are not yet fully understood. Regardless of the microscopic origin of spin-transfer, the dynamics of the magnetization under the influence of a spin polarized current can be described with a modified Landau-Lifshitz-Gilbert (LLG) equation, which can be numerically solved. This is the basis of all simulation results described below.

The spin torque term added in the LLG equation is fundamentally new from the precession term (the first term in the equation) and the Gilbert damping term (the second term). The precession term conserves the magnetic energy and determines the frequency of the precession. The damping term dissipates energy during precession, making the magnetic system relax to a local minimum. **The spin torque can have both effects: it can be a source of precessional motion as an effective field and it can act as damping (or antidamping) as well.** It is this dual nature that makes the dynamics of the magnetization under the effect of a spin polarized current interesting.

Paragraph A.3.1 describes the dynamics of a single domain particle using a LLG equation including a spin-torque term within a macrospin approximation. Paragraph A.3.2 considers the dynamics of a thin magnetic layer from a micromagnetic point of view. Paragraph A.3.4 summarises a more particular study: the (dynamic) noise induced by spin-transfer in CPP-GMR read heads.

A.3.1. Switching dynamics with a spin-torque term

Using a LLG equation with a Slonczewski spin-torque term (similar to eq. (19)), and treating the magnetization of the free layer as a macrospin, J.Z. Sun was among the first to analyze the spin-current induced precession dynamics [1]. He used the following dimensionless variables:

- magnetization: $m=M/M_s$
- magnetic field: $h=H/M_k$
- easy-plane anisotropy field: $h_p=4\pi M_s/H_k$
- effective spin current: $h_s=(\hbar/2e)g(\theta)j/tM_sH_k$
- natural time unit: $\tau=\gamma H_k\tau_r/(1+\alpha^2)$

All the real variables are as defined before, expressed in centimeter-gram-seconds units; τ_r is the real time. In the initial state the free layer's magnetization is considered to be slightly misaligned with respect to the x direction. Temperature effects are not taken into account (0 K simulations).

A.3.1.a. Time evolution of the magnetization during spin-current induced switching

Fig. A.3 – 1 shows the dynamics of the magnetization reversal under the effect of a spin polarized current. The additional spin-torque term in the LLG equation generates an additional precession motion. A characteristic of current-induced precession is that the torque changes sign when the magnetization crosses the equatorial position, causing the reversal of the precession direction.

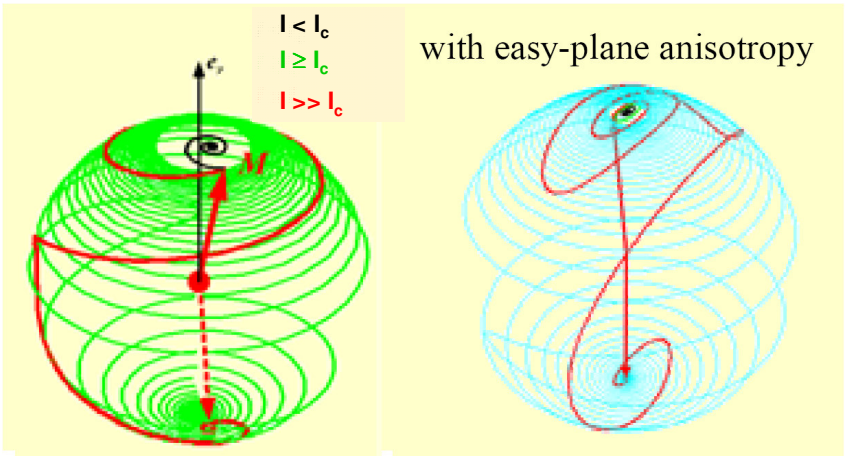

Fig. A.3 - 1 Magnetization trajectories during current induced reversal in the presence of uniaxial anisotropy, with (**right**) and without (**left**) easy-plane anisotropy, for different values of the applied current, as compared with the switching current. (Extracted from ref. 1.)

Unlike field-induced switching, the critical currents needed to induce the reversal highly depend on the easy-plane anisotropy defined on the previous page (see eq. (32)), because current induced switching involves a good deal of out-of-plane precession. The presence of an easy-plane anisotropy leads to an elliptical distortion of the trajectory, with the cone angle more spread out in the easy plane.

A.3.1.b. Effect of a strong easy-plane anisotropy and high current, low field distortion of *M(I)*

In the presence of a spin polarized current and a high easy-plane anisotropy (which emulates the experimental case of very thin layers), the hysteresis loop $\vec{M}(h_S)$ (or resistance versus current - R(I) - in experiments) changes shape (Fig. A.3 - 2).

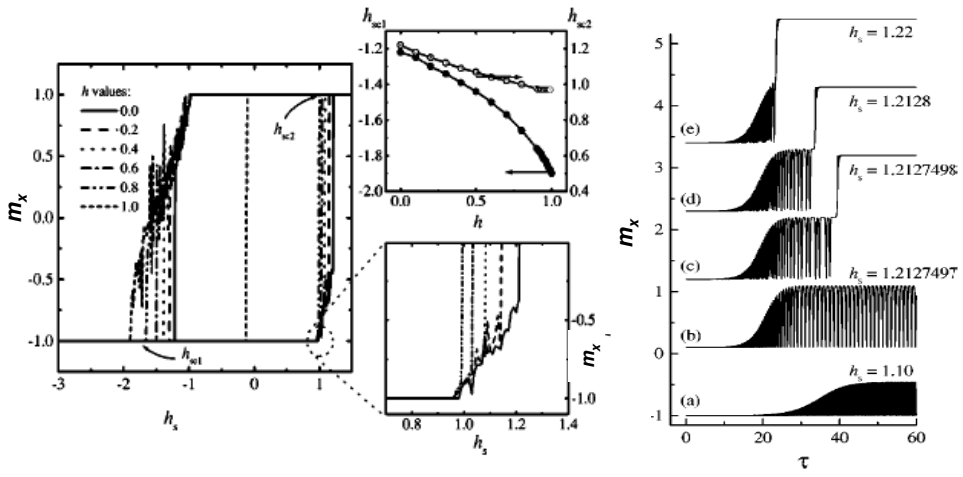

Fig. A.3 - 2 Left: Spin-current induced switching hysteresis loop $\vec{M}(h_S)$ for different applied fields, when a strong easy-plane anisotropy is considered (corresponding to that of cobalt). Analytic formulae for the instability currents give only the onset of the switching and predict a slight linear dependence on the applied field. The actual switching currents are rather higher and do not depend linearly on the field. **Right:** Evolution of steady-state precession and switching as the applied current is increased. Curves are shifted vertically for clarity. (Extracted from ref. 1.)

As the current first exceeds the instability threshold, a sloped region appears in the $\vec{M}(h_S)$ curve. This region corresponds to a steady-state precession with an oblong-

shape trajectory, resulting from an increase in the effective damping for large cone-angle dynamics. As long as the magnetization does not cross the equator, it undergoes a steady-state precession. When the magnetization crosses the equator, however, due to the change of sign of the spin torque, the precession accelerates and eventually leads to switching.

It is important to note that analytic formulae (32) are deduced from stability conditions, so they only express the current values where one or the other state becomes unstable. This does not guarantee that the magnetization will cross the equator and switch. The real switching currents are rather higher than the calculated values. A more appropriate calculation [2] analyzes the nature of the spin-induced precession states and uses bifurcation theory to determine more complicated expressions for the switching currents. However, the simple formulae above account reasonably well for the experimental results published to-date, especially in the low current / low field regime.

A.3.1.c. High current, high field switching threshold

Fig. A.3 – 3 shows an example of simulated $\vec{M}(h)$ hysteresis loop obtained for a high spin current (the applied current is constant, and the magnetization is plotted as a function of the sweeping magnetic field). The polarization of the current is opposed to the initial direction of the magnetization.

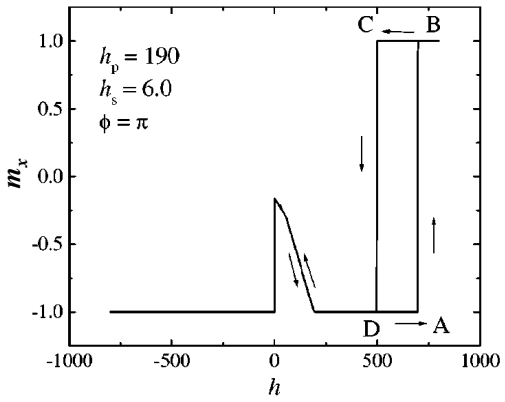

Fig. A.3 - 3 Simulated variation of the magnetization as a function of the applied magnetic field, in a presence of a high spin current. (Extracted from ref. 1).

For $h < 0$ both the applied field and the spin current force the magnetization to point along -x. If $0 < h < h_p$, the competition between field (which tends to align $\vec{M}$ along +x) and current (which tends to align $\vec{M}$ along -x) generates a steady state precession. As h approaches h_p, the magnetization comes to rest along an out of plane direction. Between $h_p < h$ and point "A" the magnetization is forced along –x. At point "A", the effect of the field finally overcomes that of the current, and the magnetization switches. The switching is hysteretic.

Although Sun's numerical simulations account for the first experimental results [3], they can hardly explain high field / high current dynamics. Their main limitation is that the layer is considered as single domain. For high fields and currents, large cone-angle motion as well as stable states with significant out-of-plane components of the magnetization lead to spin-wave excitation and domain formation. Similarly, the effect of current-induced Oersted field is not taken into account. A proper treatment of these phenomena requires full micromagnetic simulations.

A.3.2. Micromagnetic study of magnetization dynamics with spin-torque

Li and Zhang [4] used micromagnetic simulations to analyze the precession states induced by spin currents and to study the switching speed and thermal effects in such systems. Positive current is defined so that the electrons flow from the thin to the thick layer, and the following notation is used:

$$a_J = \frac{\hbar}{2e} \cdot g(\theta) \cdot \frac{1}{t} \cdot j \tag{33}$$

The magnetization of the free layer is supposed to be pinned along the easy axis of the free layer, in the positive x direction. In a very thin free layer, the magnetization can be considered uniform in the current (z) direction, so that two-dimensional micromagnetic modeling is accurate enough; also, spin-torque per unit volume is large for a given current density. The effect of temperature on the dynamical behavior is addressed by including a random thermal field in the effective magnetic field, so that

the LLG equation is converted into a stochastic differential equation with multiplicative noise. The results are obtained considering a small discretization time interval (3 ps).

A.3.2.a. Hysteresis loops with spin torques

In agreement with the macrospin calculations, micromagnetic simulations show that when a spin torque is considered, the hysteresis loop displays three different features (see fig. A.3 – 4):

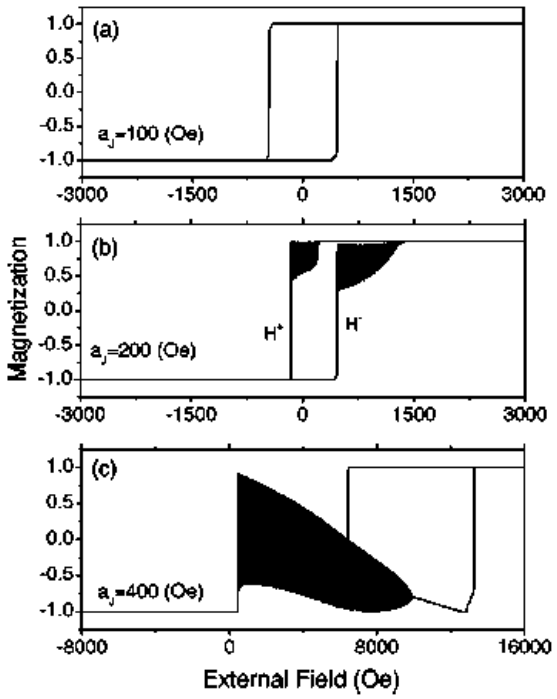

Fig. A.3 - 4 Hysteresis loops for different values of the applied current. (Extracted from ref. 4).

1. For small currents ($|a_J| < 2\pi\alpha M_s$), the loops are not affected by spin-torques;
2. For currents of intermediate values, the hysteresis loops show precessional states; the coercivity is decreasing with increasing current and the loops shift towards higher negative fields;
3. For high values of the current ($|a_J| < \alpha(2\pi M_s + H_k)$), the loops show multiple jumps and the precessional states expand to a large range of magnetic fields; moreover, there is a region in the loops where magnetization increases with decreasing field.

Additional calculations were performed for temperatures ranging from 0 to 300 K, yielding similar results. The temperature quantitatively changes the current threshold for excitations, but the main point is that even at 0 K, current induced magnetic excitations can exist, since they are generated by the competition between field and spin-torque and not merely by thermal activation.

A.3.2.b. Magnetization-current loops

For external fields lower than the anisotropy field, $|H_{ext}| < H_k$, the M-I loops are square and the switching currents are close to the values determined from the analytical expressions (see fig. A.3 – 5).

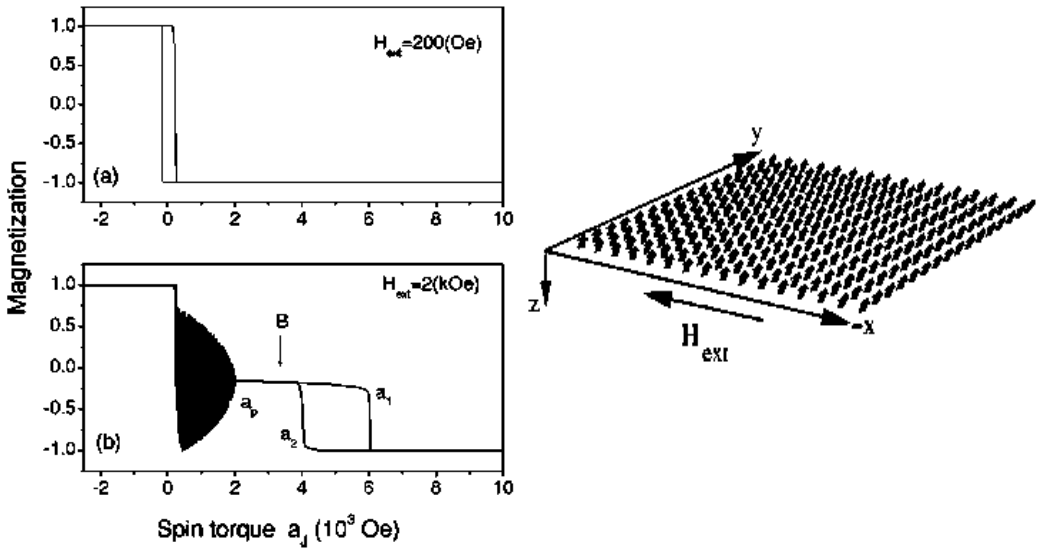

Fig. A.3 - 5 Left: M-I loops for different applied magnetic fields. **Right:** Magnetic moments at point "B". (Extracted from ref. 4.)

For external magnetic fields higher than the anisotropy and for currents higher than the critical current, the magnetization enters a steady precession. Further increase of the current leads to attaining new stable states (labeled "B" on fig. A.3 - 5). At even higher current densities, the "B" states become unstable and hysteretic switching occurs. The values of the current where the two jumps take place (a_1 and a_2) can be determined from the macrospin model. The boundary between precession and "B" states, a_p, and the orientation of the magnetization at point "B" can also be established. It turns out that

the states labeled “B” correspond to an out-of-plane stable direction of the magnetization.

A.3.2.c. Out-of-plane stable states, precession and energy pumping

The existence of the “B” states, which have considerable out-of-plane components, is a signature of spin-torque: without it, for any in-plane applied field, the magnetization should be in-plane. These states are only possible because the energy dissipation through Gilbert damping is balanced by the energy pumped by the spin-current in the system.

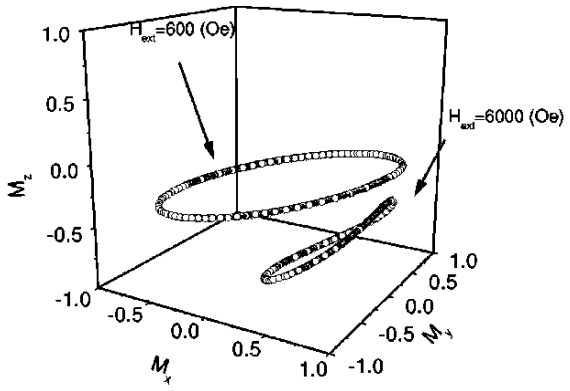

Fig. A.3 - 6 Trajectories for the two degenerate stable precession states for a_J = 400 Oe. (Extracted from ref. 4.)

At a given current and field, there are two degenerate stable out-of-plane precession orbits: one in the lower and one in the upper half-plane (Fig. A.3 – 6). Even at 0K, the magnetization can jump between the two orbits. The frequency of the jumps increases with the temperature, since they can be thermally activated.

A.3.2.d. Switching speed and thermal effects

In general, switching time can be fitted reasonably well by $t_s^{-1} \sim a_J - a_C$. For a pulsed current, at a given pulse amplitude (higher than the critical current) a

corresponding minimum pulse duration is required to achieve current-driven magnetization reversal. The width-amplitude switching probability diagram (fig. A.3 - 8, left) has a shape known as “critical slowing down” in statistical physics. It is found that most of the reversal time is spent at the beginning of the switching.

Thermally assisted magnetization reversal is conventionally modeled using the Néel-Brown formula:

$$\tau = f_0^{-1} \cdot \exp(E_b / k_B T) \tag{34}$$

where τ is the thermal switching time,

E_b is the barrier energy and

f_0 is the attempt frequency (~ 10^9 s^{-1}).

At finite temperature, the reversal probability increases with the spin-torque; positive spin-torque leads to faster thermal switching, while negative torque results in slower thermal reversal (see fig. A.3 – 7, right). The distribution of relaxation times can be well fitted with the Arrhenius formula, but the energy barrier depends on the spin-torque: positive current favors low energy barrier. This remark leaded later on to the magnetic temperature model, described in the paragraph A.2.5.

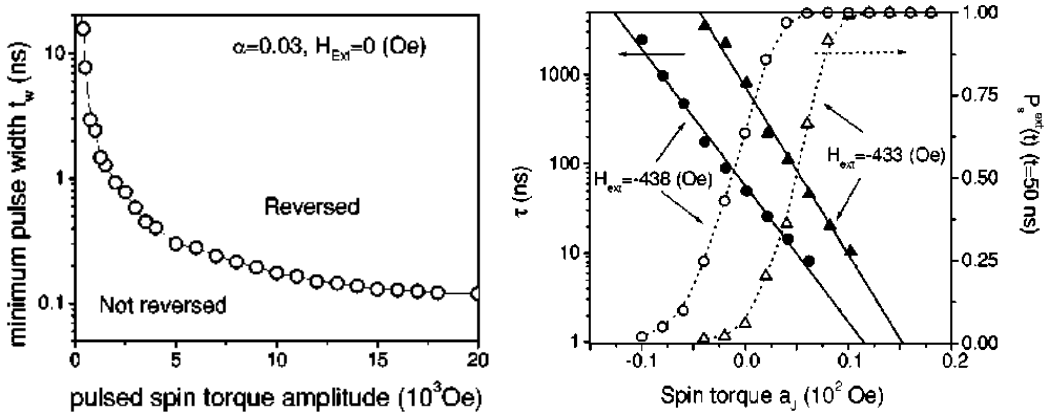

Fig. A.3 - 7 Left: Minimum pulsed spin-torque width versus amplitude for zero applied field. **Right:** Relaxation time (solid lines) and switching probability (dashed lines) as a function of spin-torque at room temperature, for two different applied fields.

The geometry considered in the simulation of Li and Zhang is very close to that of most experimental studies, allowing for a direct comparison. While a good agreement is found over several aspects, there are details where simulation and experiment differ

(see the next chapter). At least part of the disagreements can be explained by the fact that the value used for the exchange constant (4×10^{-11} J/m) is several times higher than any other known in the literature, which means that this particular simulation is closer to macrospin calculations than to full micromagnetics; therefore, it cannot account for any incoherent dynamics that might appear in the system. Similarly, the modeling does not consider the effect of the Oersted field.

A.3.3. Influence of the Oersted field

Torres et al. [5] have used standard 3D micromagnetic simulations to investigate the influence of current-induced Oersted field in structures similar to the ones described in the previous paragraph. They considered a Slonczewski-like LLG equation, including terms corresponding to the antiferromagnetic dipolar coupling between the two magnetic layers and the circular-symmetry Oersted field.

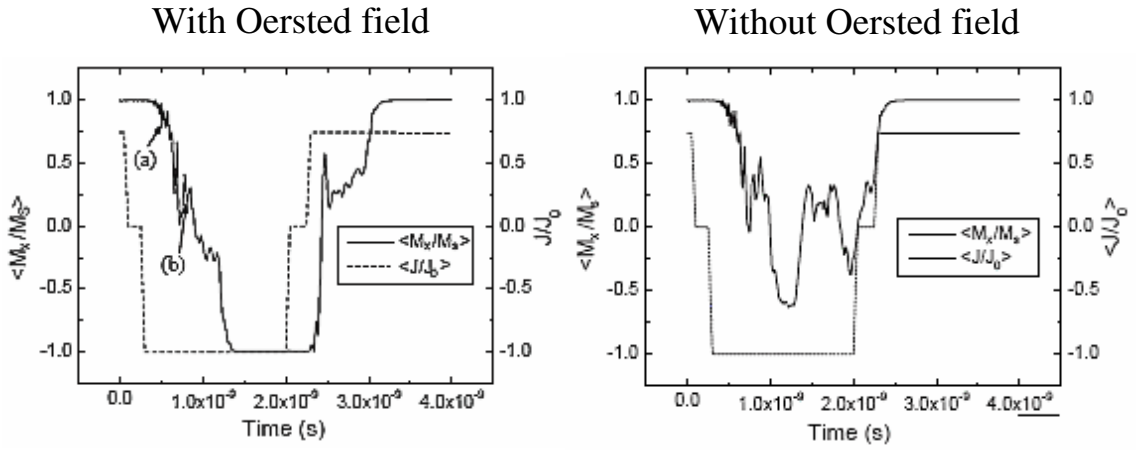

Fig. A.3 - 8 Time evolution of the projection of the magnetization of the free layer along the moment of the polarizing layer and of the applied current when the effect of the Oersted field is considered (**left**) and when it is ignored (**right**). (Extracted from ref. 5).

In their case, the pillars have a circular cross-section with a diameter of 130 nm. The positive sense of the current is defined so that the electrons flow from the

polarizing to the thin layer. In this configuration, the free layer reveals a complex switching behavior involving highly inhomogeneous magnetization configuration with multiple domains.

The main result of the analysis of Torres et al. is that the Oersted field plays a crucial role in the switching, and has to be taken into account when trying to interpret experimental results. Indeed, when a high magnetic field is applied (1400 Oe), favoring the parallel alignment of the magnetic moment of the free layer with respect to the magnetization of the polarizing layer, for the same value of negative applied current, the antiparallel state is only reached when considering the Oersted field (Fig. A. 3 – 8). The Oersted field helps to the formation of domains against the applied field (but in the direction favored by the spin-torque and assisted by the dipolar coupling) and thus triggers the switching.

A.3.4. Spin-transfer induced noise in CPP-GMR read heads

J.G. Zhu and X. Zhu exploited micromagnetic modeling to investigate spin-transfer induced magnetic noise in CPP-GMR read heads, both at 0 K and at the functioning temperature of such devices (60 °C) [6]. They used the LLG equation with spin-transfer torque to determine the frequency-dependent response of the sample for constant current and field. The spin-transfer torque dependence on the angle between the two magnetizations was ignored. It was found that there exists a critical sense current density beyond which the spin-transfer effect yields a substantial noise with a pronounced $(1/f)^n$ spectral contribution at frequencies below 1 GHz. J.G. Zhu and X. Zhu were the first to point out that **the $(1/f)^n$ magnetic noise arises from essentially chaotic magnetization precession excited by spin-transfer**.

The model structure is a CPP spin-valve read head with synthetic antiferromagnetic pinned layer and a composite CoFe10/NiFe18 free layer (the thickness of each layer is given in Å). The reference layer is a 22 Å thick CoFe layer. The pinning field is supposed to be around 1000 Oe. A pair of ideal permanent magnets are considered as biasing for head stabilization, so that they are abutted to the spin-valve sensor stack with a non-magnetic separation of 20 Å on each side

(M_rT = 0.4 memu/cm²). Soft magnetic shields are also taken into account. The track width and the stripe height are 80 nm; the shield-to-shield spacing is 90 nm. The polarization of the current was $p_0 = 0.3$ when not specified otherwise, for either sense of the current. The positive current is defined so that the electrons flow from the pinned to the free layer.

Thermal effects are modeled as in Li and Zhang's simulations; the integration time step remained always lower than 10 ps. The effect of current-induced Oersted field was taken into account. When spin-transfer is ignored, the joint action of Oersted and biasing field causes the formation of a "C"-state in the free layer (Fig. A.3 – 9).

When an external field is applied, the magnetization of the free layer rotates with respect to that of the reference layer, as consequence of the superposition of the biasing field (which favors a perpendicular orientation) and the applied field (oriented parallel to the reference layer's moment). In zero applied field, and when the current is low, the two magnetizations are perpendicular ("quiescent state").

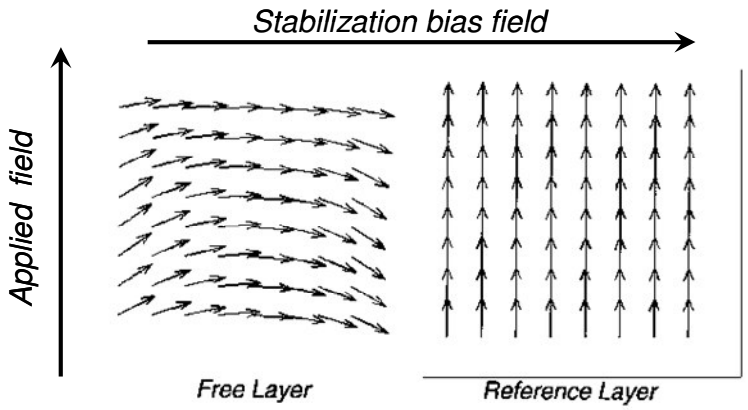

Fig. A.3 - 9 Calculated magnetization configuration in the free and the reference layer, for an applied current of 4 mA, when only the Oersted field of the current is considered. A "C"-state is formed in the free layer, due to the superposition of the circular Oersted field and the high stabilization bias field from the permanent magnets. (Adapted from ref. 6).

Given the small sensor dimension, the main source of noise (when spin-transfer is ignored) is the thermally activated gyromagnetic spin precession in the free layer (mag-noise). In the presence of spin-transfer, the noise is significantly enhanced, with an important *1/f* spectral content (Fig. A.3 - 10). The noise power integrated on the

(0, 1) GHz region is about one order of magnitude higher when spin-transfer is considered.

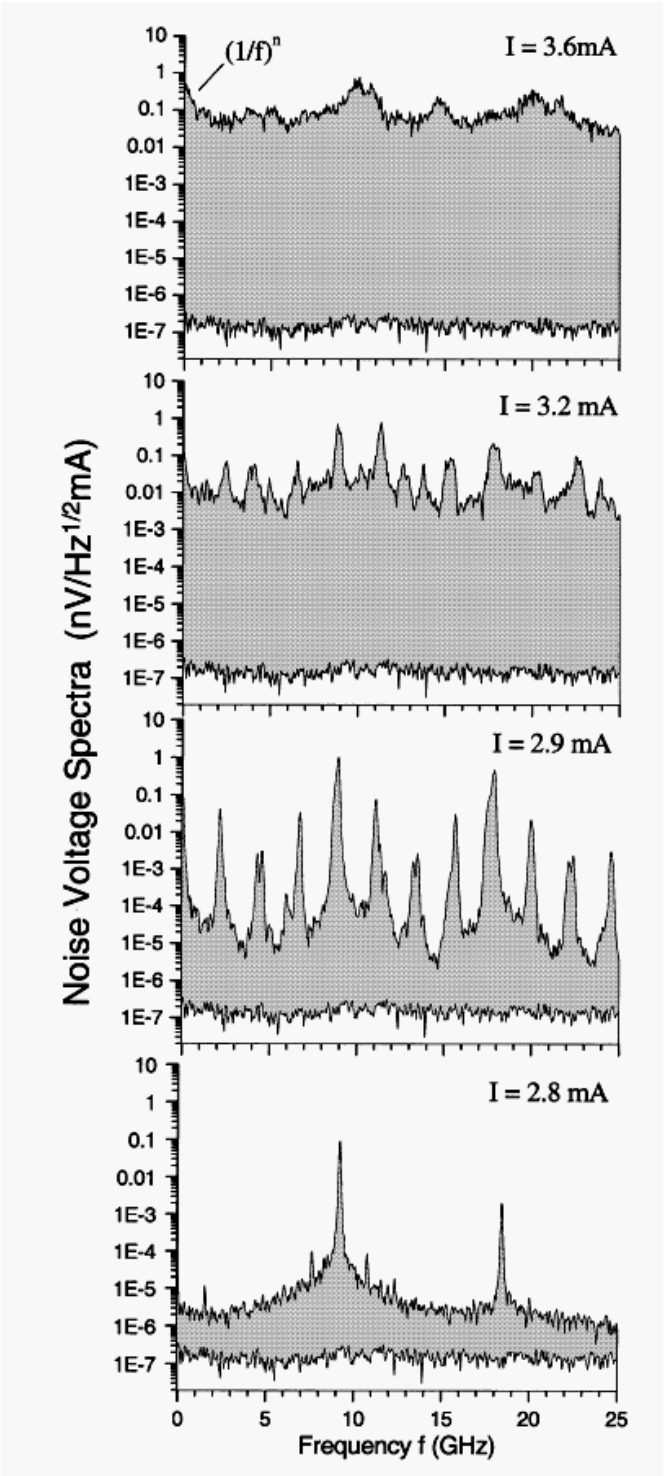

Fig. A.3 - 4 0 K calculated voltage spectra of spin-transfer induced noise for increasing current. The baseline in each figure is the voltage spectrum of the static magnetization state (at 2.7 mA). (Extracted from ref. 6).

To study solely the effect of spin-transfer, without considering thermal induced noise, the evolution of microwave spectra with increasing current was monitored at 0 K (Fig. 3.A – 10).

When the current is below a critical value (2.7 mA), the magnetization is stationary. At 2.8 mA, the spectrum shows a well-defined resonance peak with a significant lower second harmonic. This resonance corresponds to a virtually uniform magnetization precession in the free layer that is excited by the current. As the current is increased to 2.9 mA, the resonance peak is quartered; the harmonic peaks have significant amplitude, but the original peak is still a bit higher. At 3.2 mA, the peaks multiply and become random, and the entire spectrum noise rises. At 3.6 mA, a $(1/f)^n$ spectral component becomes evident under 2 GHz. The rise of the entire spectrum noise is rather a consequence of continued peak frequency division which occurs in a random fashion. Such spectral progression gives a clear indication that spin-transfer induced excitations evolve from coherent magnetization precession to chaotic dynamics as the current is increased.

The onset current of spin-transfer induced noise is when the energy pumping rate from the spin-torque becomes equal to that of dissipation through Gilbert damping. A slightly higher current density excites a uniform magnetization precession in the free layer. During a precession cycle, the system's energy increases part of the time and decreases the rest of the time, so that a dynamic energy balance is reached. At higher current densities, spatial inhomogeneous spin waves are generated to dynamically store and dissipate the energy pumped in. In consequence, the magnetization dynamic becomes rather chaotic, generating a $(1/f)^n$ noise spectral component. Increasing the temperature will result into a further increase of incoherence.

A.3.5. Conclusion

Numerical simulations have put forward several new aspects regarding spin-transfer effects:

1. Current induced magnetization switching involves a considerable amount of out-of-plane precession, which is time-consuming; the precession direction changes when the magnetization crosses the equator;

2. Spin-transfer can induce stable out-of-plane states and out-of-plane precession; the precession can be coherent for intermediate currents and becomes chaotic at high currents;

3. The precession states are the result of a *dynamic* energy balance between energy pumping and energy dissipation.

Other simulations, not presented here, indicated that spin-torque can generate non-uniform dynamics of magnetization [7] and studied the thermal effects more in detail [8]. Finally, it should be mentioned that all the theoretical models and the simulation described above consider that the pinned layer's magnetization is not affected by spin-transfer.

Resumé :

L'interaction entre un courant polarisé en spin et l'aimantation d'une couche mince induit une dynamique des moments locaux différente de celle connue auparavant (qui a lieu, elle, sous l'effet d'un champ magnétique externe). Des simulations numériques ont essayé de rendre compte des détails des processus de renversement et de précession entretenue de l'aimantation, induits par le transfert de spin. Les calculs les plus simples traitent la couche libre comme monodomaine. Des études plus évoluées font appel à des simulations micromagnétiques et mettent en évidence l'importance de champ d'Oersted induits par le courant, de l'activation thermique, et, surtout, de la dynamique chaotique des moments locaux sous l'action du courant polarisé.

Dans toutes ces études, la dynamique de l'aimantation en présence du transfert de spin est décrite en utilisant une équation de type Landau-Lifshitz-Gilbert contenant un terme supplémentaire (nommé 'couple de transfert de spin'), qui rend compte de l'action du courant polarisé. Ce nouveau terme est responsable du caractère novateur de la dynamique induite par le transfert de spin et a une nature duale: il peut aussi bien induire, qu'amortir (ou, au contraire, amplifier) un mouvement de précession. L'équation Landau-Lifshitz-Gilbert peut être résolue numériquement, fait exploité dans toutes les simulations micromagnétiques décrites dans ce chapitre.

References:

[1] J.Z. Sun, Phys. Rev. B **62**, 570 (2000)

[2] T. Valet, submitted for publication in Appl. Phys. Lett. (2004)

[3] J.A. Katine et al., Phys. Rev. Lett. **84**, 3149 (2000)

[4] Z. Li and S. Zhang, Phys. Rev. B **68**, 024404 (2003)

[5] L. Torres et al., J. Magn. Magn. Mater. **286**, 381 (2005)

[6] J.-G. Zhu and X. Zhu, IEEE Trans. Magn. **40**, 182 (2004)

[7] J. Miltat, J. of Appl. Phys. **89** 6982-6984 (2001)

[8] Z. Li and S. Zhang, Phys. Rev. B **69**, 134416 (2004)

Chapter 4. Experimental state-of-the-art

The possibility of switching the magnetization of a layer by applying a spin-polarized current was demonstrated experimentally for the first time in 1999 [1]. Given the extraordinary interest brought about by the potential applications of this phenomenon (as a writing scheme for MRAMs, or, more recently, as a new working principle for magnetic RF oscillators), it would be utopian to try to give a complete overview of the results published to-date. The selection below was a matter of personal choice.

Most of the studies published to-date concerned samples with a structure of minimum complexity – typically Co thick / Cu / Co thin (or, alternatively, Co/Cu/NiFe) stacks –, usually patterned into elliptical shapes in order to insure a strong uniaxial anisotropy [2]. If both cobalt layers are patterned, a strong dipolar coupling is exerted on the thin layer (around a few hundreds of Oe). This field shifts the magnetoresistance loop corresponding to the switching of the thin cobalt layer accordingly; moreover, such interaction can be highly non-uniform (much stronger on the edges than in the centre of the pillar), which can generate incoherent magnetic excitations. To simplify matters and minimise dipolar coupling between layers, the thick layer is left unpatterned, when possible.

Much is known nowadays about such samples. Although some details still excite controversies, the results are fairly well understood and mostly interpreted in terms of spin-transfer torques generated by the polarized current on the magnetic moment of the free layer. Most of the results described below have been obtained on this type of samples.

More complicated multilayers (including spin-valves with synthetic antiferromagnetic pinned polarizing layer [3], tunnel junctions [4], and multilayers where Ru layers were inserted between the free layer and the top current lead [5]) have only started to be investigated recently. From the data presently available, apart from variations in the critical current density, the behaviour of complex multilayers seems to be consistent with that of simple Co/Cu/Co samples.

A.4.1. Static measurements

"Static" experiments include magnetoresistance measurements with a constant sense current and measurements where a dc current is swept in order to obtain the resistance-current characteristics for a fixed applied magnetic field. Such experiments aim usually at reconstructing the stability current-field phase diagram. Other experiments referred to as "quasistatic" are resistance versus time measurements for a constant applied field and current, when the time resolution is poor (milliseconds to seconds).

A.4.1.a. First experiments on current induced magnetization switching

We owe the first clear experimental demonstration of current induced magnetization reversal to a group from the Cornell University [6]. The example below was not the very first result they published. (The first experiments were conducted on circular pillars with lateral size of 130 nm, very susceptible to the influence of Oersted fields and showing multiple step transitions.)

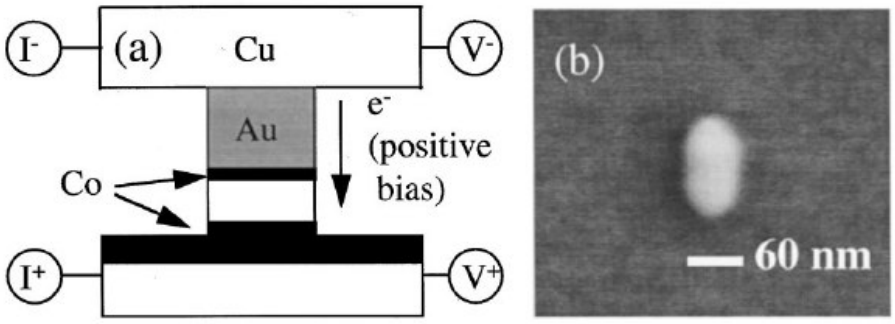

Fig. A.4 - 1 Left: Schematic vertical cross-section of the device. Positive current is defined as electrons flowing from the thin to the thick Co layer. **Right:** SEM image of the nanopillar (seen from above), before it is covered by the top Au electrode. (Extracted from ref. 6.)

The samples used for the study referred to here were elliptical Co400/Cu60/Co25 pillars (where the thickness of the layers given in Å), with an

estimated lateral size of 60×130 nm² [6]. The high aspect ratio insures that there is a well-defined uniaxial (shape) anisotropy, which favors single domain behavior in sufficiently small thin film structures. The thick cobalt layer is left unpatterned, so as to avoid strong dipolar fields acting on the free layer, arising from the interaction with the polarizer (Fig. A.4 – 1).

Fig. A.4 – 2, left, shows the low sense current magnetoresistance curve for a device as described above. In zero applied magnetic field, the sample is in a low-resistance state, corresponding to the parallel alignment between the magnetization vectors of the two layers. At $H = \pm 50$ Oe, sharp jumps are measured to a high resistance value, attributed to the antiparallel configuration of the two magnetic moments. The thick Co layer being unpatterned, its magnetization will switch first, aligning along the applied field. At $H = \pm 900$ Oe, the applied field becomes strong enough to switch the magnetization of the thin Co layer, so that beyond these values, both layers are parallel to the field and thus the system jumps back to the low resistance state. The gradual decrease of the resistance between the two transitions can be interpreted as a reversal domain nucleation, followed by a partial propagation through the free layer.

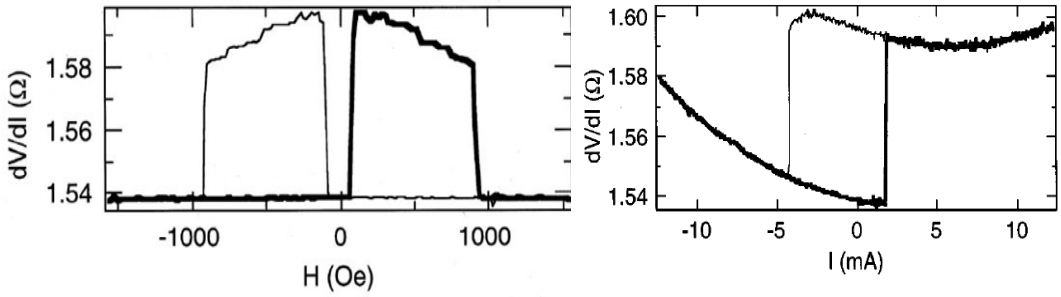

Fig. A.4 - 2 Left: Magnetoresistance curve (differential resistance *dV/dI* as a function of magnetic field *H* applied parallel to the long axis of the ellipse). **Right:** Differential resistance *dV/dI* as a function of the applied current *I*. (Extracted from ref. 6).

When sweeping the current (Fig. A.4 – 2, right), the resistance registers abrupt transitions between the same levels as on the magnetoresistance curve. This allowed the authors to conclude that **by applying a spin-polarized current with the appropriate sign and intensity it is possible to switch the magnetization of the free layer back and forth between the parallel and antiparallel state.** Starting with the sample in the parallel state, a positive current of about 2 mA is needed to switch the moment of the

free layer to the antiparallel orientation. This is consistent with the convention for the sign of the current: the positive current is defined so that the electrons flow from the free to the pinned layer, thus favoring the AP state (see chapter 2). Increasing the positive current above the critical value does not lead to any other change in the relative orientation of the magnetization (the increase in the resistance is simply due to Joule heating). To switch back to the P state, it is necessary to apply a negative current (defined as electrons flowing from the thick to the thin layer) of about -4 mA.

The dependence of the switching on the direction of the current is strong evidence that the spin-transfer mechanism is responsible for the switching and not the Oersted field generated by the current. Oersted fields can create vortex states, but such effects are symmetric with respect to the current direction. Furthermore, they lead to a reduction of the amplitude of the resistance jump, since the magnetic configuration of the free layer is no longer perfectly parallel or antiparallel to the moment of the reference layer.

A.4.1.b. Stochastic nature of the switching currents and thermal activation

It turns out that **the exact values at which the free layer switches vary from sweep to sweep** [7]. A histogram for I_c^{P-AP} of a Co400/Cu60/Co30 circular nanopillar with a lateral size of 50 nm is shown in fig. A.4 – 3, left. Such behavior was expected, since magnetic reversal driven by spin-polarized current is (partially) thermally activated (see Chapter 3 - paragraph A.3.2.d).

Further confirmation of the stochastic nature of switching is obtained in experiments where a sample is held at a fixed current near the switching threshold (Fig. A.4 – 3, right). There is always a waiting time before switching. This time depends on the current and also displays a broad distribution. The probability *P(t)* that the free layer has not switched can be fitted with an exponential decay, in agreement with the simulation of Li and Zhang (see Chapter 3). Also in good agreement with the simulation is the fact that the distribution of critical currents shifts strongly towards larger values of the current when the sample is cooled or the sweep rate *dI/dt* is increased. This is a

strong indication that **spin-polarized current induced magnetization reversal is a thermally activated reversal process for which the effective barrier depends on *I*.**

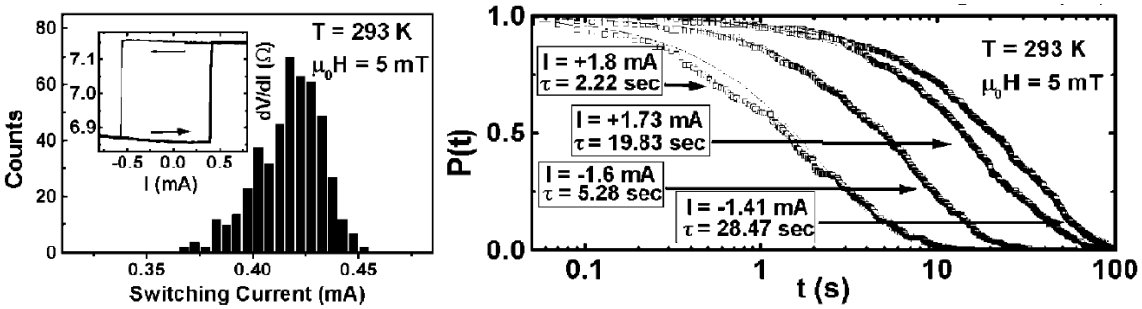

Fig. A.4 - 3 Left: Distribution of the switching currents for parallel to the antiparallel transition. Inset: differential resistance as a function of current for the same device. **Right:** Probability of switching as a function of the waiting time, for different values of the current. (Extracted from ref. 7.)

A.4.1.c. "Static" phase diagrams

Different models predict different expressions for the switching (instability) currents as functions of the magnetic field. By plotting the critical currents on the applied field, one can obtain a stability phase diagram. Fig. A.4 – 4 shows the phase diagram as predicted by Slonczewski's model (in solid lines), when the positive sign of the current is defined as electrons flowing from the thick to the thin layer, and no asymmetry as a function of θ is taken into account [8]. In-between the critical lines, in the center of the phase diagram, both the parallel and the antiparallel states are stable (this is called the "coercivity region"). Outside the critical lines, only one state (either P or AP) is stable, or none of them is. These last regions, where precession states are expected, were not plotted, for clarity. The critical lines intersect the ordinate axis in $a_{c0} = \pm\alpha 2\pi M_s$. The vertical boundaries correspond to the applied field overcoming the in-plane anisotropy H_d (eq. (20) for the instability currents are only valid as long as the applied field is below this limit). When an effective field term (induced by spin-transfer) is considered, Slonczewski's phase diagram will be shifted on the field axis with a quantity that depends on the applied current: $H_{app} \rightarrow H_{app} + b_J$. b_J can be positive

or negative, so the vertical boundaries will be rotated clockwise or counterclockwise, accordingly (Fig. A.4 – 4, left, dashed lines).

Both Slonczewski's model and the model of Zhang, Levy and Fert are zero temperature calculations. Finite temperature effects may be accounted for considering an additional Langevin random field in the modified LLG equation, as explained in chapter 3. This results in a finite probability for thermally activated switching with an activation barrier for magnetization reversal that depends linearly on the current. When thermal effects are taken into account, critical currents are reduced and Slonczewski's phase diagram is modified as seen in fig. A.4 – 4, right (dashed line).

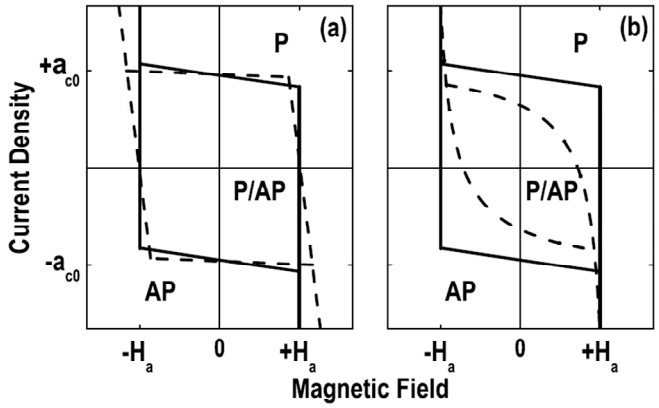

Fig. A.4 - 4 Solid lines: calculated phase diagram for a single domain magnetic thin layer with uniaxial anisotropy, according to Slonczewski's spin-torque model (at 0 K). Dashed lines: **(a)** stability phase diagram with an additional Zhang-Levy-Fert effective field term, for $b_J < 0$; **(b)** finite temperature stability phase diagram in Slonczewski's model. The regions where precessional states are expected have been omitted for clarity. (Extracted from ref. 8.)

Therefore, one way of testing the validity of different spin-transfer models, and, generally, of accounting for spin-transfer effects in various structures, is to study the stability phase diagrams. For pillars with an unpinned reference layer, only half of the phase diagram can be measured. Indeed, when applying magnetic fields larger than the coercivity of the polarizer and in the direction opposite to its magnetization, its moment will be reversed. To measure the entire phase diagram, it is necessary to pin the reference magnetic layer by exchange bias with a neighboring antiferromagnet.

Fig. A.4 – 5, fig. A.4 – 6, and fig. A.4 – 7 present phase diagrams of various types of samples, measured at different temperatures by several groups. Generally, the phase-diagrams are interpreted using the spin-torque approach; the exception is ref. [8], where the authors argue that they found evidence of spin-current induced effective field, whose order of magnitude is about five times weaker than the spin-transfer torque.

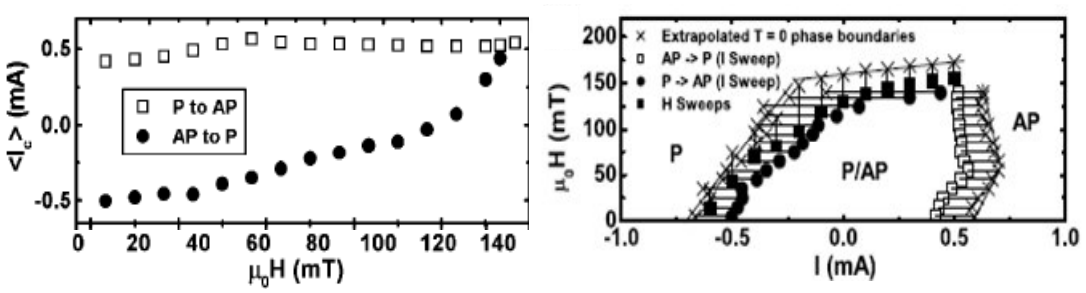

Fig. A.4 - 5 Stability phase diagram for the same sample and current sign convention as in paragraph A.4.1.b, as measured at room temperature (**left**) and as extrapolated at 0 K from the data at room temperature (**right**). The current-field axes are switched between the two figures. (Extracted from ref. 7).

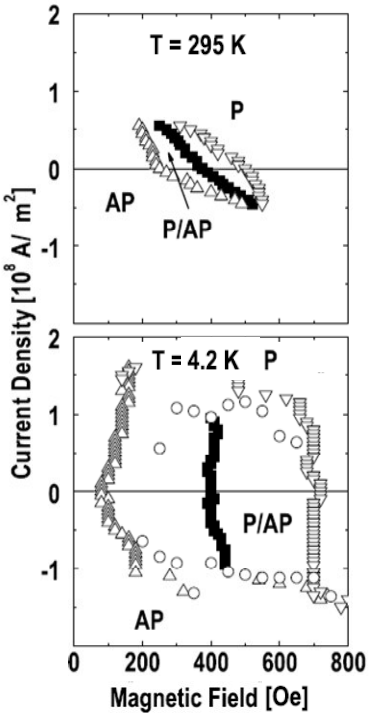

Fig. A.4 - 6 Phase diagrams measured at 295 and 4.2 K on a 50×100 nm² nanopillar with the following structure: Co120/Cu100/Co30, where the thickness of each layer is given in Å. The current is conventionally positive for electrons flowing from the thick to the free layer. (Extracted from ref. 8.)

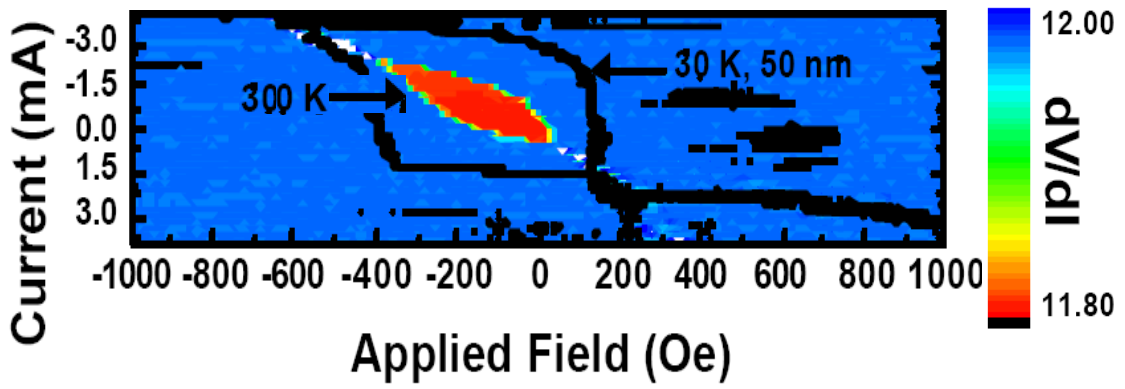

Fig. A.4 - 7 Phase diagrams measured at 300 and 30 K on a nanopillar with hexagonal cross-section with a short axis of 50 nm. The structure of the multilayer was: PtMn175/CoFe15/Ru8/CoFe19/Cu40/CoFe10/NiFe24, where the thickness of each layer is given in Å. The current is conventionally positive for electrons flowing from the free to the pinned layer. Positive field is applied in the opposite to the magnetization of the reference layer, thus favoring the AP state. (Extracted from ref. 9.)

From an experimental point of view, it is quite difficult to discriminate an effective field generated by the spin current from any other fields that might arise in the structure. In particular, it is not easy to differentiate between the effective field and the Oersted field which may also produce a shift of the hysteresis loop that depends linearly on the applied current, if the current is not distributed uniformly through the pillar. (If the contact resistance is comparable with that of the nanopillar, the current may flow asymmetrically through the structure and generate a net bias field proportional to the current.)

A.4.1.d. Telegraph noise in the coercivity region of the phase diagram

Inside the coercivity region, telegraph noise switching is observed when the applied field and spin current oppose each-other. This is a consequence of the stochastic nature of current induced magnetization reversal. In the case of field-induced telegraph noise, which appears when a field is applied perpendicular to the easy axis, the moment jumps between two closely separated angles. On the contrary, when the telegraph noise is generated by a spin-current, the resistance variation between the two states matches

the magnetoresistance amplitude, indicating that the magnetization of the thin layer jumps back and forth between the parallel and the antiparallel state. Moreover, the variation of the dwell times in the two states when the current is modified is very different from their dependence on the field.

For the same sample as in paragraph A.4.1.b, whose phase diagram is shown in fig. A.4 – 5, telegraph noise is measured near $\mu_0 H$ = 140 mT and I = +0.5 mA (Fig. A.4. – 8). When the field is fixed and the current is increased, the dwell time in the parallel state decreases exponentially, while the dwell time in the antiparallel state is only slightly increased. When the current is held constant and the field is varied, the dwell time in the antiparallel state decreases exponentially, while the dwell time in the parallel state increases much more slowly.

When studying the temperature dependence of the dwell times, it was found that the data was consistent with the spin-torque model, but not with the effective temperature theory [10].

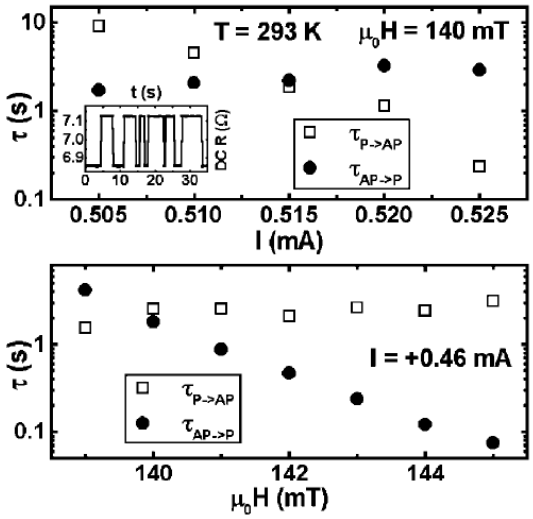

Fig. A.4 - 8 Dwell time in the two states when the current (**top**) or the field (**bottom**) is varied. Positive current favors the AP state, positive field favors the P alignment. Inset: dc resistance versus time for $\mu_0 H$ = 140 mT and I = +0.51 mA. (Extracted from ref. 7.)

Evidence of telegraph noise can be found in all the coercivity region of the phase diagram, albeit dwell times that can be very different in the two states, as well as the resistance variation amplitudes between the two levels (Fig. A.4 - 9, right).

A.4.1.e. "Instability" current versus switching current

As predicted by numerical simulations (see paragraph A.3.1.b), when measuring at low temperatures, it becomes evident that the resistance versus current loops are not square, like the magnetoresistance loops (Fig. A.4 - 9, left). Starting with the sample in the low-resistance P state, as I is swept towards positive currents, a gradual increase is measured in the resistance prior to the abrupt switching to the AP orientation. The onset of the gradual resistance variation is defined as the instability current, while the real switching current is the current where the sharp resistance transition takes place. Similar behavior is found when starting with the sample in the AP state and sweeping the current towards negative values.

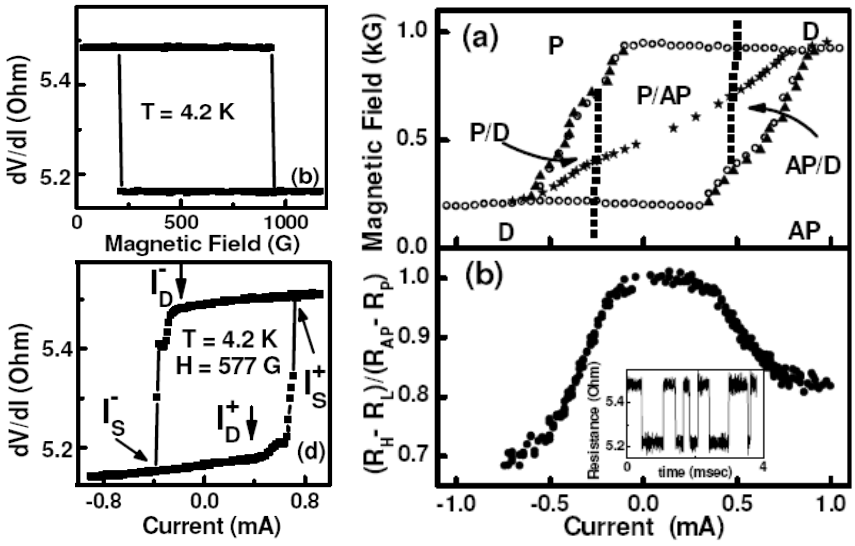

Fig. A.4 - 9 Left: magnetoresistance (**top**) and differential resistance versus current (**bottom**) measured at 4.2 K on a NiFe200/Cu60/NiFe20 pillar with a 60×130 nm² elliptical cross-section and both magnetic layers patterned. The shift of the magnetoresistance loop is due to the magnetostatic coupling between the two Permalloy layers; the resistance versus current loop is measured for an applied field that compensates the coupling. **Right: (a)** Phase diagram reconstructed from the resistance versus current (full symbols) and magnetoresistance (open symbols) data at 4.2 K. The switching current I_S (full triangles) and the instability current I_D (full squares) are as defined on the resistance versus current loop. (The stars mark the I and H for which the dwell times for both resistance states are approximately 1 ms, at different temperatures from 300 K (at high currents) to 4.2 K (at low currents)). **(b)** Current dependence of the amplitude of the two-level fluctuations normalized by the GMR amplitude, as a function of current, for H = 957 Oe. Inset: telegraph noise at I = 1 mA. (Extracted from ref. 10.)

In agreement with the simulation results, microwave measurements (see paragraph A.4.2.b) allowed to identify the instability current and the gradual increase of the resistance as due to the excitation of dynamical states in which the free layer undergoes steady-state precessional motion. In good accord with the theory, the instability currents, given by eq. (20), depend very weakly on the applied field (Fig. A.4 -9, right). The actual switching currents, however, vary strongly with H.

At 300 K, is difficult to distinguish the rounding of the resistance-current loops due to the onset of dynamical states from the gradual increase of resistance caused by Joule heating. Also, the dynamics at room temperature is expected to be less coherent.

A.4.1.f. GMR versus switching currents

It has been shown that the spin-torque amplitude (that is, the inverse of the switching currents) is proportional to the pillar magnetoresistance [11]. Experiments were carried out where the GMR was varied through three different methods: by inserting a strongly spin-scattering layer between the magnetic trilayer and one of the electrodes, by introducing a spacer with short spin-diffusion length between the thin and the thick magnetic layers, and by varying the angle between the two magnetic moments. In all cases, it was found that the resistance variation ΔR and the inverse of the switching currents vary linearly (Fig. A.4 – 10, a). As both $1/I_S$ and ΔR are inversely proportional to the area of the pillar, cross-section variations between the samples do not affect the linear dependence of the two parameters, as they would only lead to scaling along the two full fit lines in fig. A.4 – 10, a.

These results have been qualitatively interpreted in terms of polarization variation within a simple ballistic model. If p is a parameter describing the current polarization under the influence of the thick F_1 layer, when the thin ferromagnet F_2 is removed, both the magnetoresistance and the switching currents are proportional to p (Fig. A.4 – 10, b); thus the linear dependence between the two parameters.

It has been also pointed out that the GMR increase alters not only the switching currents amplitude, but also their asymmetry; no interpretation concerning this finding was proposed.

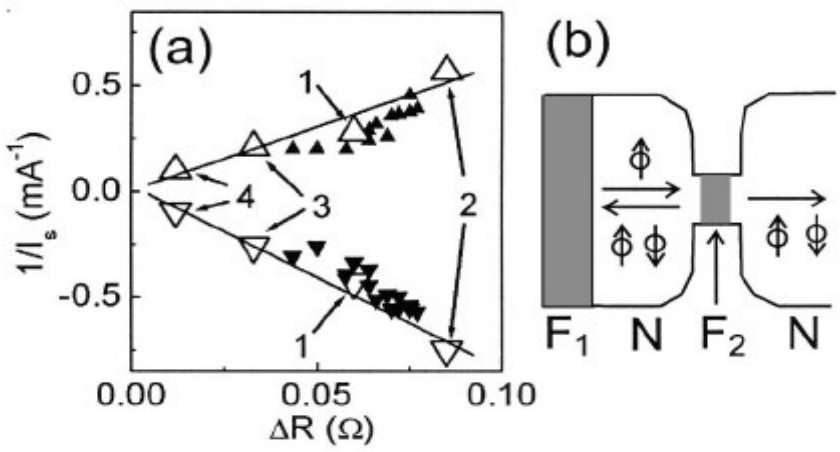

Fig. A.4 - 10 (a) Dependence of the inverse of the switching current on the resistance variation between the high and low resistance states. The open symbols denote samples with different structures. The data marked by full symbols was obtained by varying the angle between the magnetizations of the two ferromagnetic layers of one and the same structure. Upward (downward) triangles: $1/I_S^{P\to AP}$ ($1/I_S^{P\to AP}$). Solid lines: best fit to the data, excluding angle variation. **(b)** Schematic drawing of electron scattering in nanopillars.

A.4.2. Dynamic measurements

"Dynamic" measurements denote frequency-dependent experiments (in the gigahertz range), time-resolved measurements, when the resolution varies between nanoseconds and microseconds, and pulse-induced switching, where the current pulse length is of the order of nanoseconds.

A.4.2.a. Switching probability

Static experiments have already put forward the stochastic nature of spin current induced magnetization reversal. Another way of analyzing this aspect is to investigate the switching probability for different current pulse amplitudes and lengths. Among other things, such studies lead to establishing the write speed of various devices, in view of possible MRAM applications.

Fig. A.4 – 11 shows the switching probability as a function of the pulse duration for two different pulse amplitudes [12]. As expected, the switching probability increases with the length and the amplitude of the pulse. For a given pulse amplitude, the switching probability increases smoothly from 0 to 1 with the pulse duration. This trend is consistent with two types of switching behavior: thermal activation over a barrier and dynamical reversal when the barrier between the two states is completely suppressed.

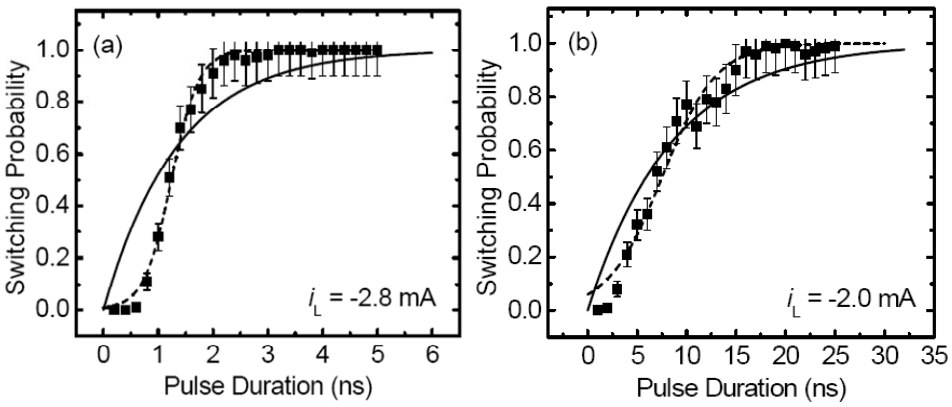

Fig. A.4 - 11 Switching probability as a function of pulse duration for two pulse amplitudes. Solid line: simple exponential fit. Dashed line: better fit using a Fermi distribution function with two free parameters. (Extracted from ref. 12.)

In zero effective field and in the absence of spin polarized current, the free layer's orientation is bistable, indicating the presence of an energy barrier separating two stable magnetization states. Static measurements have already brought evidence that spin-torque can modify the height of the energy barrier, hence the thermal activation rate for switching (see the previous paragraph). Therefore, thermally activated reversal is expected at lower values of the current, where the height of the barrier was lowered, but not suppressed. In this case, the switching probability has a simple exponential form as a function of the pulse duration:

$$P(t_d) = 1 - e^{-t_d / \tau} \tag{35}$$

where t_d is the pulse duration and τ the dwell time in the initial state, which depends on the barrier height and thus on the current. For higher currents, the barrier is entirely suppressed, and the reversal should take place through a deterministic trajectory. The switching probability should remain zero until the pulse duration exceeds the time

required for the magnetization to dynamically evolve past the hard axis, then it should sharply increase to one. The switching speed should increase with the current [13], so for higher currents, shorter pulses should be required for consistent switching.

The experimental data in fig. A.4 – 11 does not exactly fit any of the two switching regimes, indicating a rather complicated transition between fully dynamic and fully thermally activated reversal. However, as the pulse amplitude is lowered, the deviation from the exponential law valid for thermally activated switching diminishes, and is expected to fit the data for lower currents than considered.

When studying the temperature dependence of the switching probabilities, it was found that the two transitions (P→AP and AP→P) behave quite differently: decreasing the temperature surprisingly increases the switching speed of the AP→P transition, while it only marginally affects the P→AP switching speed [14]. This experimental result cannot be accounted for within the macrospin model, as the latter predicts an acceleration of the switching speed when increasing the temperature. A qualitative interpretation has been proposed, explaining the thermal de-activation as a consequence of the increased incoherency of the system, partially generated by the spatial non-uniform Oersted field generated by the current [14]. However, this phenomenon is not fully understood to-date.

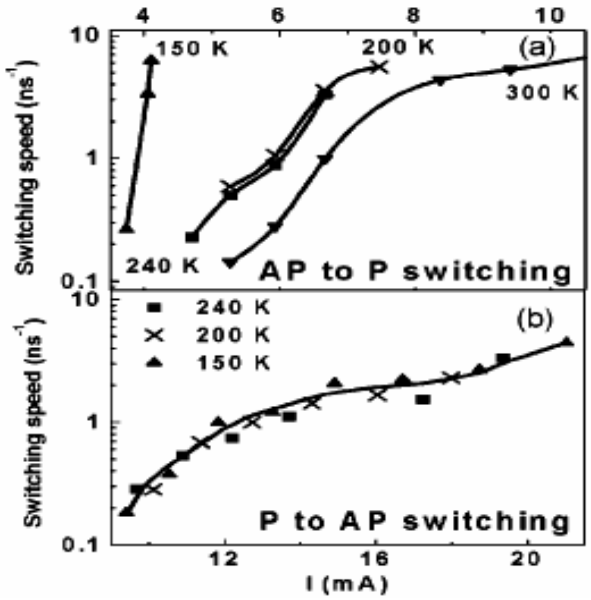

Fig. A.4 - 12 Temperature and current amplitude dependence of the switching speed, for both transitions. (Extracted from ref. 14).

A.4.2.b. Frequency-dependent experiments and the dynamic phase diagram

Frequency-dependent electrical techniques allow for the investigation of high-frequency oscillatory modes induced by spin-currents, for which static measurements have provided only indirect evidence. The spin-polarized currents generate torques on the magnetization of the thin magnetic layer, which induce oscillations of the latter relative to the thick layer's moment. Consequently, under a dc bias current and constant applied field, spin-transfer induced magnetic dynamics produces a time-varying voltage with typical frequencies in the microwave range. The spectra of microwave power can be measured using a heterodyne mixer circuit, described in ref. 15.

When measuring the differential resistance as a function of current, a hysteresis loop is obtained as long as the applied field is lower than the anisotropy. For higher fields, a reversible step is measured, together with a peak which has been attributed to the onset of dynamical magnetic excitations (Fig A.4 – 13, b). The irrefutable proof was brought by frequency-dependent measurements (Fig A.4 – 13, c and d).

For the sample in Fig A.4 - 13, merely background noise is found on the power spectra as long as the current is lower than the onset of the step in the differential resistance curve. From I = 2 mA, a signal starts to be resolved at around 16 GHz (a second harmonic peak is also present, see inset). This peak grows with the current up to I = 2.4 mA, after which the dynamics changes to a different regime. These initial signals can be fitted with the formula for small angle elliptical precession, if assuming a saturation magnetization about twice lower than the values known in the literature (Fig A.4 – 13, e). Based on this agreement, the signals were identified as arising from small-angle elliptical precession of the free layer, as predicted theoretically (see chapter 3). The cone angle was estimated to be around 10°, and the misalignment between the precession axis and the direction of the thick layer magnetization approximately 9°.

As the current is increased between 2.4 and 3.6 mA, the nanomagnet exhibits additional dynamical regimes. The microwave power is increased by two orders of magnitude, the peak frequencies shift down abruptly and the low-frequency background becomes so large that some peaks are difficult to distinguish. The large amplitude signals persist up to 6 mA (the same value of the current at which there is a shoulder in the differential resistance curve), where the measured power drops sharply.

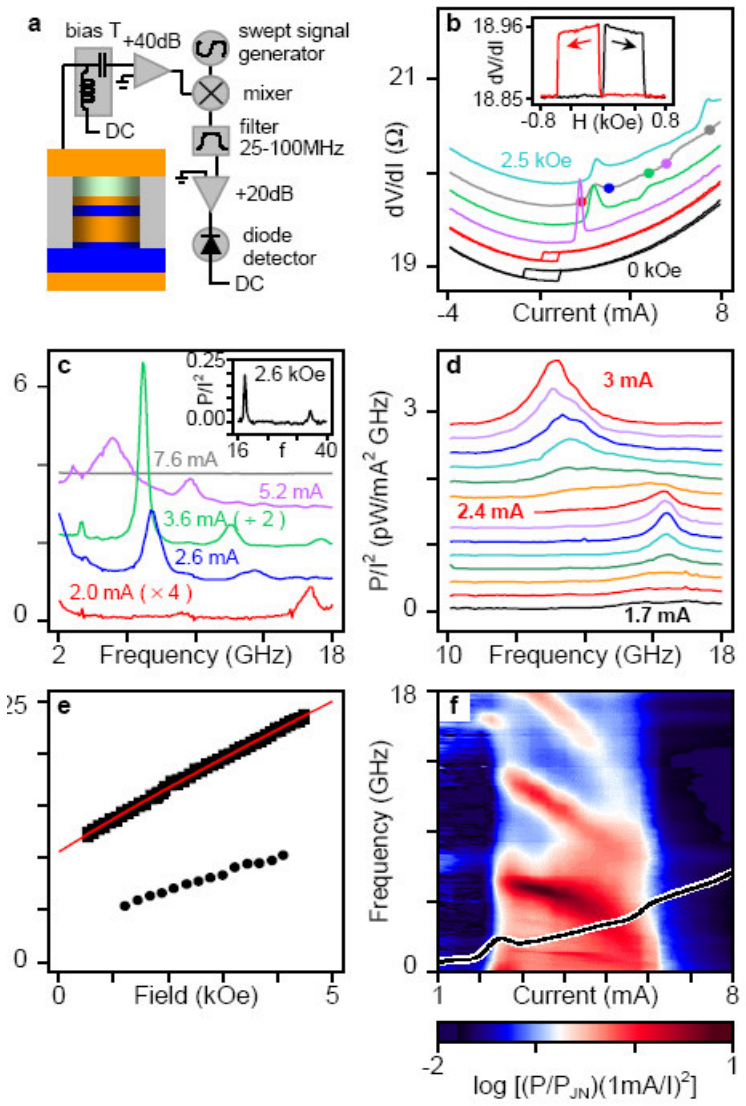

Fig. A.4 - 13 **(a)** Sample (70×130 nm² Co400/Cu100/Co30 pillar, with the thick layer left unpatterned) and the heterodyne mixer circuit. **(b)** Differential resistance versus current for the following applied fields: 0, 500, 1000, 1500, 2000 and 2500 Oe (from bottom to top). Color dots on the curve measured at 2000 Oe correspond to the spectra in (c). Inset: magnetoresistance near $I = 0$. **(c)** Microwave spectra measured at 2000 Oe, with the Johnson noise subtracted, for the following currents: 2, 2.6, 3.6, 5.2 and 7.6 mA (from bottom to top). Inset: Spectrum at 2.6 mA, 2600 Oe, for which both *f* and *2f* peaks are visible. **(d)** Microwave spectra at 2000 Oe, for currents between 1.7 (bottom) and 3 mA (top) in 0.1 mA steps. **(e)** Magnetic field dependence of the small-amplitude signal frequency (top) and the fundamental peak in the large amplitude regime (bottom), at 3.6 mA. **(f)** Microwave power density (in color scale) versus frequency and current for an applied field of 2000 Oe. The black line is the differential resistance versus current curve from (b). The curves in (b), (c), (d) are offset vertically for clarity. (Extracted from ref. 15.)

Microwave signals can also be measured under certain conditions in the coercivity region (Fig A.4 – 14, d). They have been attributed to fluctuations of the free layer's moment away from the easy axis, without crossing the equator and leading to reversal, in good agreement with the numerical simulations of Sun (see chapter 3).

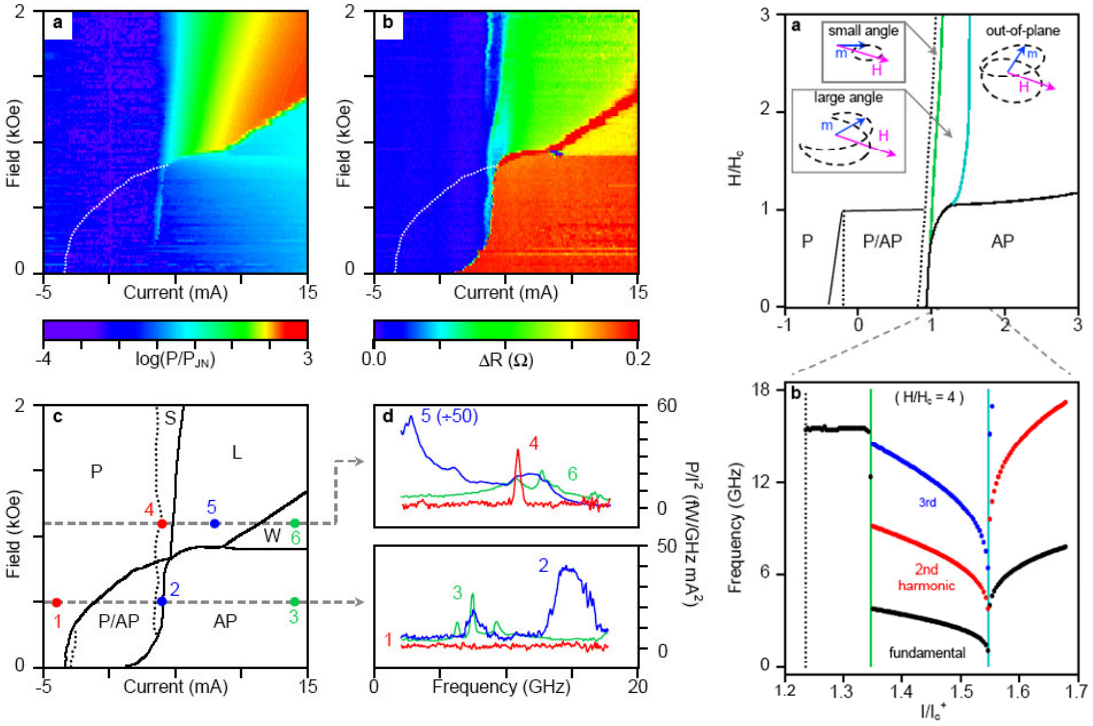

Fig. A.4 - 14 Left: (a) Microwave power above Johnson noise (in color scale) versus *I* and *H*. The field is swept from negative to positive values. The dotted line marks the AP to P transition. **(b)** Differential resistance (in color scale) versus current and field, Joule heating subtracted. **(c)** Room-temperature experimental dynamical stability phase diagram extracted from (a) and (b). S / L indicates the small / large-angle precessional regime and W a state with resistance between P and AP and only small microwave signal. The color dots correspond to the microwave spectra at 500 Oe and 1100 Oe shown in **(d)**. **Right:** Results of numerical solution of the Slonczewski LLG equation for a single-domain nanomagnet at zero temperature. **(a)** Theoretical dynamical phase diagram. **(b)** Dependence of frequency on current including both fundamental frequency and harmonics in the measurement range. (Extracted from ref. 15.)

Single-domain numerical simulations based on a Slonczewski-type LLG equation provided a fairly good understanding of the experimental results (Fig A.4 – 14). The zero-temperature calculations suggest that the large amplitude

microwave signals correspond to large angle, approximately in-plane precession of the moment of the free layer. The abrupt jump to lower frequencies marks the onset of this mode, characterized by decreasing frequencies with increasing current and large power in the harmonics.

The simulation does not explain the presence of the broadband instability appearing in some spectra in the low frequency range; the authors suggested that it might be caused by fluctuations from the large-angle precessional orbit into other modes of similar energy. Another unexplained result was the "W" region in Fig A.4 – 14. The macrospin simulation predicted approximately circular out-of-plane precessional modes in that range of currents and fields, which should produce signals orders of magnitude higher than the obtained spectra.

For all the unexplained details, this experiment demonstrated beyond doubt that spin-transfer can induced magnetization precession. The oscillation frequency, in the gigahertz range, can be tuned by changing either the current or the applied field. Moreover, recent results showed that a small alternative current added to the constant electrical bias generates a frequency modulated spectral output [16]. These effects can be applied in new magnetic devices, such as resonators or microwave sources, which may be very interesting for wireless telecom applications. Such oscillators would allow a dynamic frequency allocation, solving the saturation problem of the telecom frequency bands. These devices would answer the market need for very large band oscillators with a strong quality factor Q (since the largest peak in the measured power spectra was more than 40 times higher than the room temperature Johnson noise in the system), while their architecture would remain simple and inexpensive.

A.4.2.c. High frequency telegraph noise in the precession region of the phase diagram

As mentioned above, frequency-dependent measurements have put forward not only a clear illustration of high-frequency precessional motion generated by spin-transfer, but also an unexpected "broadband instability" region. It was demonstrated that the broadband instability is the consequence of large angle

fluctuations between two distinct states, experienced by the magnetization of the free layer in response to the dc current [17]. The fluctuations occur on time scales ranging from microseconds to fractions of a nanosecond and can be observed on the same range of currents and fields as the coherent high-frequency precessional excitations (see the previous paragraph). This two-states switching induced by the spin-polarized current is caused by large amplitude collective motion of the entire device, at rates that can be higher than 2 GHz.

Spin-transfer induces random telegraph noise with frequencies ranging between Hz and kHz has also been measured in the coercivity region. However, the telegraph noise in the coercivity region and the broadband instability are two fundamentally distinct phenomena: while in the coercivity region ($H_{app} < H_c$, $I < I_c$) two energy minima corresponding to two well defined magnetostatic states (P and AP) are accessible, for $H_{app} > H_c$, where the broad-band instability is measured, there is only one (if $I < I_c$) or even no (if $I > I_c$) energy minimum and magnetostatic state available. For the telegraph noise measured in the coercivity region, the resistance variation between the two states can be as high as the magnetoresistance amplitude, implying a 180° reversal of the magnetization. In the case of the broadband instability, the device exhibits resistance changes of up to 50% of the complete reversal, indicating that the spin-torque induces (meta)stable configurations of the magnetization, the properties of which are function of both applied field and current. An Arrhenius-Néel two-state analysis describing a thermally activated process over a barrier can be used as a way of parameterizing the effects of spin-torque and applied field on the system. This analysis leads to a calculated barrier height between the two bistable states about 100 times lower in the case of the broadband instability than in the coercivity region.

When measuring in an applied field higher than the anisotropy field, the resistance versus current cycle consists of a reversible transition and no longer of a hysteresis loop (Fig A.4 – 15, top-left). The position of the step (I_c) is a function of the applied field and is correlated with the appearance of two-state telegraph switching of the free layer's magnetization. Below I_c, the sample lies primary in the low resistance state, although it switches occasionally and very rapidly into and out of the higher resistance configuration. The transient time between the states is quite fast (~ ns). As the current is increased to I_c, the switching occurs with greater frequency and the time spent

in the high resistance state is increasing. The step in the dc resistance occurs when the dwell times in the two states are approximately equal. As seen on the resistance versus current curves too, above I_c the sample stays mainly in the high resistance state.

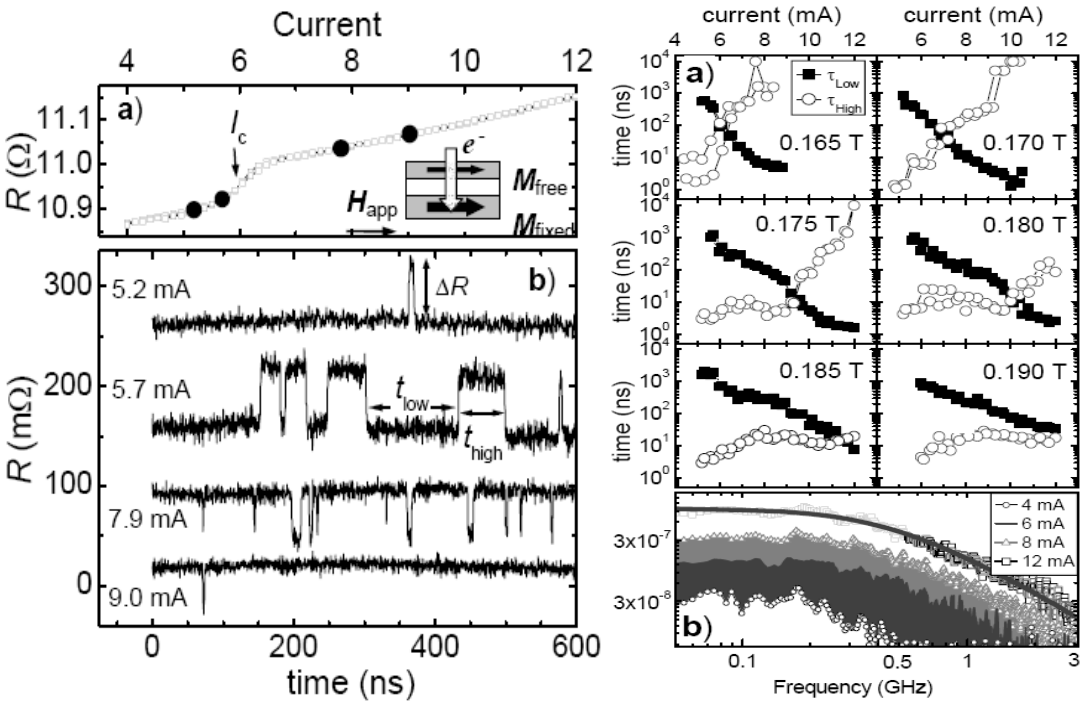

Fig. A.4 - 15 Broadband instability for a 50×100 nm² pillar with the following structure: IrMn70/Co75/Cu40/Co30 (thicknesses in Å). **Left: (a)** Resistance versus current curve in an applied field of 0.1 T. Full black circles denote currents for real time traces below. Inset: device structure, field and current direction. **(b)** Real time resistance fluctuations at several values of the current. **Right: (a-f)** Measured dwell times versus current, for different applied fields. **(g)** Power spectrum at 0.24 T showing high frequency broadband instability (with Lorentzian fits). (Extracted from ref. 17.)

The dwell times in the two states vary with the current in a markedly different fashion (Fig A.4 – 15, top-right). On a logarithmic scale, τ_{low} is roughly linear with the current, whereas τ_{high} is a more complicated function of I. Moreover, τ_{high} depends strongly on the applied field, while τ_{low} remains roughly linear and mainly shifts to higher currents, slightly changing slope. Therefore, the authors pointed out that the high and the low resistance states must evidently be distinct functions of current and field.

Finally, the range of currents over which fluctuations are observed increases with the field: the onset current of the fluctuations is a relatively weak function of the field, but the threshold where fluctuations cease moves rapidly towards higher currents. In other words, when higher fields are applied, the fluctuations are not more stabilized.

A.4.3. Conclusion

Much is known nowadays about spin-momentum transfer in simple Co/Cu/Co metallic pillars:

1. The critical currents are of the order of 10^7 A/cm² and they depend on the entire structure, including the leads; therefore, using special capping layers can reduce the critical currents; this direction should be pursued for memory applications;
2. The two critical currents are usually asymmetric in zero applied field;
3. Plotting the critical currents as a function of the applied field (or the resistance as function of current and field) one may establish a static stability phase diagram; increasing the temperature reduces the critical currents and generally induces a rounding of the critical lines;
4. The spin polarized current leads to a decrease of the energy barrier between the parallel and antiparallel states; the switching is thermally activated and therefore stochastic; this leads to telegraph noise inside the coercivity region;
5. Pulse-induced switching demonstrates that the reversal is thermally activated and stochastic (for low currents) or dynamic and deterministic (for high current), or a mixture of the two; the switching speed depends differently on the temperature for the two transitions, possibly due to the non-uniformity of micromagnetic configurations;
6. Spin-current can induce magnetization precession states inside and outside the coercivity region; plotting the integrated power as a function of current and field is one way of obtaining a dynamical phase diagram;
7. The frequency of the precession is of the order of gigahertz and can be tuned by changing the current or the field; superimposing a small alternative current can lead to frequency modulation and phase lock-in, which is important for oscillators applications;

8. The precession cone varies with the current; the peak amplitudes can be up to 40 times higher than the noise background, which is also important for oscillators applications;

9. Spin-currents can induce telegraph noise with frequencies higher than 2 GHz in regions of the phase diagram where only one or no state is stable.

The results are usually interpreted using Slonczewski's spin-torque model. Most of the experimental findings can be accounted for, even though some details are still unclear. Not much data has yet been published on more complicated pillars. The data that is available seems to be consistent with the results obtained on simple pillars.

Resumé :

La possibilité de renverser l'aimantation d'une couche mince en appliquant un courant polarisé a été démontrée expérimentalement pour la première fois vers la fin de l'année 2000. Depuis, un grand nombre de travaux ont été menés dans ce domaine, motivés par les applications potentielles des effets de transfert de spin. La plus part de ces études concernent des structures très simples, de type Co/Cu/Co. Ces empilements sont habituellement gravés pour fabriquer des piliers avec une taille latérale de l'ordre de 100nm ; alternativement, le multicouche peut être laissé non-patterné, pendant que un contact métallique avec un diamètre de 40nm (typiquement) est réalisé au-dessus de la couche libre.

Si quelques détails suscitent toujours des controverses, les résultats des différents groupes, obtenus pour des échantillons similaires sont en bon accord et généralement assez bien compris en prenant en compte le couple de transfert de spin. Ce chapitre tente de donner une vue d'ensemble des résultats expérimentaux (obtenus à travers des mesures statiques ou dynamiques à température variable) qui mettent en évidence les particularités des effets induits par le courant polarisé.

References:

[1] J.A. Katine et al., Phys. Rev. Lett. **84**, 3149 (2000)

[2] Some examples include, apart from ref. 1:

J. Grollier et al., Appl. Phys. Lett. **78**, 3663 (2001)

J.-E. Wegrowe et al., Appl. Phys. Lett. **80**, 3775 (2002)

J.Z. Sun et al., Appl. Phys. Lett. **78**, 3663 (2001)

S. Urazhdin et al., Phys. Rev. Lett. **91**, 146803 (2003)

[3] N.C. Emley et al., Appl. Phys. Lett. **84**, 4257 (2004)

D. Lacour et al., Appl. Phys. Lett. **85**, 4681 (2004)

M. Covington et al., Phys. Rev. B **69**, 184406 (2004);

[4] Y. Huai et al., Appl. Phys. Lett. **84**, 3118 (2004)

G.D. Fuchs et al., Appl. Phys. Lett. **86**, 152509 (2005)

[5] Y. Jiang et al., Phys. Rev. Lett. **92**, 167204 (2004)

[6] F.J. Albert et al., Appl. Phys. Lett. **77**, 3809 (2000)

[7] E.B. Myers et al., Phys. Rev. Lett. **89**, 196801 (2002)

[8] M.A. Zimmler et al., Phys. Rev. B **70**, 184438 (2004);

[9] D. Lacour et al., poster presented at JMC9, Nancy (2004)

[10] I.N. Krivorotov et al., Phys. Rev. Lett. **93**, 166603 (2002)

[11] S. Urazhdin et al., Appl. Phys. Lett. **84**, 1516 (2004)

[12] S. Kaka et al., arXiv:cond-mat/0411363 (2004)

[13] J.Z. Sun, Phys. Rev. B 62, 570 (2000)

[14] A.A. Tulapurkar et al., Appl. Phys. Lett. **85**, 5358 (2004)

[15] S.I. Kiselev et al., Nature **425**, 380 (2003)

[16] M.R. Pufall et al., Appl. Phys. Lett. **86**, 082506 (2005)

[17] M.R. Pufall et al., Phys. Rev. B **69**, 214409 (2004)

Part B :

Spin-transfer effects in spin-valves developed for CPP-GMR heads

Chapter 1. Motivation

The low field giant magnetoresistance of spin-valves [1] has been used in magnetoresistive read heads for computer disk drives since 1998. The current technology uses multilayers where the current is flowing parallel to the plane of the structure (current-in-plane (CIP) geometry).

Very significant progress was achieved in the preparation and optimization of spin-valves in terms of magnetic and transport properties, in order to keep pace with the steady increase in the storage area density of disk drives. Research and development in the field was concerned with:

1. Improving the overall structural quality of the stacks by appropriate choice of buffer layers;
2. Improving the biasing of the pinned layer, by using antiferromagnetic materials with higher Néel temperature, and offering higher exchange bias energy, by means of synthetic pinned layers;
3. Optimizing the thickness of each individual film;
4. Introducing nano-oxide (NOL) layers at appropriate locations in the stack to favor specular reflection of the electrons in the active part of the spin-valve;
5. Reducing the shunting of the current in the parts of the stack which do not contribute to the GMR;
6. Designing new multilayers (dual spin-valves, spin-filter spin-valves…) with more active interfaces or thinner free layers, in order to increase the GMR sensitivity.

At present, a GMR amplitude of 20% is attained in CIP spin-valves. However, unless a new breakthrough occurs, the present performance is close to the ultimate limit, not so much in terms of GMR amplitude, but where the compromise between amplitude and suitable magnetic properties for read-head applications is concerned. The read-head industry expects to be able to push forward the present technology for about two years, after which alternative solutions will have to be found. *Seagate* just started producing CPP-TMR heads and it seems likely that other companies will follow, especially considering the significant improvement introduced by the discovery of extremely high TMR amplitude achieved in MgO based tunnel junctions.

As a result, the current perpendicular-to-plane (CPP) geometry is receiving a growing interest [2]. From a practical point of view, measuring the CPP-GMR in metallic multilayers at room temperature requires the patterning of the multilayer in the form of submicron pillars connected with a bottom and a top electrode. Reducing the lateral dimension of the pillar is important in order to achieve resistance levels appropriate for the device (typically 30 Ω). Furthermore, for read-head applications, lowering the lateral size of the pillar will also allow for a higher spatial resolution of the reading process.

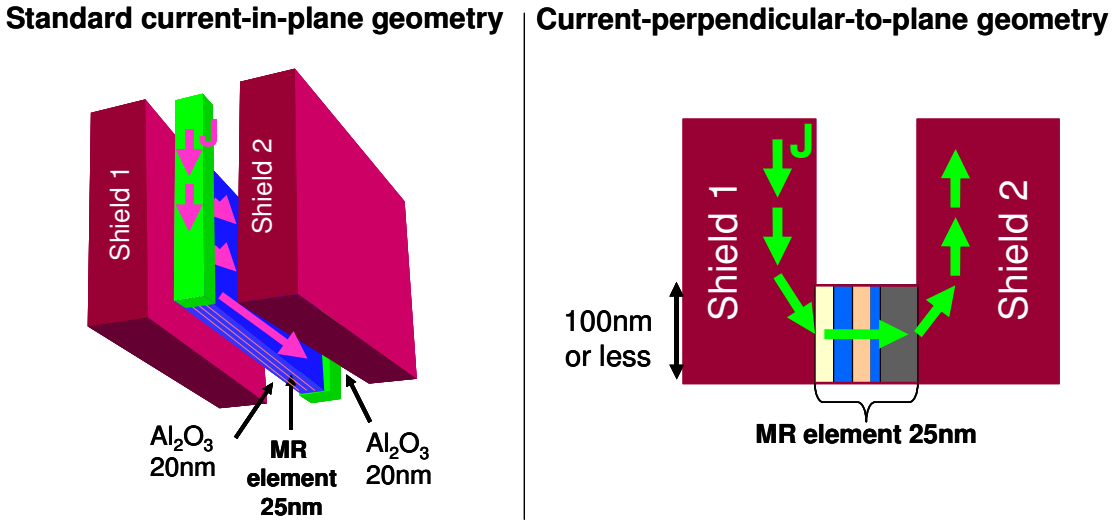

Fig. B.1 - 1 Schematic drawing of the standard CIP (**left**) and the CPP geometry (**right**) for GMR read head devices.

There are several advantages of the proposed CPP read-head design over the standard CIP technology:

1. The width of the read gap can be decreased down to 25 nm (as compared to 65 nm for CIP), improving the spatial resolution along the track;
2. The heat evacuation from the sensor is better in CPP than in CIP; therefore, more current can be applied through the device during the reading process, resulting in an increase in the signal to noise ratio;
3. The design and technology required for CPP heads at very small dimensions (150 nm and below) are much simpler than in CIP.

The current densities used in GMR heads are between 10^7 A/cm² and 10^8 A/cm², of the same order of magnitude as the currents at which spin-torque induced magnetic excitations are observed. Such effects can generate noise and influence the biasing of the magnetic heads; it is therefore important to study and understand them in order to control their influence. This constituted the main motivation for the present study.

The CPP-GMR in metallic magnetic multilayers can be intrinsically very large. Indeed, CPP-GMR exceeding 100% were reached for instance in (Co/Ag) multilayers at low temperature [3]. However, these large amplitudes were obtained in multilayers for which strong saturation fields were necessary or high hysteresis effects were observed. Such structures cannot be used for read-head devices, which require a high susceptibility of the free layer. Moreover, a good control of the relative orientation of the magnetization in the successive magnetic layers has to be achieved using fields of reasonable intensity. Therefore, CPP spin-valve stacks comparable to those developed for CIP-GMR have to be used.

The main drawback of the CPP design is that the highly resistive antiferromagnetic or buffer layers included in the stack are measured in series with the active part of the spin-valves (instead of in parallel as in the CIP geometry). In consequence, the measured GMR amplitude is significantly diminished. To reduce the detrimental effect of the high serial resistance of the antiferromagnetic and/or buffer layers, the relative resistance of the active part of the spin-valve must be increased. Two possible solutions are currently under study:

1. Introducing nano-oxide layers in the free and/or pinned layers, or even in the non-magnetic spacer layer. These very thin layers (typically 0.5 to 1 nm thick) are discontinuous. Their effect is to locally constrain the current paths through very narrow pinholes, increasing the local effective resistivity around each pinhole. This is equivalent to having a stack of variable cross section, narrow in the active part and broad in the inactive part of the stack. It has been shown that an increase by a factor 33 in $A \times \Delta R$ could be attained at room temperature when using NOL [4]. However, it is not clear yet how reliable are such structures, considering the extremely high current densities which may flow through these small pinholes.

2. Laminating the free and pinned layers by inserting very thin layers of non-magnetic material (e.g. replacing CoFe 3 nm by (CoFe 1 nm/Cu 0.3 nm)$_2$/CoFe 1 nm). The non-magnetic (Cu) layers should be sufficiently thin to provide a strong ferromagnetic coupling between the successive magnetic (CoFe) layers, so that they magnetically behave as a single layer [5]. Regarding the transport, each CoFe/Cu interface produces the same spin-dependent scattering as 20 nm of bulk Co. Therefore, the spin-diffusion length is significantly reduced in laminated layers, which means that a high current polarization can be achieved using very thin films. It is this type of samples which were investigated in the experimental part of this work.

Resumé :

La magnétorésistance géante des vannes de spin a été exploitée comme principe de fonctionnement des têtes de lecture pour les disques durs des ordinateurs depuis 1998. La technologie actuelle utilise des multicouches dans lesquelles le courant est appliqué parallèlement aux interfaces (têtes CIP). Néanmoins, en suivant les tendances actuelles de miniaturisation, on prévoit que ces dispositifs atteindront leur limite technologique dans deux ans; après, il sera nécessaire de trouver des solutions alternatives. Ainsi, il a été proposé d'utiliser une architecture dans laquelle le courant est appliqué dans la direction perpendiculaire au plan des couches (têtes CPP). Comme les piliers dans lesquels on étudie le transfert de spin, ces structures contiennent une couche piégée, qui agit en tant que polariseur, et une couche libre. En plus, les courants de fonctionnement de ces nouvelles têtes seraient de l'ordre de $10^8 A/cm^2$, c'est-à-dire du même ordre de grandeur (ou plus grands) que les courant nécessaires pour induire des effets de transfert de spin mesurables (notamment le renversement par courant polarisé ou l'excitation des états de précession entretenue). En conséquence, on s'attend à voir apparaître des effets similaires dans les têtes CPP, qui perturberaient leur fonctionnement. Il est donc important de comprendre le transfert de spin dans ces structures pour pouvoir minimiser le bruit qu'il induit. Ceci a constitué la principale motivation de ce travail.

D'un autre côté, à l'époque où cette étude a commencé, la communauté scientifique s'intéressait plutôt aux effets de transfert de spin dans des multicouches simples Co/Cu/Co. L'investigation de ce phénomène dans des vannes de spin très complexes, comme celles utilisées pour les têtes CPP, a amené un point de vue différent sur le sujet.

References:

[1] B. Dieny et al., J. Appl. Phys. **69**, 4774 (1991)

[2] W.P. Pratt Jr. et al., Phys. Rev. Lett. **66**, 3060 (1991)
M.A.M. Gijs et al., Phys. Rev. Lett. **70**, 3343 (1993)

[3] S.F. Lee et al., Phys. Rev. B **46**, 548 (1992)

[4] K. Nagasaka et al., J. Appl. Phys. **89**, 6943 (2001)

[5] H.Oshima et al., J. Appl. Phys. **91**, 8105 (2002)

Chapter 2. Experimental details

The samples were fabricated by *Headway Technologies* [1] as part of a development process oriented towards optimizing spin-valves for CPP-GMR heads – and not especially for investigating spin-transfer effects. Consequently, the structure was considerably more complicated than in the previous studies. Moreover, the samples had a square (almost circular) cross-section, and therefore no uniaxial shape anisotropy.

The characterization was completed at *Spintec*.

B.2.1. Sample structure

The experiments described in part B were conducted on four types of sputtered spin-valves (Fig. B.2 – 1):

a. BufferLayer/Seed/IrMn70/**CoFe10/Ta1/CoFe10/Ru8/(CoFe9/Cu3)×3/CoFe8/ Cu26/ (CoFe10/Cu3)×2/CoFe10**/Capping Layer;

b. Buffer Layer/Seed/IrMn70/**CoFe30/Ru8/(CoFe8/Cu3)×3/CoFe12/ Cu30/(CoFe10/Cu3)×2/CoFe10**/Capping Layer;

c. Buffer Layer/Seed/IrMn70/**CoFe30/Ru8/(CoFe8/Ag6)×3/CoFe12/ Cu30/(CoFe10/Cu3)×2/CoFe10**/Capping Layer;

d. Buffer Layer/Seed/IrMn70/**CoFe30/Ru8/(CoFe8/Ag6)×3/CoFe12/ Cu30/(CoFe10/Ag6)×2/CoFe10**/Capping Layer.

The thickness of each layer is given in Å. As a guide for the eye, for each wafer, the pinned layer is written in blue, the reference layer in purple and the free layer in green. In all four types of samples, both the free and the reference layer were laminated either by Cu or by Ag thin layers.

The purpose of the lamination is to increase the resistance of the part of the spin-valve which is active from the point of view of the CPP-GMR, namely the

reference layer / Cu / free layer stack. As mentioned in the previous chapter, the active part is measured in series with the other layers, which reduces the CPP-GMR ratio because of their very high resistance (in particular, the antiferromagnetic layer has a much more important resistivity than the CoFe or Cu layers). The GMR enhancement due to lamination is significant since, for example, each CoFe/Cu interface has a resistance equivalent to that of about 4 nm of bulk CoFe [2]. An improvement from 1.5% to 2.2% of the CPP-GMR was observed when using CoFe layers laminated by inserting very thin Cu layers, as compared with non-laminated structures [3]. However, the measured boost in the GMR amplitude was lower than expected from the enhancement of the active's part resistance, because of significant spin-flip at each CoFe/Cu interface. Indeed, it has been shown that the conduction electrons loose about 25% of their polarization at each Co/Cu interface [3]. The same order of magnitude of depolarization may be expected at $Co_{50}Fe_{50}$/Cu interface. Consequently, the electrons are almost fully repolarized along the direction of the local magnetization after having crossed less than 2 nm of the laminated stack. This fairly short effective spin diffusion length in the laminated layers is responsible for the moderate benefit of lamination.

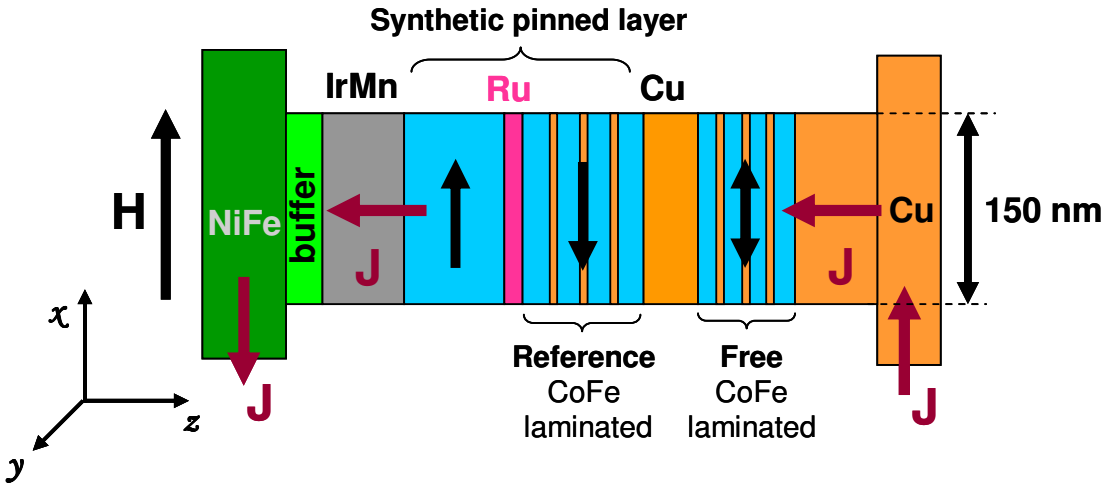

Fig. B.2 - 1 The structure of the samples includes a laminated CoFe free layer and a laminated synthetic pinned layer. The pillars have a "square" section with a lateral size generally between 90 nm and 170 nm. The magnetization of the AP1 (polarizing / reference) layer is oriented along the $-\vec{u}_x$ direction; consequently, a positive applied field favors the *antiparallel* state. The positive current is defined as electrons flowing along the $\vec{u}_z$ direction (from the reference to the free layer), therefore favoring the *parallel* orientation of the free layer with respect to the reference one.

Finally, as argued before [4], spin-transfer induced effects are expected to be significant in these samples, although the polarizing / reference layer (4.4 nm) is much thinner than in the commonly used samples for the study of spin-torque. The thickness of the AP1 layer is even smaller than the spin diffusion length in bulk $Co_{50}Fe_{50}$ (6 ± 1 nm) at room temperature [3]. Due to the lamination of the reference layer and the increased interfacial scattering and higher density of thermally activated magnetic fluctuations [3], the effective spin diffusion length in the laminated stack is reduced to 1.2 ± 0.1 nm. Consequently, the current can acquire a significant polarization despite the low thickness of the reference layer. Moreover, the free layer itself is several times thicker than the SDL. On one side, this implies that the switching currents are expected to be high. On the other hand, the free layer can also act as a polarizer, so that considerable spin-momentum transfer may appear in the synthetic pinned layer as well.

A 1 μm thick NiFe layer is deposited before the spin-valve. This layer, which is patterned to obtain the bottom electrode, is meant to constitute one of the magnetic shields in the real read-head device. The top electrode is made of Cu.

B.2.2. Sample fabrication

As mentioned above, the samples used for studying spin-transfer effects in spin-valves for CPP-GMR heads were fabricated by *Headway Technologies*. The fabrication process is described in fig. B.2 – 2.

First, the NiFe bottom lead is patterned, using optical lithography and dry etching, to obtain a stripe with its longer dimension (12 μm) along the pinning direction of the reference layer. Next, electron-beam lithography and ion-beam etching were used to fabricate square pillars (with rounded corners) with a nominal lateral size of 150 nm. The actual size of the samples (deduced from resistivity measurements) varied mostly between 80 and 170 nm. An insulator layer (alumina) was then deposited, so as to separate the top and the bottom current lines. The top contacts were opened through a lift-off process. The last steps of the patterning procedure were the sputtering and patterning of the top Cu lead, perpendicular to the bottom one. The layout allowed for four-probe measurements, with two contacts placed each current line.

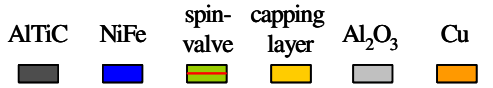

The metallic multilayer is sputtered on an AlTiC substrate.

Optical lithography and dry etching are used to pattern the bottom electrode.

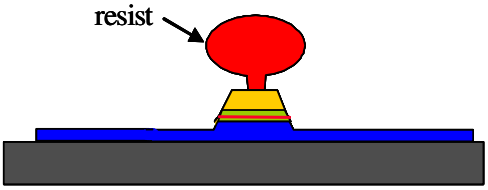

Electron-beam lithography and ion-beam etching are employed to pattern the pillar. The etching stops at the NiFe layer. The resist is not stripped after etching.

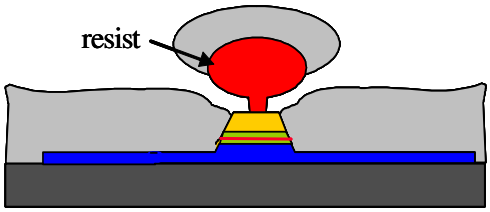

An oxide layer is deposited to insure the insulation between the top and bottom electrodes.

A lift-off technique is used to recover the contact with the pillar: the resist is stripped, removing simultaneously the oxide deposited on top of it.

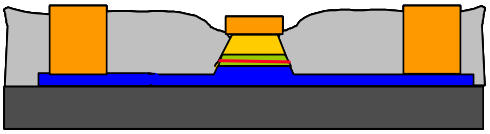

The contacts to the bottom current line are opened.

Fig. B.2 - 2 Patterning process for the samples, involving optical lithography (for the current lines), electron beam lithography (for the pillars), dry etching and a lift-off technique. The samples were fabricated by *Headway Technologies*.

B.2.3. Experimental setups for transport measurements

This paragraph describes the equipment used for the static (B.2.3.a) and the frequency-dependent experiments (B.2.3.b).

B.2.3.a. Experimental setup for static measurements

A simple setup which allows for four-probes measurements at room temperature was used for the static experiments. External magnetic fields up to +/-950 Oe could be applied with a small electromagnet, connected to a Kepco power source. For the first experiments, a Keithley 2400 sourcemeter was used both as a current source and as a voltmeter. Although quite reliable as a current source, the Keithley 2400 is less accurate as a voltmeter. A time-shifting voltage offset becomes evident when measuring small signals. The offset, which can be different for negative and positive voltage, appears as a divergence in the resistance versus current (R(I)) curves around $I = 0$. For the later experiments, the Keithley 2400 was used solely as a current source, and the voltage was more accurately measured by a Keithley 2182 nanovoltmeter. The sample is contacted using two sets of high frequency probes. The setup is computer-controlled through a GPIB interface, and can also serve for time-dependent measurements with a resolution of about 100 ms.

Alternatively, magnetoresistance curves could be recorded using a standard KLA Tencor tester. The tester encloses of two sets of coils which can generate fields with a variable angle and with a maximum available intensity of +/-1200 Oe. The applied field is measured through Hall probes. Unfortunately, there is a very strong field gradient vertically, and since the Hall probes are placed slightly higher than the sample itself, the field acting on the multilayer is not accurately known. Consequently, the free layer's coercivity measured with the tester was systematically higher than that determined using the home-made experimental setup.

The KLA Tencor tester cannot be used for R(I) scans, but it offers the possibility of measuring the MR properties at temperatures ranging from room temperature (25 °C) to 110 °C. This option was exploited in order to determine the thermal variation of the

resistance in the two magnetic configurations (parallel (P) and antiparallel (AP)) (see the next chapter).

B.2.3.b. Experimental setup for frequency-dependent measurements

The same home-made setup as described above was used for high frequency measurements, with slight modifications. In this case, only one set of high frequency probes was contacted to the sample. A high frequency coaxial cable connected the probes and the ac+dc end of a bias tee. The Keithley sourcemeter was connected to the dc exit. The ac port of the bias tee was plugged into a low-noise, high frequency preamplifier which transmitted the signal to a 26.5 GHz Agilent spectrum analyzer with 3 MHz resolution bandwidth [6]. Two different MITEQ preamplifiers were used: one which provided a 45 dB gain up to 10 GHz, with a noise figure of 2 dB [7], and the second with a 29 dB gain up to 8 GHz, with a noise figure of 3 dB [8].

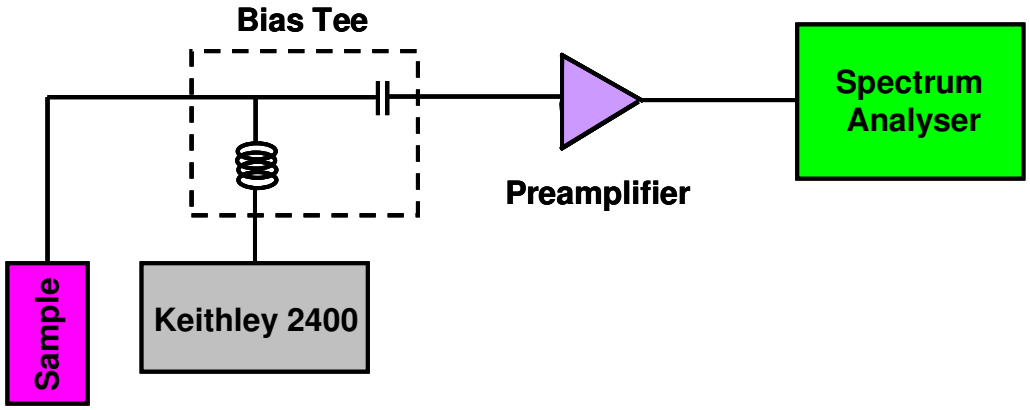

Fig. B.2 - 3 Schematic drawing of the experimental setup used for microwave measurements.

Resumé :

Ce chapitre décrit en détail la structure des échantillons, la géométrie, le mode de fabrication, et l'équipement utilisé pour les mesures et précise la convention de signe pour les sens positifs du champ et du courant appliqué.

Les échantillons contiennent une couche synthétique piégée par échange. Pour augmenter la résistance de la partie active de la vanne de spin (c'est-à-dire la succession couche de référence/espaceur/couche libre), les couches de référence et libres ont été laminées par insertion des très fines couches non-magnétiques.

En utilisant (entre autres) une étape de lithographie e-beam et une de lift-off, les vannes de spin ont été processées pour fabriquer des piliers de section circulaire avec un diamètre de l'ordre de 100nm.

Le courant positif est défini comme des électrons qui se déplacent de la couche de référence vers la couche libre (favorisant l'alignement parallèle entre les moments magnétiques de la couche libre et celle de référence). Tout champ positif est appliqué dans la direction opposée à l'aimantation de la couche de référence et favorise l'état antiparallèle.

References:

[1] *Headway Technologies*, 678 Hillview Dr, Milpitas CA 95035, US

[2] W. Oepts et al., Phys. Rev. B **53**, 14024 (1996)

[3] M. Li et al., submitted for publication to Appl. Phys. Lett.(2004)

[4] K.J. Lee et al., J. Appl. Phys. **95**, 7423 (2004)

A. Deac et al., to be published in J. Magn. Magn. Mater. (2005)

A. Deac et al., accepted for publication in Phys. Rev. B (2005)

[5] KLA Tencor tester

[6] Agilent PSA E4440A

[7] MITEQ AFS42-00101000-20-10P-42

[8] MITEQ AFS3-00100800-32-LN

[9] T. Devolder et al., submitted for publication to Phys. Rev. Lett. (2004)

Chapter 3. Static experiments: phase diagrams

Generally, the resistance of the samples on each wafer ranged between 4 and 9 Ω. The maximum magnetoresistance amplitude was:

- 2.9% and 2.6% for the two types of pillars whose free and reference layers were laminated with Cu (structures “a” and “b” in paragraph B.2.1);
- 2.4% for the pillars with Ag laminated reference layer and Cu laminated free layer (structure “c” in paragraph B.2.1);
- 2.1% for the pillars with Ag laminated free and reference layer (structure “d” in paragraph B.2.1);

The coercivity of the free layer ranged between 5 and 200 Oe for all four types of samples. In most cases, the coercivity was below 100 Oe, i.e. the free layer was much softer in these samples than the thin layers used in previous experiments reported in the literature. The dispersion from sample to sample was probably due to differences in the size or detailed shape of the pillars, especially at their edges, and to variations in the thickness of the (laminating) layers. A variation of 1 Å of the thickness of the non-magnetic films used for the lamination of the free and the reference layers can induce remarkable changes in the magnetostriction coefficients, which can in turn result in an increase of the anisotropy of the layers, if mechanical tensions are applied on the wafers during deposition or processing.

A shift up to a few tens of Oe was measured at low current in most samples in the position of the minor hysteresis loop associated with the switching of the free layer. This shift is due to the magnetostatic stray field from the pinned layer. As a result, in zero applied magnetic field, the samples were in the antiparallel state. This means that the stray field corresponds to a dominant interaction with the AP1 layer, which is closer to the free layer and slightly thicker than AP2 (see fig. B.2 – 1).

In most samples, the magnetization of the pinned layer started to switch around 1000 Oe, remaining unaffected in the range +/-900 Oe. Eventual excitations produced in the reference layer are not considered in this part.

In the discussion of the results, we use the following sign conventions (Fig. B.2 - 1):

1. **A negative applied magnetic field is oriented along the magnetization of the reference AP1 layer; therefore, it favors the parallel alignment of the magnetizations of the two layers. (It follows that positive field favors the antiparallel orientation.);**
2. **For negative current, the electrons flow from the free to the pinned layer, favoring the antiparallel state. (Inversely, for positive current, the electrons move in the opposite direction and favor the parallel state).**

All the results described below were obtained at room temperature, with the obvious exception of the temperature dependence of the sample resistance.

Generally, although the size varied from one sample to another, it was found that their behavior was remarkably similar (with few exceptions). The examples presented below are representative for the each category.

B.3.1. Current induced magnetization switching

At the time when this study was initiated, spin-transfer effects were known to appear in very simple structures, typically Co/Cu/Co and Co/Cu/NiFe, including a polarizing Co layer at least 10 nm thick. It was therefore unclear whether it was possible to observe current induced magnetization switching in the spin-valves deposited by *Headway*, which had such complicated structures and very thin polarizing layers.

Fig. B.3 – 1 (a) shows a minor magnetoresistance loop measured with a sense current of -0.4 mA, on a sample with Cu-laminated magnetic layers (structure a), with a lateral size of 89 nm (Sample 1). At such current density ($-5*10^6$ A/cm²), we do not expect any spin-transfer induced effects. The coercivity of the free layer sample is H_c = 91 Oe. The magnetostatic field from the synthetic pinned layer shifts the loop towards negative fields (i.e. the magnetostatic stray field is positive: H_{ms} = 48 Oe), thus favoring the AP state. The low resistance state, R_{min} = 8.78 Ω, corresponds to the P

alignment, and the high resistance state, R_{max} = 8.97 Ω, to the AP configuration. The MR amplitude for low current is 2.16%. The same relative resistance variation is found between the two resistance levels on the R(I) curve in Fig. B.2 – 3 (b) and the values of the resistance in the low and high resistance states are also very close to the ones measured in the P and AP configurations on the R(H) loop (R_{min} = 8.79 Ω and R_{max} = 8.99 Ω), demonstrating that the magnetization of the free layer can be switched between the two states by applying a current of the appropriate sign.

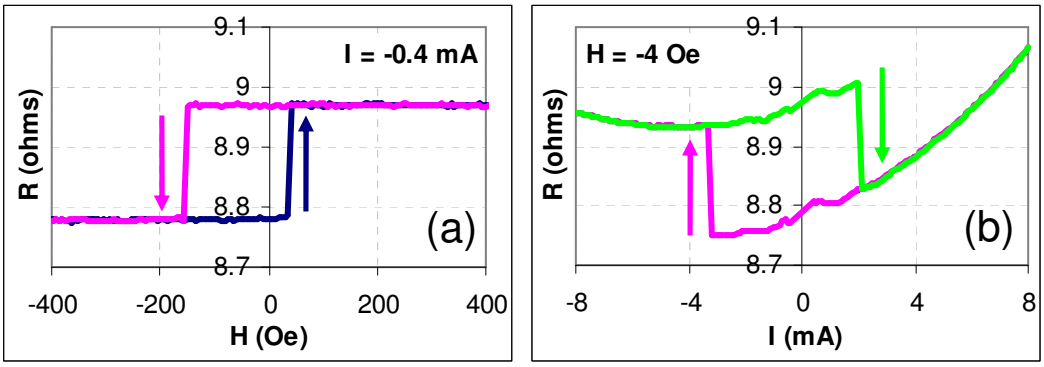

Fig. B.3 - 1 (a) Magnetoresistance curve for a 89 nm pillar with Cu laminated layers, measured with a -0.4 mA sense current. **(b)** Resistance versus current curve for the same sample in (nearly) zero applied field.

Starting with the sample in the AP state, a positive current $I_c^{AP\to P}$ = 2 mA ($j_c^{AP\to P}$ = 2.52*10^7 A/cm²) is needed in order to switch to the P state. Increasing the current more leads to heating the sample, as indicated by the parabolic resistance increase. When sweeping the current towards negative values, a P→AP transition occurs for $I_c^{P\to AP}$ = -3.3 mA ($j_c^{P\to AP}$ = 4.16* 10^7 A/cm²), after which the sample remains in the AP state until a positive current is applied. The sign of the switching currents is in agreement with the sign convention. The order of magnitude of the critical currents is the same as the reported in the literature for simpler structures. Both for the MR and the R(I) curves, the transitions between the two states are very sharp, suggesting that the sample is switching between two single-domain states.

As argued before (part B, chapter 1), spin-transfer induced appear in these samples because of the lamination of the reference layer, which reduces the effective

spin diffusion length in the laminated stack to 1.2 ± 0.1 nm and insures that the current can acquire a significant polarization.

Given the complex nature of the *Headway* samples, before attempting a deeper analysis of spin-transfer effects, it is important to ascertain the influence of various details of the structure which may not be important in terms of spin-torque, but can influence the experimental results. A noteworthy factor is the presence of the NiFe electrode.

B.3.2. Preliminaries: Influence of the NiFe electrode

First of all, as mentioned in chapter 2, the NiFe electrode is patterned so that its longer dimension is along the pinning direction of the pinned layer. As such, the total field acting of the free layer is fairly well known as long as the external field is applied along the axis in question, but not when the field is applied along a different arbitrary direction. In all the experiments described in this thesis, the external field was either parallel or antiparallel to the pinning direction of the SAF layer.

The presence of the NiFe electrode becomes obvious on the MR and R(I) curves through two different effects: an asymmetric heating (and resistance variation) as a function of the sign of the current, and the presence of noise in the resistance versus current and magnetoresistance curves around $H = 0$ Oe.

B.3.2.a. Asymmetric heating

Fig. B.3 – 1, b shows raw data. The resistance change due to heating was not subtracted, and is highly asymmetric for the two directions of the current. The same effect is even more noticeable on curves where no switching occurs (Fig B.3. – 2, a). The asymmetric heating is a consequence of the different nature of the top and the bottom electrode (Cu and NiFe, respectively), known as the Peltier effect: when a

voltage is applied on the junction between two metals, it induces a temperature gradient between the two leads; the sign of the temperature gradient depends on the sign of the applied voltage.

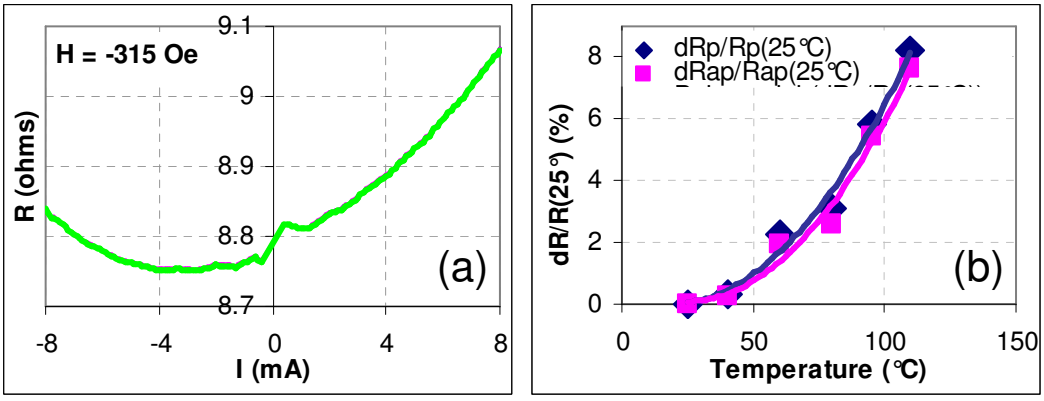

Fig. B.3 – 2 (a) Resistance versus current variation when no current induced switching occurs, for the same sample as in fig. B.3 – 1. (The sample remains in the parallel state). The resistance change as function of current is solely due to heating. **(b)** Relative resistance variation as a function of temperature, in the two states, measured on a different sample. Solid lines: best fit (guide for the eye).

For positive voltage, the hot electrode is the Cu / pillar system; under negative voltage, the hot electrode is the NiFe lead. The measured resistance variation is due to the combination of Joule heating (~ I^2) and Peltier heating / cooling (~ I). In order to estimate the temperature variation due to the combined Joule and Peltier effects, we have measured the thermal variation of the pillar resistance in the range 25 – 110 °C (Fig.B.3 -2, b). According to fig.B.3 -2, b, increasing the current from 0.4 mA to 8 mA yields a resistance increase of 2.95%. The comparison with fig.B.3 -2, a indicates that this corresponds to a raise in temperature of about 50 °C between 0 and 8 mA. For negative currents, a decrease of resistance of about 0.5% is first observed (from –0.4 mA to –5 mA), when the Peltier cooling dominates the Joule heating. At higher negative currents (between –4 mA and –8 mA), the resistance increases with 0.5%, since the Joule heating becomes more important than the Peltier cooling (Fig.B.3 -2, a). According to fig.B.3 -2, b, this corresponds to a temperature variation of less than 10 °C.

These temperature variation estimations are averaged over the entire pillar. Locally, the temperature change can be even larger. Samples having two identical leads do not show any heating dependence on the polarity of the current, supporting the interpretation of the asymmetrical heating in terms of Joule and Peltier effects.

B.3.2.b. Noise in very low applied field (+/-15 Oe) and "inverse" coercivity

Under certain conditions, some of the samples showed a so-called "inverse" coercivity: when measuring a magnetoresistance loop, starting with the sample in the P configuration, the transition to the AP state occurs at more negative fields than the transition back to P (Fig. B.3 - 3, a). The "inverse" coercivity always appears when the magnetoresistance loop is approximately centered on zero applied field and the two transitions are quite close to each other (the "coercivity" is of the order of 5 Oe) and relatively sharp.

When the loop is shifted from zero or very slated, a spike is recorded in the same range of fields as the "inversed" coercivity (Fig. B.3 - 3, c and d). Both features have the same origin (the presence of the NiFe electrode) and the "inverse" coercivity is an artifact caused by an inappropriate choice of the field sweep step when measuring the magnetoresistance curve.

Given its dimensions, the coercivity of the NiFe electrode is very low; this layer saturates in fields of the order of 5 Oe. As such, its magnetization changes orientation between approximately +5 and -5 Oe, and consequently the magnetostatic interaction between the electrode and the free layer changes sign. For negative field values, the magnetization of the NiFe electrode is oriented along the field and the reference layer, and the magnetostatic interaction between the electrode and the free layer is such that it tends to orient the magnetization of the latter in the antiparallel state with respect to the reference layer. For positive fields, the NiFe magnetization changes sign, so that the dipolar coupling on the free layer favors the parallel state.

Fig. B.3 - 3, b shows the same loop as in fig. B.3 - 3, a, measured with a smaller field variation step (0.5 Oe as compared with 11 Oe in fig. B.3 - 3, a). Starting with the sample in the parallel state, a first transition to the antiparallel configuration occurs at -1 Oe. This configuration is unstable, however, because the applied field is no longer

strong enough to saturate the NiFe electrode, which breaks into magnetic domains and finally reverses to the opposite orientation around 7 Oe. At this point, the magnetostatic field exerted by the electrode on the free layer changes sign, so the real field acting on the free layer has actually the same value as before the P→AP transition was measured; the sample returns to the parallel state. Consequently, the P→AP transitions at -1 and 14 Oe are actually one and the same, since they correspond to the same real field on the free layer. A similar interpretation can be applied to the AP→P transitions at 11 and -4 Oe. In other words, the two apparently different loops in fig. B.3 - 3, b are identical. It is to be noted that their coercivity is positive. It emerges as negative in fig. B.3 - 3, a because of the field step being too high, so that only the P→AP transition at -1 Oe and AP→P transition at 12 Oe are measured. When the loop is shifted to larger fields, or very slanted, the reversal of the NiFe comes out as a spike around $H = 0$ Oe.

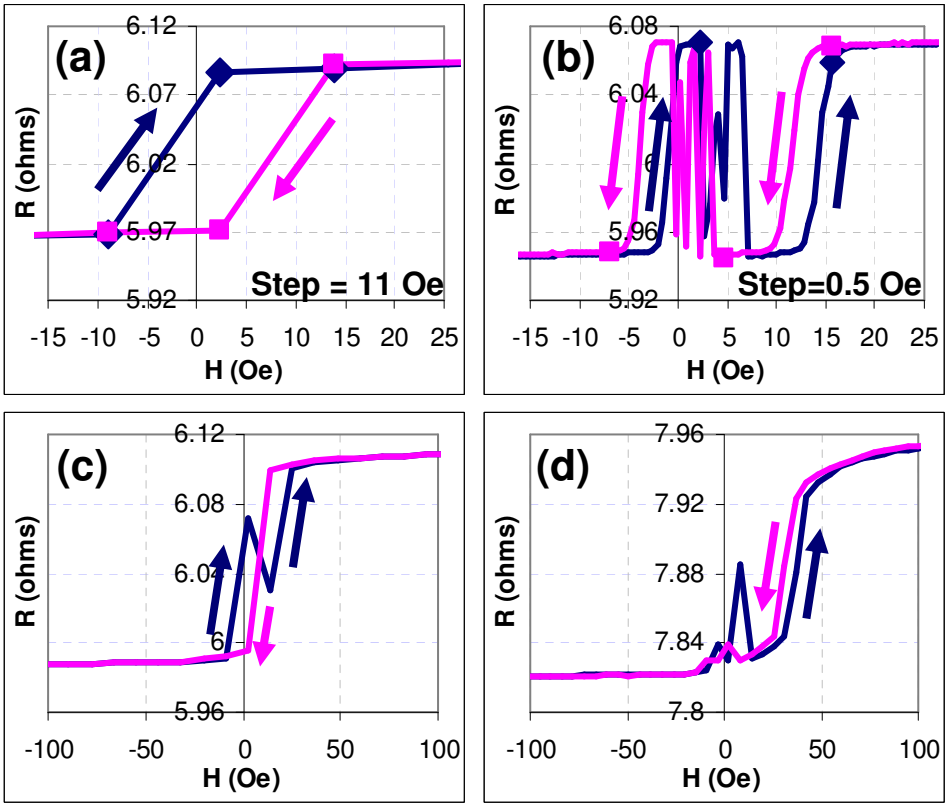

Fig. B.3 – 3 (a) Magnetoresistance loop showing a 5 Oe "inverse" coercivity. The field was swept with an 11 Oe step. The P→AP / AP→P transition occurs between -9 and 2 Oe / 14 and 2 Oe. **(b)** Same loop as (a), measured with a 0.5 Oe sweep step. The squares mark the points in fig (a). **(c)** and **(d)** Loops shifted from zero, showing spikes in very low field.

Although they do appear as peculiar features on the MR curves, and the noise induced by the reversal of the NiFe electrode may be mistaken for spin-torque induced telegraph noise, none of these effects is the result of spin-transfer.

B.3.3. Phase diagram: general trends and macrospin modeling

Apart from the necessity of understanding and minimizing spin-transfer effects in CPP-GMR heads in order to insure the good functioning of these devices, the study of spin-torque induced phenomena in such complex spin-valves was interesting in itself. For one thing, owing to the use of an exchange biased polarizing layer, it was possible to investigate all four quadrants of the I-H magnetic stability phase diagram. (In Co/Cu/Co pseudo-spin-valves such as described in part A, chapter 4, only the two quadrants corresponding to fields oriented along the magnetization of the thick layer can be reconstructed, since applying the field in the opposite direction eventually reverses the moment of the reference layer.) Although lately structures with increasing degree of complexity have been investigated, including CPP spin-valves with synthetic pinned layers [1, 2] or magnetic tunnel junctions [3], this was one of the first studies to report on a complete phase diagram including both directions of the applied magnetic field. It was also the first study of spin-transfer effects in metallic exchange biased spin-valves comprising a pinned synthetic antiferromagnetic (SAF) reference layer and a (very) soft free layer. For the first time, the entire critical lines were obtained both from resistance versus current curves R(I) for different applied fields, and from the magnetoresistance R(H) curves measured with various sense currents. The two sets of critical lines are compared and interpreted by analyzing the stability of the solutions of Landau-Lifshitz-Gilbert equation including the spin-torque term, within a macrospin model.

The results presented in this paragraph have been obtained measuring a pillar with a lateral size of 87 nm, with Cu laminated free and reference layer (structure “a”). Considering the size of the sample, an applied current of 1 mA corresponds to a current density of about $1.26*10^7$ A/cm².

B.3.3.a. Evolution of the resistance versus current curves with the applied magnetic field

Fig. B.3 - 4 shows the evolution of the resistance versus current characteristics while increasing the applied negative magnetic field.

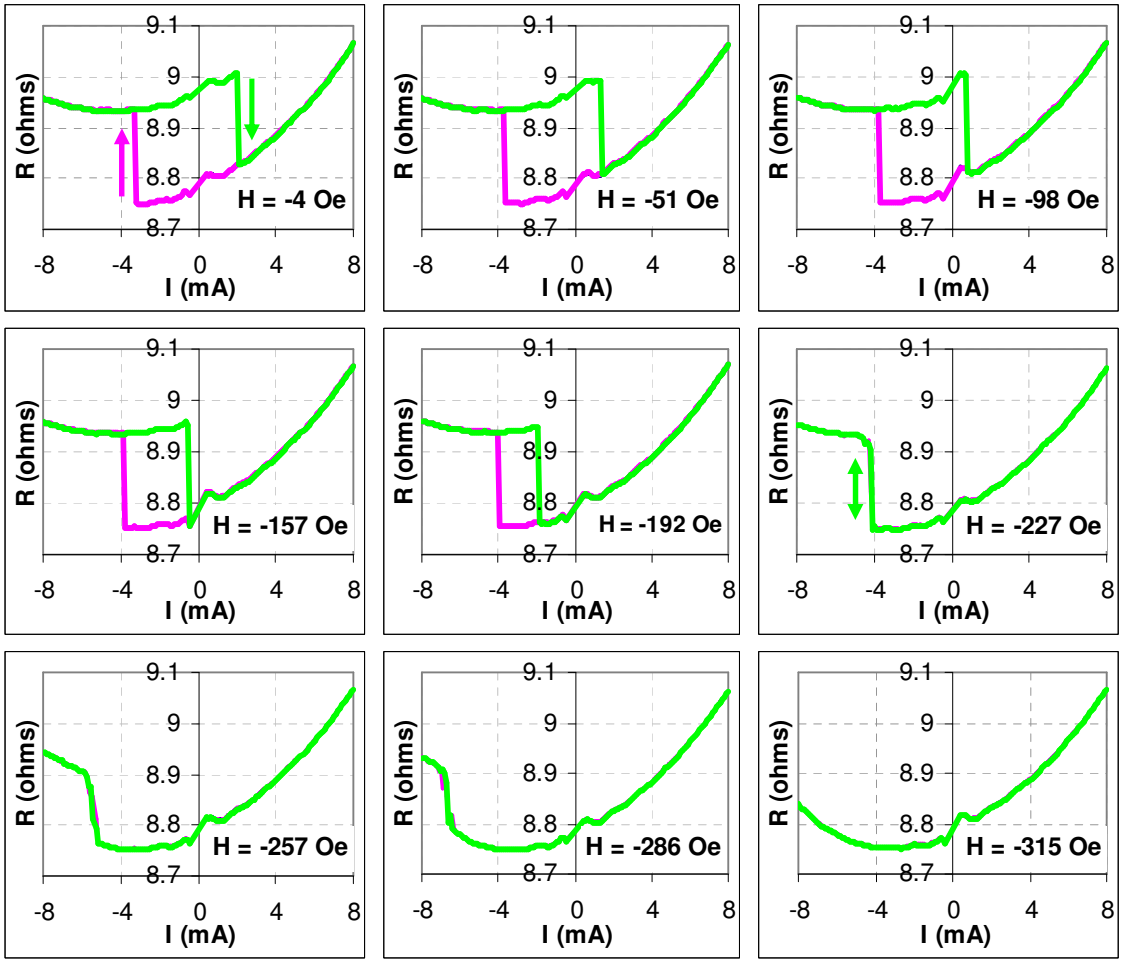

Fig. B.3 - 4 Resistance versus current characteristics for increasing values of the negative applied field.

Considering the conventions for positive fields (which favor the AP state), and for the sign of the current (positive current favors the P alignment), as long as the external field is not large enough, the AP→P transition occurs in positive currents, and the P→AP transition is induced by negative currents, as expected. At -51 Oe, when the magnetostatic field from the pinned layer is approximately compensated by the external

field, a strong asymmetry is observed between the two switching currents, as predicted by Slonczewski's ballistic model (see part B, chapter 2). Increasing the external field induces a shift of the loop towards more negative currents. The AP→P transition shifts slowly at low fields (between 0 and approximately -140 Oe), and faster at larger fields. Simultaneously, the coercivity is gradually reduced, the AP→P transition shifting more rapidly than the P→AP . At -227 Oe, the curve is practically reversible. At -315 Oe, the maximum applied current is no longer sufficient for inducing a P→AP transition, and the sample remains in the P state (under the influence of the applied field).

The sample behavior in positive fields is unusual (Fig. B.3 - 5). When H = 0 Oe, a strong telegraph noise is measured in the range of currents where the free layer should be in the P state (between $I_c^{AP\to P}$ = 2.2 mA and maximum applied current, 8 mA). The noise diminishes when increasing the field, but, at the same time, a gradual reversible transition towards a higher resistance state appears for high currents. The onset of this transition is moving towards lower currents when the field is increased. Simultaneously, the AP→P transition induced by spin-transfer is moving towards higher values of the current. For H > 37 Oe, the sample remains in (or close to) the AP state and no clear switching is observed.

Another unexpected detail is the evolution of the P→AP switching between -4 and 7 Oe. While the AP→P transition shifts gradually towards higher positive currents when increasing the field (from 2.1 mA at -4 Oe to 2.2 mA at 1 Oe and finally 2.5 mA at 7 Oe), the P→AP transition exhibits a less progressive behavior: the system switches back to the AP state at -3.3 mA for an applied field of -4 Oe, 1.7 mA for 1 Oe and then again -2.7 mA for 7 Oe. However, when considering all the curves in fig. B.3 – 4 and fig. B. 3 – 5, it becomes obvious that merely the curve at 1 Oe is irregular. All the measured samples showed relatively chaotic behavior and strong noise close to H = 0 Oe, although the magnetostatic interaction between the reference and the free layer varied considerably from sample to sample. As such, it appears that the 'chaotic' R(I) characteristics is related solely to the external field, and not to the total field acting on the free layer's magnetization. Since for spin-transfer induced phenomena only the total field is important, it is very likely that this detail is not a particularity of spin-transfer in these structures, but rather a consequence of the switching of the NiFe electrode in low applied fields.

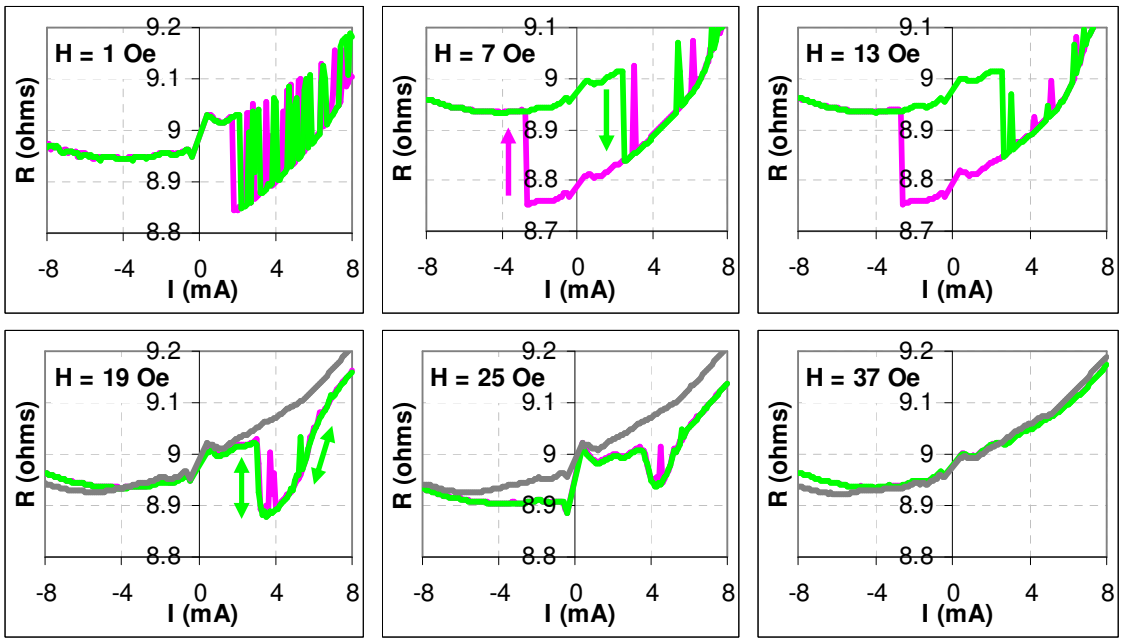

Fig. B.3 - 5 Resistance versus current characteristics for increasing values of the positive applied field. The divergence around I = 0 mA (very obvious on the curve obtained for H = 25 Oe) is an artifact caused by the time-shifting voltage offset introduced by the Keithley sourcemeter (see chapter 2). The grey curve is measured at 600 Oe, when the resistance remains (close to) that of the AP state.

B.3.3.b. Evolution of the magnetoresistance curves with the sense current

An alternative procedure for studying spin-transfer induced effects consists in monitoring the evolution of the magnetoresistance curves with the applied current (Fig. B.3 - 6 and Fig. B.3 - 7).

Increasing the negative sense current (Fig. B.3 - 6) up to –3 mA induces a slight shift of the loop towards negative fields; this observation is in good agreement with the fact that for negative currents the spin-transfer torque tends to stabilize the AP state, since the electrons are flowing from the free to the pinned layer. The coercivity is not much affected in this range of current. Between –3 mA and –4 mA, the P→AP transition jumps from ~ 0 Oe to ~ -200 Oe, and the coercivity becomes virtually zero. The current density is large enough to induce the P→AP transition of the free layer. The AP→P transition still occurs under the influence of the field. Increasing the current over

-4 mA causes a faster shift of the loop, and possibly the formation of a vortex distortion. The transition between the two states becomes more and more slanted with the increasing negative current. In addition, the magnetoresistance amplitude drops from 2.16% for I = -0.4 mA to less than 1.5% at +/-7.5 mA.

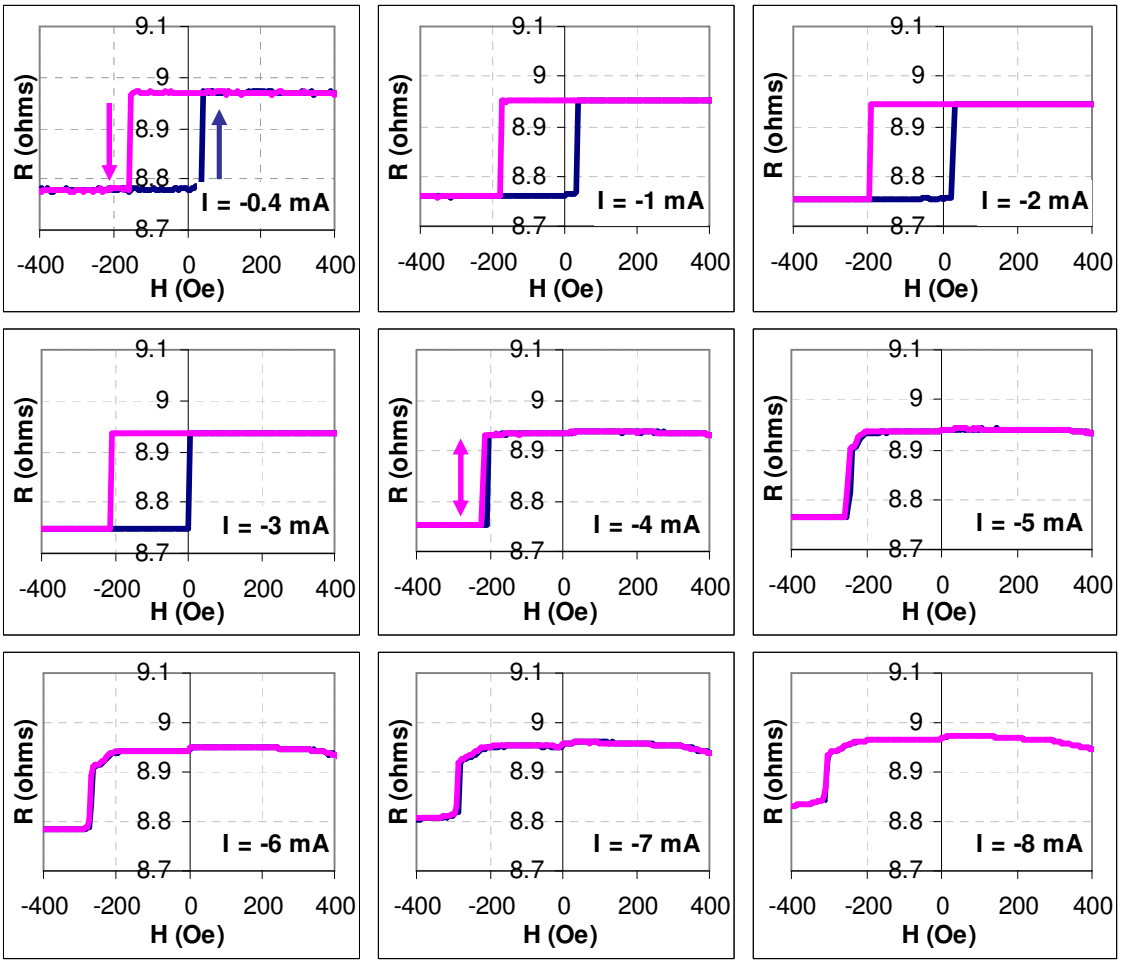

Fig. B.3 - 6 Magnetoresistance curves measured for increasing values of the negative sense current.

When applying a positive sense current (Fig. B.3 - 7) up to 2 mA, the transition AP→P is shifting slightly towards more positive fields, while the P→AP transition remains practically unaffected. At I = 2 mA, the switching becomes reversible. Increasing the current further yields only a more pronounced slanting of the transition, but no additional shift is measured. The magnetoresistance amplitude is decreasing progressively, as in the case of increasing negative sense currents.

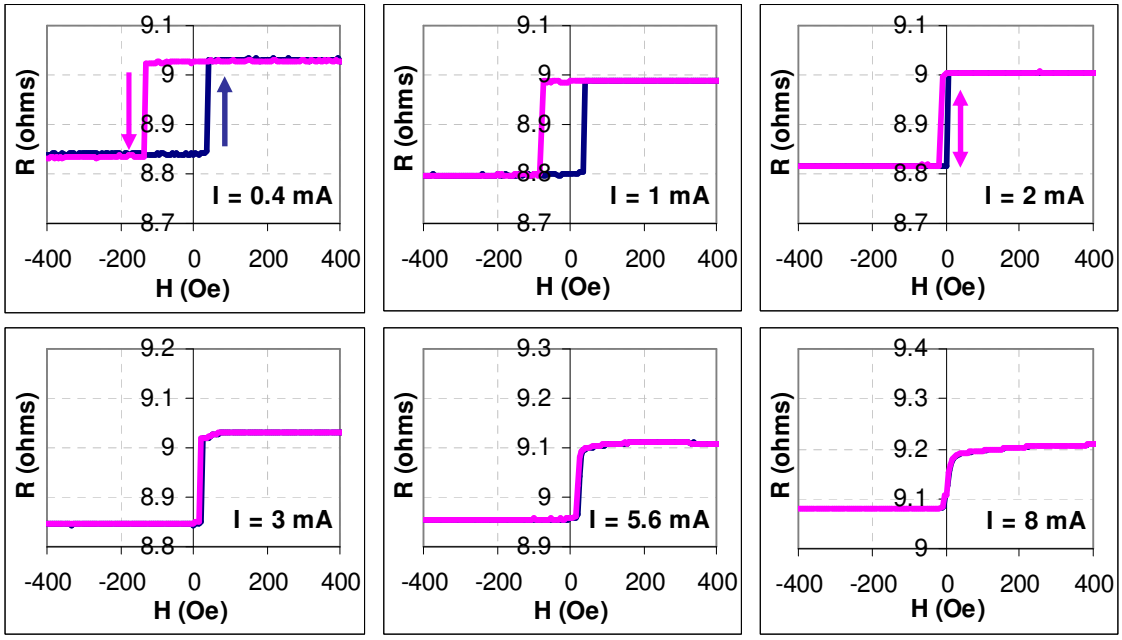

Fig. B.3 – 7 Magnetoresistance curves measured for increasing values of the positive sense current.

B.3.3.c. Static phase diagram

A remarkably good agreement is obtained when superimposing on the same plot the critical lines from the resistance versus current curves for constant applied (negative) magnetic fields, and from the magnetoresistance curves measured with different (negative and positive) sense currents (Fig. B.3 - 8).

Following the approach of Grollier et al. [4], we have plotted the switching currents ($I_c^{AP\to P}$ and $I_c^{P\to AP}$) or the switching fields ($H^{AP\to P}$ and $H^{P\to AP}$) for hysteretic loops, and the beginning and the end of the transitions (I^{start} and I^{end}, or H^{start} and H^{end}), if they were reversible. Four distinct types of regions can be identified on the phase diagram:

1. A central region (the 'coercivity' region) where both the P and the AP states are stable (in-between the $I_c^{AP\to P}$ and $I_c^{P\to AP}$, $H^{AP\to P}$ and $H^{P\to AP}$ curves, respectively, in dark pink in fig. B.3 – 8);
2. A region where only the P state is stable (above the $I_c^{AP\to P}$ / $H^{AP\to P}$ and I^{start} / H^{start} lines, in light blue in fig. B.3 – 8);

3. A region where only the AP state is stable (under the $I_c^{P\to AP}$ / $H^{P\to AP}$ and I^{end}/ H^{end} lines, in light pink in fig. B.3 – 8);

4. Two regions where neither state is stable (between the I^{start} and I^{end}, respectively H^{start} and H^{end} curves, in grey in fig. B.3 – 8).

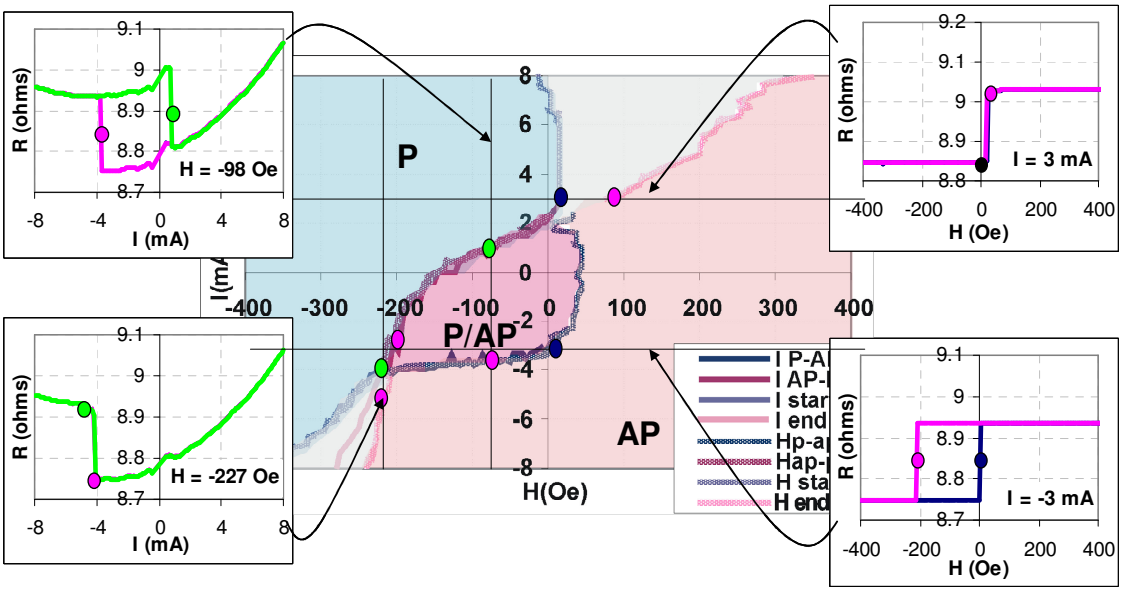

Fig. B.3 – 8 Phase diagram obtained from the resistance versus current curves for constant applied (negative) magnetic fields, and from the magnetoresistance curves measured with different (negative and positive) sense currents. The switching currents ($I_c^{AP\to P}$ and $I_c^{P\to AP}$) or the switching fields ($H^{AP\to P}$ and $H^{P\to AP}$) were plotted for hysteretic loops, or the beginning and the end of the transitions (I^{start} and I^{end}, or H^{start} and H^{end}), if they were reversible. The dotted lines represent the theoretical fit.

Both series of measurements (R(I) for different H and R(H) for different I) have been repeated, yielding similar results. Moreover, when plotting the current density as a function of the reduced field, defined as the total field acting on the free layer divided by the coercivity, it was found that the critical current densities in zero reduced field have very similar values for samples of the same structure (Fig. B.3 – 9).

Fabricating pillars with a lateral size of the order of 100 nm is a delicate process; on the surface of a wafer, the size varies from sample to sample, and so do the coercivity and the magnetostatic field. Plotting the phase diagram as current density versus reduced field is an elegant way of comparing different samples, regardless of the

variation of geometrical details. The sample size is calculated taking into account the structure and the experimentally determined values for the resistance and the magnetoresistance, as described in paragraph B.4.3.

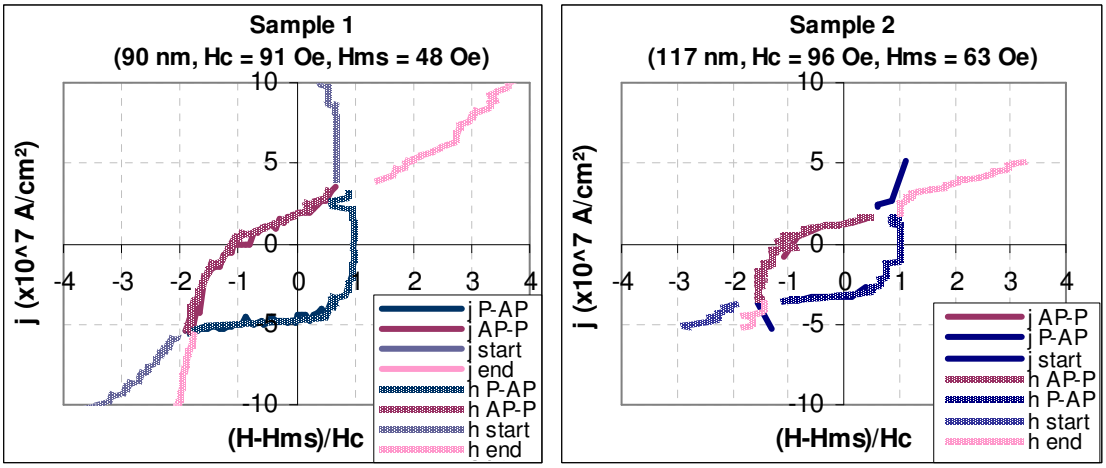

Fig. B.3 – 9 Phase diagrams plotted as current density versus reduced field (defined as total field acting on the free layer divided by the coercivity) for the same sample as in the previous figures (**left**, structure a) and for a second sample (**right**, structure b). Both samples had the reference and the free layer laminated with Cu. The critical current densities in zero total field have very similar values for the two samples.

B.3.3.d. Switching current distribution

As explained in part A, chapter 4, current induced magnetization switching is a (partially) thermally activated phenomenon, and consequently has a stochastic nature: when repeatedly measuring the same R(I) loop, the switching does not always occur for exactly the same values of the current (Fig. B.3 – 10). For the sample in fig. B.3 – 9, both switching currents distributions have a width of about 1 mA.

Accordingly, the critical lines on the phase diagrams in fig. B.3 – 9 are rather guides for the eye than exact border lines, since they have been obtained through single measurements under given conditions (i.e. for a fixed value of applied field, the corresponding R(I) characteristics was measured only one time; idem for the magnetoresistance curves).

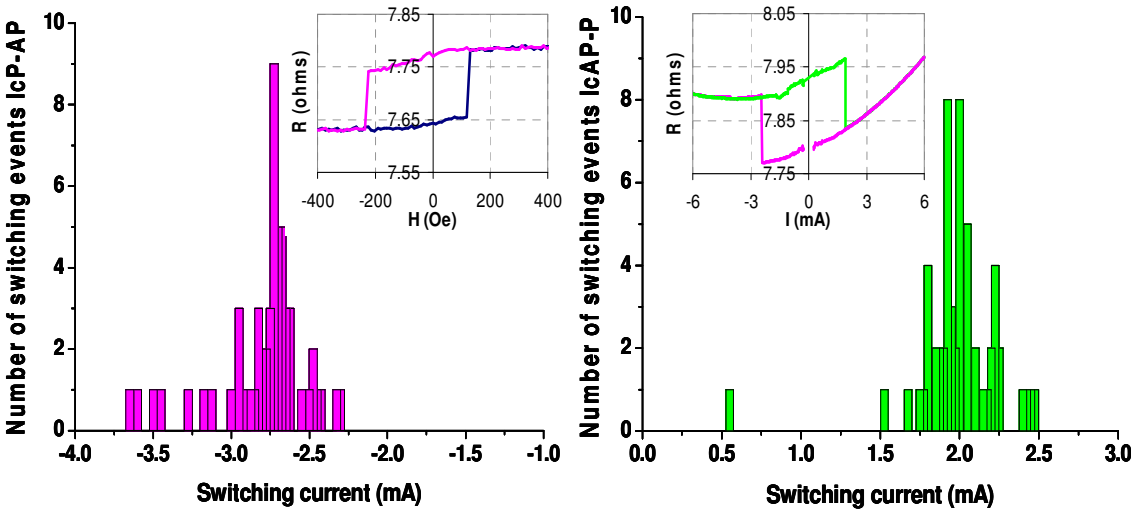

Fig. B.3 - 10 Switching histograms for the two critical currents ($I_c^{P\to AP}$, **left**, and $I_c^{AP\to P}$, **right**) measured on a different sample (sample 3) that those showed in fig. B.3 – 9. The histograms were reconstructed from a total number of 57 R(I) loops measured in an external field of -8 Oe. Inset: magnetoresistance curve (left) and resistance versus current characteristics (right) for the same sample.

B.3.3.e. Macrospin modeling

Following the macrospin approach of the spin torque induced dynamics [5, 6], and taking into account our conventions for the direction of the field and current, the Landau-Lifshitz-Gilbert equation of motion for the free layer magnetization can be written:

$$\frac{\partial \vec{m}}{\partial t} = -\gamma\ \vec{m}\times\left[H_{res}\vec{u}_x - H_d\left(\vec{m}\cdot\vec{u}_z\right)\cdot\vec{u}_z\right] + \alpha\cdot\vec{m}\times\frac{\partial\vec{m}}{\partial t} - \frac{\hbar}{2e}\cdot\frac{\gamma}{M_s t}\cdot g(\theta)\cdot j\cdot\vec{m}\times\left[\vec{m}\times\left(-\vec{u}_x\right)\right] \tag{19}$$

(See page 26 for notations and fig. B.2 - 1 for the definition of the coordinate system.)

The first term in Eq. (19) is the field induced precession term; the second is the Gilbert damping, and the third is the contribution of the spin-torque. The spin-torque can act as damping or anti-damping, depending on the relative effects of the total field and the applied current (see part A, chapter 3). Note that in our coordinate system, the

magnetization of the pinned layer is parallel to $-\vec{u}_x$ (negative field favors the P alignment).

Eq. (19) can be solved following Grollier et al.'s method [6]. After projection on the *x*, *y*, *z* axes, and considering that the magnetization of the free layer is close to either the P or the AP state ($m_x = \mp 1 ; \dot{m}_x = 0$), the following system is obtained:

$$\begin{cases} \dot{m}_y = \mp \dfrac{\hbar}{2e} \cdot \dfrac{\gamma}{M_s t} \cdot g(\theta)\, j m_y - \gamma (H_{res} \mp H_d) m_z \pm \alpha \dot{m}_z \\ \dot{m}_z = \gamma H_{res} m_y \mp \dfrac{\hbar}{2e} \cdot \dfrac{\gamma}{M_s t} \cdot g(\theta)\, j m_z \mp \alpha \dot{m}_y \end{cases} \quad (35)$$

Replacing $\dot{m}_y$ from the first equation into the second, and $\dot{m}_z$ from the second into the first, and neglecting the terms $\alpha^2 \dot{m}_y$ and $\alpha^2 \dot{m}_z$ ($\alpha \sim 10^{-2}$-10^{-3}), one gets:

$$\begin{cases} \dot{m}_y = \pm \left[-\dfrac{\hbar}{2e} \cdot \dfrac{\gamma}{M_s t} \cdot g(\theta) j + \alpha \gamma H_{res} \right] m_y - \left[\alpha \dfrac{\hbar}{2e} \cdot \dfrac{\gamma}{M_s t} \cdot g(\theta) j + \gamma (H_{res} \mp H_d) \right] m_z \\ \dot{m}_z = \left[\alpha \dfrac{\hbar}{2e} \cdot \dfrac{\gamma}{M_s t} \cdot g(\theta) j + \gamma H_{res} \right] m_y \pm \left[-\dfrac{\hbar}{2e} \cdot \dfrac{\gamma}{M_s t} \cdot g(\theta) j + \gamma (H_{res} \mp H_d) \right] m_z \end{cases} \quad (36)$$

Separating the two variables, the following equation is obtained:

$$\ddot{m}_y \mp \left[-2 \frac{\hbar}{2e} \cdot \frac{\gamma}{M_s t} \cdot g(\theta) j + \alpha \gamma (2 H_{res} \mp H_d) \right] \dot{m}_y + \left[(1+\alpha^2) \left(\frac{\hbar}{2e} \cdot \frac{\gamma}{M_s t} \cdot g(\theta) j \right)^2 + (1+\alpha^2) \gamma^2 H_{res} (H_{res} \mp H_d) \right] m_y = 0 \quad (37)$$

The solutions of this equation are of the type

$$m_y = A e^{kt}$$

where *k* is the solution of the equation:

$$k^2 \mp \left[-2 \frac{\hbar}{2e} \cdot \frac{\gamma}{M_s t} \cdot g(\theta) j + \alpha \gamma (2 H_{res} \mp H_d) \right] k + \left[(1+\alpha^2) \left(\frac{\hbar}{2e} \cdot \frac{\gamma}{M_s t} \cdot g(\theta) j \right)^2 + (1+\alpha^2) \gamma^2 H_{res} (H_{res} \mp H_d) \right] = 0 \quad (38)$$

for which:

$$\Delta = -\left[2\alpha\frac{\hbar}{2e}\cdot\frac{\gamma}{M_s t}\cdot g(\theta) j\right]^2 + (\alpha\gamma H_d)^2 -$$

$$-4\alpha\gamma(2H_{res} \mp H_d)\frac{\hbar}{2e}\cdot\frac{\gamma}{M_s t}\cdot g(\theta) j - 4\gamma^2 H_{res}(H_{res} \mp H_d) \quad (39)$$

Considering $j \sim 10^{11}$ A/m², $H_d \sim 1$ T for CoFe, $H_{res} \sim 10^{-3}$-10^{-1} T in most of the cases, $g \sim 0.1$, the first term in eq. (39) is of the order of 10^{12} s^{-2}, the second 10^{16} s^{-2}, the third 10^{17} s^{-2}, and the last is between 10^{18}-10^{22} s^{-2}, so one can write:

$$\Delta = -4\gamma^2 H_{res}(H_{res} \mp H_d) \quad (40)$$

For each state (P/AP), if Δ is negative, both solutions of eq. (39) are complex; if the real part of k is positive, m_y grows in time and the state is unstable. When Δ is positive, the state becomes unstable if at least one of the solutions of eq. (38) is positive.

We thus obtain the following stability conditions:

1. **the P state is unstable when:** (41)

$$j < \frac{2e}{\hbar}\frac{\alpha M_s t}{g(0)}\left(-\frac{H_d}{2} + H_{ms} - H_k + H\right) \quad , \text{ if } H < -H_{ms}+H_k ;$$

$$j < \frac{2e}{\hbar}\frac{\alpha M_s t}{g(0)}\left(-\frac{H_d}{2} + H_{ms} - H_k + H\right) + \frac{2e}{\hbar}\frac{M_s t}{g(0)}\sqrt{(H_{ms} - H_k + H)(H_d - H_{ms} + H_k - H)}$$

$$, \text{ if } H > -H_{ms}+H_k ;$$

2. **the AP state becomes unstable for:** (42)

$$j > \frac{2e}{\hbar}\frac{\alpha M_s t}{g(\pi)}\left(\frac{H_d}{2} + H_{ms} + H_k + H\right) - \frac{2e}{\hbar}\frac{M_s t}{g(\pi)}\sqrt{-(H_{ms} + H_k + H)(H_d + H_{ms} + H_k + H)}$$

$$, \text{ if } H < -H_{ms}-H_k ;$$

$$j > \frac{2e}{\hbar}\frac{\alpha M_s t}{g(\pi)}\left(\frac{H_d}{2} + H_{ms} + H_k + H\right) \quad , \text{ if } H > -H_{ms}-H_k .$$

B.3.3.f. Discussion

In order to fit the experimental phase diagram, to a good approximation, formulae (41) and (42) can be used to determine the critical lines characterizing the currents at which magnetic switching is observed (Fig. B.3 - 11). A reasonably good agreement with the experimental data was obtained for the following parameters: H_c = 91 Oe, H_{ms} = 48 Oe, H_d = 16000 Oe, α = 0.01, $g(0)$ = 0.246 and $g(\pi)$ = 0.526. H_c and H_{ms} are experimentally determined. $g(0)$ and $g(\pi)$ were taken as fit parameters, but the values we found are close to those calculated by Stiles and Zangwill for Co/Cu/Co trilayers ($g(0)$ = 0.2 and $g(\pi)$ = 0.6) [7]. The values considered for H_d and α are typical for such structures. Phase diagrams for different samples with the same structure could be fitted using the same values for H_d, α, $g(0)$ and $g(\pi)$.

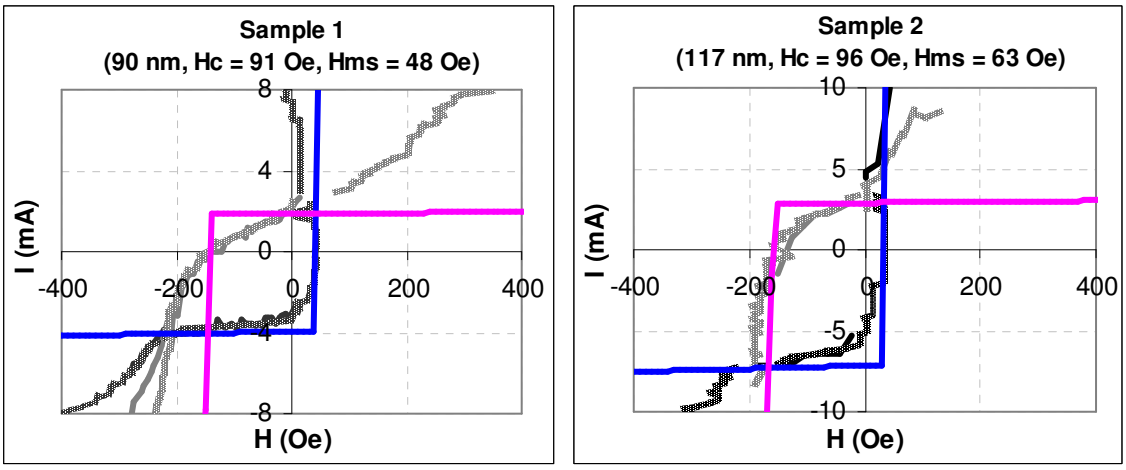

Fig. B.3 - 11 Phase diagrams for different samples having the same structure can be fitted replacing in eq. (41) and (42) the values determined experimentally for H_c and H_{ms} and the same values for the fit parameters (H_d = 16000 Oe, α = 0.01, $g(0)$ = 0.246 and $g(\pi)$ = 0.526). Sample 1 and sample 2 are the same as in fig. B.3 – 9.

Above the blue dotted line, the P state is stable; the AP state is stable under the pink dotted line. Consequently, five regions can be distinguished: one region where both states are allowed (in the center of the diagram), one region where only the P state is stable, one region where only the AP state is permitted and two regions where neither state is allowed (high positive / negative fields and currents). In these latter regions, the current generates magnetic excitations in the free layer, which has been recently

demonstrated experimentally [8]. In a macrospin model [7], these excitations are identified as steady precession of the free layer's magnetization.

As predicted by Slonczewski's ballistic model (see part A, chapter 2), there is a strong asymmetry ($I_c^{AP\to P} > I_c^{P\to AP}$) when the applied field compensates the magnetostatic interaction from the pinned SAF layer (H = -51 Oe, for sample 1). In other words, **spin-transfer is much stronger in the AP than in the P state (for positive than for negative currents**). The measured $I_c^{AP\to P} / I_c^{P\to AP}$ ratio is, however, lower than calculated using Slonczewski's formula for $g(\theta)$ as a function of the polarization of the current.

Using this simple macrospin model several features of the experimental phase-diagram can be explained:

1. The general shape of the phase diagram, as well as the existence of four types of regions (P stable, AP stable, both P and AP allowed and both P and AP unstable, i.e. precession region);
2. The values of the applied field for which the border lines change from a roughly linear dependence to a parabolic one (H = 43 Oe for P, H = -139 Oe for AP stable, in the case of sample 1), as well as the linear dependence of the instability current for P when H < 43 Oe and for AP when H > -139 Oe, and the parabolic(-like) dependence elsewhere;
3. The values of $I_c^{AP\to P}$ and $I_c^{P\to AP}$ for H = 0 Oe;
4. The slope of $I_c^{P\to AP}$ as a function of H for –210 Oe < H < 43 Oe.

The main disagreements between the model and the experimental results are:

1. The slope of $I_c^{AP\to P}$ as a function of H for H > -139 Oe;
2. The curvature of I^{end} for H < -139 Oe;
3. The linear dependence of the instability current for P, when H < -200 Oe.

Various arguments can be put forward to explain the differences between theory and experiment, as follows:

The theoretical critical lines on the phase diagram are calculated at T = 0 K. It has been shown that thermal effects reduce the critical currents and the switching fields

in the coercivity region and cause a rounding of the phase diagram, as well as an increase of the slope of the critical lines in the coercivity region [9] (see part A, chapter 4). It is difficult to treat the thermal effects quantitatively for two different reasons: first, for positive currents the temperature of the sample increases very rapidly with the current, while for negative currents the temperature of the sample is approximately constant; second, an Arrhenius-type treatment would not necessarily be appropriate in this case, since the dwell time of the telegraph noise caused by the spin-transfer is of the order of the attempt time used in the Arrhenius law of thermal activation ($\tau_0 \sim 1$ ns).

From a general comparison of the theoretical and the experimental phase diagram, it is found that the macrospin model fits the P→AP transition (which occurs mostly for negative currents) better than the AP→P one (observed most of the times for positive currents). Such behavior has been observed earlier in simpler structures (see part A, chapter 4). In our samples, the agreement between theory and experiment is expected to be better at negative currents, which are less affected by heating effects.

The effect of the finite temperature on the switching fields is taken into account by using the measured room temperature coercivity of the sample instead of the 0 K anisotropy field in the formulae for the critical lines; as a consequence, the experimental critical lines and the theoretical fits change slope for the same values of the field.

It is important to note that within this simple macrospin model, the calculated critical lines correspond to the values of the current where a given state becomes unstable (the so-called "instability currents" in part A, chapter 4). As it was often commented in the literature, it does not necessarily follow that the free layer actually switches to the opposite orientation. On the other hand, from an experimental point of view, for the hysteresis curves measured at room temperature, it is virtually impossible to distinguish between the instability and the switching currents. Moreover, for the reversible curves, it is difficult to identify the exact beginning and end of the transitions between the two states. All these details could result into incongruities between experiment and theory.

The disagreements between the theoretical and experimental limits of the steady precession region can be also partially explained by the fact that the model does not

consider the influence of the Oersted field generated by the current. This field can be quite important in the high currents region (about 50 Oe for an applied current of 5 mA), favoring the formation of a vortex distortion, not taken into consideration by the macrospin model. Several micromagnetic studies have underlined the importance of the Oersted field in the investigation of current induced magnetization switching [10, 11]. It was even suggested that in Co/Cu/Co circular nanopillars with a diameter of 130 nm (similar to our samples), the field induced by the current plays a crucial role in promoting the switching [11]. Even for samples with important shape anisotropy, several features of the phase diagrams cannot be explained without taking into account the Oersted field [10].

The formation of a vortex distortion in the free layer for high applied currents also yields a decrease in the magnetoresistance amplitude, but other effects intrinsic to the spin-transfer contribute as well.

First, for large currents and fields favoring opposite configurations, the spin polarized current can induce out-of-plane stable states or very fast precession of the magnetization of the free layer along in-plane or out-of-plane orbits (see part A, especially chapters 3 and 4). The time constant of our experimental setup being quite long (of the order of 100 ms), the precession states cannot be monitored directly. However, if the average direction of the magnetization is deviated from the parallel or antiparallel orientation, the measured resistance will correspond to the projection of the moment of the free layer along the magnetization of the reference layer. Consequently, when the system experiences a transition from the parallel state to an out-of-plane precession orbit, the relative variation of the resistance will be lower than the full magnetoresistance amplitude.

Second, different micromagnetic [10] and experimental studies (see part A, chapter 4) have shown that spin-transfer can cause telegraph noise either between the P and AP states (inside the coercivity region) or between almost P and AP states corresponding to different precession trajectories, even at 0 K (see part B, chapter 5). The dwell time of such telegraph noise is much shorter (of the order of nanoseconds) than the characteristic time of our experiment (100 ms), which means the resistance we measure is statically averaged over this interval.

The decrease of the magnetoresistance in high currents is probably the conjoint consequence of all these phenomena, and only high resolution time-resolved and frequency-dependent measurements could shade more light onto this point.

For positive currents and fields, it is interesting to note that the system evolves to a static resistance level which is closer to that of the antiparallel state (favored by the field) than to that of the parallel configuration (favored by the current) (see the second transition appearing on the R(I) curves measured for positive applied fields, fig. B.3 – 5). Frequency-domain experiments demonstrate that the onset of the reversible transition corresponds to an increase of the precession angle, since the precession frequency is decreasing. When the static resistance approaches that of the AP configuration (at large positive currents), the microwave spectra show evidence of strong high frequency telegraph noise (see chapter 5). However, positive current favors the parallel orientation of the magnetization of the free layer with respect to the reference layer, and (hysteretic) switching to the P state occurs for currents of the order of 2-3 mA. Consequently, an evolution of the system towards a higher resistance state for currents larger than the critical current (and an increase of the precession cone) can only be induced by an increasing positive / non-uniform field, which would de-stabilize the P configuration. Since no additional field is applied, other than the static external field specified on each R(I) curve, the only other contribution that would justify such a behavior is the Oersted field. Indeed, without spin-torque, the joint effect of the positive applied field, positive magnetostatic interaction from the reference layer (which is much stronger on the edges than in the center) and circular-symmetry Oersted field, the local moments of the free layer would arrange themselves into an off-centered vortex state, with a majority of moments pointing along the positive direction of the field (close to AP alignment with respect to the magnetization of the reference layer). Increasing the current leads to an increased spin-torque (favoring the P orientation), but also an enhanced Oersted field and an important heating of the sample (at least 50 K). Under these conditions, the parallel state, which is already disfavored by the magnetostatic interaction between layers, may become highly unstable. It is also possible that the precession cone increases with the applied current for most of the local moments, given the joint effect of applied, magnetostatic and Oersted fields. Such effects, however, cannot be taken into account within the frame of a simple macrospin model, but only through micromagnetic simulations.

The reason why such behavior was only observed for positive currents and fields, and not for the opposite polarities, may also be understood along this line of reasoning: negative currents bring the free layer into the AP state, favored by the dipolar interaction between layers. This situation is thus considerably more stable than the one described above. Moreover, hardly any heating is measured for negative currents. As such, the effect of the increasing Oersted field is expected to be much less dramatic in the range of currents investigated in the experiment.

Several studies have shown that the macrospin model is a poor approximation for describing the magnetic dynamics of the free layer during the current induced magnetization switching (see part A, chapter 3). Indeed, the dynamics is most often very chaotic before, during the reversal and within the precession region [10]. Nevertheless, the simple theory presented above offers a satisfactory semi-quantitative comprehension of the general features of the I-H phase-diagram.

Overall, the general trends characterizing spin-transfer in complex spin-valves with SAF exchange biased layer and laminated magnetic films are found to be consistent with the widely studied Co/Cu/Co nanopillars. The comparison holds mainly for negative fields, since, as mentioned several times before, in simple pseudo-spin-valves with an unpinned reference layer, only the part of the phase diagram corresponding to fields applied parallel to the reference layer can be fully investigated

B.3.3.g. Telegraph noise

Several previous studies have pointed out the stochastic nature of current induced magnetization switching and have analyzed in detail telegraph noise inside the coercivity region and in the precession area of the phase diagram (see part A, chapter 4).

Like the simple Co/Cu/Co pillars, the *Headway* CPP-GMR head spin-valves also exhibited strong telegraph noise in various ranges of currents and fields. The sample in fig. B.3 – 12 shows telegraph noise in the coercivity region. On the resistance versus current characteristics, the system is in the antiparallel state at -55 Oe and for negative currents higher than -3.1 mA. Indeed, when monitoring the evolution of the resistance

in time under the same applied field and with a constant bias current of -4 mA, no transition to the P state is resolved for the duration of the experiment (300 s). At -3 mA (that is, for a bias current equal to the switching current), occasional jumps to the P state do occur, but the pillar remains mainly in the AP state. At -2 mA, the dwell time becomes larger for the minimum resistance state, but sporadic transitions to the maximum resistance level still arise. At -1 mA, the system remains in the P state for the extent of the measurement.

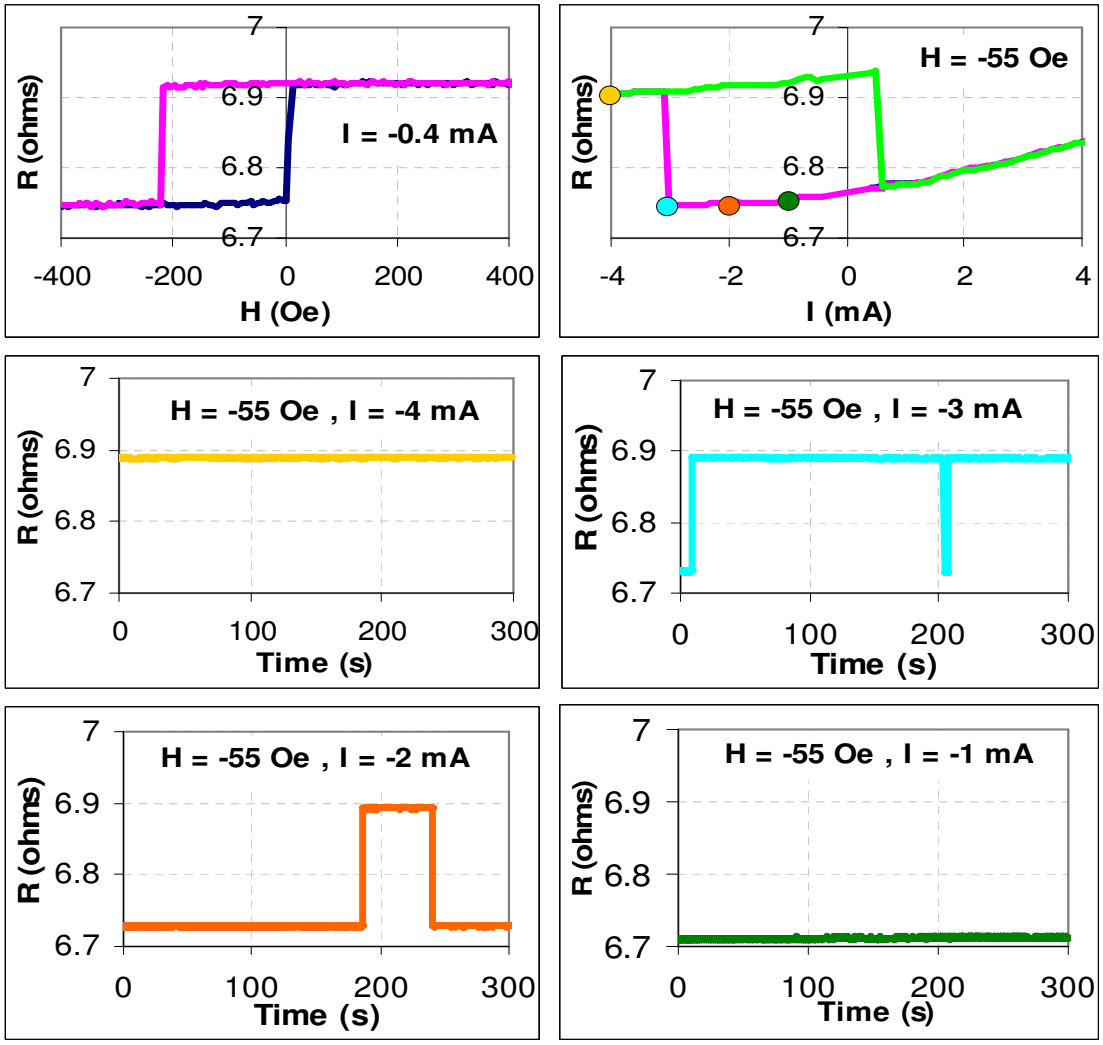

Fig. B.3 – 12 Telegraph noise between the P and AP states inside the coercivity region for sample 4. **Top left:** Magnetoresistance curve measured with low sense current (in the absence of spin-torque effects). **Top right:** Resistance versus current characteristics for an external field of -55 Oe. The colored dots indicate the values of the current for which the resistance versus time curves showed below were obtained. **Middle** and **bottom:** Resistance versus time at -55 Oe, for various values of the constant applied current.

Noise is also present outside the coercivity area, and manifests itself no only in (poorly) time-resolved measurements, but on the magnetoresistance and resistance versus current curves as well, and it is often accompanied by random variations of coercivity (Fig. B.3 - 13).

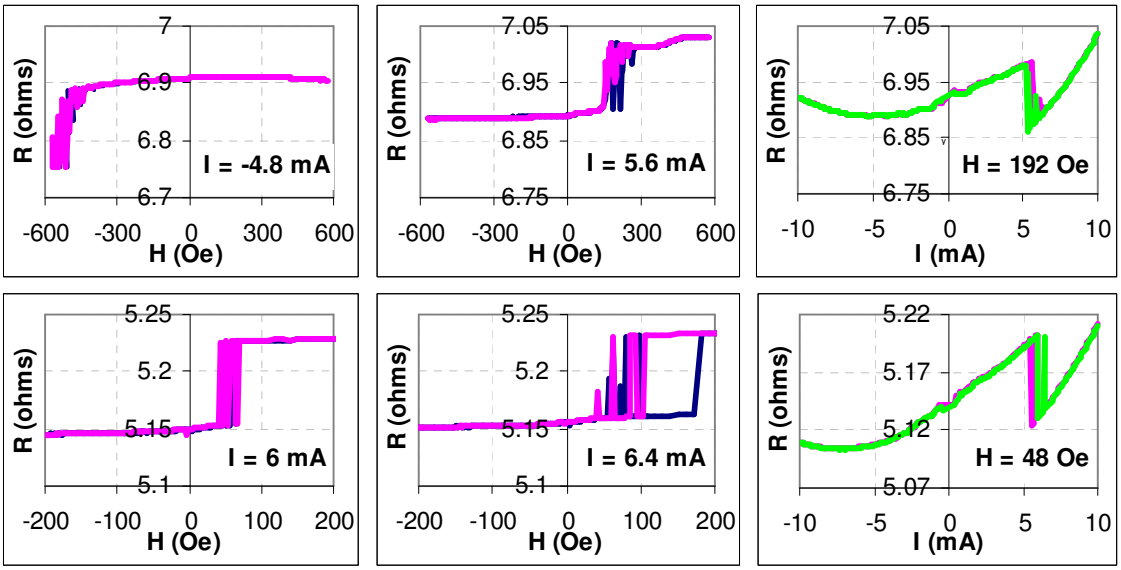

Fig. B.3 – 13 Magnetoresistance and resistance versus current curves showing noise in the precession region of the phase diagram. **Top:** Same sample as in fig. B.3 - 12 (sample 4), showing noise in the precession region for both signs of the current. **Bottom:** Different sample (sample 5), which only exhibits noise positive currents; the noise is accompanied by random variations of coercivity.

Although evidence of two-level fluctuations was found for both signs of current and field, telegraph noise is usually stronger (and for some samples only present) for positive currents. This detail is not unexpected, since telegraph noise is one of the characteristics of spin-transfer and the investigation of the phase diagrams proved that spin-transfer is stronger for positive currents.

Given the poor time resolution of our static experimental setup, long measurement times were required in order to establish the dwell times in the two states for given values of current and field. This invariably ended in degrading the samples before any complete analysis could be fulfilled through time-resolved measurements. However, the overall characteristics of spin-transfer in this pillars being qualitatively

similar to those well-known of Co/Cu/Co structures, no remarkable difference should be encountered when trying to quantify two level fluctuations behavior.

B.3.3.h. General trends: conclusion

Current induced magnetization switching can be observed in complex spin-valve structures developed for CPP magnetic heads, and their general behavior is qualitatively similar to that of simple Co/Cu/Co pillars. Spin-transfer is larger in the AP configuration (that is, for positive currents, with electrons flowing from the reference to the free layer) than in the P state (for negative currents). Stronger telegraph noise is found for positive currents. The macrospin model can reasonably well account for the experimental results.

B.3.4. Very low coercivity samples

Theoretically (see part A, chapter 2), one does not expect spin-transfer effects to be much influenced by the coercivity (anisotropy) of the free layer. Indeed, the critical currents depend mainly of the saturation magnetization, and only very weakly on the anisotropy. However, a higher anisotropy insures that the sample behaves more like a single-domain particle and is less influenced by the non-uniformity of various fields acting on the system (such as magnetostatic interaction between the layers – which is stronger close to the edges of the samples and weaker in the middle – or Oersted field induced by the current – which has a circular symmetry).

The results presented in this paragraph were obtained on a 107 nm sample (sample 6) with the reference layer laminated with Ag and the free layer laminated with Cu (structure “c”). The coercivity of the free layer was 6 Oe, and the (average) 15 Oe magnetostatic field from the reference layer favored the antiparallel state.

B.3.4.a. Evolution of the resistance versus current characteristics with the applied field

It was shown that in the case of high coercivity nanopillars (which can be well fitted with the macrospin model), for relatively low fields acting on the reference layer, the AP→P transition occurs at positive values of the current, while currents of the opposite sign are necessary to bring the sample back in the AP state. Increasing the applied field yields a more accelerated shift of the corresponding transition, simultaneously reducing the coercivity until the transition between the two states becomes practically reversible.

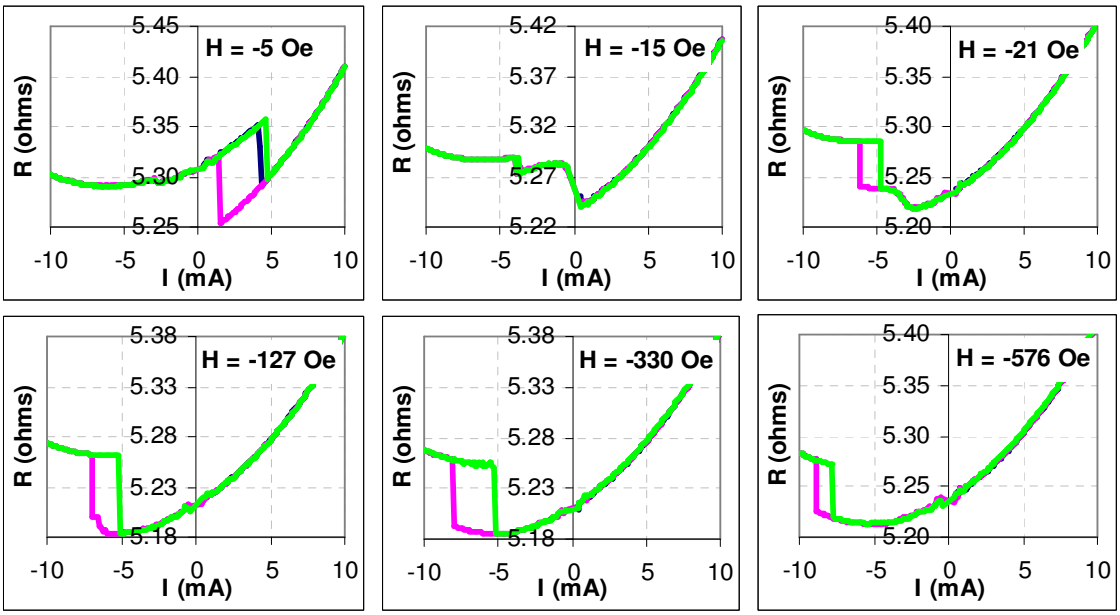

Fig. B.3 – 14 Resistance versus current curves for increasing values of the negative applied field, for a low coercivity sample with the reference layer laminated with Ag and the free layer laminated with Cu.

Fig. B.3 – 14 shows the evolution of the R(I) loops when increasing the negative applied field for a very low coercivity sample. Unlike high coercivity pillars, at -15 Oe, when the magnetostatic interaction from the reference layer is compensated and the total field acting on the free layer is virtually zero, no hysteresis loop is obtained when measuring the R(I) characteristics, but only a two-step reversible transition. When increasing the total field acting on the free layer (with one sign or the other) the

hysteresis is recovered (see the curves at -5 or -21 Oe). Unexpectedly, raising the negative applied field up to -330 Oe leads to an increase of coercivity, since the P→AP transition moves more rapidly towards negative currents than the opposite one. The typical behavior is only retrieved for negative fields higher than -330 Oe: the AP→P transition (favored by the field) shifts faster and the coercivity is gradually reduced.

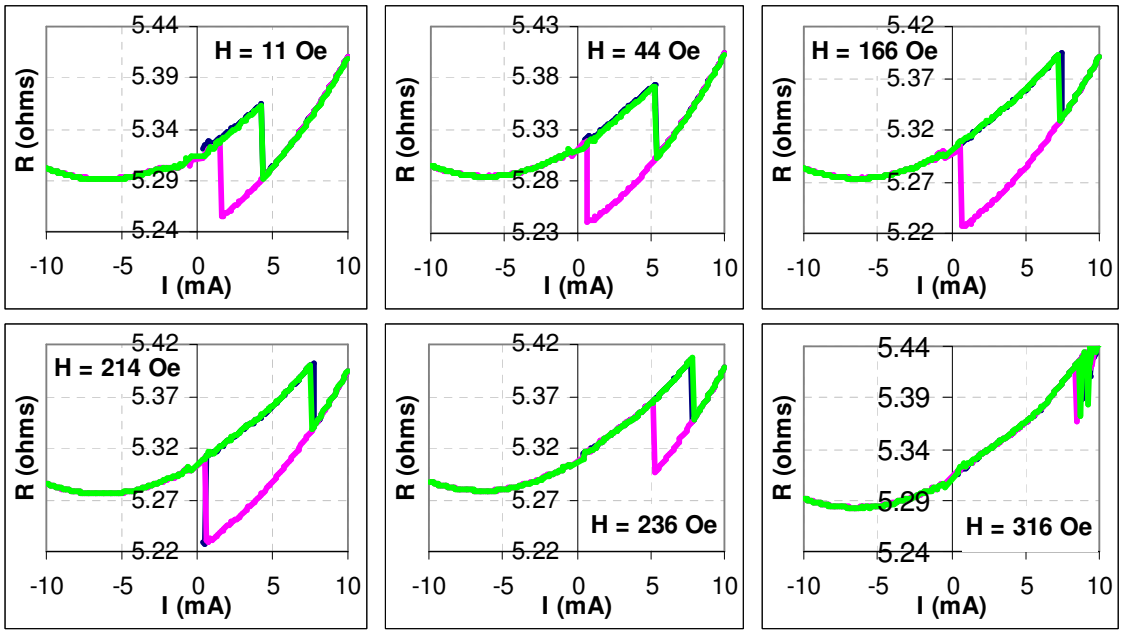

Fig. B.3 – 15 Resistance versus current curves for increased values of the positive applied magnetic field, measured for the same sample as above.

For positive fields, the situation is much the same (Fig. B.3 – 15). While expecting a steady decrease of coercivity with the applied field, as in the case of higher coercivity samples, it is found that the measured coercivity is increasing up to 190 Oe, since the AP→P transition is shifting rapidly towards high positive currents, while the transition backwards is not much affected by the field. Between 190 Oe and 300 Oe, the P→AP transition jumps randomly from one positive value of the current to another, while the AP→P transition continues to move progressively (albeit more slowly than for lower fields). Above 290 Oe, the curves show strong noise for the high positive currents, where the sample should remain in the parallel state. For field larger than 330 Oe, no transition can be identified on the R(I) characteristics.

B.3.4.b. Evolution of the magnetoresistance curves with the sense current

As predicted by the macrospin model and similar to the simple Co/Cu/Co nanopillars, for high coercivity samples, increasing the positive or negative sense current induces a slight decrease of the coercivity of the magnetoresistance loops; when the current is high enough to provoke switching, the corresponding transition jumps close to the opposite one and switching between the two states becomes practically reversible. Increasing the current even more yields a further shift of the reversible transition and a decrease of the magnetoresistance amplitude.

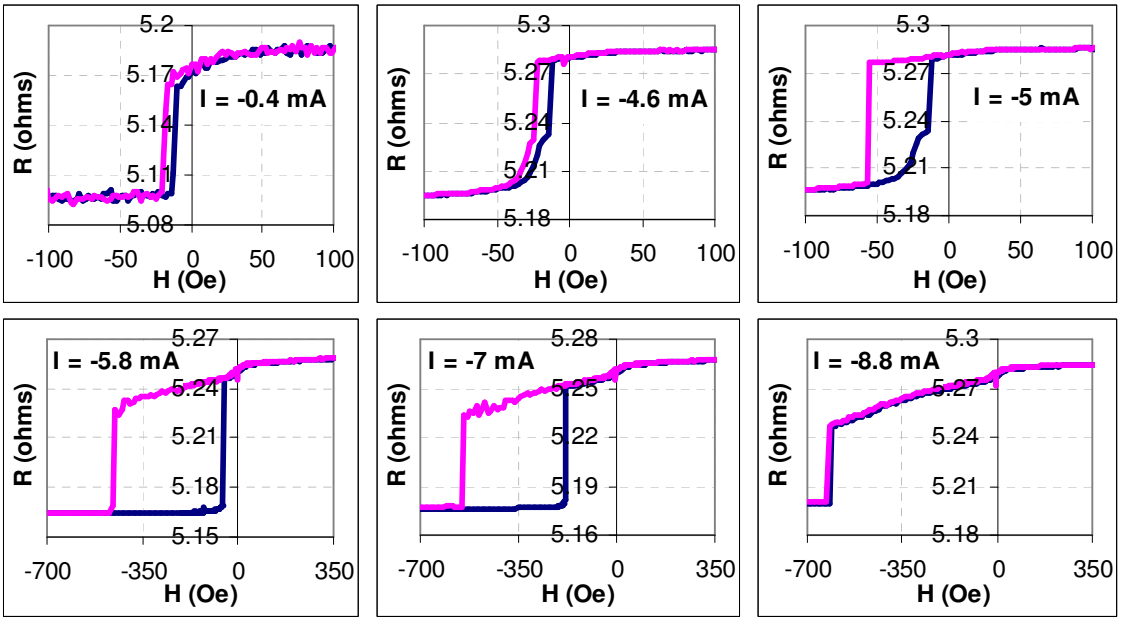

Fig. B.3 – 16 Magnetoresistance curves for increasing values of the negative sense current. The field scale is changed between the top and the bottom row of graphs.

For low coercivity samples, the evolution of the MR curves with the sense current is more complicated (Fig. B.3 – 16 and Fig. B. 3 – 17). Between -0.4 and -4.6 mA, both transitions shift simultaneously towards higher negative fields, so that the coercivity is practically unchanged (Fig. B.3 – 16). While the two transitions are very sharp at low currents, they develop a more progressive lower part above -3 mA. Starting from -4.6 mA, the P→AP transition moves very slowly towards higher negative fields, while the opposite switching shifts very rapidly with the current. The coercivity reaches a maximum of approximately 220 Oe around -6 mA. For currents higher than this value,

the shift of the P→AP transition in considerably accelerated, so that the coercivity is basically cancelled at -8.8 mA. Continuing to increase the current determines a further shift of the reversible transition, as well as a drop in the magnetoresistance amplitude. It is to be noted that the shape of the transitions between the two states also changes with the current: for currents larger than -4.6 mA, a sharp jump is registered between the low resistance level and an intermediate state, followed by a monotonic increase towards the high resistance level.

For positive currents between 0.4 and 1.2 mA, the magnetoresistance loops are essentially unaltered. Starting from 1.4 mA and up to approximately 2.6 mA, the P→AP transition jumps randomly between 0 and 620 Oe, while the reverse switching occurs for values of the field varying very weakly with the current. Consequently, the coercivity takes random values between 6 and 310 Oe. At 2.8 mA, it reaches a maximum of 330 Oe. For higher currents, both transitions move progressively with the current, but in opposite directions: the P→AP transition shifts towards lower values of the field, while the AP→P switching occurs for increasing positive field. Eventually, the transition between the two states becomes reversible (around 9 mA). Further increase of the applied current yields only the shift of the reversible transition towards higher fields, as well as a decrease of the magnetoresistance amplitude.

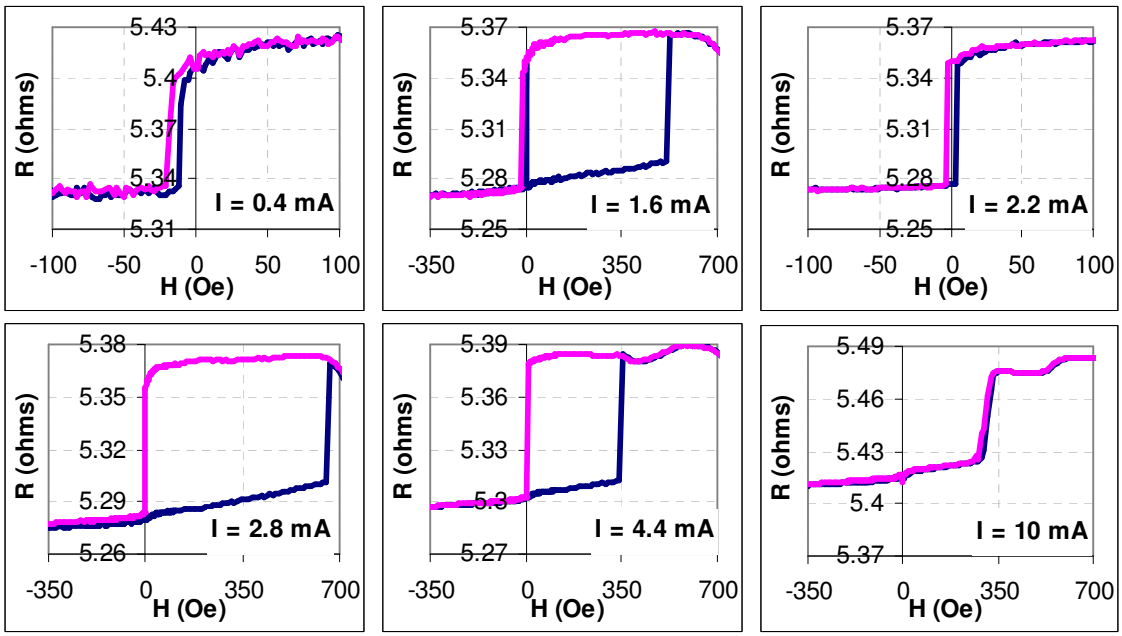

Fig. B.3 – 17 Magnetoresistance curves for increasing values of the positive sense current. Please note the change of field scale among the graphs.

Similar to the case of negative applied currents, the shape of the P→AP transition is particular on the curves showing high coercivity: it consists in a very progressive increase from the low resistance level and up to an intermediate resistance state, followed by a sharp jump towards the high resistance level.

Another detail worth mentioning is the wave-like dependence of the high resistance state with the field, at high positive values of the sense current (Fig. B.3 – 17). The exact profile of R_{high} as a function of field depends of the value of the applied current.

B.3.4.c. Phase diagram

For high coercivity samples, the phase diagram consists in a central coercivity region (at low currents / low fields), two areas where only one state is stable (either P or AP) and finally two regions where none of the states is allowed and which were identified as the regions where precession states are excited (for high currents / high fields favoring opposite configurations). The critical lines separating these areas could be fitted with the macrospin model (eq. (41) – (42)); each critical line changes slope once over all the range of applied fields (see fig. B.3 – 11).

In the case of low coercivity samples, the phase diagram shows a more complicated pattern (Fig. B.3 – 18), as expected from the evolution of the resistance versus current (magnetoresistance) curves with the applied field (current). Apart from the expected central (low) coercivity area (which is hard to identify when plotting the critical lines over all the range of applied fields), there are two large domains of increased coercivity. These regions appear for values of current and field where precession states are predicted. The two precession regions (where only reversible transitions are measured) emerge for high currents and high fields favoring opposite orientations of the free layer's magnetization, and outside the high coercivity areas (close to the bottom-left and the top-right corners of the large scale phase diagram). Outside the critical lines, the system is in a stable state (P mostly for positive currents and negative fields, AP for negative currents and positive fields).

The agreement between the critical lines deduced from the resistance versus current and the magnetoresistance curves is reasonably good, as in the case of the high coercivity samples, with the notable exception of positive current increased coercivity region, and between -30 and -10 Oe applied field (see the low field range phase diagram). The positive current increased coercivity area covers the range of fields and currents where telegraph noise-like, random coercivity variations are measured. Between -30 and -10 Oe the resistance versus current characteristics consist in two-steps reversible transitions. -30 and -10 Oe are approximately the field values which induce the switching between the two states in the absence of spin-transfer effects.

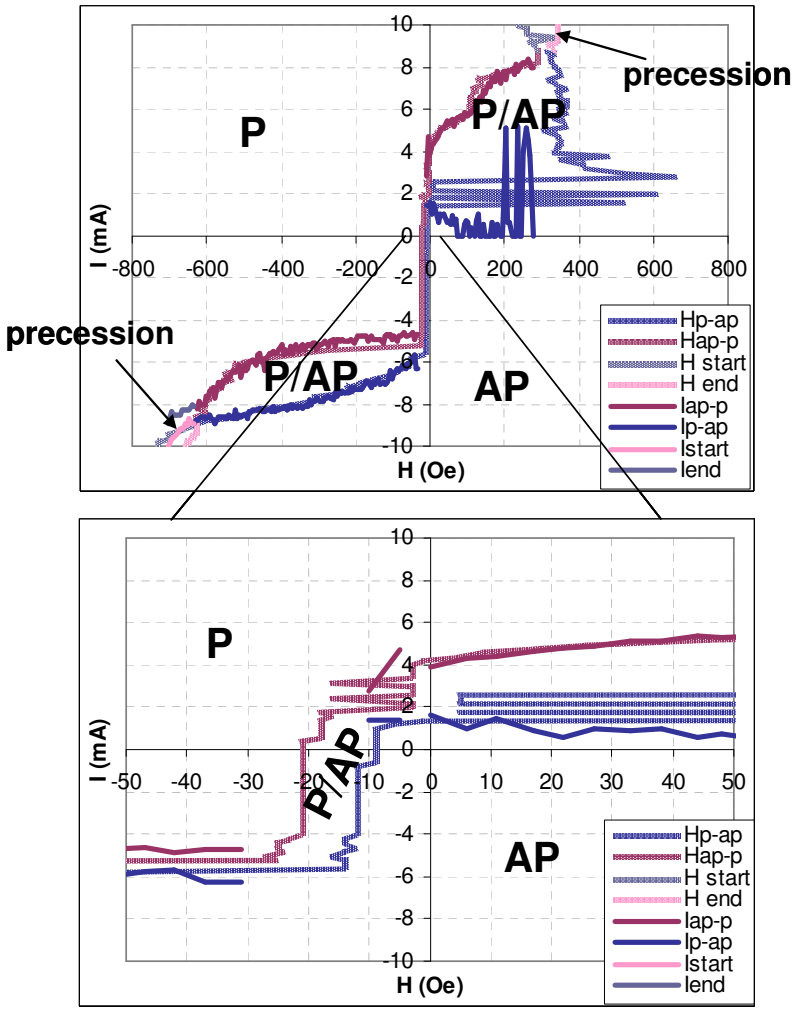

Fig. B.3 – 18 Phase diagram for the same sample as in the previous figures. **Top:** Phase diagram for the entire range of applied fields. **Bottom:** Phase diagram for applied fields of the same order of magnitude as the coercivity of the sample.

In order to compare low and high coercivity samples, the low field-range phase diagram of sample 6 and that of sample 2 were plotted in the reduced coordinates system (Fig. B.3 -19). When doing so, the similarity between the two phase diagrams becomes obvious. Moreover, although in the case of low coercivity samples no hysteresis resistance versus current curves could be obtained when the total field acting on the free layer is close to zero, the values of the critical currents deduced from the magnetoresistance curves are very similar to those measured for high coercivity samples.

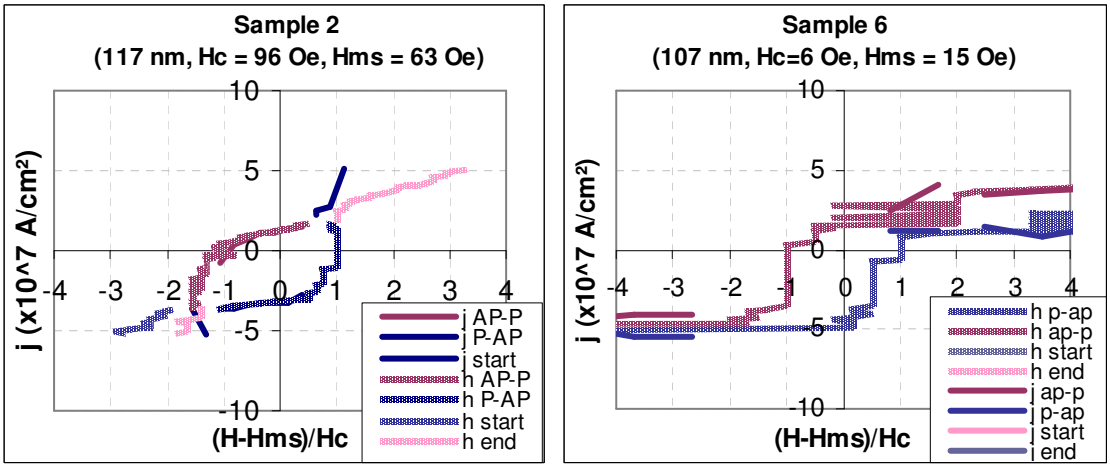

Fig. B.3 – 19 Left: Phase diagram of sample 2 (same as in fig. B.3 – 9). **Right:** Low field-range phase diagram for sample 6 (the same as in fig. B.3 – 19, bottom). Both diagrams are plotted in the reduced coordinates system.

B.3.4.d. Discussion

The square-shaped low-field range phase diagram of sample 6 can be fitted using the macrospin model and the same values for the damping parameter α and the demagnetizing field H_d as in the case of sample 1 and sample 2 (Fig. B.3 – 20). (The free layer having the same structure for the three samples, H_d and α should be the same).

As mentioned in the previous paragraph, experiments on pillars with different coercivities show that the critical currents do not depend on the coercivity of the sample in question. This result is in good agreement with the theoretical predictions: according

to eq. (41) – (42), the instability currents depend only very weakly on the coercivity of the free layer. Actually, there are two main incongruities between the experimental phase diagrams for the low coercivity samples and the predicted phase diagram (or the phase diagrams for high coercivity samples):

1. The presence of increased coercivity areas on the experimental phase diagram;
2. The zero-hysteresis resistance versus current curves (two-steps reversible transitions) obtained for low values of the total field acting on the free layer.

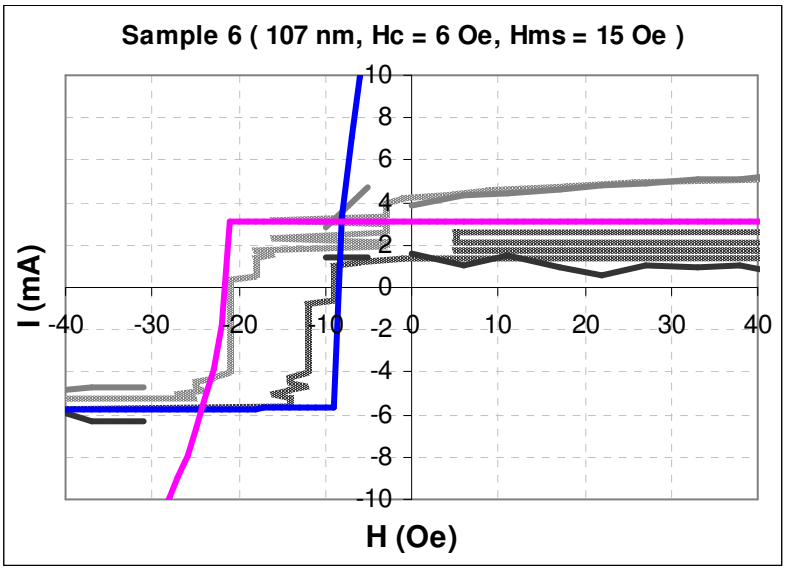

Fig. B.3 - 20 Theoretical fit based on eq. (41) - (42) for the low-field range phase diagram of sample 6. The fit parameters are: H_c = 6 Oe, H_{ms} = 15 Oe (experimentally determined values), H_d = 16000 Oe, α = 0.01, $g(0)$ = 0.24, $g(\pi)$ = 0.44. The values taken by $g(\theta)$ are different for the two pillars, as the angle dependence function depends on the structure of the multilayer, which is different for the two samples above (see chapter 4).

Although it is difficult to make a quantitative analysis without micromagnetic simulations, both details can be understood qualitatively by considering the role played by the Oersted field induced by the current. At 1 mA, for a nanopillar with a lateral size of about 100 nm, the Oersted field reaches values up to 20 Oe at the edges of the nanopillar. If the sample has a very low coercivity (e.g. 6 Oe for sample 6), it is very likely that for low applied fields, when sweeping the current between -10 and 10 mA (corresponding to Oersted fields around 200 Oe), a vortex state is induced in the free layer. Hence the two-step reversible transition that appears on the R(I) curves measured

while in external fields of the order of the coercivity of the sample. On the other hand, when recording a magnetoresistance curve with relatively weak sense currents (below +/-2 mA), the Oersted field remains comparatively lower (up to 40 Oe); the maximum positive and negative applied fields (+/-700 Oe) insure that the free layer is well saturated in one direction or the other, so that the behavior of the sample remains closer to that of a single domain particle. Increasing the negative sense current yields first the formation of a vortex distortion, which causes the initially sharp transitions to develop a more progressive lower half. Simultaneously, the two transitions are shifting towards higher fields, as a consequence of the increasing spin-torque acting on the local moments. For currents over -4.6 mA, the superposition of the strong Oersted field and the high applied magnetic field determines rather the formation of a "C"-state than a vortex configuration. Both the considerable coercivity enhancement and shape of the transitions support this interpretation. The coercivity is increasing as long as both transitions are induced by the various magnetic fields acting on the system, reaching its maximum for sense currents just lower than the critical current (approximately -6 mA). As soon as the applied negative current becomes larger than the switching current, the AP→P transition (favored by spin-transfer) starts to shift rapidly towards higher fields, and the coercivity is gradually reduced.

A similar reasoning can be applied to positive currents, while bearing in mind that spin-transfer effects are stronger for this configuration (see paragraph B.3.3). In the case of sample 6, the positive switching current is around 3 mA. Indeed, the maximum coercivity is reached at 2.8 mA; for higher currents, the AP→P transition, favored by the current, starts to shift towards higher fields and the coercivity is decreasing.

It was mentioned before that spin-transfer is a stochastic phenomenon and that generally, the *Headway* spin-valves showed stronger telegraph noise for positive than for negative currents. While it is difficult to account for every detail of the experimental results, it seems likely that for positive currents of the order of the switching current, the complicated interplay between stochastic current induced switching and Oersted and applied field effects leads to random coercivity variations.

Under the effect of positive currents much larger than the critical currents, the high coercivity samples showed evidence of precession states excited even for current / field configurations where no such states are permitted when neglecting the Oersted field. Moreover, frequency-dependent experiments on low coercivity samples

showed that the wave-like variation of the high resistance level as a function of the applied field, which appears for positive currents higher than the switching current, is related to a complicated pattern of chaotic dynamics (see the next chapter). As such, it is not surprising that the critical lines deduced from the R(I) and the MR curves do not superpose for high positive fields and currents. Indeed, it would be unlikely that during two identical experiments under the same external conditions (two R(I) sweeps for the same value of the applied field, or two MR curves for the same sense current) the same high resistance local moment configuration should be attained in this region of the phase diagram.

B.3.4.e. Low coercivity: conclusion

In conclusion, even for very low coercivity samples, the square-shaped coercivity region of the phase diagram, predicted by the macrospin model, can be reconstructed from the magnetoresistance curves measured for relatively low applied currents. As predicted theoretically, the critical currents (deduced from MR curves) do not depend much on the coercivity of the free layer: according to eq. (41) – (42), the instability currents are proportional to $H_c + H_d$, where the demagnetizing field (H_d = 16000 Oe) is at least two orders of magnitude higher than the coercitive field (H_c = 1-100 Oe). However, while for high coercivity samples the macrospin model is a satisfactory approximation (at least for static experiments), in the case of very low coercivity nanopillars, the effects of the current-induced Oersted field cannot be neglected. Full micromagnetic simulations would be necessary in order to account for every detail of the experimental results.

B.3.5. Static phase diagrams: conclusion

As expected, strong spin-transfer effects, including switching, are observed in complicated spin-valves developed for CPP-GMR heads. Although the polarizing layer is significantly thinner than those used in previously published experiments, lamination insures that a high current polarization can be attained in its vicinity. The study of static

phase diagrams has put forwards several important aspects to be considered before moving to further analysis of the data or dynamic experiments:

1. Spin-transfer effects are stronger in the AP than in the P state (that is, for positive than for negative currents, where positive currents are defined as electrons flowing from the reference to the free layer);

2. The switching current densities are of the order of 10^7 A/cm², as in the case of Co/Cu/Co pillars. However, the structure of the free layer has not been optimized to this minimize the switching currents, its thickness (3.6 nm) being several times larger than the characteristic length for spin-transfer (~ 1 nm) and spin diffusion length (~ 1.2 nm);

3. Phase diagrams for several samples can be fitted reasonably well using the same parameters;

4. Plotting the phase diagrams on reduced coordinated seems more appropriate for comparing samples with different size, coercivity, and dipolar coupling between the layers;

5. Current induced magnetization switching is a stochastic phenomenon; the switching current distribution is considerable at room temperature (+/-0.5 mA);

6. Generally, more telegraph noise appears for positive than for negative currents;

7. Oersted and dipolar fields effects have to be taken into account in these square-section (almost circular) nanopillars: they are responsible for exciting precession states in areas of the phase diagram where the macrospin model does not allow any, in high coercivity samples; in very low coercivity pillars, the field induced by the current leads to complicated phase diagram patterns;

8. For very low coercivity samples, the behaviour of the free layer is closer to that of a macrospin when measuring magnetoresistance curves than when sweeping the current in order to obtain the R(I) characteristics, because the strong applied fields help to maintain the configuration of the local moments closer to a single domain state.

Resumé :

Ce premier chapitre présentant des résultats expérimentaux est dédié aux mesures statiques, qui ont pour but la reconstruction du digramme de phase qui donne la stabilité de chaque état en fonction du courant et du champ appliqué. Il existe deux façons de remonter au diagramme de phase: la plus commune est d'étudier l'évolution des courbes de résistance en fonction du courant (R(I)) quand le champ (constant) appliqué change ; la deuxième modalité est d'analyser l'influence du courant de mesure sur les courbes de magnétorésistance. Ces deux types de mesures aboutissent aux mêmes lignes critiques qui délimitent les zones de stabilité des différents états sur le diagramme de phase, qui peut être interprété dans le cadre d'un simple modèle macrospin. Les diagrammes de phase des différents échantillons sont très similaires, et, notamment, les densités des courants critiques nécessaires pour induire le renversement de la couche libre en champ (total) nul prennent des valeurs très proches d'un échantillon à l'autre.

La dernière partie de ce chapitre discute l'influence de la coercitivité de la couche libre sur le diagramme de phase statique. Si les échantillons à forte coercitivité ont un comportement proche de celui prédit par le modèle macrospin, les effets des camps d'Oersted induits par le courant deviennent de plus en plus importants au fur à mesure que la coercitivité diminue.

References :

1. M. Covington et al. , cond-mat/0312505 (2003)
2. N.C. Emley et al., Appl. Phys. Lett. **84**, 4257 (2004)
3. Y. Huai et al., Appl. Phys. Lett. **84**, 3118 (2004)
4. J. Grollier et al., Appl. Phys. Lett. **78**, 3663 (2001)
5. A. Fert et al., J. Magn. Magn. Mater. **272-276**, 1706 (2003)
6. J. Grollier et al., Phys. Rev. B **67** , 174402 (2003)
7. M.D. Stiles and A. Zangwill, J. Appl. Phys. **91**, 6812 (2002)
8. S.I. Kiselev et al., Nature **425**, 380 (2003)
9. M.A. Zimmler et al., Phys. Rev. B **70** , 184438 (2004)
10. K.J. Lee et al., Nature Materials **3**, 877 (2004)

Chapter 4. Influence of the laminating material

As mentioned in part A, chapter 4, it has been observed that ΔR is inversely proportional to the switching currents [1, 2] and also that the asymmetry between the two critical currents ($I_c^{AP\to P}$ and $I_c^{P\to AP}$) is increasing with the GMR. While the correlation between ΔR and the switching currents could be qualitatively explained based on a simple ballistic spin-transfer model, no interpretation was offered as yet for the dependence of the critical currents' asymmetry on the GMR amplitude.

The four types of spin-valves ("a"-"d"), whose structure was given in paragraph B.2.1, were fabricated at *Headway* as part of a development process aiming at increasing the resistance variation ΔR between the parallel and antiparallel state. This chapter describes the influence of the materials used for laminating the magnetic layers on the GMR amplitude, and its relation to spin-transfer properties. The results (including the relation between ΔR and the switching current asymmetry) are semi-quantitatively interpreted using a code based on a model that extends the Valet-Fert theory to any magnetic multilayers [3].

B.4.1. Experimental results

As explained in chapter 2, paragraph B.2.1, samples with four different structures have been analyzed. Type "a" and "b" have both the reference and the free layers laminated with Cu; the difference between their structures is minimum. Nanopillars with structure "c" have the reference layer laminated with Ag and the free layer laminated with Cu. Samples "d" have both layers laminated with Ag.

Replacing Cu with Ag as laminating material alters several parameters which play a role in determining the CPP-GMR amplitude (such as the interfacial scattering asymmetry γ, the interfacial resistance between CoFe and the laminating material, the

spin diffusion length in the laminating material, etc – see part A, chapter 1). The most important is the interfacial scattering asymmetry γ.

Several groups have measured the scattering asymmetry at the interface between CoFe and Cu (always at low temperature); the obtained values ranged from 0.5 to 0.85, depending on the deposition method and the interface quality (the value obtained for sputtered multilayers was 0.7 - see part A, chapter 1, table A.1).

Comparatively much less is known about the CoFe/Ag interface. The only known reference announces a CoFe/Ag interfacial scattering asymmetry of 0.85 [4].

According to these values, the GMR of the active part of the spin-valves is likely to increase (if anything) when replacing Cu with Ag as laminating material. If this variation is measurable, samples with both the reference and the free layer laminated with Cu (structures "a" or "b") should have the lowest GMR, nanopillars with the both layers laminated with Ag (structure "d") are predicted to attain a higher ΔR, and mixed spin-valves (structure "c") should exhibit an intermediate value.

B.4.1.a. Magnetoresistance change with the structure

The magnetoresistance of the active part of the spin-valves, which may be altered when gradually replacing the Cu laminating layers with Ag, cannot be directly measured. The two parameters which can be determined experimentally, the GMR and the absolute resistance variation ΔR, are strongly influenced by other extrinsic factors and can be misleading. The measured GMR, though independent of the lateral size of the nanopillar, is highly affected by any supplementary contact (serial) resistance which may appear. On the other hand, the contact resistance does not alter the absolute resistance variation ΔR, but the latter is inversely proportional to the cross-section of the sample. A more representative quantity for comparing different multilayers, independent of the contact resistance and the lateral size, would be the $\Delta R \times A$ product, but the actual cross-section of each sample is unknown and cannot be determined through transport measurements.

Both for investigating spin-transfer effects and for CPP-GMR read-head applications, it is very important to fabricate nanopillars with lateral size below 150 nm.

In the case of CPP-GMR heads, this guarantees an appropriate level of device resistance. For current induced magnetization switching, a smaller cross-section minimizes the influence of the Oersted field and insures that the free layer behaves more like a single-domain particle under the effect of the current. However, the fabrication of such tiny magnetic objects with reproducible properties is a delicate matter and various technical problems may arise. Relatively small variations of the lateral size can have serious consequences in terms of resistance. An accidental superficial oxidation or an incomplete resist stripping may not only increase the resistance of the nanopillar, but also affect the measured GMR amplitude, since they appear as an additional resistance (so-called "contact resistance") measured in series with the active part of the spin-valve. Changes in the shape of the nanopillars or the quality of their edges may have a high impact on the coercivity of the free layer, and so on. Consequently, even on the same wafer, samples with allegedly identical shape and size can have very different properties. A minimum of statistics is, therefore, necessary when comparing samples with different structures, in order to distinguish between the dispersion of properties caused by an imperfect fabrication process and real differences induced by changes in the spin-valve structure.

	a	**b**	**c**	**d**
Number of samples measured	653	680	491	119
Number of defect samples	555 (85%)	561 (82.5%)	358 (73%)	95 (80%)
Number of samples working	98 (15%)	119 (17.5%)	133 (27%)	24 (20%)
Most common GMR	2.7%	2.3%	2%	1.9%
Maximum GMR	2.9%	2.6%	2.4%	2.1%

Table B. 1 Overview of the magnetoresistance properties of the four wafers. For about 80% of the samples measured the patterning process was unsuccessful.

Table B.1 summarizes the outcome of a statistical analysis of the four wafers in terms of magnetoresistance (similar trends were found for the absolute resistance

variation, ΔR). About 80% of the samples measured on each wafer were not exploitable (either the top contact was not opened properly or they showed no measurable magnetoresistance). For the remaining 20%, the GMR amplitude varied considerably even on the same wafer (Fig. B.4 – 1).

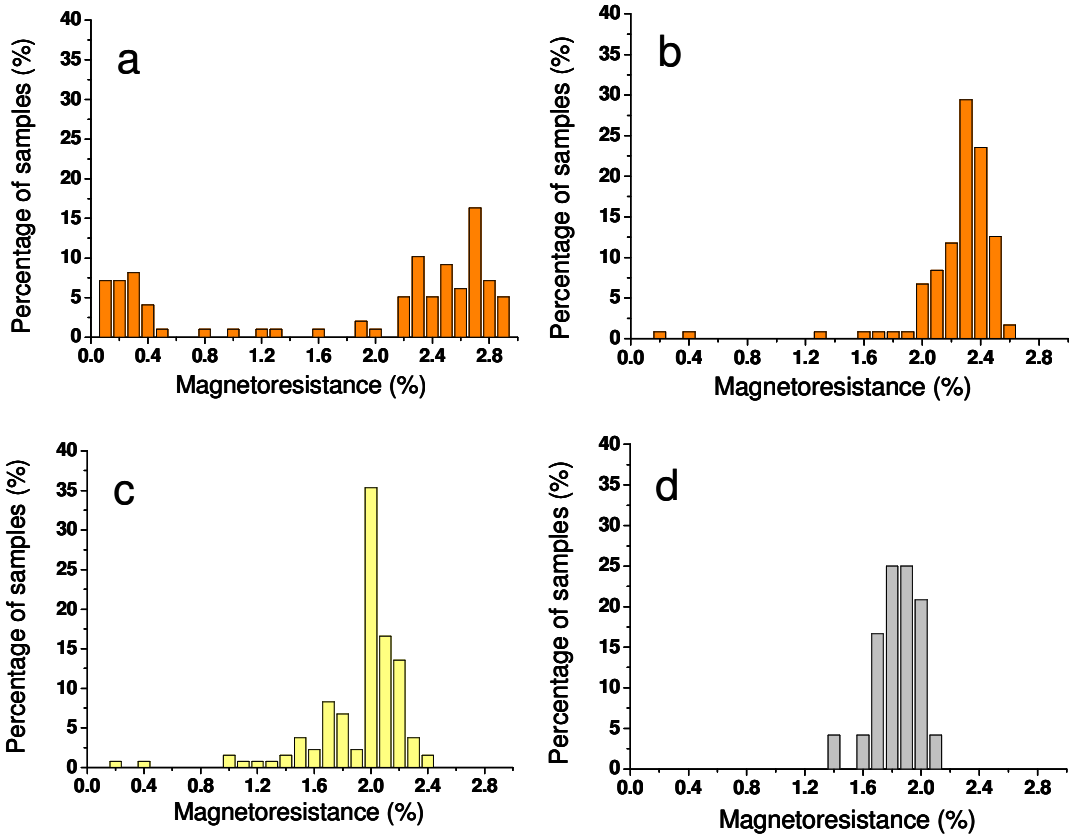

Fig. B.4 - 1 Magnetoresistance histograms for the four wafers, where the number of nanopillars showing a certain GMR level is expressed as percentage of the total number of working samples for a given structure ("a", "b", "c" or "d", as indicated on each figure).

Unexpectedly, both the maximum GMR amplitude and the most common magnetoresistance value measured for each wafer are found to be decreasing as Cu laminating layers are progressively replaced with Ag. However, this result alone is inconclusive, since the difference between the GMR values of different structures is well within the GMR distribution for each type of spin-valves, and could be explained by an (accidentally) increasing additional contact resistance from wafer to wafer.

B.4.1.b. Magnetoresistance versus switching currents values and asymmetry

According to ref. [1], if the measured GMR decrease from spin-valves "a" to "d" reflects the change in the multilayers rather than accidental variations of the contact resistance, it should be correlated with an increase of the critical currents and a decrease of their asymmetry.

Fig. B.4 – 2 shows phase diagrams of representative samples of each of the four structures, and table B.2 gives an overview of experimentally determined parameters for CPP-GMR transport and spin-transfer.

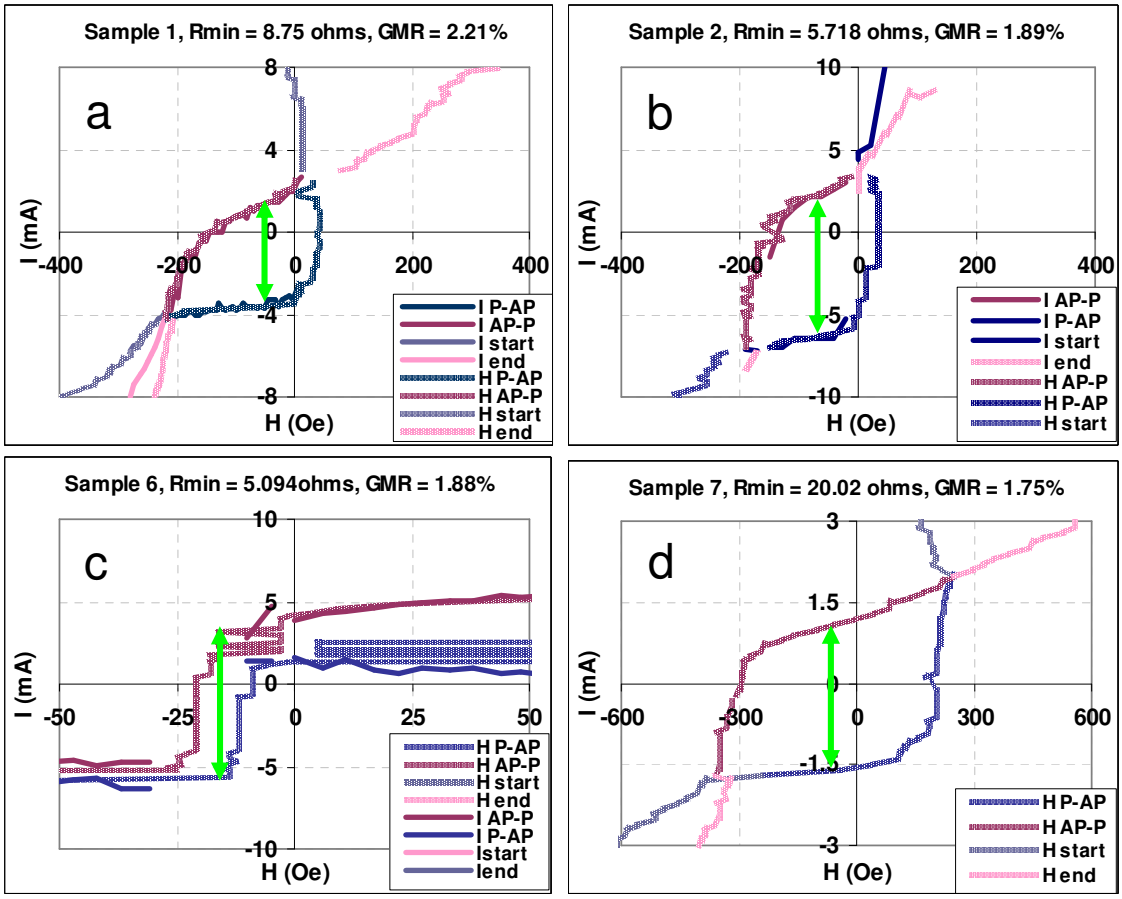

Fig. B.4 - 2 Phase diagrams for samples with different structures ("a"-"d"), as indicated on each graph. Samples 1, 2 and 6 have been described in detail in the previous chapter. Green arrows indicate the switching currents when the field acting on the free layer's magnetization is cancelled (that is, when the applied field compensates the dipolar interaction from the pinned SAF layer).

As explained in the previous paragraph, the measured GMR amplitude is decreasing from structure "a" (sample 1 : 2.21%) to structure "d" (sample 7 : 1.75%); accordingly, the asymmetry of the switching currents is considerably reduced (starting from 2.64 for sample 1 and down to 1.57 for sample 7). On the other hand, the resistance variation ΔR and the critical currents show a more complicated trend, owing to considerable differences in the samples' cross-sections (as suggested by their very different resistance).

	a (Sample 1)	**b** (Sample 2)	**c** (Sample 6)	**d** (Sample 7)
$R_{min}(\Omega)$	8.75	5.718	5.094	20.022
$R_{max}(\Omega)$	8.95	5.826	5.19	20.372
$\Delta R(\Omega)$	0.2	0.108	0.096	0.35
GMR(%)	2.21%	1.893%	1.88%	1.75%
$I_c^{AP\rightarrow P}$ (mA)	1.4	2.6	3.3	1.05
$I_c^{P\rightarrow AP}$ (mA)	-3.7	-6.2	-5.7	-1.65
$I_c^{average}$ (mA)	2.5125	4.4	4.5	1.35
$I_c^{AP\rightarrow P} / I_c^{P\rightarrow AP}$	2.64	2.38	1.74	1.57

Table B. 2 Experimental values for the CPP-GMR and critical currents for the same samples as in fig. B.4 – 2. Both the resistance and the switching currents depend on the cross-section of the nanopillars, which cannot be determined experimentally. The critical currents are given for the case when the total field acting on the free layer is cancelled. $I_c^{average}$ is calculated as the average of the absolute values of $I_c^{P\rightarrow AP}$ and $I_c^{AP\rightarrow P}$.

Using the values in table B. 2, it is possible to show that the inverse of the switching currents ($1/I_c$) increases linearly with ΔR (Fig. B.4 – 3). As explained in ref. [1], plotting $1/I_c$ as a function of ΔR facilitates the comparison of samples with different lateral sizes. Indeed, since both the resistance change and the inverse of the

critical currents are inversely proportional to the area of the nanopillars, variations of the cross section would only result in a shift along the linear dependence in fig. B.4 – 3.

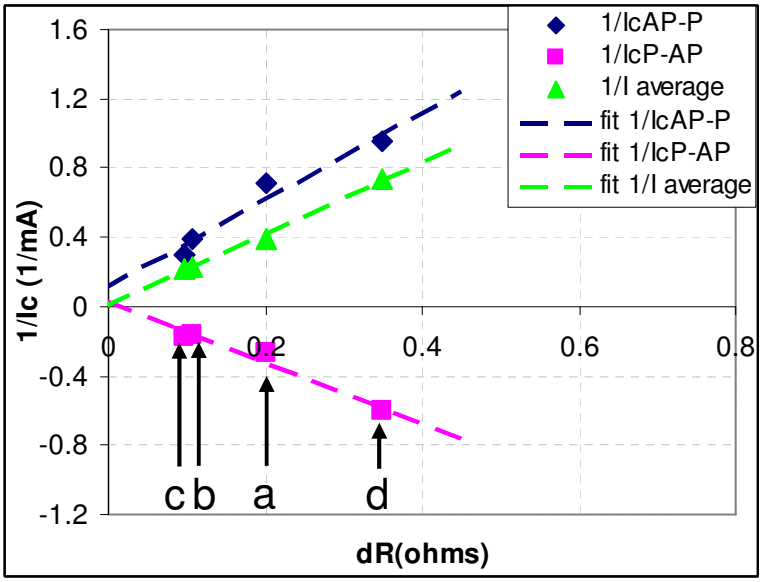

Fig. B.4 - 3 The critical currents are inversely proportional to the magnetoresistance. The points correspond to the values in table B. 2.

Unfortunately, though it proves beyond doubt that the inverse of the switching current depends linearly on the magnetoresistance, this kind of purely experimental analysis does not lead to any conclusion regarding the influence of the laminating material, since the variations of ΔR from sample to sample seem to be more dictated by the important lateral size dispersion than by structural changes. To establish whether there is an influence of the structure, one would have to either fabricate samples with very reproducible geometrical properties, or to determine the cross-section and the contact resistance of each pillar, and study the relation between the GMR and the critical current densities, which are size-independent. (It is however unsurprising that such a conclusion should be reached. Even in ideal structures, the variation of $R \times A$ which could be theoretically expected when replacing Cu laminating layers with Ag thin films would be of the order of merely few percent. To observe these variations experimentally, the cross-section of the pillars should be controlled with a similar precision, which is practically impossible.)

B.4.2. Modeling: extension of the Valet-Fert theory

The Valet-Fert theory [5] established two coupled equations which describe the variations of spin currents and chemical potential through a multilayer in the CPP configuration. In ref. [5], these equations were used to calculate the CPP resistance and magnetoresistance through a single interface between two magnetic layers or in multilayers consisting of an infinite number of the same bilayer repeat (see part A, chapter 1). Starting from the Valet-Fert model, a transfer matrix method was developed by Strelkov et al. [3] so as to derive a general expression for the spin-valve resistance, which can account for any magnetic multilayer, however complex.

Based on the general expression of the CPP resistance deduced analytically, Strelkov et al. also developed a code which computes CPP measurable transport properties (such as R and CPP-GMR) from the transport parameters of each layer and interface in the stack (spin-dependent resistivities, spin-dependent interfacial resistances, spin-diffusion lengths, etc). It is also allows for calculating the spin currents at any point in the multilayer and accounting for finite lateral size effects by taking into account scattering at the edges of the pillars.

B.4.3. Method and discussion

B.4.3.a. Method

The code developed by Strelkov et al. was used in order to compute the CPP resistance of the two possible magnetic configurations (parallel and antiparallel), the magnetoresistance and the spin currents for the four types of spin-valves. Since interfacial spin-memory loss was not originally introduced either in the Valet-Fert theory or in the calculations of Strelkov et al., the CoFe/Cu or CoFe/Ag interfaces in stacks were entered in the program as fictional layers of finite thickness. These "layers" were considered to have the same bulk scattering asymmetry β as the interfacial scattering asymmetry $\gamma_{CoFe/Cu}$ or $\gamma_{CoFe/Ag}$ and a resistivity such that the product between the resistivity and the thickness of the "layer" is equal to the resistance of the interface.

A spin diffusion length is also introduced for the "layer", so that the interfacial spin-memory loss δ equals SDL divided by the thickness of the interface. With the exception of $\gamma_{CoFe/Ag}$, the intervening magneto-transport parameters are well-know; the used values (extracted from the literature) are given in the Annex. The interfacial scattering asymmetry $\gamma_{CoFe/Cu}$ was considered to be 0.7, as measured for sputtered layers.

The only adjustable parameters to fit the data, both for the experimental magnetoresistance / average critical current dependence on the structure, and regarding the switching current asymmetry, were the contact resistance and $\gamma_{CoFe/Ag}$. Indeed, to our knowledge, there is only one publication [4] announcing an experimentally determined value for the interfacial scattering asymmetry between CoFe and Ag layers. As mentioned before, for $\gamma_{CoFe/Cu}$, the reported values vary with more than 50%, depending on the interface quality and the deposition method, and it is likely that the same is true in the case of $\gamma_{CoFe/Ag}$. Assuming $\gamma_{CoFe/Ag} = 0.45$ (about half the measured value, 0.85), a good agreement is found between experimental results and calculations based on the extended Valet-Fert model, as described below. The contact resistance is rather sample-dependent that determined by the structure. For samples with a lateral size of the order of 100 nm, such as investigated here, it can be as high as the resistance of the spin-valve itself. In the calculation, the contact resistance was placed at the interface between the free layer and the top electrode.

No scattering at the edges of the pillars was considered.

B.4.3.b. GMR versus average critical currents

The first step was to calculate the magnetoresistance for each of the four structures, in the absence of any additional contact resistance ($r = 0$). The results are given in table B. 4; these are the maximum GMR values which can be attained by the multilayers, since any additional resistance measured in series with the active part of the spin-valves lessens the obtained magnetoresistance.

Then, for each sample, the contact resistance was tuned so as to adjust the calculated GMR to the experimentally determined value (Table B. 3).

Once the contact resistance is determined, it is possible to calculate the resistance (expressed in Ω×μm²) of the parallel and antiparallel states, as well as the resistance variation ΔR. Knowing the calculated resistance×area and the measured resistance, the cross-section of each pillar can be deduced by dividing the computed R_{min}, R_{max} or ΔR to the corresponding experimentally determined value. (For finding the area, it is not necessary to know the contact resistance, since the latter does not affect ΔR; by estimating the contact resistance, the cross-section can be determined from any of the resistance values.)

	a (Sample 1)	**b** (Sample 2)	**c** (Sample 6)	**d** (Sample 7)
r(mΩ×μm²)	33	41	23	15
R_{min}(Ω×μm²)	0.07057	0.07858	0.05845	0.04831
R_{max}(Ω×μm²)	0.07214	0.08008	0.05956	0.04916
ΔR(Ω×μm²)	0.00157	0.0015	0.00111	0.00085
GMR(%)	2.22%	1.9%	1.89%	1.76%
a(nm)	89	117	107	49
$j_c^{AP\rightarrow P}$ (A/cm²)	1.768	1.899	2.88	4.165
$j_c^{P\rightarrow AP}$ (A/cm²)	-4.671	-4.529	-4.98	-6.664

Table B. 3 Calculated CPP-GMR and spin-transfer parameters: *r* is the contact resistance, which was adjusted so as to fit the calculated GMR to the measured value for each sample; R_{min} and R_{max} are the resistances of the parallel and antiparallel configurations; ΔR is the resistance variation between the two states; *a* is the lateral size of each pillar (the cross-section is deduced by dividing the calculated resistance levels / resistance variation to the measured values); the critical current densities are determined as the measured switching currents, divided by the calculated nanopillar area.

By knowing the lateral size of each sample and the switching currents, it is possible to calculate the critical current densities.

Both the maximum GMR and the average switching current densities so determined characterize the structure and do not depend on the size of the investigated nanopillars. The calculated GMR amplitudes increase, and the switching current densities are reduced when gradually replacing the Cu laminating layers (which have a high interfacial scattering asymmetry with CoFe) with Ag (which is assumed to have a lower interfacial asymmetry) (Fig. B.4 – 4).

	a (Sample 1)	**b** (Sample 2)	**c** (Sample 6)	**d** (Sample 7)
$GMR^{max}(\%)$	4.45	4.25	3.32	2.6
$j_c^{average}$ (A/cm²)	3.219	3.214	3.93	5.4145

Table B. 4 Maximum GMR calculated for each type of spin-valves (assuming no contact resistance, $r = 0$) and the average critical current density for each case. $j_c^{average}$ is determined as the average of the critical current densities in table B.3. Both the maximum GMR and the average critical current density depend only on the multilayer, and are independent on the cross-section.

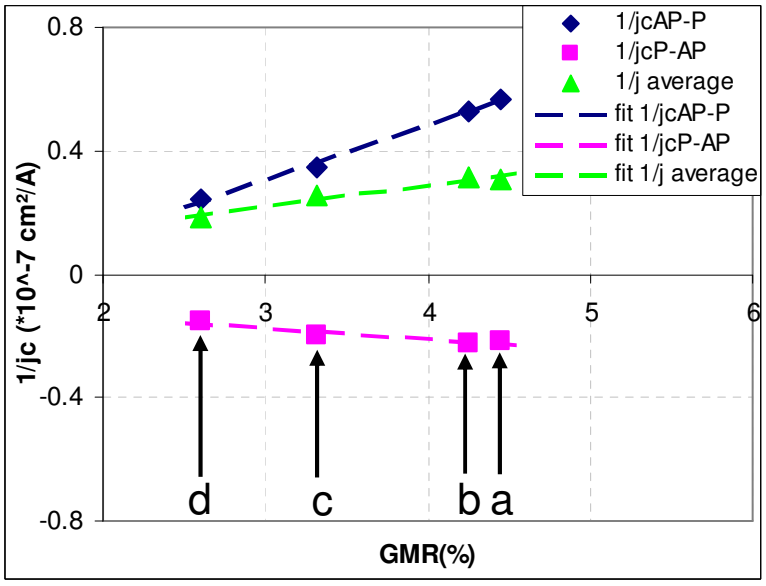

Fig. B.4 - 4 Inverse of the switching current densities versus the calculated maximum GMR for the four structures. Both parameters decrease as the Cu laminating layers are gradually replaced by Ag thin films.

Moreover, knowing the magneto-transport parameters for each material and interface, it is possible to predict accurately enough the evolution of the critical currents from the calculated GMR variation. Table B. 5 presents a comparison of the GMR and the inverse switching current densities ratios for any two of the four types of spin-valves investigated. In all the cases, the calculated ratios fit the measured values within an error bar of +/-25%.

	x = b (Sample 2)	**x = c** (Sample 6)	**x = d** (Sample 7)
GMR_a/GMR_x (predicted)	1.05	1.34	1.71
$j_x^{average}/ j_a^{average}$ (measured)	1	1.22	1.68

	x = c (Sample 6)	**x = d** (Sample 7)
GMR_b/GMR_x (predicted)	1.28	1.63
$j_x^{average}/ j_b^{average}$ (measured)	1.22	1.68

	x = d (Sample 7)
GMR_c/GMR_x (predicted)	1.28
$j_x^{average}/ j_c^{average}$ (measured)	1.38

Table B. 5 The calculated GMR ratios, the average polarization ratios and the measured critical current density fractions are in good agreement.

B.4.3.c. Switching currents and their asymmetry versus polarization and $g(\theta)$

As it has been explained in part A, chapter 2-4, the switching currents are inversely proportional to $g(\theta)$, which is a function of the polarization of the current and the angle between the magnetic moments of the two layers. The current polarization can

be calculated at any point in the multilayer using the code of Strelkov et al.. At the same time, only the spins which are not collinear with the magnetization of the free layer can generate a torque. In other words, although in the vicinity of the free layer the current is polarized both by the free and the reference layer, only the polarization induced by the reference layer contributes to spin-transfer, since the spins polarized by the free layer can only be collinear to its moment.

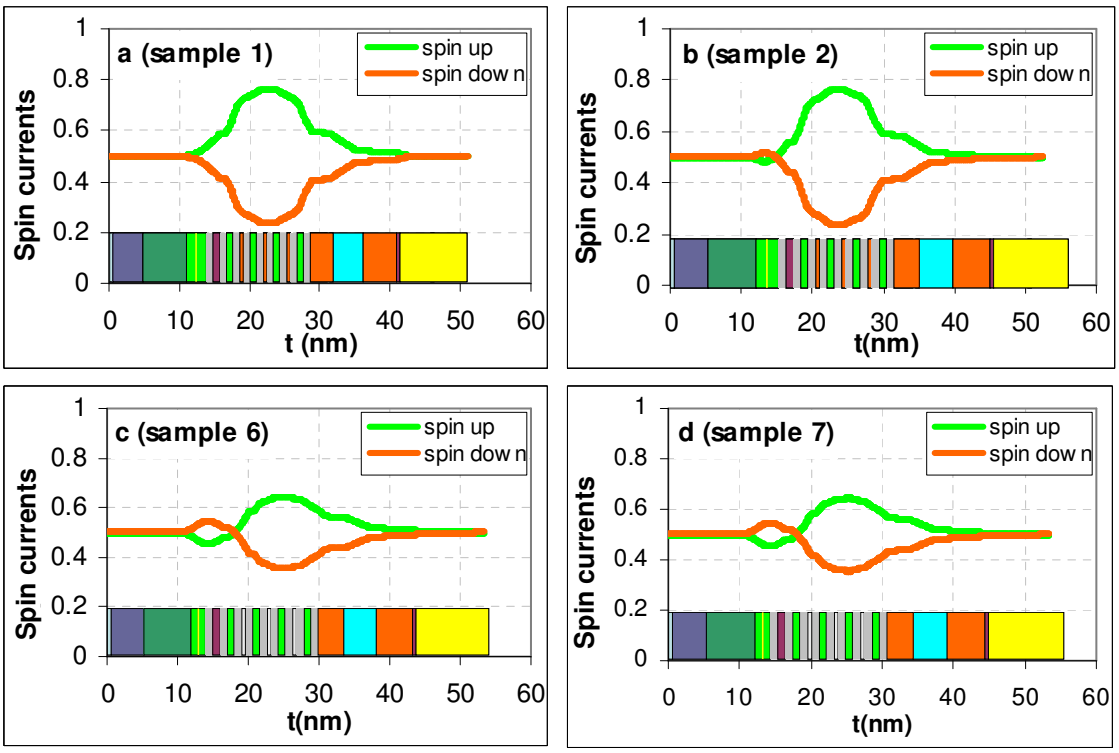

Fig. B.4 - 5 Calculated spin currents as a function of thickness for one sample of each structure, as indicated on each graph. Inset on each graph: schematic drawing of the spin-valve, with the non-magnetic "free" layer in light blue.

In order to determine the polarization of the current induced solely by the reference layer, the free layer was replaced in the program with a non-magnetic layer whose spin-diffusion length was taken to be the weighted mean of the SDL of the constituting individual layers (CoFe and Cu or Ag). The obtained evolution of the spin-currents along the direction perpendicular to the plane of the layers is given in fig. B.4 – 5 for each of the analysed samples. It is important to remark that the spin currents do not depend merely on the magneto-transport properties of the spin-valves,

but also on the contact resistance; as such, if the variation of the *r* is significant over the surface of the wafer, the spin currents and the polarization can vary from sample to sample.

The polarization of the current at the interface between the spacer and the free layer, calculated as the difference of the two spin currents, is given in table B. 6 for each of the four samples. Knowing the polarization, it is possible to evaluate *g(θ)* when the magnetic moment of the free layer is close either to the P or the AP orientation by using eq. (18) (see Slonczewski's model, part A, chapter 2). The obtained values, as well as the switching current asymmetry deduced from them, are also given in table B.6.

	a (Sample 1)	**b** (Sample 2)	**c** (Sample 6)	**d** (Sample 7)
P	0.166	0.152	0.112	0.098
g(0)	0.048	0.046	0.031	0.026
g(π)	0.119	0.113	0.07	0.057
g(π)/g(0)	2.48	2.45	2.28	2.19
$j_c^{P\to AP}/j_c^{AP\to P}$ (measured)	2.64	2.38	1.73	1.57

Table B. 6 *P* gives the current polarization at the interface between the free layer and the spacer *g(0)* and *g(π)* are calculated according to eq. (18) (Slonczewski's model, part A, chapter 2). *g(π)/g(0)* is the predicted current asymmetry, as compared with the experimentally determined value $j_c^{P\to AP}/j_c^{AP\to P}$.

The calculated critical current asymmetry evolution with the structure reflects the general trend of the experimental values, although it does not perfectly fit the data (the error bar is as high as 40%). It is noteworthy that while the calculated current asymmetry decreases with the polarization, it remains always higher than 2:

$$\frac{g(\pi)}{g(0)} = 2\cdot\left[1+\frac{1}{2\left[\left(\frac{1+P}{2\sqrt{P}}\right)^3-1\right]}\right]$$

where P < 1 in all the cases. However, considering that eq. (18) is only a first approximation for *g(θ)* (see part A, chapter 2), and that current induced switching is a stochastic phenomenon and the critical current distributions are of the order of +/-0.5 mA for samples of this size, the agreement between theory and experimental results can be regarded as satisfactory.

	x = b (Sample 2)	**x = c** (Sample 6)	**x = d** (Sample 7)
$g(0)_a/g(0)_x$	1.04	1.55	1.85
$j_x^{P\text{-}AP}/\ j_a^{P\text{-}AP}$ (measured)	0.97	1.06	1.43
$g(\pi)_a/g(\pi)_x$	1.05	1.7	2.09
$j_x^{AP\text{-}P}/\ j_a^{AP\text{-}P}$ (measured)	1.07	1.63	2.36

	x = c (Sample 6)	**x = d** (Sample 7)
$g(0)_b/g(0)_x$	1.48	1.77
$j_x^{P\text{-}AP}/\ j_b^{P\text{-}AP}$ (measured)	1.1	1.47
$g(\pi)_b/g(\pi)_x$	1.61	1.98
$j_x^{AP\text{-}P}/\ j_b^{AP\text{-}P}$ (measured)	1.51	2.19

	x = d (Sample 7)
$g(0)_c/g(0)_x$	1.19
$j_x^{P\text{-}AP}/\ j_c^{P\text{-}AP}$ (measured)	1.34
$g(\pi)_c/g(\pi)_x$	1.23
$j_x^{AP\text{-}P}/\ j_c^{AP\text{-}P}$ (measured)	1.44

Table B. 7 Predicted and calculated switching current densities evolution with the structure.

Using the values for $g(\theta)$ from table B.6, it is also possible to predict the evolution of each of the switching currents when replacing the Cu laminating layers with Ag (Table B.7).

Finally, one has to remember that all the calculations above are solely based on the polarization of the current. Unfortunately, for the time being, the program developed by Strelkov et al. cannot account for the effects of transversal spin accumulation, and neither does the formula used for $g(\theta)$ (eq. (18)). It is likely that when considering such effects, a better fit of the data might be achieved and possibly switching current asymmetries below 2 might be explained.

B.4.4. Conclusions

Experimental results show that when replacing Cu with Ag as laminating material, the measured magnetoresistance is decreasing, as well as the switching current asymmetry, while the critical currents themselves are rising. The data can be reasonably well interpreted using CPP-GMR calculations based on the extension of Valet-Fert theory to any type of multilayers, assuming that the interfacial scattering asymmetry between Ag and CoFe is lower than in the case of Cu and CoFe. By calculating the current polarization at the interface between the spacer and the free layer and introducing it into Slonczewski's simple formula for $g(\theta)$, it is possible to explain the enhancement of the switching currents and the decrease in their asymmetry as being related to a drop of spin polarization at the interface.

Resumé :

Les résultats expérimentaux montrent que toute modification structurale des échantillons qui induit une variation de la magnétorésistance implique aussi une modification des courants critiques (de renversement). Il se trouve que les courants critiques sont inversement proportionnels à la GMR. En plus, quand la magnétorésistance diminue, l'asymétrie des courants critiques (en champ total nul) décroît aussi. Ces effets peuvent être compris comme une conséquence d'une perte de polarisation du courant à l'interface entre l'espaceur et la couche libre, entraînée par la modification de la composition des échantillons.

La polarisation du courant peut être calculée à tout point dans le pilier en utilisant une extension du modèle Valet-Fert. On peut ainsi expliquer la relation linéaire entre la GMR et l'inverse des courants critiques. Il est ensuite possible de prédire l'évolution de l'asymétrie quand la magnétorésistance varie en introduisant la valeur calculée de la polarisation dans la formule (balistique) de Slonczewski, qui donne la variation des courants de renversement en fonction de l'angle entre les moments magnétiques de la couche libre et celle de référence.

References :

[1] S. Urazhdin et al., Appl. Phys. Lett. **84**, 1516 (2004)

[2] N.C. Emley et al., Appl. Phys. Lett. **84**, 4257 (2004)

[3] N. Strelkov et al., J. Appl. Phys. **94**, 3278 (2003)

[4] W.P. Pratt Jr. et al., J. Appl. Phys. **73**, 5326 (1993)

[5] T. Valet and A. Fert, Phys. Rev. B **48**, 7099 (1993)

Chapter 5. Frequency-dependent experiments

Understanding spin-momentum transfer induced magnetization precession is at present one of the most challenging research topics in magnetism, motivated by its potential applications for new magnetic resonators or microwave sources for wireless telecom devices. Such oscillators would allow a dynamic frequency allocation, thus solving the saturation problem of telecom frequency bands. These devices would address the market need for very large band oscillators with a strong quality factor (Q), while keeping their architecture simple and inexpensive. However, the fabrication of an industrially attractive prototype requires the identification and evaluation of parameters and / or configurations which influence (and maximize) the output power and the quality factor of the output spectra.

On the other hand, current induced precession in CPP-GMR heads generates noise and influences the biasing of the device; as for static spin-transfer effects, it is important to study and understand the dynamic phenomena in order to control (and minimize) their influence.

This chapter describes the results of frequency-dependent experiments on the same spin-valves as analyzed in the previous two sections. Only signals up to 10 GHz could be measured, since neither the design of the samples nor the preamplifier were adapted to very high frequency studies.

Although both the simulations of Zhu and Zhu [1] presented in part A, chapter 4, and the experimental results illustrated here are dedicated to the study of spin-transfer induced precession in spin-valves for CPP-GMR heads, there are several differences between our samples and those considered in their simulations:

1. Our samples do not have the permanent magnets for biasing;
2. The lateral size of the samples was about twice higher in our case, so the effects of the Oersted field are more important;
3. In our samples, the magnetic layers were laminated, which considerably reduces the SDL.

B.5.1. Precession states of the free layer: general trends

As for static experiments, the general trends characterising spin-transfer induced dynamics are described for high coercivity nanopillars, for which Oersted field effects are comparatively less important than in the case of very low coercivity spin-valves.

B.5.1.a. Static characterization

The results below were obtained on a pillar of structure "a" with a calculated lateral size of 104 nm (sample 8). The coercivity of the free layer at low current was H_c = 100 Oe; similar to the samples referred to in the previous chapters, the dipolar coupling (H_{ms} = 104 Oe) favoured the antiparallel orientation between the moments of the free and the reference layers (Fig. B.5 – 1, left). However, since both H_c and H_{ms} were defined as the average between the corresponding values measured at +/-0.5 mA, they might be slightly underestimated.

When the total field acting on the free layer is zero, the critical currents are somewhat lower than in other samples of similar size: $I_c^{AP\rightarrow P}$ = 1 mA and $I_c^{P\rightarrow AP}$ = -3.6 mA (Fig. B.5 – 1, right).

The static phase diagram in Fig. B.5 – 2 summarizes the characteristics of current induced switching for this pillar.

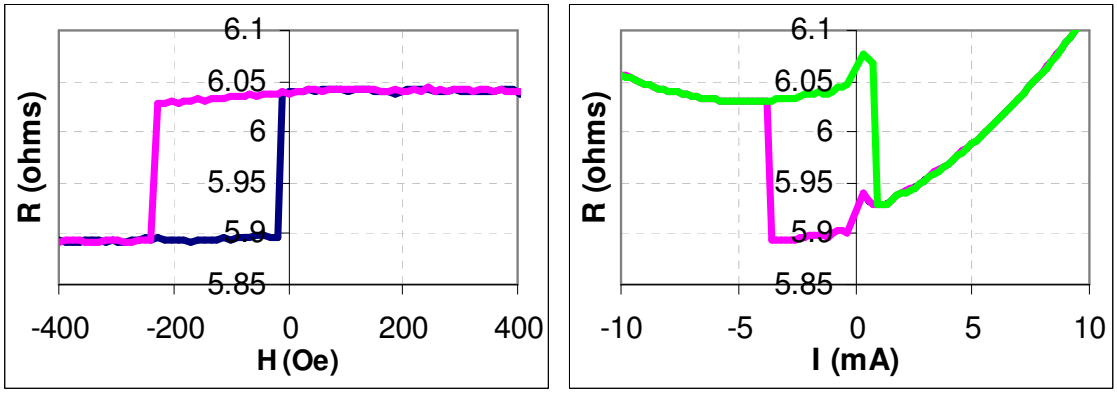

Fig. B.5 - 1 Minor magnetoresistance loop in the absence of spin-transfer effects (**left**) and resistance versus current characteristics when the applied field compensates the dipolar coupling between the layers (**right**).

The second transition towards an intermediate resistance level, which appeared for the sample 1 on the resistance versus current characteristics measured in low positive applied field (see chapter 3), comes into sight in weak negative fields in the case of sample 8, since the magnetostatic interaction with the reference layer (104 Oe) is higher than in the case of sample 1 (48 Oe) (Fig. B.5 – 3, a). (Taking into consideration the dipolar interaction between layers, for sample 8, an applied field of -9 Oe corresponds to a total field of 95 Oe acting on the magnetization of the free layer; for sample 1, a 19 Oe external field gives a resultant field of 67 Oe, so the total field is positive in both cases.)

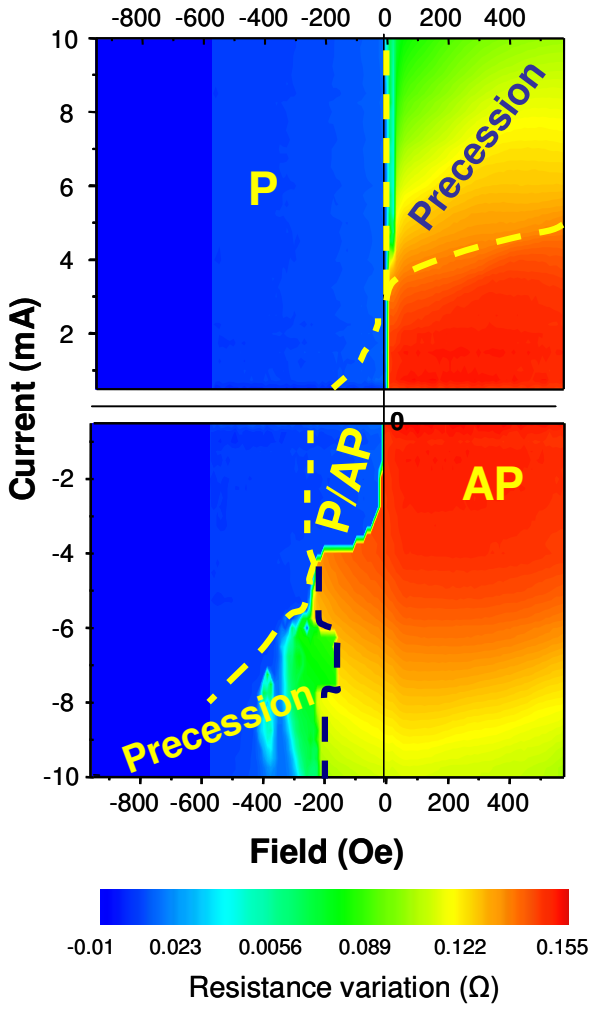

Fig. B.5 - 2 Static phase diagram for sample 8, presented as a contour plot of the resistance variation with respect to the low resistance level. The superimposed dotted lines mark the critical lines as defined in chapter 3. No data point was measured for fields between -950 Oe and -570 Oe; this range is included in the plot so as to facilitate the comparison with the dynamic phase diagram (see the next paragraphs).

A second transition towards an intermediate resistance level is also present in high negative currents on the R(I) curves recorded for intermediate negative applied fields (Fig. B.5 – 3, b). This is, however, different from the positive current / positive field second transition, as it appears for fields where the R(I) characteristics demonstrate reversible switching between a stable state (P) and a dynamic regime (while for positive fields, the second transition is present even on curves that show hysteretic switching between the two stable states, P and AP). Its onset moves to higher currents as the negative field is increased. Similar behavior has already been observed in Co/Cu/Co pillars for the same current / field configuration (see part A, chapter 4) and is associated to a change of dynamic regime, within the borders of the precession region, as defined by the macrospin model. (Remember that the second transition in positive current / positive field appears in areas of the phase diagram where the macrospin model predicts a stable state and its onset shifts towards lower currents as the field is increased; see chapter 3 for more details.)

For the same (negative) current / field values (currents higher than -7 mA, fields around -400 Oe) where the second transition is measured on the R(I) characteristics, the presence of a kink was recorded on the MR curves (Fig. B.5 – 3, c). The position of the kink remains unaffected when larger negative currents are applied, but its amplitude diminishes and its width increases. This feature was present in several samples (but not in all), giving rise to peculiar patterns in the negative fields / negative currents region of the phase diagram (Fig. B.5 – 2). Its presence is neither structure nor size dependent, and seems more related to peculiarities of the detailed micromagnetic configuration.

The general shape of the magnetoresistance curve at high negative currents (Fig. B.5 – 3, c) resembles the ones obtained through micromagnetic simulations by Sun [2] and by Li and Zhang [3], in the high current / high field switching threshold (see part A, chapter 3). In their case, the kink was attributed to out-of-plane steady precession and out-of-plane stationary states, as the field is varied. However, the similarity is likely to be only superficial, since in the simulations the kink extends over a large range of fields (about 200 times the anisotropy field, that is, for sample 8, over 20000 Oe), as compared to a maximum of 100 Oe found experimentally. Moreover, it is expected that the magnetization starts to get out-of-plane when the total field acting of the free layer is cancelled (that is, around -100 Oe for sample 8) and returns to the parallel state when the increasing field overcomes the effect of the current, only to register a transition towards the antiparallel configuration for even higher values of the

applied field. On the contrary, in the experiment, the resistance starts to increase when the total field on the free layer is around -350 Oe, returns to the (almost) parallel state around -250 Oe, and reaches the antiparallel orientation for an approximate total field of -100 Oe, that is, in a lower field than that where the kink is measured.

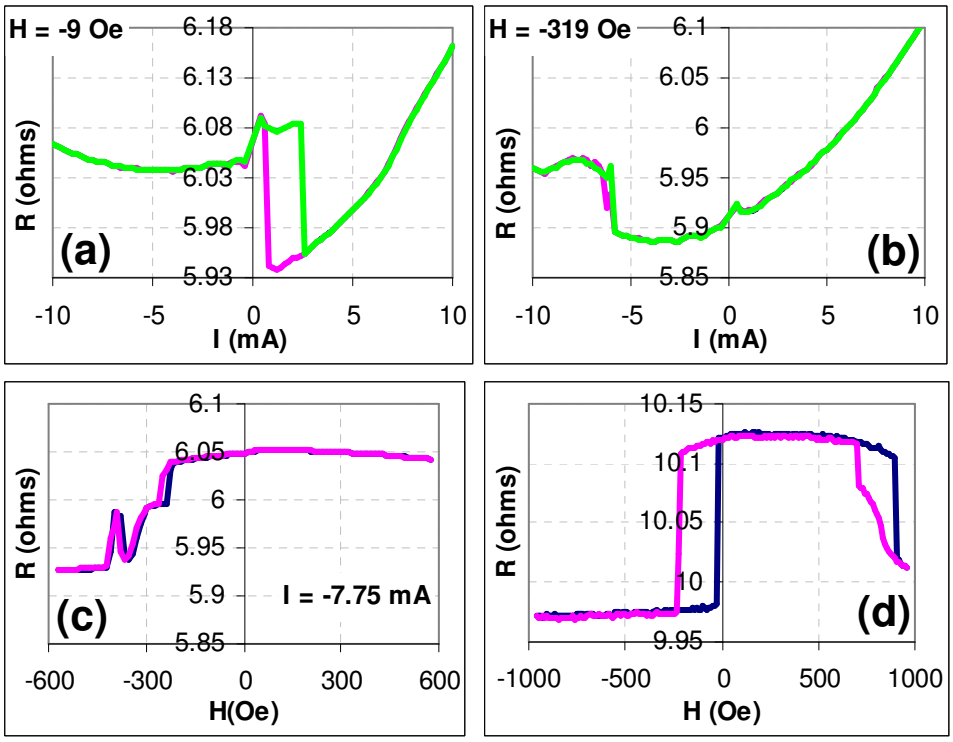

Fig. B.5 - 3 Particular features of sample 8: **(a)** Resistance versus current characteristics measured for an applied field of -9 Oe, showing the second (gradual) transition towards an intermediate resistance level starting from 5 mA. **(b)** Resistance versus current characteristics measured for an applied field of -319 Oe, showing the second (gradual) transition towards an intermediate resistance level, starting from -7.5 mA. **(c)** Magnetoresistance curve obtained for a -7.75 mA sense current, presenting a kink around -400 Oe. **(d)** Magnetoresistance curve measured with a very low sense current (no spin-transfer effects), showing the minor loop corresponding to the reversal of the free layer in low negative fields; the pinned layer partially switches between 650 and 1000 Oe. (a), (b) and (c) are obtained through four-points measurements; only two probes were used for (d), which was recorded just prior to starting the frequency dependent experiments, with the corresponding experimental setup.

As seen in fig. B.5 – 3, d, the pinned layer undergoes a partial reversal between 650 and 900 Oe. Frequency dependent measurements were carried out only for fields up

to 570 Oe, since the state of the reference layer is uncertain for larger values of the positive applied field.

For sample 8, microwave spectra were recorded for currents between -10 and 10 mA, with a 0.5 mA step. For each current, the applied field was varied from -950 to 570 Oe, with an increase pace of about 53 Oe.

The gain introduced by the preamplifier has been subtracted from all the spectra showed in this chapter. The oscillations which appear as superimposed on the higher amplitude signals are an artefact caused by multiple signal reflections between the sample and the preamplifier. Low current noise has also been subtracted from all the curves.

B.5.1.b. Dynamic behaviour for positive currents & fields

To elucidate the nature of the positive field second transition towards an intermediate resistance level (see fig. B.5 – 3, a), microwave spectra were measured at –9 Oe for various values of the current (Fig. B.5 – 4). A signal starts to be resolved for I = 2.5 mA, that is, when the applied current equals $I_c^{AP\rightarrow P}$ on the -9 Oe R(I) characteristics. According to the simulations of Zhu and Zhu [1] (see part A, chapter 3, paragraph A.3.4), this peak corresponds to a virtually uniform precession of the magnetization of the free layer, excited by the current. The second harmonic, which should appear in the scanned frequency range, is predicted to be considerably lower than the fundamental and is probably covered by the noise.

The amplitude of the initial peak grows when increasing the current up to 3 mA, but no frequency shift can be noticed. Between 3 and 3.5 mA, the peak splits in two (simulation expects it to by quartered), so that the amplitude of the original signal at 4.5 GHz drops considerably. The second peak appears around 6.5 GHz, and cannot be considered a harmonic of the first one. As the current is increased to 4.5 mA, more and more power is pumped into the second peak, and the initial signal diminishes visibly. Since none of the peaks shifts with the current, this dynamic mode can be identified as small-angle precession.

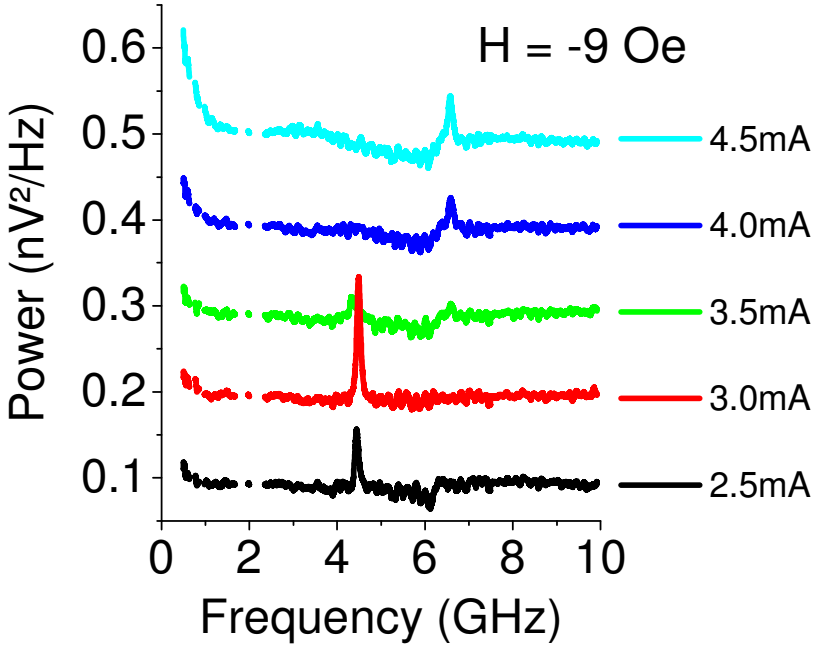

Fig. B.5 - 4 Microwave spectra measured at -9 Oe applied field, equivalent to a 95 Oe total field acting on the magnetization of the free layer, for currents between 2.5 mA (where the first signal is resolved) and 4.5 mA. The curves have been offset for clarity. Since the peaks do not shift with the current, these signals are attributed to small angle FMR precession.

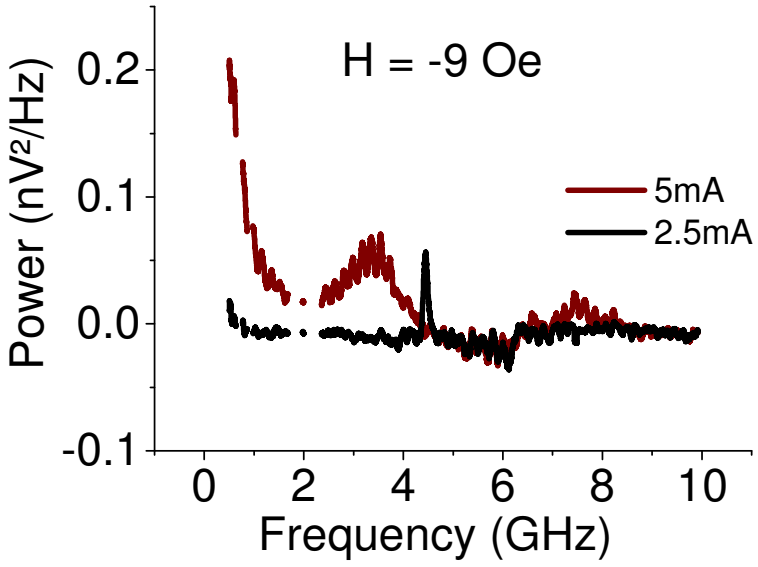

Fig. B.5 - 5 Microwave spectra at –9 Oe. At 5 mA, the main peak jumps suddenly to lower frequency, marking the onset of the large angle precession regime.

Between 4.5 and 5 mA, a sudden frequency drop is measured (Fig. B.5 – 5) and the local moments of the free layer enter another regime – large angle dynamics. The peaks broaden and the second harmonic becomes visible on the spectra. This change of dynamic regime marks the onset of the second transition in fig. B.5 – 3, a.

At -9 Oe, the peak frequency is only slightly altered between 5 and 6.5 mA. For higher fields, both the fundamental and the harmonic shift towards lower frequencies when increasing the current (Fig. B.5 – 6).

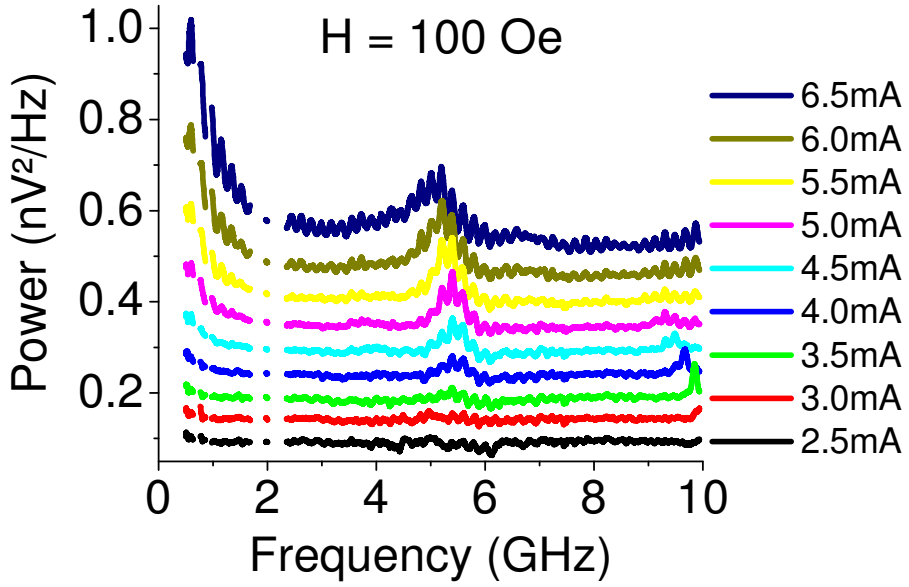

Fig. B.5 - 6 Microwave spectra at 100 Oe. The main peak does not shift with the current up to 4.5 mA (in the small angle FMR precession regime). Between 5 and 6.5 mA, a red shift is measured, corresponding to large angle in-plane precession with increasing cone angle. The curves have been offset for clarity.

In agreement with the results of Zhu and Zhu, the *1/f* – like noise, which is hardly present on the spectrum measured at 2.5 mA, rises rapidly with the current, as the dynamics of the system becomes more and more incoherent. Starting from 7.5 mA, the *1/f* – like noise is replaced by a very high amplitude peak, centred around 0.5 GHz. As the current is increased to 10 mA, its amplitude is greatly enhanced and the peak moves towards higher frequencies, attaining 1 GHz for the maximum applied current. Simultaneously, the entire spectrum noise becomes more important, until the higher frequency large angle precession peaks (still visible at 7.5 mA around 3.5 GHz) cannot

be distinguished any longer (Fig. B.5 – 7). When the current is held constant and the field is increased, the maximum power reached by the low frequency peak is diminished (see phase diagram below, fig. B.5 – 9). Maximum amplitude is attained at -9 Oe and 10 mA.

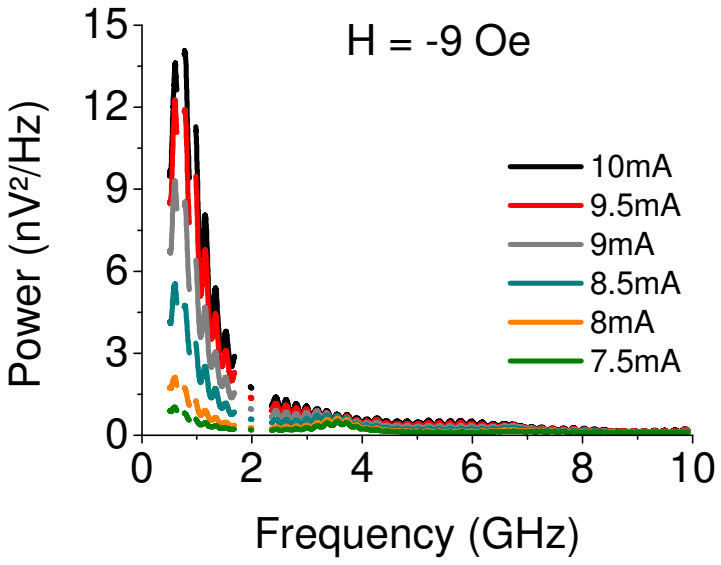

Fig. B.5 - 7 Microwave spectra at -9 Oe, for currents between 7.5 and 10 mA, showing an increasing low frequency peak of considerable amplitude.

According to Zhu and Zhu, the first resonance peaks are obtained when the energy pumping rate from the spin-torque becomes equal to that of the dissipation through Gilbert damping. For the corresponding value of the current (in this case, 2.5 mA), it should be possible to calculate the resonance frequency using Kittel's formula for small-angle FMR excitations [4] :

$$f = \frac{\gamma}{2\pi}\sqrt{(H + H_k + H_{ms})(H + H_k + H_{ms} + H_d)} \qquad (43)$$

where H_k is the anisotropy field and the other notations are as defined in chapter 3.

The actual 0 K anisotropy field is unknown, but it can be evaluated supposing that within a Stoner-Wohlfart model $H_k = H_c$, and using the following formula describing the coercivity shrink as consequence of thermally activated reversal [5]:

$$H_c = H_k \left[1 - \sqrt{\frac{k_B T}{\frac{1}{8\pi} H_d V H_k} \ln\left(\frac{f_0 \tau_m}{\ln 2} \right)} \right] \tag{44}$$

where f_0 ~ 10^9 Hz is the "attempt frequency" [6], τ_m ~ 1 s is the characteristic measurement time, T ~ 310 K is the temperature and V is the volume of the free layer. With the experimentally determined H_c = 100 Oe at 310 K, the 0 K anisotropy is estimated to be around 180 Oe.

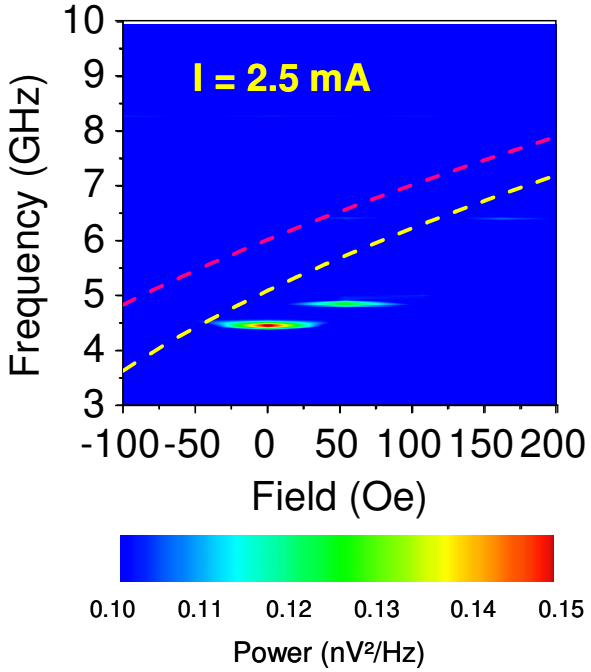

Fig. B.5 - 8 Measured and calculated frequency shift at 2.5 mA. The fit lines were determined using Kittel's formula and the 310 K coercivity (yellow line) or the calculated 0 K anisotropy field (red line), respectively.

Fig. B.5 – 8 shows the dependence of the resonance frequency on the applied field, as compared with the calculated values. To fit the data, the demagnetizing field was taken to be H_d = 16000 Oe, the same as for fitting the static phase diagrams in chapter 3. For the evaluated H_k, the theoretical precession frequencies (in red) are about 25% higher that the measured values. On the other hand, the agreement is rather satisfactory when replacing H_k in Kittel's formula by the zero current coercivity

H_c = 100 Oe (in yellow on the figure), as a way of accounting for thermal effects which may appear.

The dynamic phase diagram can be constructed by plotting for each value of applied current and field the obtained output power, integrated over the whole measured frequency range, multiplied by 1 mA² and normalized by the square of the current (since the amplitude of the obtained signal depends on the input power) (Fig. B.5 – 9).

As the *1/f* noise or low frequency peak becomes larger and the overall spectrum noise rises, more (normalized) integrated power is obtained. For a given value of the applied field, the power increases with the current. When the current is kept constant, the power and the noise generally decrease with the increasing field.

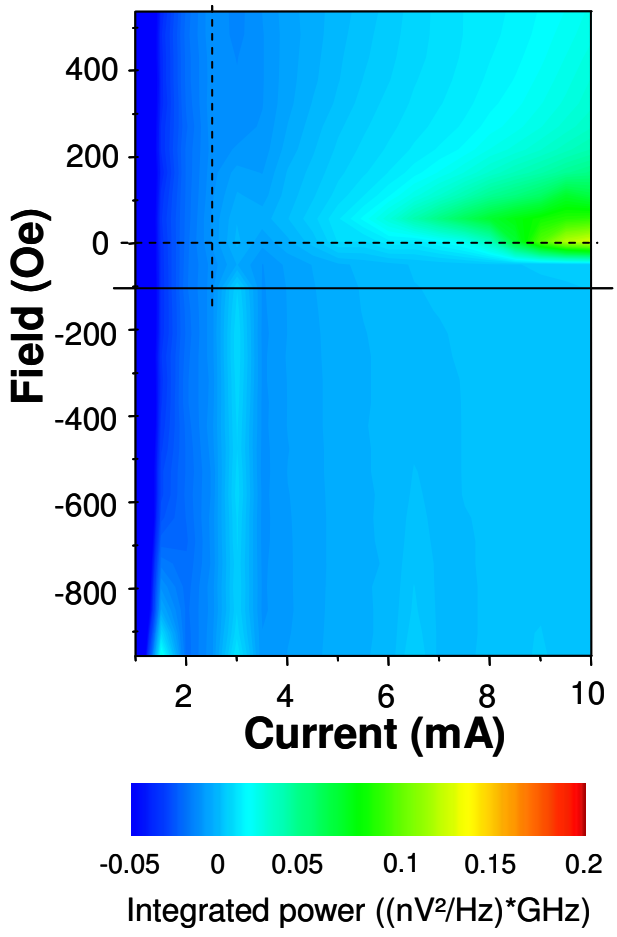

Fig. B.5 - 9 Positive current dynamic phase diagram for sample 8: the integrated power over the measured frequency range, normalized by the square of the applied current, is plotted as function of current and field. The spectra in fig.B.5 – 4, B.5 – 5 and B.5 – 7 were obtained for different currents along the horizontal dotted line. The vertical dotted line marks the current for which the data in fig. B.5 – 8 was measured.

As for the static experiments, the general trends characterising spin-transfer induced dynamics in spin-valves for CPP-GMR heads are found to be qualitatively similar to those of simple Co/Cu/Co pillars (see part A, chapter 4, paragraph A.4.2.b), except from the large amplitude dynamics measured in low negative applied fields, where the macrospin model predicts a stable P state (second transition in positive currents, see chapter 3). The reasons why such behaviour should occur have been discussed in chapter 3. The low power region labelled "W" on the Cornell phase diagram does not appear in our case simply because we did not apply enough current (currents higher than 10 mA irreversibly damage the samples). It is to be noted, though, that the results described above are obtained in the opposite current / field configuration (positive field / current favours the AP / P state) with respect to the one considered for the experiments of the Cornell group [7].

B.5.1.c. Dynamic behaviour for negative currents & fields

The behaviour of the sample in negative fields and currents is comparable to the previously described configuration, with two notable differences:

1. The peaks corresponding to small angle FMR and large angle precession are commonly lower and wider, and
2. More power is obtained for the low-frequency peaks or *1/f* noise, as compared with the positive current / positive field spectra.

Fig. B.5 – 10 shows the negative current dynamic phase diagram of sample 8 (the colour scale is the same as in fig B.5 – 9). Though its pattern is more complicated, the general trends are the same as described above. The incoherency and the power increase with the current and decrease with the field. The onset of the high power area (light blue-green on the figure) occurs for higher values of the current than in the opposite configuration (around –6 mA, as compared to 4.5 mA in fig. B.5 – 9). This is in good agreement with the results of static experiments, which have suggested that spin-transfer is stronger for positive that for negative currents.

Power spectra measured for different values of the dc current when the field is held constant (-319 Oe, just outside of the coercivity region; see the static R(I) characteristics measured at this field in fig. B.5 – 3, b) are shown in fig. B.5 – 11.

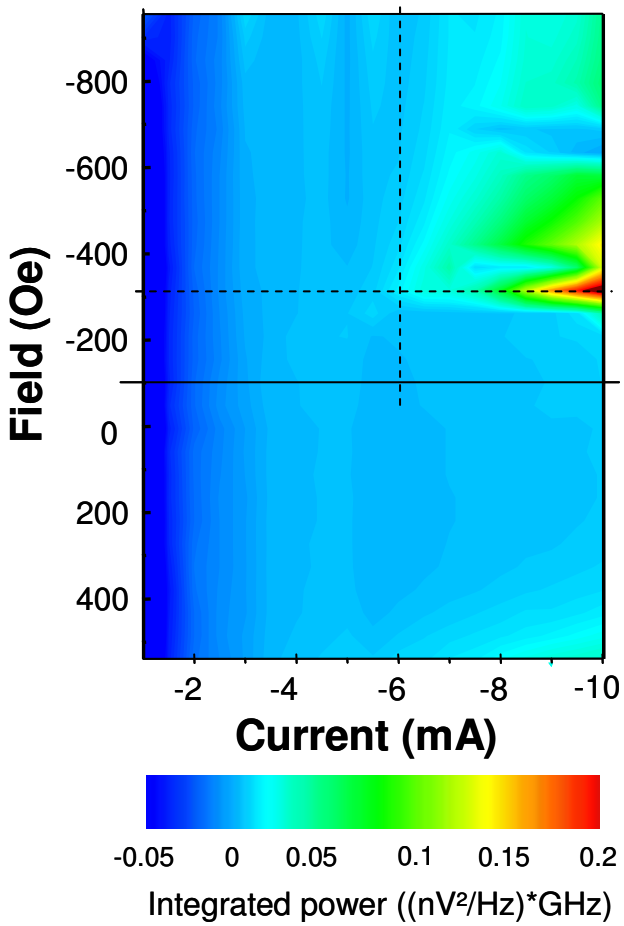

Fig. B.5 - 10 Negative current dynamic phase diagram. The dotted lines mark the values of current (vertical) and field (horizontal) where the spectra in fig.B.5 – 11, B.5 – 12 and B.5 – 13 were recorded.

When a resonance signal starts to be resolved, at -6 mA (around 5.5 GHz) the low frequency peak and the overall noise level are already so high that the resonance signal can hardly be distinguished. The 5.5 GHz peak itself is considerably wide; its maximum amplitude frequency does not seem to shift with the current up to -7 mA. At -7.5 mA, a slight red shift is measured; for larger negative currents, the peak is completely covered by the background noise.

The low frequency (1 GHz) peak is present on the spectra recoded with currents above -6 mA (fig. B.5 – 12). As in the opposite current / field configuration, its amplitude increases with current (while shifting slightly towards higher frequencies) and decreases with field, reaching a maximum at -10 mA and -319 Oe, where the static

resistance is found to have an intermediate value (fig. B.5 – 3, b). The peak power is considerably more important than obtained for positive currents of similar amplitude (see for comparison Fig. B.5 – 7).

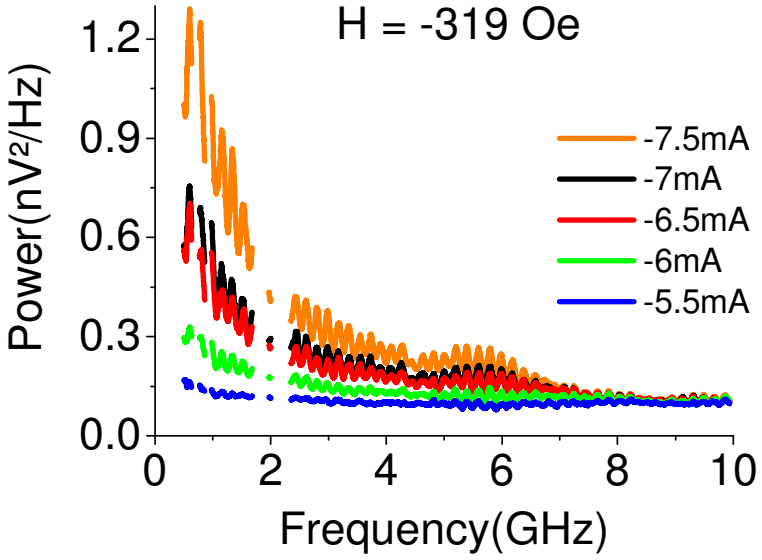

Fig. B.5 - 11 Power spectra measured at –319 Oe, for currents up to -7.5 mA, as indicated. A weak, large peak is visible around 5.5 GHz.

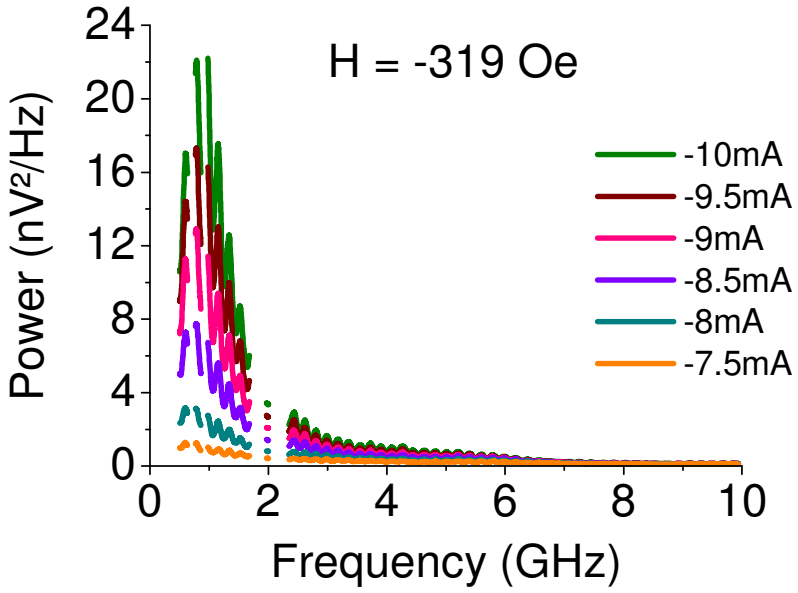

Fig. B.5 - 12 Power spectra measured at –319 Oe, for currents between -7.5 and -10 mA.

As mentioned above, for negative currents, the first signals are resolved at -6 mA ($1.67 \times I_c^{P \to AP}$). The peak amplitude being extremely low and their width rather large, it is difficult to establish beyond doubt whether they correspond to small or large-angle precession (that is, whether they shift with the current or not). However, in the case of positive currents, the small-angle motion persisted up to 4.5 mA ($4.5 \times I_c^{AP \to P}$); if the same ratio is conserved (although there is no indication that it should), small angle precession should be maintained until the negative currents reach values of about -16 mA ($4.5 \times I_c^{P \to AP}$). It seems thus likely that it should be possible to fit the -6 mA peak frequency dependence on the applied field with Kittel's formula (Fig. B.5 – 13).

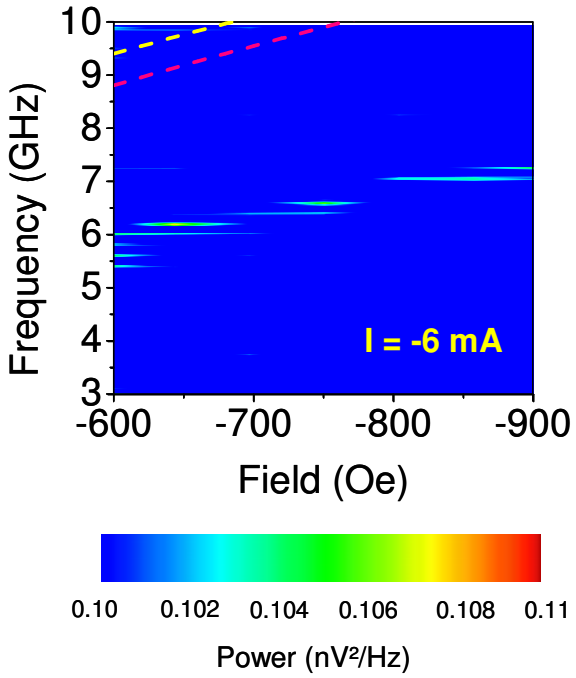

Fig. B.5 - 13 Small angle precession frequency variation with the applied field. The spectra were measured at –6 mA. The dotted lines represent the theoretical fit using Kittel's formula and the anisotropy or the coercivity field (red and yellow curve, respectively).

When doing so, the agreement between experimentally determined and theoretically estimated values is found to be much less satisfactory than for positive currents. Indeed, even when using the coercivity, the calculated frequencies remain 50% higher than the measured values. Moreover, although the peaks can be followed on a larger scale of fields, their amplitude is considerably lower than in fig. B.5 – 8. While,

in a first approximation, one would expect the output power to vary as the input power, that is, as I^2, a maximum amplitude of 0.105 nV²/Hz is reached at -6 mA, as compared with 0.15 nV²/Hz at 2.5 mA.

It is of course not to be excluded that the -6 mA signals are generated by large angle motions of the local moments, and consequently the Kittel's formula fit is inappropriate. It is possible that other small-angle precession peaks may appear at lower currents, but they simply have too less amplitude to be measured with our experimental setup. Nevertheless, experiments on simple Co/Cu/Co nanopillars have shown that for the same configuration (field / current favoring the P / AP state, respectively) small angle precession can persist up to currents more than twice higher than the switching value; moreover, the disagreement between the data obtained by Kiselev et al. and the predicted frequencies was comparable with that obtained in our case [7]. (To fit the experimental results, they had to assume a demagnetizing field about twice lower than commonly used for Co layers.) One can therefore presume that this important deviation from calculated frequency values is rather a signature of spin-transfer for this particular current / field configuration than a misinterpretation of the data.

B.5.1.d. Dynamic versus static phase diagram

The agreement between the static and dynamic phase diagrams is remarkably good (Fig. B.5 – 14). Generally, large normalised integrated power is obtained in the regions where the static resistance has an intermediate value between those of the parallel and antiparallel configurations. In both quadrants of the phase diagram, the highest level of normalized integrated power is reached for the maximum applied current (+/-10 mA), for values of the field which mark the exit from the coercivity region in static measurements. In the areas where relatively coherent small angle precession states are excited, the resistance is found (unsurprisingly) to be very close to that of the corresponding state (P or AP).

Both phase diagrams show a similar complicated pattern in the negative currents / negative field quadrant. Interestingly, a low power area can be identified roughly between –600 and -700 Oe. In this region, the spectra are very similar to those

obtained at higher / lower field, being dominated by the 1 GHz peak. Yet the maximum amplitude reached by the low frequency signal is significantly less important than attained for the same currents outside this field interval. Even more, the power does not seem to depend on the applied current, nor does the field interval where the amplitude drop takes place. To-date, the physical meaning of this experimental result remains unclear – especially since, unfortunately, no data is available in the corresponding region of the static phase diagram, which would have possibly shed more light on the matter.

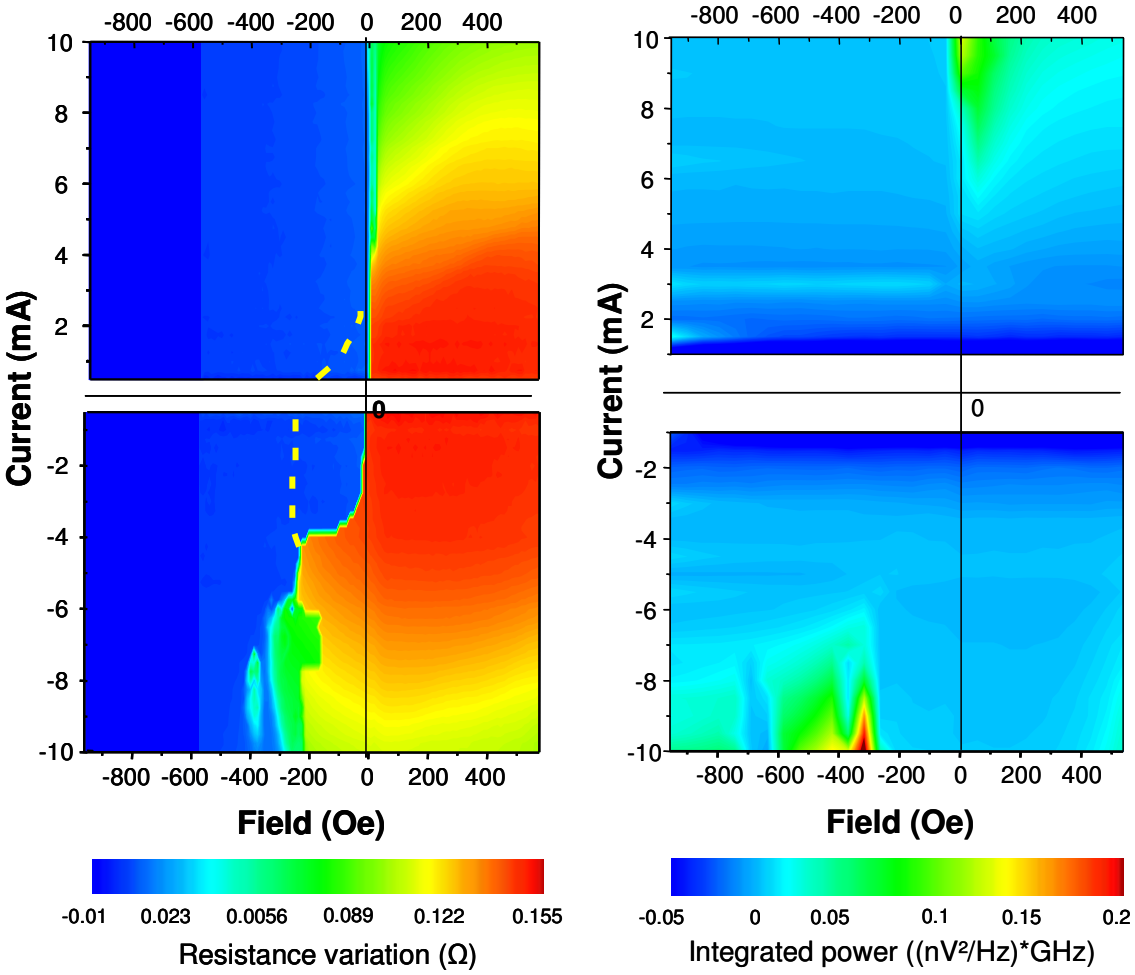

Fig. B.5 - 14 Static (**left**) versus dynamic (**right**) phase diagram, for sample 8. As explained above, for the static phase diagram, the absolute resistance variation (as compared with the resistance of the parallel state) was plotted as function of current and field; the yellow dotted line represents the AP→P transition. For static experiments, the field was varied between –570 and 570 Oe (the blue area between –950 and –570 Oe is a drawing). For the dynamic phase diagram, the color scale corresponds to the normalized integrated power.

B.5.1.e. Micromagnetic simulations

As explained in part A, chapter 3, spin-transfer can induce non-uniform magnetization dynamics as well as chaotic behaviour. In particular, the simulations of Zhu and Zhu suggested that the dynamics becomes more and more incoherent as the current is increased above the critical values. As such, although the simple macrospin model can account reasonably well for the results of static experiments (especially where the coercivity region is concerned), only full micromagnetic simulations can explain several details of the microwave data.

For example, within the macrospin model, multiple peak spectra are not allowed. Still, Zhu and Zhu showed that rising the current leads to an increase of the degree of incoherency of the system and consequently to a continued peak division which occurs in a random fashion.

Supposing that the free layer behaves like a single domain, it is also difficult to explain why the measured small angle precession frequencies can be fitted reasonably well for positive currents, when for the opposite situation the calculated values are considerably higher than those experimentally determined. Similarly, for currents favoring the P state, fields favoring the AP orientation, Kiselev et al. had to assume a demagnetizing field about half the known value in order to fit their results.

Also, it has been put forward by the same group that the "W" region on their phase diagram, where only very low power spectra are measured, emerges for values of current and field where the macrospin model predicts approximately circular out-of-plane processional modes, which would produce large microwave signals.

To bring an answer to the questions above, full micromagnetic simulations have been performed by Dr. K.J. Lee [8], on samples mimicking those of the Kiselev et al., for simplicity.

The positive sign of the current / field are defined as in the Cornell experiment (positive current / field favours the AP / P state, respectively), thus opposite to the convention used in our case.

i) Switching

According to the single domain model, current induced magnetization switching occurs through coherent precession (see for example the results of J.Z. Sun, part A, chapter 3, paragraph A.3.1). Nonetheless, even inside the coercivity region, full micromagnetic simulations have shown that spin-torque induced dynamics is considerably more complicated (Fig. B.5 – 15). The magnetic moments of the free layer undergo three different dynamic stages prior to the switching:

1. **Growth of the precessing end domains**: As the current is turned on, because of the spatially non-uniform demagnetising field, which is much stronger at the edges than in the middle, the moments at the two long ends of the free layer start precessing. The end domains precess slightly asymmetrically, as a consequence of the clockwise Oersted field, and grow in time until they almost join each other and the magnetization dynamics changes to stage 2;

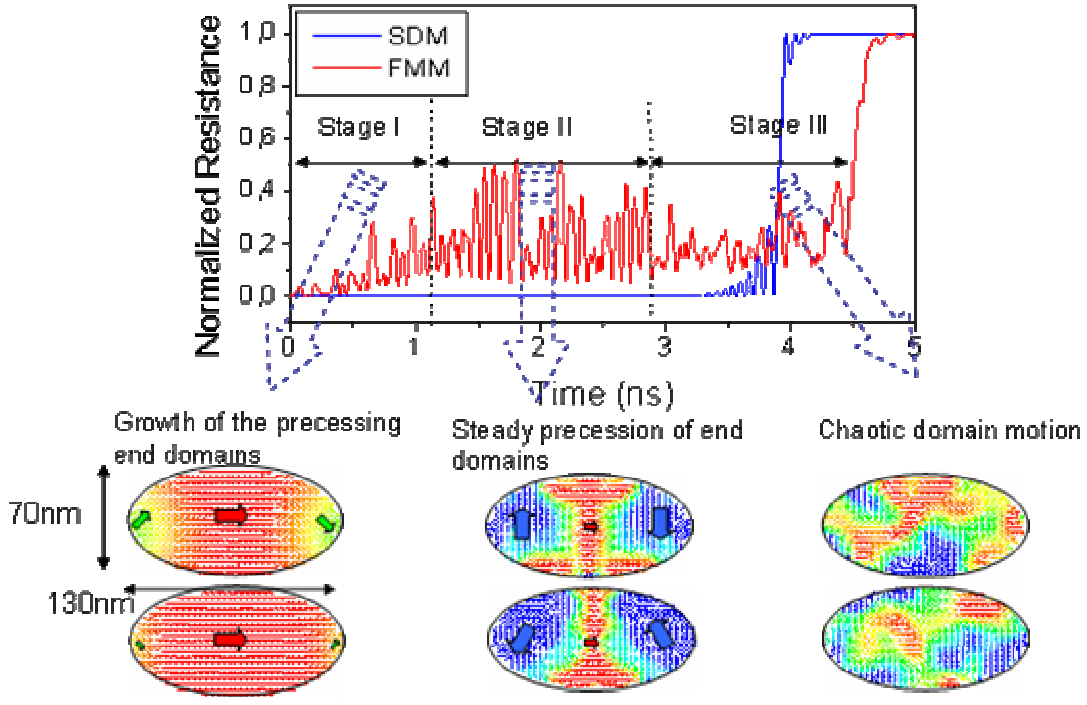

Fig. B.5 - 15 Current induced magnetization switching for I = 4 mA and H = 0 Oe, as seen in full micromagnetic simulations, for Co/Cu/Co pillars with important uniaxial shape anisotropy, as defined on the figure.

2. **Steady precession of the end domains**: The end domains, which have almost joined each other, continue precessing together for a while. The magnetization at the centre of the cell remains stationary along the initial direction, because the local torque is still too weak;

3. **Chaotic domain motion**: Once the magnetization at the centre of the free layer starts precessing, an increasing spatial incoherency is observed, both in the precession frequency and the local moment direction. The domain motion becomes totally chaotic and finally the magnetization switches.

ii) Dynamic phase diagram

Fig. B.5 – 16 shows a contour plot of normalised integrated power, as obtained from full micromagnetic simulations. Coherent excitations are only observed in a very narrow range of currents, between 1.6 (which marks the onset of small-angle magnetization precession) and 2 mA. This range depends on the relative importance of the exchange energy, which tends to stabilize a coherent motion of the local moments, and the other contributions to the local fields which are spatially non-uniform and therefore generate incoherent excitations. Consequently, reducing the lateral size of the nanopillar or increasing the anisotropy would widen the coherent precession current range.

The simulated spectra for the current / field values labelled A, B and C along line 2 are presented in fig. B.5 – 17. At point A (I = 3 mA), the magnetization of the free layer undergoes a small-angle precession motion with an average cone angle of about 6°. The corresponding peak, centered around 13 GHz, is wide and its amplitude is considerably lower than calculated within the macrospin model (inset). A low frequency *1/f*-like noise is also present, as a consequence of the chaotic nature of incoherent spin-wave excitation (I = 3 mA is outside the coherent precession range).

In full micromagnetic simulations, large amplitude precession modes are found only in a limited range of current and field (red and yellow area on the phase diagram), as compared with single domain calculations (see part A, chapter 4, fig. A. 4 – 14, right). The maximum integrated power is obtained at point B (I = 7 mA), where the spectrum shows a very large peak around 1 GHz, as well as the initial FMR peak which

has shifted towards lower frequencies and is almost covered by the increased overall noise.

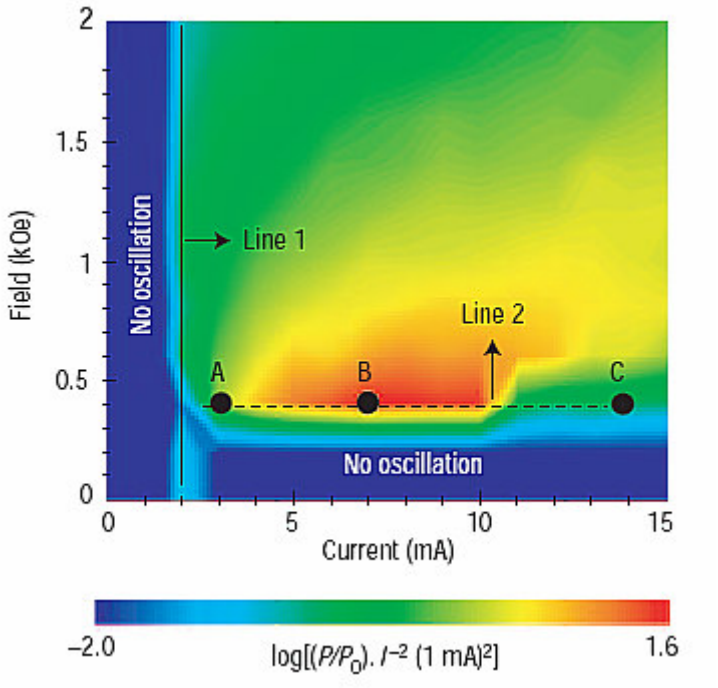

Fig. B.5 -16 Full micromagnetic simulation dynamic phase diagram. The spectra were calculated for the interval 0.1-30 GHz.

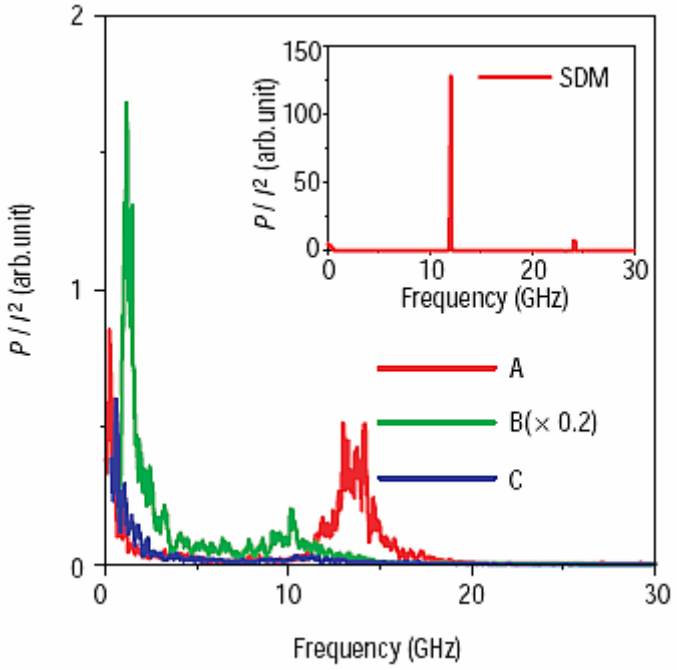

Fig. B.5 - 17 Calculated spectra corresponding to the current / field values marked A, B, C along Line 2 in fig. B.5 – 16. Inset: Macrospin microwave spectrum at I = 7 mA, H = 600 Oe.

The "W" region (point C on Line 2) corresponds to the formation / annihilation of dynamic vortices through the interplay of large Oersted fields and spin-torque. The dynamics becomes more and more incoherent and the large current spectra show only *1/f* noise without any high frequency peak. At larger fields, which partially compensate the spatial non-uniformity of the field induced by the current, small and broad peak structures can be found at high frequencies, besides the *1/f* noise.

iii) Small angle FMR frequencies

Full micromagnetic simulations also proved that it is possible to reproduce the experimentally determined small-angle precession frequencies without assuming an artificially reduced value of H_d in Kittel's formula (Fig. B.5 – 18). The difference between the predicted and the measured values is caused by incoherent spin-waves excitation, which reduces the apparent saturation magnetization and cannot be accounted for within a single domain model.

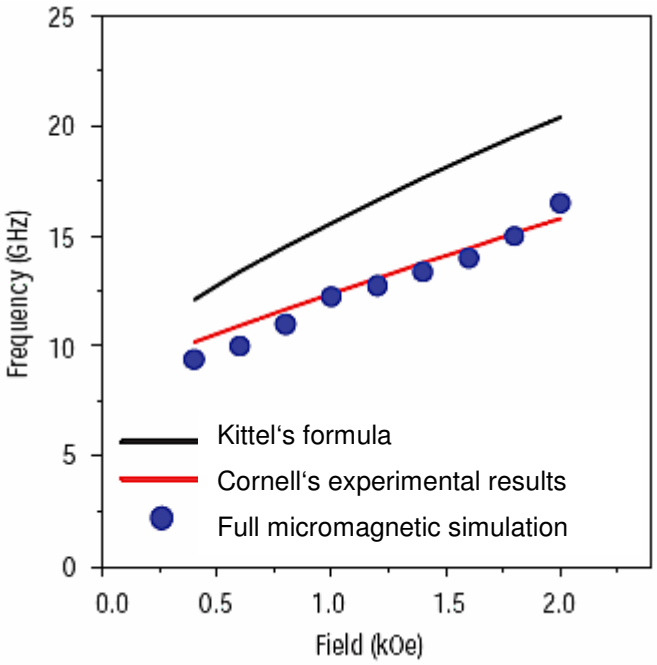

Fig. B.5 - 18 Small-angle precession frequencies: comparison between the experimental results of Kiselev et al., fit using Kittel's formula and the generally accepted value for H_d in Co (~15000 Oe), and simulation results.

iv) Telegraph noise in the precession region

In the red area of the phase diagram, where the maximum integrated power is obtained (at point B, for example), the precession frequency of the local magnetic moments is of about 10 GHz. The corresponding peak, however, is very wide and almost covered by the noise, and most of the power is concentrated into the 1 GHz signal (see the green spectrum in fig. B.5 – 17). As seen in fig. B.5 – 19, this unexpected low frequency signal is generated by random fluctuations between almost parallel and antiparallel magnetic configurations. The dynamics of the low resistance state (A) is driven by spin-transfer torque, leading to spin-wave excitation. The dynamics of the high resistance state (B) is different, since it is governed by the field and consequently no spin-waves are generated.

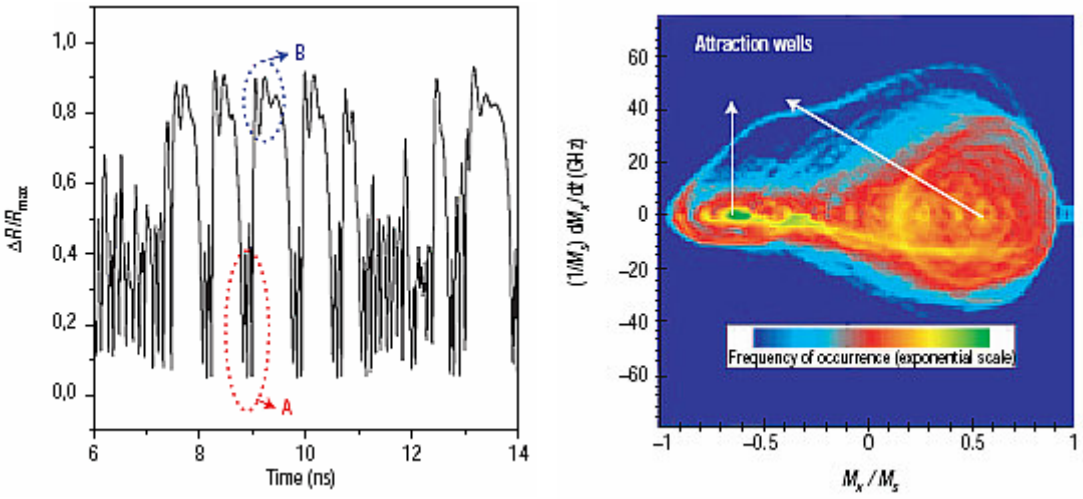

Fig. B.5 - 19 Telegraph noise at zero temperature in the precession region at point B. **Left:** Variation of the normalized differential resistance versus time. **Right:** Time trajectories in phase space showing strange attractors as in chaotic dynamics.

In the simulation, telegraph noise in the precession region is obtained even at 0 K, and thus cannot be explained by the macrospin model. While the effective temperature concept would provide a convenient representation, further analysis of the generated spin-wave modes lead to the conclusion that it is more appropriate to describe the observed random fluctuations in terms of chaotic dynamics [8]. The non-linear

magnetization dynamics induced by spin-transfer, and in particular the incoherent excitations, determine the formation of attraction wells in phase space in ranges of current and field where no energy minimum is allowed by the macrospin theory (since in the precession region the current is higher than the switching current, the field is higher than the coercivity, and they are so oriented that they favour opposite states). The attraction wells in phase space correspond to trajectories of higher probability (known as strange attractors in chaotic dynamics [9]). Random transitions between these trajectories quantitatively explain telegraph noise in the precession region, experimentally analysed in detail by Pufall et al. [10] (see part A, chapter 4, paragraph A.4.2.c).

B.5.1.f. Discussion

The simulation results described above can be summarized as follows:

1. Incoherent spin-wave excitation reduces the measured small-angle precession frequencies as compared to the values calculated using Kittel's formula; the corresponding peaks are also considerably widened and their amplitude is diminished.
2. The incoherency increases with the current.
3. The largest integrated power is obtained at relatively weak fields for the spectra showing a high low frequency peak (centred around 1 GHz) corresponding to random transitions between trajectories of higher probability, as a consequence of non-linear magnetization dynamics.

Starting from the remarks above, is possible to put forward an explanation for the difference between the positive and negative current dynamic phase diagrams measured for the *Headway* samples. One should bear in mind that in the negative current / negative field quadrant, the field is applied opposite to the dipolar interaction from the reference layer. Because the magnetostatic field is stronger at the edges than in the centre, the total field acting on the local moments might have different signs over the free layer and thus increase the incoherency of the precession. Consequently, more incoherent spin-waves should be generated for negative currents and negative fields where small-angle precession motions are observed. As such, the agreement between the precession frequencies calculated using Kittel's formula and the measured values

should be better for positive (less incoherency) than for negative currents (more incoherency). Also, the peak amplitude should be lower for negative currents, and their width more important, as observed experimentally.

Moreover, static experiments have already demonstrated that spin-transfer is more efficient for positive than for negative currents (where the positive sign of the current is as described in chapter 3, thus opposite the convention used for the simulation and in the Cornell experiments). Indeed, it takes about twice more negative current to produce the same effect (switching, for example) as a given positive current. Evidence of small-angle precession is obtained for 2.5 and -6 mA, respectively. Though the spin-torque amplitude should be roughly the same, the Oersted field, which is proportional to the current and a source of incoherence because of its spatial non-uniformity, is much higher at -6 than at 2.5 mA.

It has been also pointed out that the maximum power reached by the 1 GHz peak in the negative current half of the phase diagram is almost twice higher than the highest corresponding signal amplitude measured for similar positive current (Fig. B.5 - 20). An interpretation can be proposed as well, based on the micromagnetic simulations and static experimental results. According to the simulation, the 1 GHz peak is attributed to high frequency chaotic jumps between two stable precession orbits, one given by the field, the other given by the current, the corresponding resistance variation being close to the full GMR amplitude. The amplitude of the low frequency signal depends on the resistance variation between the two trajectories.

For negative currents and fields, the current gives a precession trajectory in the vicinity of the AP state (which is always stable in current, as demonstrated by the static curves), while the field favours an orbit close to the P state (which is stable in field), so almost the full GMR variation can be reached. In the opposite current / field configuration, the field determines a precession trajectory close to the AP state (stable in field), while the current brings the free layer into an intermediate resistance (dynamic) configuration (see the second transition in positive current on the R(I) curves). The resistance variation between the two dynamic states is thus lower and the maximum amplitude reached by the 1 GHz peak will be lower than for negative currents (Fig. B.5 – 20). The static resistance measured on the R(I) curves at 10 mA is probably the weighted mean (taking into account dwell times) of the corresponding resistance levels of the two dynamic states.

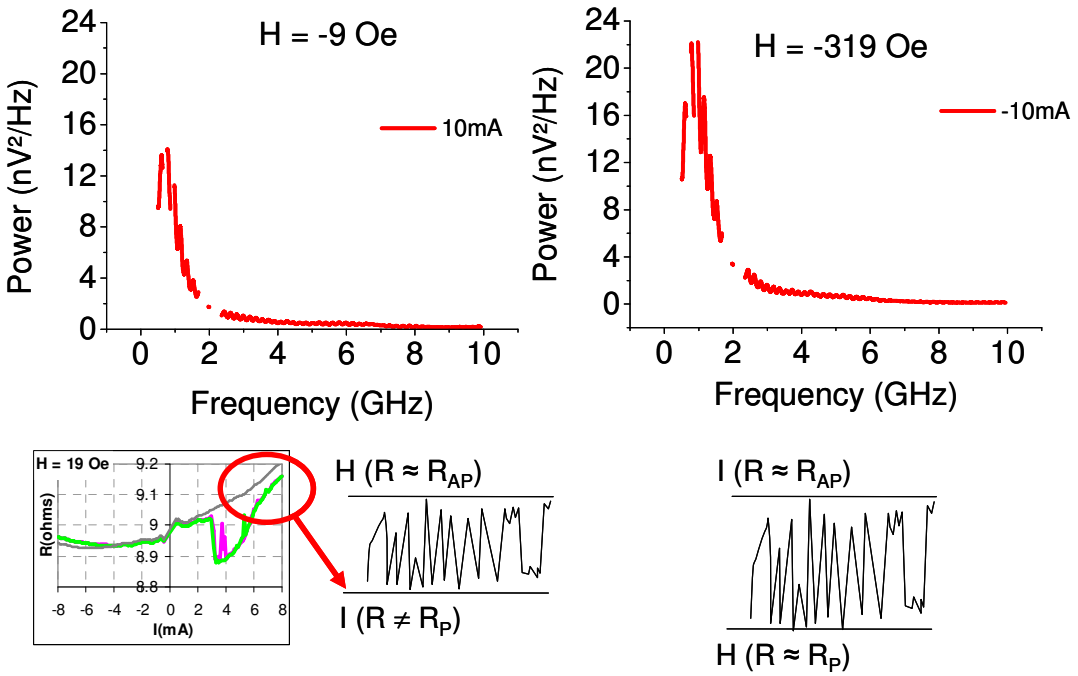

Fig. B.5 - 20 Top: The telegraph noise peak in negative current reaches almost twice the amplitude attained for similar positive currents. **Bottom:** Resistance versus current curve measured for sample 1, showing the second transition towards an intermediate resistance level in high positive currents (see chapter 3). Schematic drawing of high frequency telegraph noise for the two configurations, with the corresponding resistance variation.

B.5.2. Very low coercivity samples

The results presented below were obtained using a 125 nm pillar of structure "b" (sample 9). The coercivity of the free layer is H_c = 9 Oe. From eq. (44), the anisotropy field is estimated to be H_k = 41 Oe. As for the other samples, the magnetostatic field H_{ms} = 21 Oe is oriented so that it favours the antiparallel alignment between the magnetizations of the free and the reference layers. The critical currents were 1.6 and -3.6 mA when the field acting on the moment of the free layer is zero. (As in the case of sample 6, these values were deduced from the magnetoresistance curves variation with the sense current, see chapter 3.) Since the static phase diagrams of low coercivity pillars are rather hard to read, the outcome of static experiments on sample 9 is described in detail in paragraph B.5.2.a.

For measuring the magnetoresistance curves, the field was swept between -950 and +950 Oe, without finding any evidence for the reference layer's reversal. Consequently, microwave spectra were recorded up to 950 Oe for this sample. The field and current were varied with the same steps as for the high coercivity pillars. Details on dynamic measurements results and their discussion are given in paragraphs B.5.2.b and B.5.2.c.

B.5.2.a. Static characterization

Through static experiments, the behaviour of sample 9 was found to be very similar to that of sample 6, presented in chapter 3. The static phase diagram of sample 9 is presented in fig. B.5 – 21, left.

As explained in chapter 3 for sample 6, at intermediate values of negative currents and fields (between –2.6 and -9 mA and roughly from -100 to -500 Oe), the coercivity is significantly increased, reaching a maximum of 173 Oe at -7.2 mA (Fig. B.5 – 21). This was attributed to the formation of a "C"-state in the free layer, as a consequence of the joint effect of the applied and rather high Oersted field, as well as a relatively weak spin-torque. The magnetoresistance loops become reversible above -9 mA.

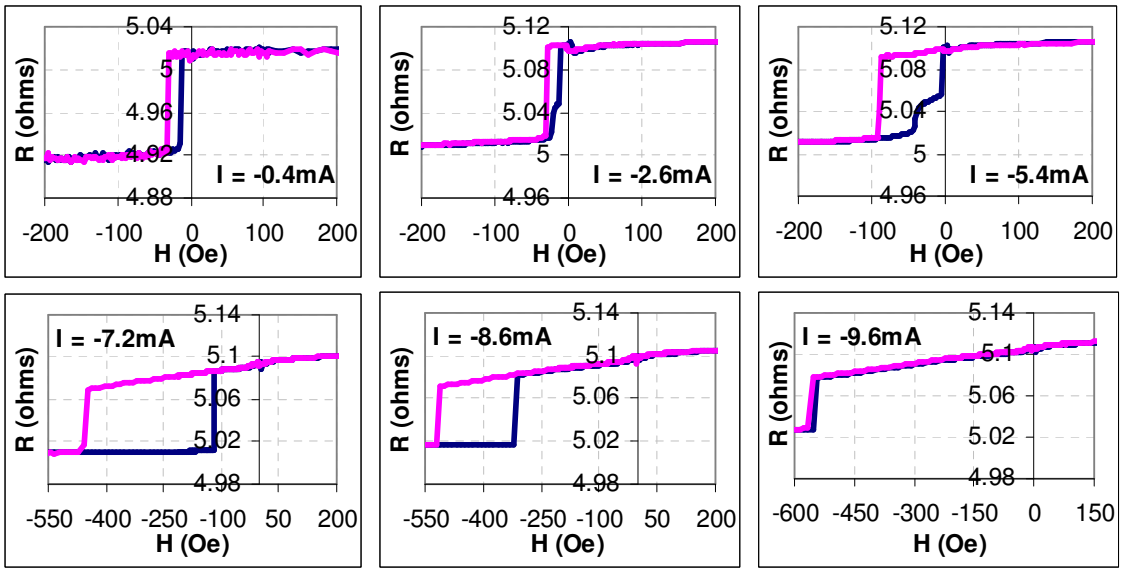

Fig. B.5 - 21 Magnetoresistance curve variation with the negative sense current, for sample 9.

At positive currents and fields, spin-transfer is expected to be considerably more efficient, and the magnetoresistance and resistance versus current curves show mainly telegraph noise between the (almost) parallel and antiparallel states (Fig. B.5 – 22). Telegraph noise occurs for currents between 5.4 and 9.4 mA and mainly for positive low fields (up to a maximum of 300 Oe at 8.8 mA), that is, when the magnetization of the free layer should be parallel to the moment of the reference layer.

Because of the magnetostatic interaction, which can be considerable on the edges of the pillar, the parallel state is highly unstable, especially when the applied field reinforced the dipolar coupling. For the same range of currents, once the free layer switches to the AP orientation, the MR curves present no evidence of persisting noise. Above 9.6 mA, the transition between the two resistance states is perfectly reversible and noise-free.

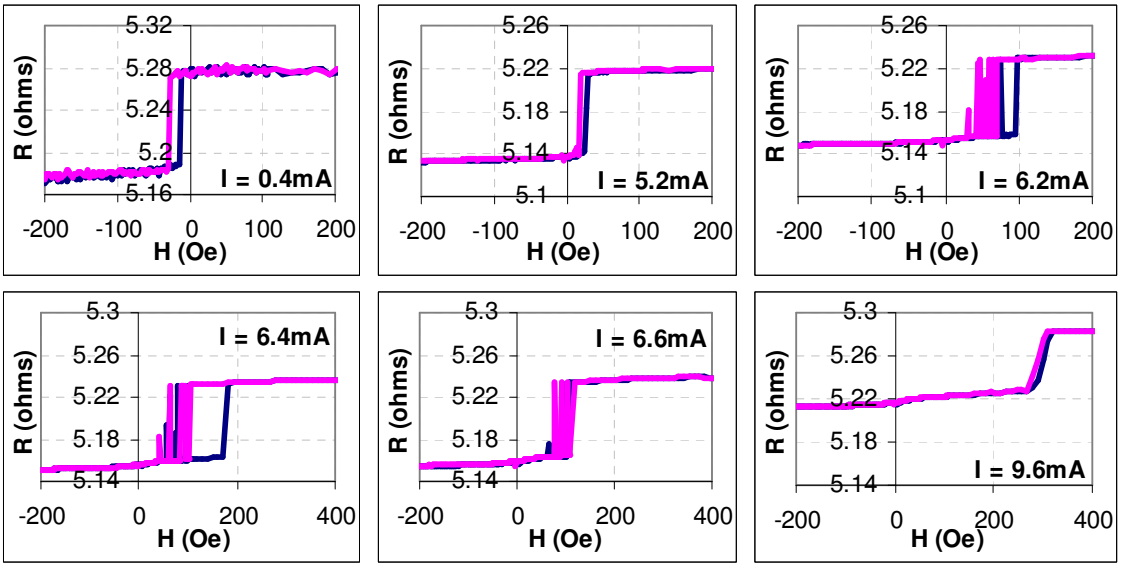

Fig. B.5 - 22 Magnetoresistance curve variation with the positive sense current, for sample 9.

Regarding the field dependence of the resistance versus current characteristics, as long as H takes values between $-H_{ms} \pm H_c$, the resistance switches reversibly between the low and an intermediate resistance level, indicating that a vortex state is probably formed in the free layer. At higher fields, the hysteretic loops between the low and high resistance states are recovered (Fig. B.5 – 23). The current "coercivity" increases with the applied negative field, reaching a maximum at -416 Oe; for higher fields, the

coercivity is gradually reduced, until the loop becomes reversible at -555 Oe. Increasing the field even more yields a shift of the reversible transition towards more negative currents. At -592 Oe, no switching can be observed any longer, as the current is swept between +/-10 mA.

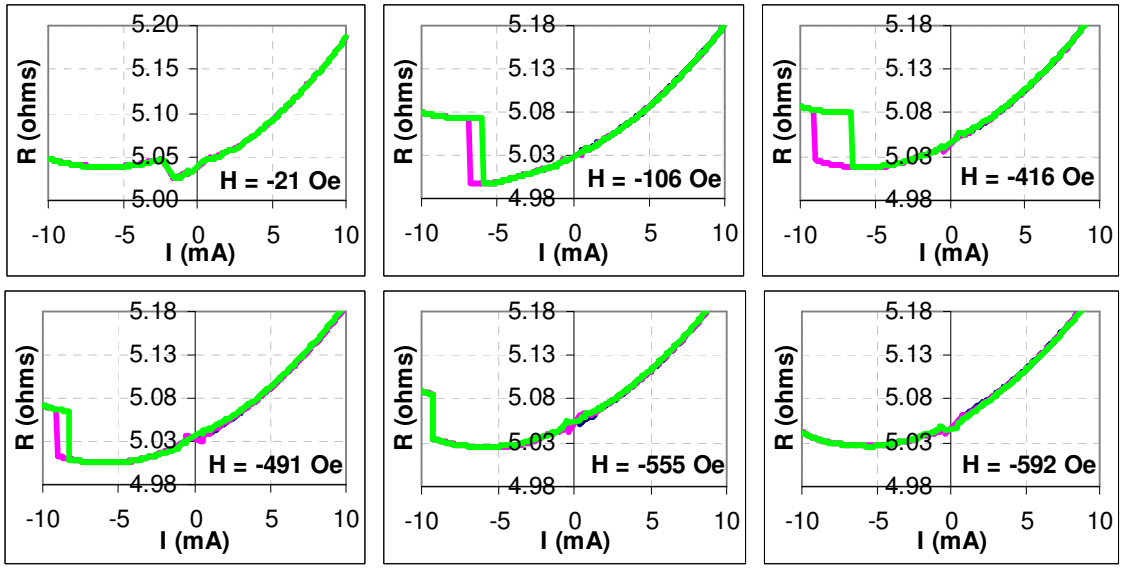

Fig. B.5 - 23 Resistance versus current characteristics for different values of the negative applied field. At -21 Oe, the magnetostatic field is compensated, so the total field is zero.

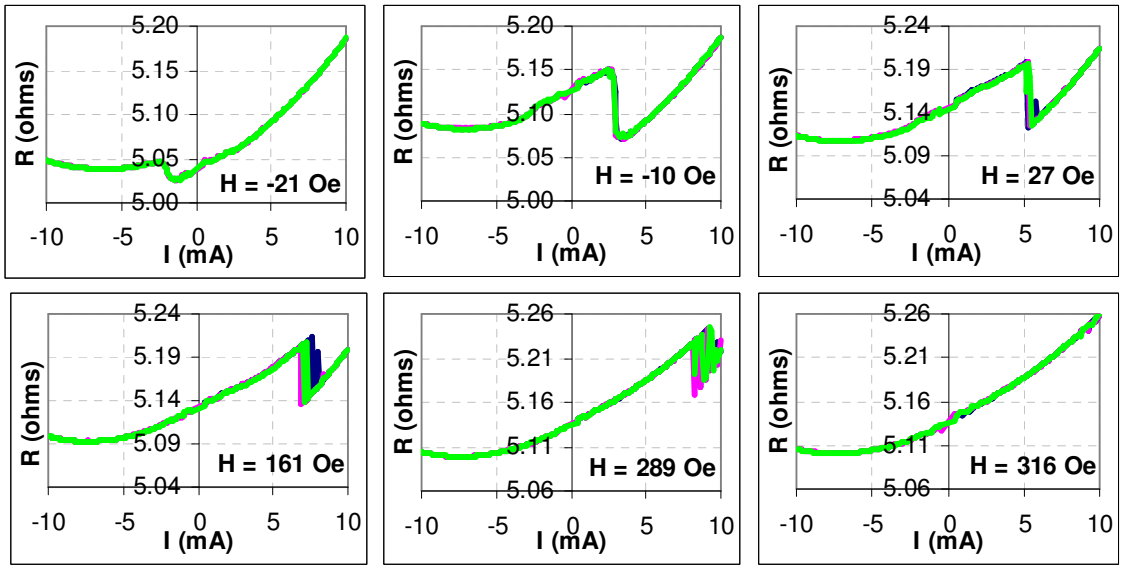

Fig. B.5 - 24 Resistance versus current characteristics for different values of the positive applied field. Given that the dipolar interaction is 21 Oe, the total field acting on the free layer is 11 Oe when the applied field is H = -10 Oe.

When the total field acting on the free layer is positive, the transition between the two states is reversible (Fig. B.5 – 24). In agreement with the magnetoresistance curves, the resistance versus current characteristics demonstrate strong telegraph noise in the range of currents where the magnetization of the free layer should be oriented parallel to that of the reference layer. The noise persists for fields up to 300 Oe, after which no obvious transition can be identified in the R(I) variation.

As mentioned above, the outcome of static experiments is summarized in the phase diagram in fig. B.5 – 25, left.

B.5.2.b. Dynamic results

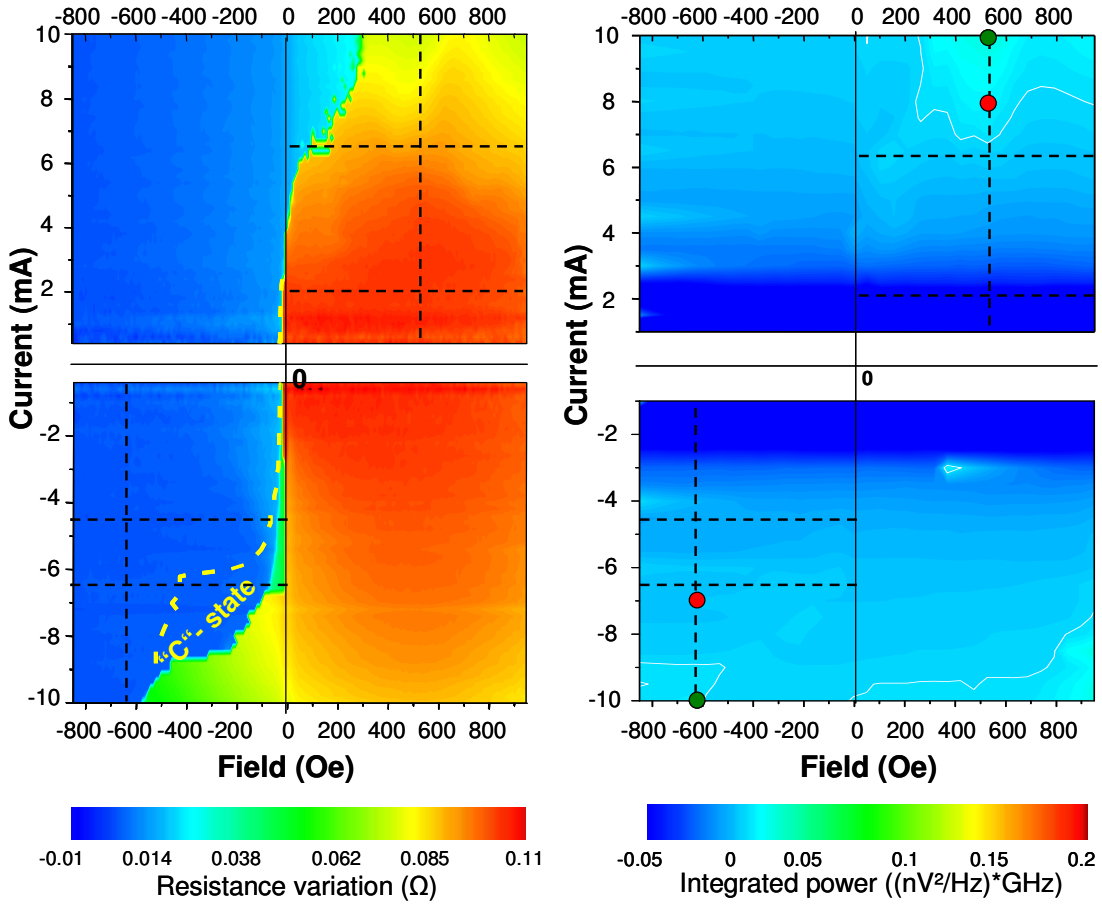

Fig. B.5 - 25 Static (**left**) and dynamic (**right**) phase diagrams for sample 9. The dotted lines and the color dots indicate the current / field valued where the curves in fig. B.5 – 26 to fig. B.5 – 30 were measured.

Though, compared to the high coercivity pillars, generally much less integrated power is obtain, the agreement between the static and dynamic phase diagrams is remarkably good in the case of sample 9 as well (Fig. B.5 – 25). As for sample 8, the highest integrated power is attained in the areas of the phase diagram where the static resistance has an intermediate value. In the "C"-state region, only a very slight increase of the integrated power is found, as compared with the adjoining areas where the microwave spectra show merely an increased level of noise. In the negative quadrant of the dynamic phase diagram, a noticeable signal enhancement appears just for high negative currents and fields, outside the "C"-state region (in the bottom-left corner). In the positive quadrant, a similar level of integrated power is reached for comparatively lower values of current and field, outside the area where both magnetoresistance and resistance versus current curves give evidence of telegraph noise.

For an applied field of -53 Oe, the first peak is resolved at 2 mA. Its frequency does not shift with the current up to -5 mA and decreases slightly between -5 mA and – 6 mA (Fig. B.5 – 26, left). The first regime is identified as small angle precession; the second is attributed to increasing cone angle dynamics, as in the case of high coercivity samples. Inside the "C"-state region, between -6.5 mA and -9 mA, the peak stops shifting and the spectra seem unaffected by the current, resembling the signals obtained for small angle precession. An obvious change of shape occurs at -9.5 mA, the current where the MR curve becomes reversible (Fig. B. 5 – 26).

Similarly, at 53 Oe, the first (weak) signal is resolved at 2 mA and the frequency-dependent curves are only slightly altered by currents below 9 mA. The spectra obtained at 9.5 and 10 mA are very similar to those exhibited at negative currents of the same intensity (Fig. B. 5 – 27).

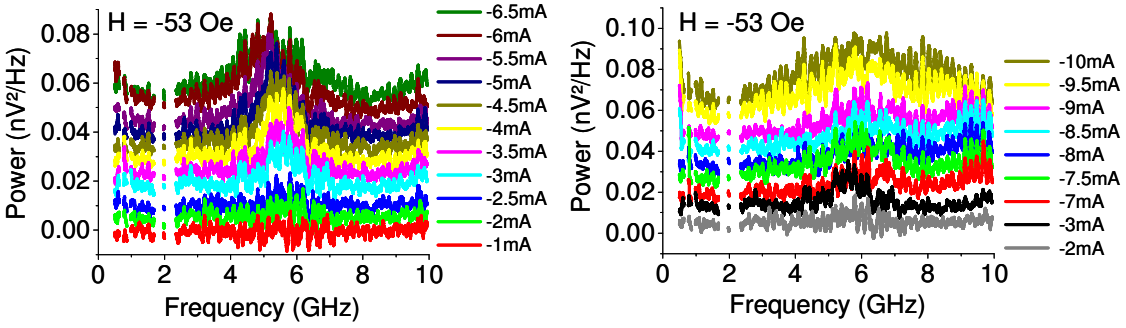

Fig. B.5 - 26 Microwave spectra at -53 Oe for different negative currents; the signal measured at 1 mA has been subtracted from all curves. The curves have been offset for clarity.

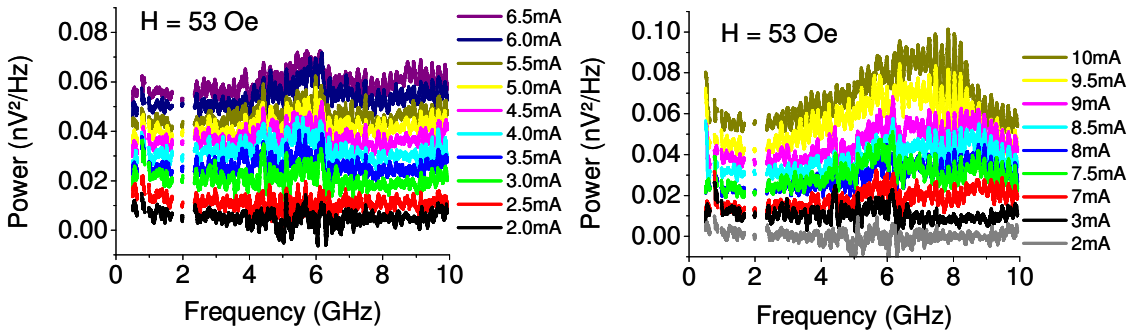

Fig. B.5 - 27 Microwave spectra at 53 Oe for different positive currents; the spectrum at 1 mA was considered as noise base line. The curves have been offset for clarity.

When trying to analyse the small angle FMR signals, the behaviour is found to be comparable to that of high coercivity samples: for positive currents, the measured frequencies are close to those predicted by Kittel's formula, while in the case of negative currents, the calculated values are abound 50% higher than those obtained experimentally (Fig. B.5 – 28).

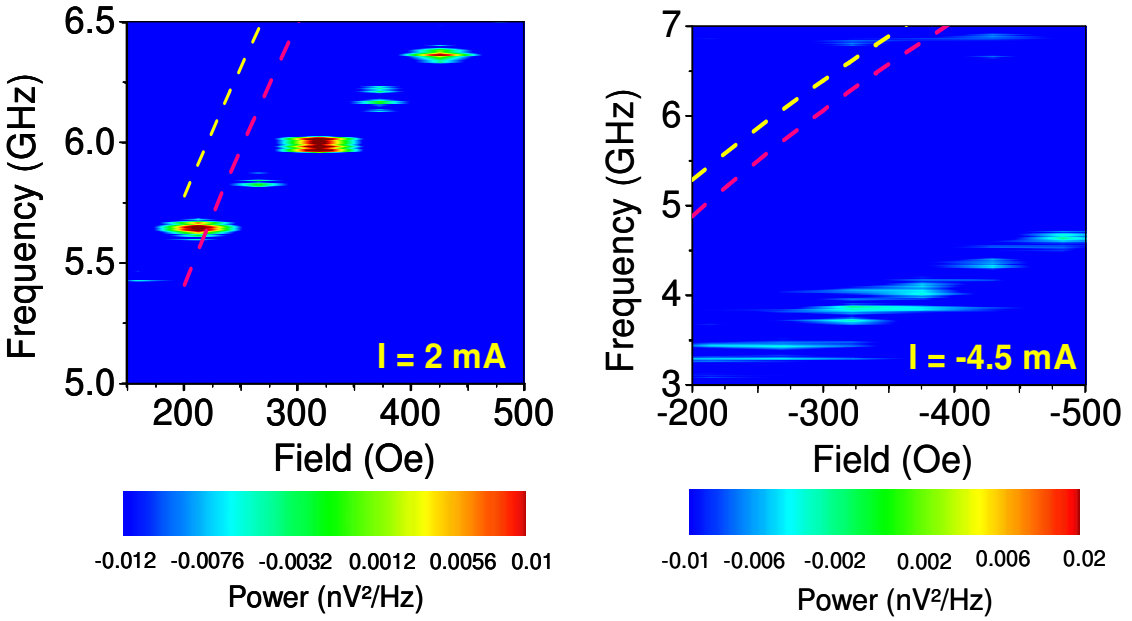

Fig. B.5 - 28 Small-angle precession frequency dependence on the applied field, and comparison with the values predicted using Kittel's formula and the coercivity (in yellow) or the anisotropy field (red). Note that the frequency scale is different between the two plots.

Also similar to the results obtained for high coercivity nanopillars, the peak amplitude is significantly lower for negative applied currents, although the current intensity is more than twice higher. Note that the frequency scale is different for the two plots in fig. B.5 – 28; the disagreement between theoretical and experimental slopes characterising the dependence of small-angle precession frequency on the applied field is not actually worse in positive than in negative currents – nor than obtained for high coercivity samples (or for simple Co/Cu/Co pillars, for that matter; see part A, chapter 4, paragraph A.4.2.b, fig. A.4 – 13, e for comparison). Considering that the exact values of the demagnetizing field and the misalignment angle between the direction of the applied field and the anisotropy axis are unknown, this incongruity is not surprising.

At intermediate currents, where static curves demonstrate the formation of "C"-states for one polarity and telegraph noise for the other, the spectra variation with the field is extremely different in the two quadrants of the phase diagram, and also compared to that measured under similar conditions for sample 8 (Fig. B.5 – 29 and Fig. B.5 – 30). Since in these regions no peak shift with the current was measured, fits were attempted for the frequency dependence on the field using Kittel's formula for small angle FMR precession.

For negative currents, only very low amplitude peaks are obtained over all the measured range of fields and frequencies (Fig. B.5 – 29). The first signal is resolved around -100 Oe, roughly for the same field where the P→AP transition occurs on the magnetoresistance curve at -6.5 mA (see the static phase diagram above). Inside the "C"-state region, between -100 and -400 Oe, the peaks are wide and appear at frequencies slightly lower than calculated using Kittel's formula, but, surprisingly, the fit is reasonably good (better than for high coercivity samples). Around -400 Oe, where the AP→P transition occurs on the R(H) characteristics, the precession frequency experiences a sudden increase, associated with a corresponding decrease of precession cone. For higher fields, the amplitude of the resonance peak diminishes considerably, while its frequency continues to shift towards higher values, in a fashion resembling the low field dependence.

For positive currents of the same intensity and fields lower than 300 Oe, both the magnetoresistance and the resistance versus current curves show mainly strong telegraph noise between two resistance levels which are close to those of the P and AP states (see the static characterization). Up to 300 Oe, the microwave spectra recorded at

6.5 mA demonstrate jumps between two low amplitude, wide precession modes (Fig. B.5 – 30). The lower frequency mode can be well predicted from Kittel's formula.

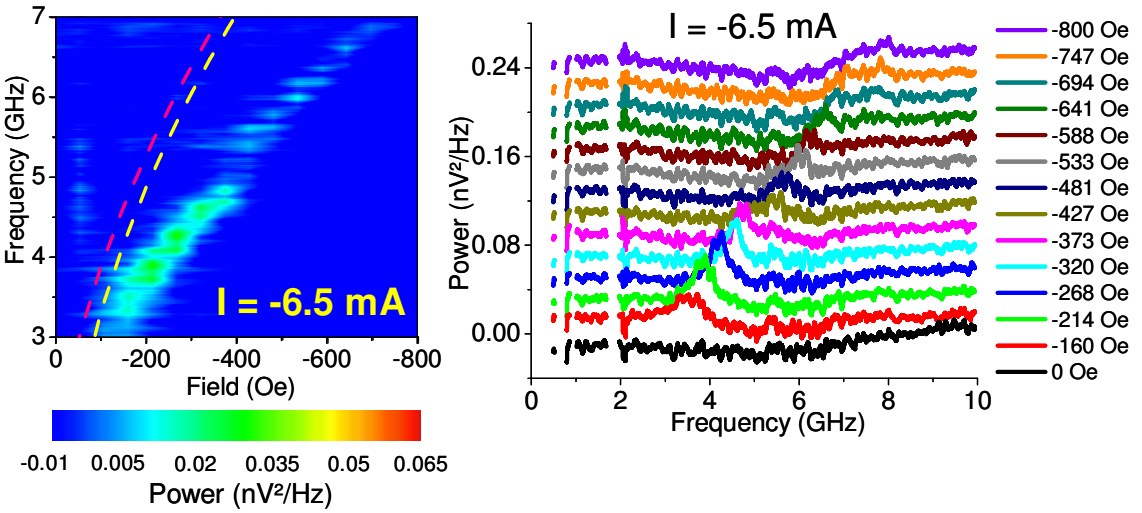

Fig. B.5 - 29 Right: Microwave spectra at -6.5 mA and different values of negative applied field. The curves have been offset for clarity. **Left:** Precession frequency versus field, with fits calculated as above.

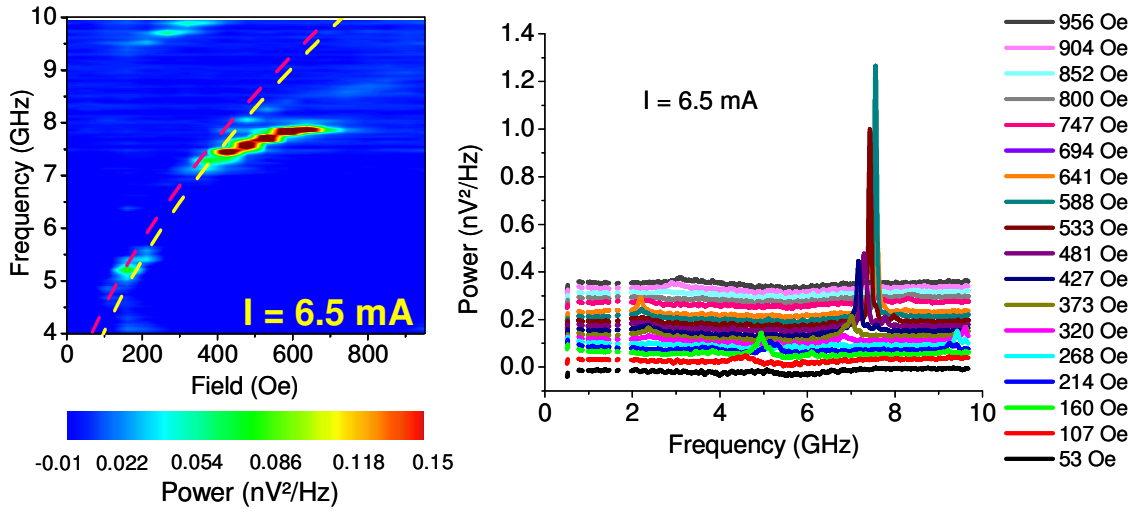

Fig. B.5 - 30 Right: Microwave spectra at 6.5 mA and different values of positive applied field. The curves have been offset for clarity. **Left:** Precession frequency dependence on the applied field and fits with Kittel's formula.

At higher fields, the spectra are dominated by a high intensity, very sharp resonance peak (40 kHz half-height width for the 7.5 GHz peak at 588 Oe, with a

maximum amplitude of 1.1 nV²/Hz reached for the same value of the field; for comparison, at negative currents of the same intensity, the maximum power of 0.03 nV²/Hz is obtained at -268 Oe, for the peak centred on 4.3 GHz, 400 MHz wide). A second low amplitude peak, considerably wider, is also present on the spectra, at slightly higher frequency than the main resonance signal. As the field is increased, less power is pumped into this second peak.

Surprisingly, although in the case of high coercivity samples the microwave spectra for similar current intensities affect principally a low-frequency (~ 1 GHz) telegraph noise peak, this signal does not appear in the case of sample 9. Moreover, the curves in fig. B.5 – 29 and fig. B.5 – 30 do not show any evidence of *1/f* noise, indicating that the precession remains more coherent than for sample 8, despite the much lower anisotropy.

The *1/f* noise appears starting from 8 mA, for both signs of the current. Essentially, once the current reaches values for which the magnetoresistance curves show reversible transitions, the behaviour of low coercivity samples becomes similar to that of high coercivity pillars, outside the coercivity area of the phase diagram.

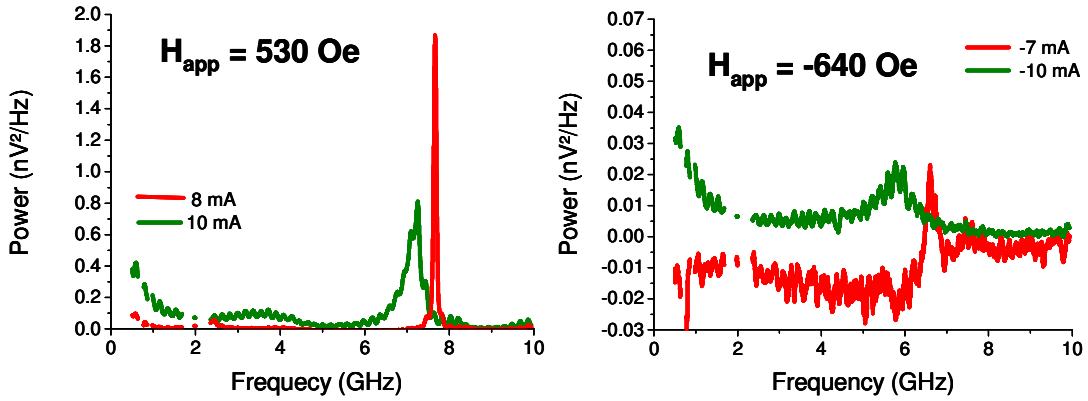

Fig. B.5 – 31 High current microwave spectra for sample 9, in the negative (**left**) and positive (**right**) quadrants of the phase diagram. The power measured at -10 mA was divided by 4, for convenience. The curves corresponding to -7 and 8 mA demonstrate the maximum attained peak amplitude for each value of the field.

Examples of microwave spectra measured at high currents and stronger fields (outside the "C"-state / static telegraph noise regions of the phase diagram) can be seen in Fig. B.5 – 31. As the current is increased over +/-7 mA, the peaks are widened and

lose amplitude; simultaneously, the *1/f* and overall noise are considerably enhanced. As for sample 8, the magnetization dynamics is less incoherent for positive than for negative currents, even at comparatively lower applied fields, demonstrated by the lower *1/f* noise and higher and sharper obtained signals. It is likely that at current intensities higher than 10 mA, the *1/f* noise would be replaced the 1 GHz peak, but experience proved that applying such voltages irreversibly damages the sample.

B.5.2.c. Discussion

The results described in the previous paragraph can be summarized as follows:

1. As long as the current is higher than the critical values but remains relatively low (before entering the "C"-state or static telegraph noise region in the negative current / negative field or positive current / positive field quadrant of the phase diagram, respectively), the trends are very similar to those observed for high coercivity samples at comparable current densities and can be understood accordingly.
2. For intermediate negative currents, corresponding to the "C"-state area of the phase diagram, only wide and very low amplitude peaks can be resolved, resembling the small angle FMR signals.
3. For positive signals of roughly the same intensity, static measurements show strong telegraph noise in the positive field region (up to 300 Oe), while dynamic experiments demonstrate jumps between two precession modes. At higher fields, the precession is remarkably coherent, more coherent than observed for high coercivity samples in any region of the phase diagram.
4. At very high currents of both signs, where the magnetoresistance curves are reversible, the behaviour is similar to that of high coercivity samples at intermediate values of the current.

Qualitatively, once the current reaches intensities where "C"-states are susceptible to appear (that is, at intermediate and high values of the current), the excited precession states are considerably more coherent than for high coercivity samples at similar currents, as if the anisotropy would be greatly enhanced (much over the anisotropy of sample 8, for example). A "C"-state is a very stable configuration, as demonstrated by its important coercivity, and higher currents are required to induce

chaotic dynamics. As such, the *1/f* noise appears only on the spectra recorded for currents of at least +/-8 mA in the case of sample 9, as compared with +/-4 mA for sample 8. For the high coercivity pillar, the *1/f* noise is replaced by the high power low frequency peak for currents of the order of +/-7 mA. If the same trend is follow, for sample 9 such signals should appear around +/-14 mA, but no spectra were measured for currents higher than +/-10 mA, so as not to damage the sample.

At -6.5 mA, the spin-torque is still too weak to overbalance the enhanced anisotropy, and the spectra show only small angle precession signals, with a cone angle that is progressively reduced as the field increases, as expected.

Interestingly, the dynamics seems considerably more coherent for positive than for negative currents of the same intensity (+/-6.5 mA). This disparity, which ceases in very high fields, cannot be explained by the difference in the Oersted field, since its amplitude is independent of the sign of the current. As explained in the paragraph discussing precession trends in high coercivity samples, another possible source of incoherence in the negative current / negative field quadrant of the phase diagram is the magnetostatic interaction from the reference layer. Indeed, the dipolar coupling can be highly non-uniform in the free layer, much stronger at the edges of the pillar than in the centre. Negative applied fields oppose the magnetostatic interaction, since they favour the parallel orientation of the magnetization of the free layer with respect to the moment of the reference layer. Consequently, as long as the magnitude of H_{app} does not overcome the dipolar field at the edges of the sample, the total field in the centre and at the borders will be oriented in opposite directions, resulting in an increase of incoherence.

This might also be a possible explanation for the comparatively more incoherent dynamics observed for high coercivity samples, since most of the high H_c pillars showed also a much stronger magnetostatic interaction between the free and the reference layers (for example, H_{ms} = 104 Oe for sample 8, as compared to H_{ms} = 21 Oe for sample 9). Moreover, the high coercivity pillars have generally a smaller cross-section that the low H_c samples, and consequently are less susceptible to the influence of the Oersted field and to higher anisotropy “C”-states formation.

At -9 Oe, sample 8 exhibited a transition from small angle to large angle precession at approximately 4.5 mA, reflected by the second transition on the R(I) curves. In the low coercivity sample, for similar or higher currents, a very stable "C"-state is formed in the free layer. At 6.5 mA and fields higher fields than 300 Oe, the system enters a stable configuration close to the AP state. Small angle precessions are thus induced, similar to what could be observed at lower positive currents and fields (2 mA and 53 Oe). As the current is more than three times larger, the power, which varies as I^2, is about ten times higher. In other words, the presence of the stable "C"-state acts as an increased anisotropy, extending the small angle precession region to larger currents and generating resonance peaks with high power and high quality factors in the positive current / positive field quadrant of the phase diagram.

Though the hypothesis exposed above qualitatively explains our data, micromagnetic calculations should to be carried out in order to verify whether this suggestion is quantitatively accurate. Micromagnetic modelling might also possibly account for details of the experimental results which remain poorly understood to-date – such as the coexistence of multiple precession modes displayed by low coercivity pillars for positive fields and intermediate positive currents. Due to the high Q, high power signals obtained in the positive quadrant of the phase diagram, current induced precession in very low H_c samples, if well understood, might prove more interesting for applications than the commonly investigated high (shape) anisotropy systems.

B.5.3. Precession states of the reference layer

Both samples described above, as well as all the other investigated pillars, exhibited an area of increased power (intermediate resistance level) in the negative current / positive field quadrant (bottom-right corner) of the phase diagram (Fig. B.5 – 32). The microwave spectra recorded in this region demonstrate very high amplitude, sharp peaks, which shift towards lower frequencies as the current or the field are increased (Fig. B.5 – 33 and Fig. B.5 – 34). While, as seen in part A, chapter 4, paragraph A.4.2.b (fig. A.4 – 14), this dependence is expected for spin-transfer induced magnetization precession in certain ranges of applied current, the frequency drop when

increasing the field is rather surprising. Even more, this quadrant actually corresponds to a stable AP state from the point of view of the free layer, since both the torque exerted by the field and that generated by the current tend to orient the magnetization of the free layer antiparallel with respect to the moment of the reference layer. Consequently, the resolved signal cannot be understood as any current or field induced dynamics excited in the free layer.

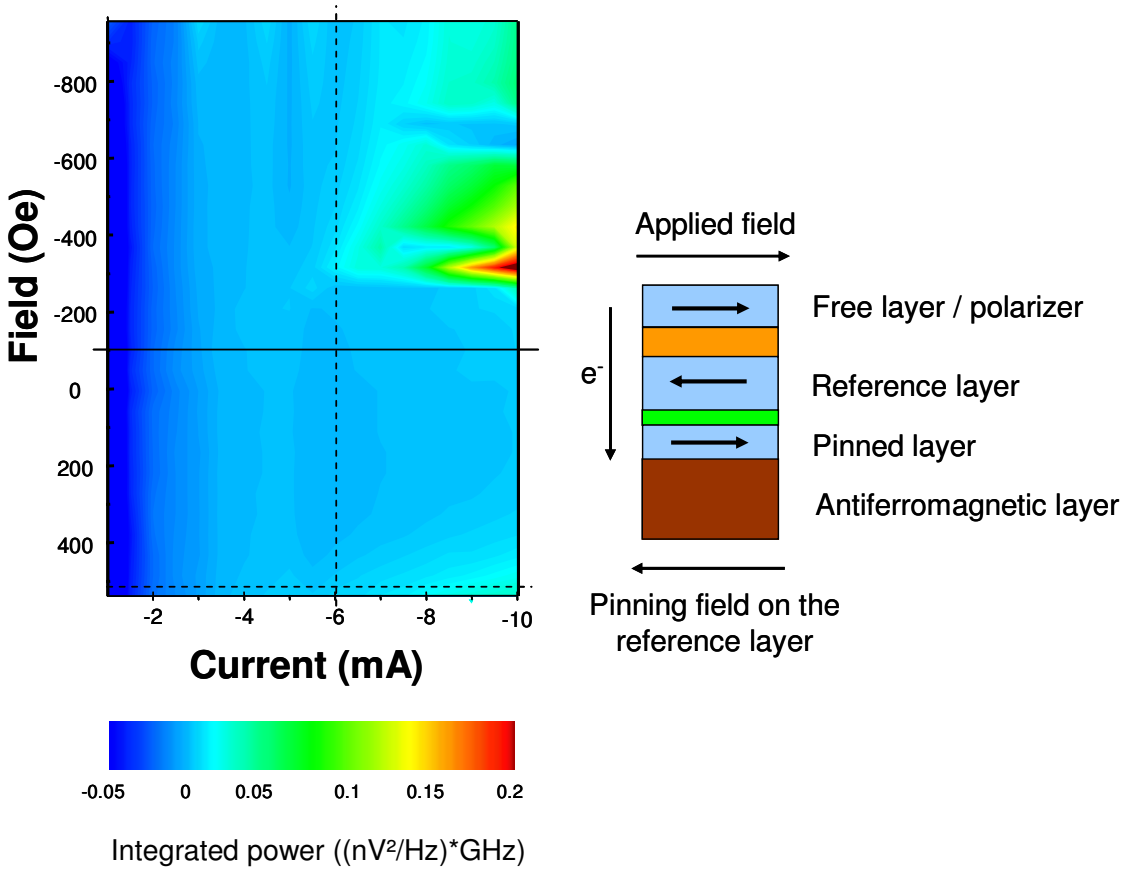

Fig. B.5 - 32 Right: Negative current phase diagram of sample 8, showing an area of increased power in the bottom-right corner. The dotted lines indicate the current (vertical line) and field values (horizontal line) where the spectra in Fig B.5 – 33 and Fig B.5 – 34 were measured, respectively. **Right:** Schematic drawing of the current / field configuration in the previously mentioned region of the phase diagram, from the point of view of the reference layer.

From the point of view of the reference layer, however, *considering the free layer as a polarizer*, the negative applied current (with electrons flowing from the free to the reference layer) generates a torque which acts so as to rotate the

magnetic moments of the reference layer parallel to the magnetization of the polarizer. The positive applied field is oriented against the pinning direction, and remains lower than the pinning field in all the investigated region of the phase diagram. **Consequently, the total field acting on the reference layer (defined as the algebraic sum $H_{pinning} + H_{applied}$) is negative and favours the antiparallel alignment between the reference and the free layer, if the free layer is considered fixed along the applied (positive) field direction. As such, for the pinned layer, the current and the field have opposite effects in this quadrant, and current induced precession may occur.**

As the positive applied field is increased between 0 and 550 Oe, the (negative) total field is diminished and consequently the precession frequency is decreasing. The first signal is resolved at 375 Oe around 6.25 GHz; as the applied field approaches the maximum applied value, the peak shifts to 5.7 GHz. Fig. B.5 – 33 also shows for comparison the small angle FMR frequencies calculated with Kittel's formula (yellow dotted line), since, as seen in Fig. B.5 – 34, at I = -5 mA, the magnetization dynamics remains in the small angle precession region. For the theoretical fit, the "coercivity" of the pinned layer was taken to be half the difference between the fields where the two sharp transitions attributed to the (partial) reversal of the pinned layer occurred in Fig. B.5 – 3, d. The "pinning" field was approximated to the shift of the loop. The value used for the demagnetizing field was the same as for the free layer, H_d = 16000 Oe. Though altogether this is a very rough approximation, not only because the values used for H_p and H_c are not necessarily very precise, but especially since the synthetic antiferromagnetic reference layer is modeled as a normal CoFe film, it proves that current-induced precession in the pinned layer can be understood in the same way as spin-transfer induced dynamics in the free layer.

At a constant applied field, the evolution of the precession frequency with the current is similar to that predicted by the macrospin model between 1.35 × I_c and 1.55 × I_c (see fig. A.4 – 14 for comparison). As the current is increased between -1 and -5.5 mA, the peak amplitude is considerably enhanced, but no obvious frequency shift occurs. Between -6 and -9 mA, the precession remains remarkably coherent, as the peak shifts gradually towards lower frequencies. The maximum intensity, obtained at 483 Oe and -9 mA (5.3 nV²/Hz), is about twice higher than maximum signal amplitude

measured for precession states in the free layer for sample 9 (see the previous paragraph). Like in the case of current induced precession in the free layer, increasing the current above -9 mA eventually leads to significant amplitude drop and widening of the main peak, as the *1/f* and overall noise become more important, reflecting an increasing incoherency of the magnetization dynamics.

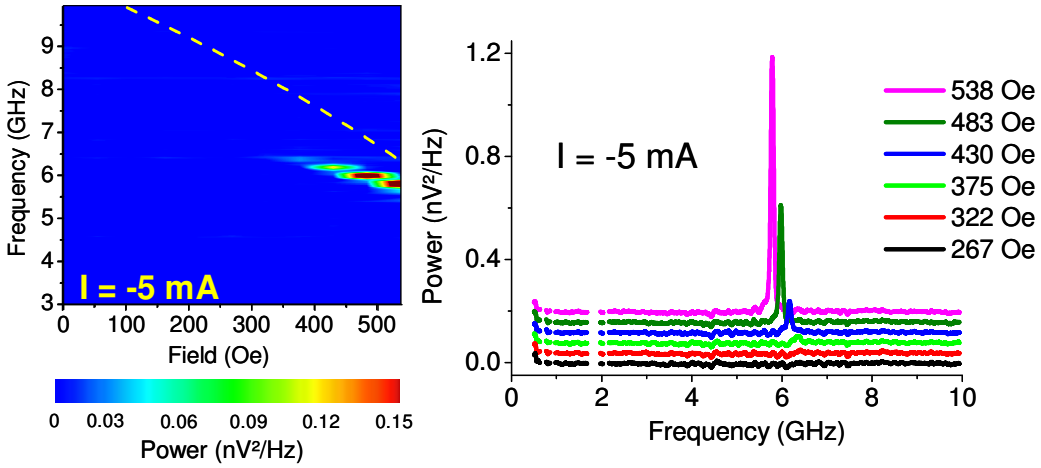

Fig. B.5 - 33 Peak frequency dependence on the applied field, for current induced precession in the pinned layer. The curves have been offset for clarity. The positive applied field is oriented opposite to the pinning direction, so that the total field acting on the pinned layer is decreasing when the applied field increases. The yellow dotted line gives the fit with Kittel's formula, using the "pinning" field H_p = -740 Oe and "coercivity" H_c = 110 Oe, as explained in the text, and a demagnetizing field H_d = 16000 Oe.

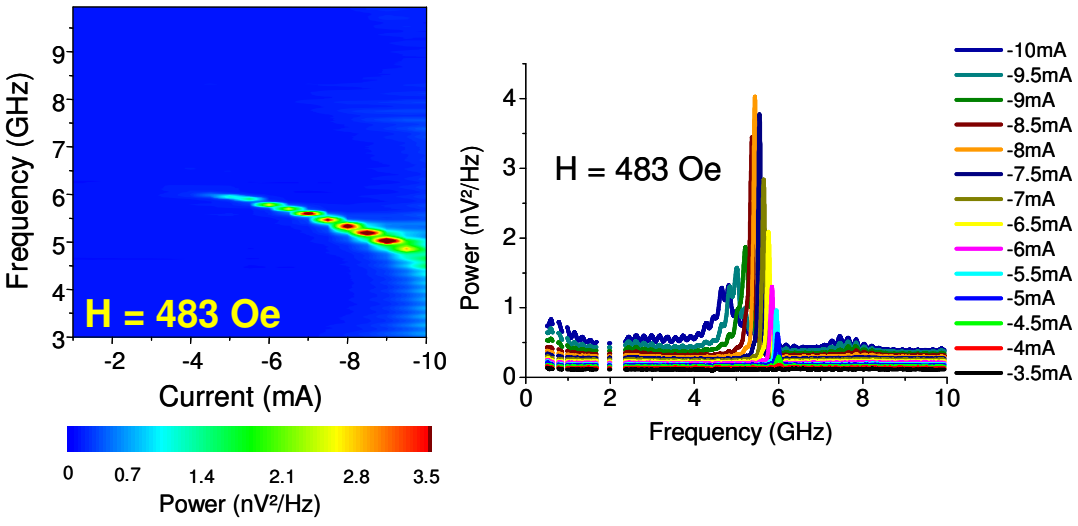

Fig. B.5 - 34 Peak frequency dependence on the applied current for current induced precession in the pinned layer. The curves have been offset for clarity.

Though this is the first unarguable evidence for such phenomena, several other studies have previously suggested that current induced effects on the reference layer cannot be ignored, even in simple spin-valves with a very thin free layer (much thinner than the spin diffusion length in the respective magnetic material) [11]. In the *Headway* samples, the thickness of the free layer is about three times larger than SDL. Calculating the spin currents as explained in chapter 4 (considering the reference layer as non-magnetic this time), the longitudinal polarization at the interface between the spacer and the reference layer is evaluated to be around 0.314 for a structure "a" nanopillar (Fig. B.5 – 35). For comparison, for the same structure and using the same approach, the polarization generated by the reference layer at the interface between the spacer and the free layer is estimated to be almost twice lower (~0.166, see chapter 4). Therefore, spin-transfer effects in the reference layer will be by far stronger than in the free layer, and may overcome the pinning field which reaches a maximum of 1200 Oe for all the investigated samples. It is possible, though, that pinning opposes chaotic dynamics excitation, insuring a higher degree of precession coherency, as compared with spin-transfer induced dynamics in the free layer.

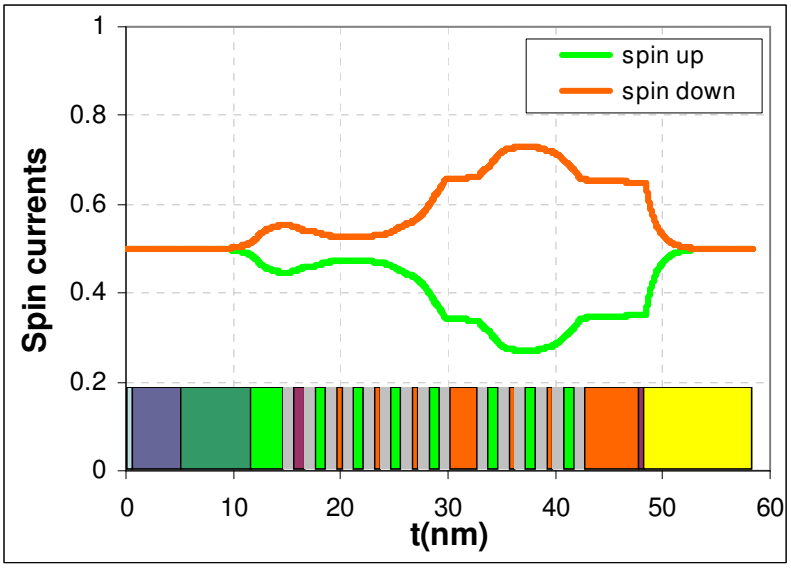

Fig. B.5 – 35 Spin-currents as a function of thickness, calculated for a nanopillar of structure "a" using the code of Strelkov et al., and considering the reference layer as non-magnetic.

No evidence was found for current-induced precession of the pinned layer, in the opposite current / field (negative field and positive current). This is, however, not

surprising, since the negative field is oriented along the pinning field, so that the total field acting on the magnetization of the pinned layer is considerably higher in than in the opposite quadrant of the phase diagram (positive field and negative current). Moreover, for positive currents, the electrons flow from the reference to the free (polarizing) layer, trying to switch the moment of the reference layer antiparallel with respect to the (supposedly fixed) free layer, so that the spin-torque is weaker ($g(0) < g(\pi)$, see chapter 4) and cannot compensate the effect of the increased total field.

Finally, though the quality factor is lower for the signals attributed to precession states in the reference layer (the best value was Q = 80, when a maximum Q = 185 was found for sample 9), the intensity of the peaks is considerably higher and the spectra are far less complicated than for the low coercivity samples. As such, it might be worth pursuing a systematic study of current induced precession in pinned layers, in view of possible applications for microwave oscillators.

B.5.4. Conclusion

Current induced magnetization dynamics was investigated for both signs of currents and fields, for frequencies up to 10 GHz. For samples with high coercivity free layers, the trends are similar with those of simple spin-valves and can be well understood using micromagnetic simulations. At intermediate and high currents, low coercivity samples show more coherent dynamics than high coercivity pillars, possibly as a consequence of the formation of a very stable "C"-state in the free layer, acting as an increased anisotropy.

Low coercivity pillars usually have larger cross-section and lower magnetostatic interaction between the layers. Because of the higher lateral size, Oersted fields are more important; the joint effect of equivalent Oersted and applied field leads to "C"–state formation, which generates more coherent dynamics. Dipolar coupling increases the incoherency in the negative field / negative current quadrant, as the negative field opposes the magnetostatic interaction. On the other hand, the (spatially inhomogeneous) dipolar coupling is larger in high coercivity pillars, so the dynamics is comparatively more chaotic.

The precession is generally more coherent for positive than for negative currents, for both types of pillars. Low coercivity pillars present considerable amplitude, high quality factor peaks in positive currents, but the dynamics is complicated, with multiple precession modes.

Very coherent precession states, generating high power signals, could be demonstrated in the pinned layer, when the field is applied against the pinning direction. It is possible that pinning insures a more coherent dynamics of the local moments. Investigating current induced magnetization precession in pillars with two pinned magnetic layers might be interesting for microwave oscillators applications.

Resumé :

Les états de précession induits par le transfert de spin dans des multicouches pour têtes CPP- GMR ont été étudiés pour les deux polarités des courants et des champs appliqués, et pour des fréquences allant jusqu'à 10GHz. Les états de précession entretenue apparaissent dans les zones du diagramme de phase où il n'existe aucun minimum d'énergie (c'est-à-dire, pour des champs plus forts que le champ d'anisotropie, et des courants plus forts que les courants critiques, favorisant des alignements opposés). Les tendances générales sont similaires aux celles mises en évidence dans les piliers simples de type Co/Cu/Co, et peuvent être comprises en faisant appel à des simulations micromagnétiques. En champ faible, quatre régimes de précession peuvent être mis en évidence, en fonction du courant appliqué: précession de faibles angles de type FMR (aux courants faibles), précession de grands angles, où l'aimantation reste principalement dans le plan de la couche, bruit télégraphique de hautes fréquences, dû à des sauts chaotiques des moments locaux entre deux trajectoires de précession possibles (aux courants intermédiaires), et finalement un régime marqué par un création/annihilation dynamique des états vortex aux courants forts. (Le dernier régime n'a pas été mis en évidence dans ces échantillons, qui ne supportent pas les courants requis.) L'incohérence augmente avec le courant. Dans les régimes de précession FMR et de précession de large angle dans le plan de la couche, la dynamique est plus cohérente quand le champ appliqué renforce l'interaction magnétostatique entre les couches et le courant favorise l'orientation parallèle que dans la configuration champ/courant opposé.

Comme suggéré déjà par les résultats des mesures statiques, la dynamique des moments locaux est plus compliqué dans le cas des échantillons à faible coercivité, pour lesquels les effets des différents champs locaux inhomogènes sont plus importants.

On a aussi mis en évidence des états de précession dans la couche piégée synthétique, beaucoup plus cohérents que la dynamique de la couche libre.

References :

[1] J.-G. Zhu and X. Zhu, IEEE Trans. Magn. **40**, 182 (2004)

[2] J.Z. Sun Phys. Rev. B **62**, 570 (2000)

[3] Z. Li and S. Zhang, Phys. Rev. B **69**, 134416 (2004)

[4] C. Kittel, *Introduction to Solid State Physics* 7th edition, 505 (Wiley, New-York, 1996)

[5] M.P. Sharrock, IEEE Trans. Magn. **26**, 1193 (1990)

[6] W.F. Brown, Phys. Rev. **130**, 1677 (1963); IEEE Trans. Magn. **15**, 1196 (1979)

[7] S.I. Kiselev et al., Nature **425**, 380 (2003)

[8] K.J. Lee et al., Nature Mat. **3**, 877 (2004)

[9] F.C. Moon, *Chaotic and Fractal Dynamics* 29 (Wiley, New-York, 1998)

[10] M. Pufall et al., Phys. Rev. B **69**, 214409 (2004)

[11] an example is B. Ozyilmaz et al., arXiv:cond-mat/0407210 (2004)

Chapter 6. Conclusions and perspectives

For the first time, spin-transfer induced effects (switching and magnetization dynamics) were investigated for both signs of currents and fields, for four types of spin-valves developed for CPP-GMR heads, with slightly different structures. The samples had laminated magnetic layers, exchange biased synthetic antiferromagnetic reference layers, free layers several times thicker than SDL and square cross-section with a lateral size of the order of 100 nm (and thus no uniaxial shape anisotropy). Though both in static and dynamic experiments the general trends are found to be qualitatively similar to those of the long analysed Co/Cu/Co pillars, some aspects were rather unexpected and should be considered when attempting applications (towards microwave oscillators, for example). Paragraph B.6.1 gives a (very) brief overview of the main results of this study; possible further developments are discussed in paragraph B.6.2.

B.6.1. Conclusions

Strong spin-transfer effects – current induced magnetization switching or precession – were observed in very complicated spin-valves developed for CPP-GMR heads. Although the polarizing layer was considerably thinner than those used in previously published experiments, lamination insured that a high current polarization could be attained in its vicinity. As in simple pseudo spin-valves, the switching current densities are of the order of 10^7 A/cm².

Generally, spin-transfer effects are stronger in the antiparallel than in the parallel configuration (for positive than for negative currents, where positive currents are defined as electrons flowing from the reference to the free layer). In static measurements, more (telegraph) noise appears for positive currents. For the same sign of the current, frequency dependent experiments proved that current induced precession is generally more coherent.

Plotting the static phase diagrams on reduced coordinates seems more appropriate for comparing samples with different size, coercivity, and dipolar coupling between the layers.

Low coercivity pillars usually have larger cross-section and lower magnetostatic interaction between the layers. Because of the higher lateral size, Oersted fields are more important. The joint effect of equivalent Oersted and applied fields leads to "C"–state formation, which generates an increased coercivity area in the negative current / negative field quadrant of the phase diagram, as well as more coherent dynamics in microwave experiments. Dipolar coupling increases the incoherency in the negative field / negative current quadrant, as the negative field opposes the magnetostatic interaction. On the other hand, the (spatially inhomogeneous) dipolar coupling is larger in high coercivity pillars, so the dynamics is comparatively more chaotic. At intermediate and high currents, low coercivity samples show more coherent dynamics than high coercivity pillars, possibly as a consequence of the formation of a very stable "C"-state in the free layer, acting as an increased anisotropy. For positive currents, low coercivity pillars present considerable amplitude, high quality factor peaks, but the dynamics is complicated, with multiple precession modes.

For the first time, very coherent precession states, generating high power signals, could be demonstrated in the pinned layer, when the field is applied against the pinning direction. It is possible that pinning insures a more coherent dynamics of the local moments.

Experimental results show that when replacing Cu with Ag as laminating material, the measured magnetoresistance is decreasing, as well as the switching current asymmetry, while the critical currents themselves are enhanced. The data can be reasonably well interpreted using CPP-GMR calculations based on the extension of Valet-Fert theory to any type of multilayers, assuming that the interfacial scattering asymmetry between Ag and CoFe is lower than in the case of Cu and CoFe. By calculating the current polarization at the interface between the spacer and the free layer and introducing it into Slonczewski's simple formula for $g(\theta)$, it is possible to explain the enhancement of the switching currents and the decrease in their asymmetry as being related to a drop of spin polarization at the interface.

B.6.2. Perspectives

Quite apart from micromagnetic simulations which should be carried out so as to elucidate the details of the dynamic behavior obtained for the two polarities of currents and fields, as well as the low H_c pillars behavior, possible applications-oriented further developments fall into one of the following categories:

1. Solutions aiming to minimize the noise caused by spin-transfer in CPP-GMR heads and propose a CPP-GMR read head architecture which is not affected by spin induced parasitic noise (paragraph B.6.2.a);
2. Suggestions on device architectures which would maximize the output power and thus be of interest for eventual applications to new microwave oscillators.

B.6.2.a. Reducing spin-transfer effects in CPP-GMR heads

Regarding the minimization of noise in CPP-GMR heads, a possible solution would be the increase of critical currents up to values higher than those required for the functioning of the head. As such, no unwanted noise would appear in these devices as a consequence of spin-transfer induced phenomena.

The critical current density necessary to observe spin-transfer effects is proportional to the thickness of the magnetic layer and to the damping constant. Consequently, the switching currents can be augmented by increasing one or both previously mentioned parameters. On the other hand, increasing any of these factors will modify other important characteristics of the read head (magnetoresistance, coercivity…), and great care should be taken for them to remain within reasonable ranges for such applications.

The **damping factor** can be altered by laminating the layer or by introducing impurities [1] (Fig. B.6 – 1). The structure of the head may contain laminated layers, but the effect of the lamination on the damping has not yet been investigated.

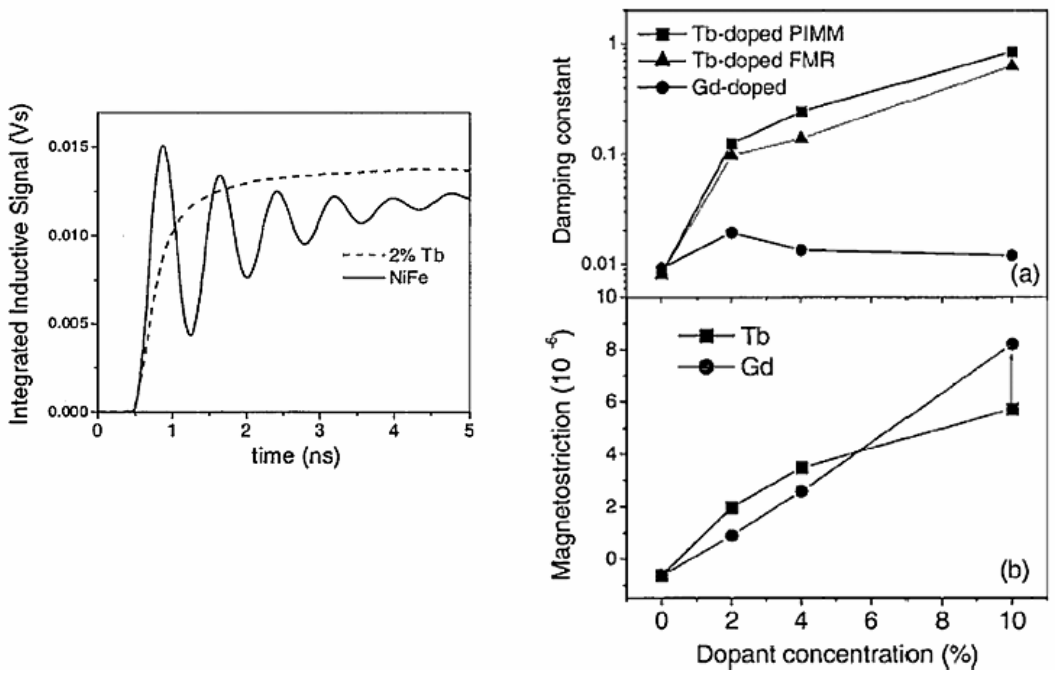

Fig. B.6 - 1 The damping constant of Permalloy can be increased with two orders of magnitude when introducing Tb impurities. (Extracted from ref. [1]).

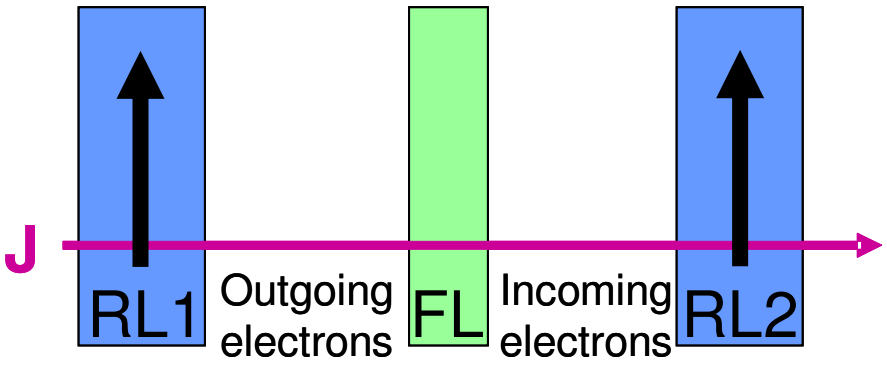

Fig. B.6 - 2 In structures consisting in two reference layers oriented parallel to each other, placed on each side of the free layer, the spin-transfer effect of the in-coming polarized electrons is expected to (partially) cancel that of the out-going spins.

Another approach for reducing spin-transfer in CPP-GMR heads consists in defining structures where these effects cancel. The entire multilayer structure determines the polarization of the current and the spin accumulation. Introducing a

second pinned layer, so that the free layer is in the middle and the magnetizations of the two pinned layers are parallel, should reduce the spin-torque induced effects in the free layer, and therefore the noise in CPP-GMR heads. The spin-torque exercised by the spin polarized electrons arriving from one pinned layer should (partially) cancel that resulting from spin accumulation between the free layer and the other pinned layer (Fig. B.6 – 2).

B.6.2.b. Spin-transfer for microwave oscillators

In the last year, the study of spin-transfer effects has become one of the most important research fields in magnetism, mainly motivated by their possible application towards microwave oscillators. For such devices, an increased output power and quality factor Q are required. The former depends on the precession cone and Q is strongly related to the coherency of the precession. It is therefore essential to find systems with a high degree of coherency.

Starting from the experimental results exposed in chapter 5, several useful points for achieving more coherent dynamics may be put forward. First, spin-transfer is larger and precession is more coherent for the opposite current / field configuration than commonly investigated in Co/Cu/Co pillars: the field (current) should be applied so as to favor the AP (P) state. Consequently, it is necessary to pin the reference layer, so as to insure that it does not switch under the effect of the field. Second, it has been shown that considerably higher peak amplitudes can be attained when exciting precession states in the pinned reference layer. A possible novel architecture for microwave oscillators could consist in a structure containing two magnetic layers oriented antiparallel to each other, both pinned by antiferomagnetic layers of different thickness or composition (Fig. B.6 – 3). The pinning field on the first pinned layer (resonator) should not be too high, so as not to inhibit any current induced precession that may be generated, but only to reduce the incoherency of the dynamics. It may prove interesting to use two synthetic antiferromagnetic layers as polarizer and resonator, or an unpatterned polarizer, in order to reduce the magnetostatic interaction which reinforces the pinning field and therefore enhances the currents required to generate magnetization

precession. To obtain a maximum current polarization, the thickness of the ferromagnetic layers should be optimized with respect to SDL.

An interesting aspect will be the study of multilayers including a polarizer and a resonator with magnetizations pinned in non-collinear directions.

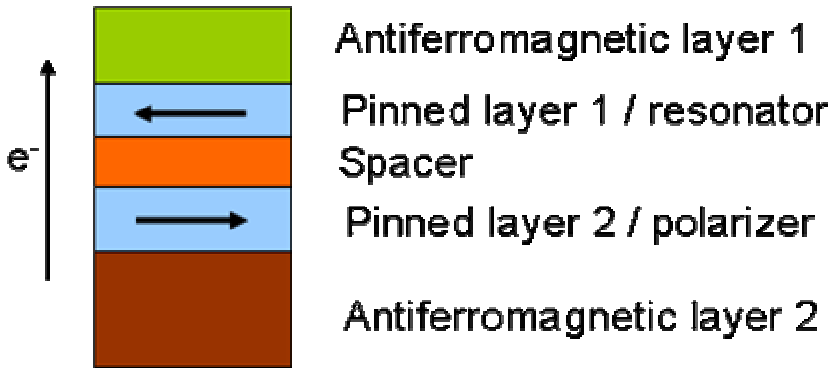

Fig. B.6 - 3 Schematic drawing of the proposed structure for microwave oscillators applications.

Conclusions et perspectives

Pour la première fois, les effets de transfert de spin (renversement et dynamique de l'aimantation) ont été étudiés dans des vannes de spin complexes, pour les deux polarités des champs et courants appliqués. Les échantillons contenaient des couches magnétiques laminées et couches synthétiques piégées par échange. Les piliers était de section circulaire (donc sans anisotropie de forme), avec un diamètre de l'ordre de 100nm. Globalement, les mesures statiques et dynamiques démontrent des comportements similaires à ceux mis en évidence dans des échantillons simples Co/Cu/Co, étudiés en détail par des différents groupes. Néanmoins, certains résultats sont plutôt inattendus et pourraient être exploités pour fabriquer des oscillateur RF basés sur le transfert de spin.

Le paragraphe B.6.1 résume les conclusions les plus importantes de cette étude et quelques directions possibles pour la poursuite de cette analyse sont synthétisées dans le paragraphe B.6.2.

B.6.1. Conclusions

Des effets de transfert de spin importants (renversement ou précession entretenue de l'aimantation, excités par un courant polarisé) on été observés dans des vannes de spin complexes, développés pour des têtes CPP-GMR. Même si le polariseur est beaucoup plus fin que dans les études précédentes, une polarisation importante du courant peut être atteinte à l'interface entre le polariseur et la couche libre, grâce à la lamination qui a pour conséquence une réduction de la longueur de diffusion de spin dans la couche respective. Comme dans les échantillons Co/Cu/Co, les densités de courants nécessaires au renversement sont de l'ordre de $10^7 A/cm^2$.

En général, dans les structures analysées, les effets de transfert de spin sont plus fort pour les courants positifs que pour des courants de signe opposé (où les courant positifs sont définis comme électrons qui se déplacent de la couche de référence vers la

couche libre, et donc favorisent l'état parallèle). Les mesures statiques mettent en évidence plus de bruit télégraphique pour le sens positif du courant. Pour la même configuration, les mesures hyperfréquence démontrent une dynamique plus cohérente des moments magnétiques locaux.

Pour comparer des échantillons avec des différentes tailles, coercitivités ou interactions dipolaires entre les couches, il est plus utile de tracer les diagrammes de phase en coordonnées réduites (densité de courant et champ total normalisé par rapport au champ coercitif).

Entre les piliers étudiés, ceux à faible coercitivité ont généralement une section plus importante et une plus faible interaction magnétostatique entre les couches. Un diamètre plus large implique des champs d'Oersted plus forts ; en fonction du champ et du courant appliqué, sous l'action simultanée du champ d'Oersted et du champ externe il est possible d'induire la formation des états « C » dans la couche libre. Ceci se traduit par l'apparition des zones de coercitivité augmenté sur les diagrammes de phase statiques, ainsi que par une dynamique plus cohérente démontrée par des mesures hyperfréquence.

L'interaction dipolaire entre les couches augmente l'incohérence de la dynamique dans le quadrant champ négatif / courant négatif du diagramme de phase. Au même temps, l'interaction magnétostatique est plus importante dans les échantillons à forte coercitivité, ce qui se traduit par une dynamique plus chaotique des moments locaux, en courants relativement faibles (régimes de précession FMR et précession de large angle dans le plan de la couche). Pour des courants intermédiaires et forts, les échantillons à faible coercitivité montrent une dynamique plus cohérente, ce qui pourrait être expliqué par la formation d'un état « C », agissant comme un anisotropie accrue. En courant positif, les spectres mesurés pour ces piliers présentent des pics de forte amplitude et facteurs de qualité importants, mais la dynamique est complexe, avec des modes de précession multiples.

Pour la première fois, nous avons mis en évidence des états de précession très cohérente excitée par le courant polarisé dans la couche piégée synthétique, quand le champ externe s'oppose au champ d'échange. Il est possible que l'amélioration de la cohérence soit une conséquence du blocage.

Les mesures prouvent qu'en remplaçant le cuivre par de l'argent comme matériau de lamination, la magnétorésistance et l'asymétrie des courants de

renversement décroît, pendant que les courants critiques augmentent. Ces résultats peuvent être interprètes en faisant appel à des calculs de type CPP-GMR, basés sur une extension du modèle Valet-Fert pour toutes multicouches, et en supposant que l'asymétrie de diffusion entre Ag et CoFe est plus faible que dans le cas de Cu et CoFe. Si on calcule la polarisation du courant à l'interface entre l'espaceur et la couche libre et on introduit cette valeur dans la formule balistique de Slonczewski pour g(θ), il est possible d'expliquer l'augmentation des courants critiques et la perte d'asymétrie comme liées à une réduction de la polarisation du courant à l'entrée dans la couche libre.

B.6.2. Perspectives

Mis à part les simulations micromagnétiques qui pourraient éclaircir différents détails du comportement des échantillons à faible coercitivité, et les études expérimentales complémentaires visant à expliquer l'amélioration de la cohérence dans les couches piégées, on peut suggérer deux directions d'étude orientées vers les applications, notamment :

1. *Etudes ayant pour but la diminution du bruit induit par le transfert de spin dans les têtes CPP-GMR ;*
2. *Etudes portant sur les modalités de maximiser la puissance de sortie et le facteur de qualité des signaux pour des oscillateurs RF.*

B.6.2.a. Réduire les effets de transfert de spin dans les têtes CPP-GMR

Une modalité de réduire le bruit induit par le transfert de spin dans les têtes CPP-GMR serait d'augmenter les courants critiques au-dessus des courants de fonctionnement de ces dispositifs.

La densité de courant nécessaire pour produire des effets de transfert de spin observables est proportionnelle à l'épaisseur de la couche libre et à l'amortissement. Il est donc possible d'accroître les courants de renversement en augmentant un de ces

paramètres ou les deux simultanément. Par ailleurs, la variation de ces facteurs pourrait jouer sur d'autres paramètres importants pour les têtes de lecture (tels que la GMR, la coercitivité, etc), qui devraient garder des valeurs acceptables pour ce type de dispositifs.

La constante d'amortissement peut être augmentée en introduisant des impuretés (Fig. B.6 – 1). L'effet de la lamination sur l'amortissement n'a pas été étudié, mais il est probable qu'il agisse dans le même sens.

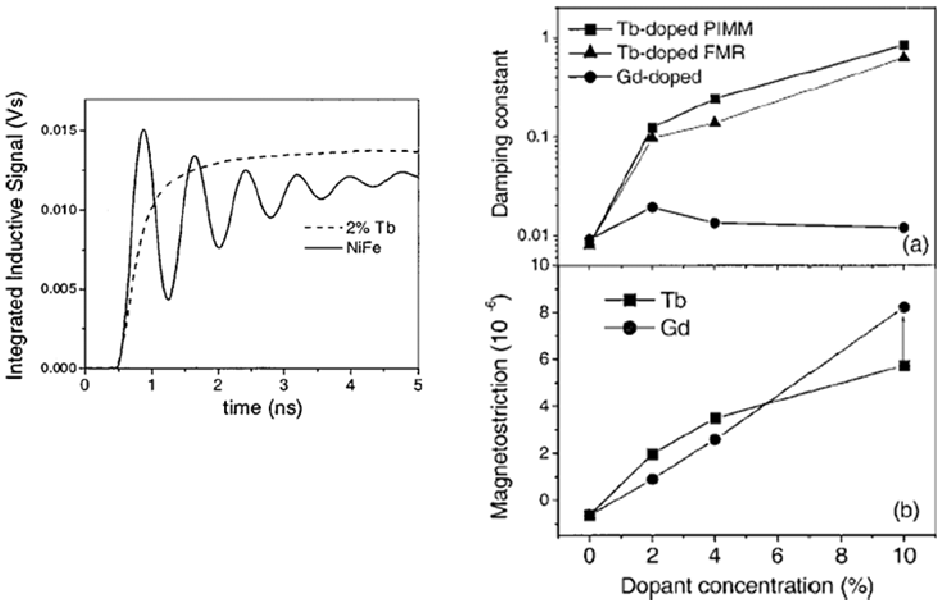

Fig. B.6 – 1 *La constante d'amortissement du NiFe peut être augmenté de deux ordres de grandeur en introduisant des impuretés de Tb.*

Une deuxième modalité de réduire le bruit induit par le transfert de spin dans les têtes serait de fabriquer des structures dans lesquelles ces effets s'annulent, comme dans des vannes de spin duales, où la couche libre se trouve entre deux couches piégées dont les aimantations sont parallèles (Fig. B.6 – 2). Dans des telles structures, le transfert de spin entre les électrons qui arrivent d'une des couches piégées et la couche libre devraient être compensé par l'accumulation de spin entre cette couche et la deuxième couche piégée.

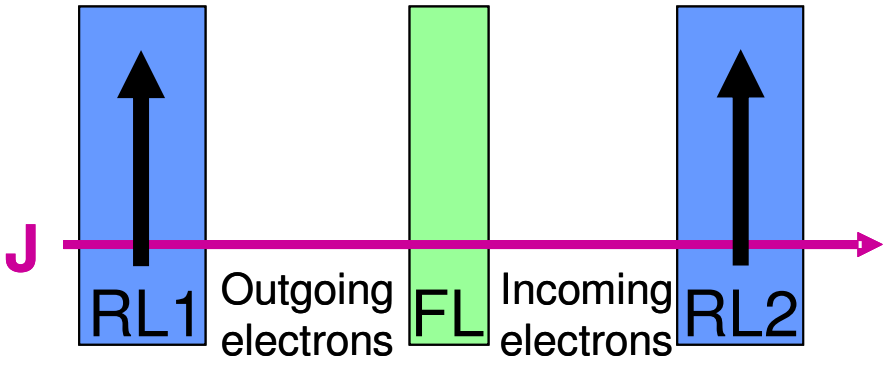

Fig. B.6 – 2 *Dans des structures contenant deux couches piégées dans la même direction, les effets de transfert de spin sur la couche libre devrait s'annuler (au moins en partie).*

B.6.2.b. Transfert de spin pour les oscillateurs RF

Dernièrement, la recherche dans le domaine des effets de transfert de spin s'oriente plutôt vers les oscillateurs RF pour télécommunications mobiles. Pour en fabriquer de tels dispositifs, il est nécessaire d'atteindre des fortes puissances de sortie, ainsi que des facteurs de qualité élevés. Ces deux paramètres sont liés à la cohérence des mouvements de précession des moments individuels. Un aspect important est donc de trouver des systèmes de haute cohérence.

À partir des résultats expérimentaux exposés dans le chapitre 5 de la partie B, on peut suggérer plusieurs modalités d'atteindre une dynamique plus cohérente des moments locaux.

Premièrement, le transfert de spin est plus important dans l'état AP, est la précession est moins chaotique quand le champ appliqué favorise cet alignement et le courant l'état opposé, que dans la configuration champ/courant contraire (qui est généralement étudiée dans les échantillons Co/Cu/Co). En conséquence, il est nécessaire de bloquer la couche de référence, pour que son aimantation ne se renverse pas sous l'effet du champ externe.

Deuxièmement, on a montré que des signaux d'amplitudes considérablement plus élevées sont obtenues en excitant des précessions de la couche piégée. Une

nouvelle architecture pour des oscillateurs RF pourrait contenir deux couches dont les aimantations sont antiparallèles, piégées avec des champs de blocage différents (Fig. B.6 – 3). Le champ d'échange sur la première couche (nommée « résonateur ») devrait être plus faible, de façon à ne pas inhiber la précession induite par le courant polarisé, mais seulement d'augmenter sa cohérence. Il pourrait être intéressant d'utiliser de couches synthétiques, ou de laisser le polariseur non gravé, pour réduire l'interaction magnétostatique entre les couches, qui est parallèle au champ d'échange et donc augmente les courants nécessaires pour générer la précession. L'épaisseur des couches magnétiques devrait aussi être optimisé par rapport à la longueur de diffusion de spin pour maximiser la polarisation du courant.

Un dispositif RF particulièrement intéressant à étudier pourrait aussi contenir deux couches piégées dans des directions quelconques, dans ou en dehors du plan des couches.

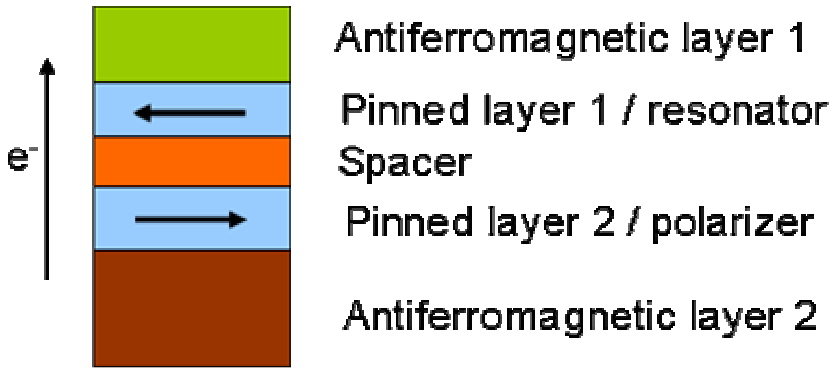

Fig. B.6 – 3 *Schéma de la structure proposée pour oscillateurs RF basés sur le transfert de spin.*

Reference :

[1] S.Russek et al, J. Appl. Phys. **91**, 8659 (2002)

ANNEX:

Parameters used for the CPP-GMR calculations

(Part B, Chapter 4)

i) Structure "a"

	Material	ρ	β	γ	r	$l_{sf}(nm)$	$t(nm)$	1^{st}	2^{nd}
1	Ta	140	0	0	0.7	7	0.5		
2	NiCr	140	0	0	0.8	6	5		
3	PtMn	200	0	0	0.8	1	7		
4	Co50Fe50	19	0.45	0	0	4	1	1	1
5	Ta	140	0	0	0.7	7	0.1		
6	CoFe	19	0.45	0	0	4	1	1	1
7	interf2	48	-0.2	0	0	3	1		
8	Ru	30	0	0	0	4	0.8		
9	interf2	48	-0.2	0	0	3	1		
10	Co50Fe50	19	0.45	0	0	4	0.9	0	0
11	inter	45	0.7	0	0	3	1	0	0
12	Cu	7	0	0	0	50	0.3		
13	inter	45	0.7	0	0	3	1	0	0
14	Co50Fe50	19	0.45	0	0	4	0.9	0	0
15	inter	45	0.7	0	0	3	1	0	0
16	Cu	7	0	0	0	50	0.3		
17	inter	45	0.7	0	0	3	1	0	0
18	Co50Fe50	19	0.45	0	0	4	0.9	0	0
19	inter	45	0.7	0	0	3	1	0	0
20	Cu	7	0	0	0	50	0.3		
21	inter	45	0.7	0	0	3	1	0	0
22	Co50Fe50	19	0.45	0	0	4	0.8	0	0
23	inter	45	0.7	0	0	3	1	0	0
24	Cu	7	0	0	0	50	2.6		
25	inter	45	0.7	0	0	3	1	0	1
26	Co50Fe50	19	0.45	0	0	4	1	0	1
27	inter	45	0.7	0	0	3	1	0	1
28	Cu	7	0	0	0	50	0.3	0	
29	inter	45	0.7	0	0	3	1	0	1
30	Co50Fe50	19	0.45	0	0	4	1	0	1
31	inter	45	0.7	0	0	3	1	0	1
32	Cu	7	0	0	0	50	0.3		
33	inter	45	0.7	0	0	3	1	0	1
34	Co50Fe50	19	0.45	0	0	4	1	0	1
35	inter	45	0.7	0	0	3	1	0	1
36	Cu	7	0	0	33	50	5		
37	Ru	30	0	0	0.45	30	1		
38	Au	10	0	0	0.1	1	10		

Nota bene: $\rho\,(\mu\Omega\,.\,cm)$ is the bulk resistivity and $r\,(m\Omega\,.\,\mu m^2)$ is the interfacial resistance. "1st" and "2nd" denote the first and the second magnetic configuration. "0" stands for "up", "1" for "down".

ii) Structure "b"

	Material	ρ	β	γ	r	$l_{sf}(nm)$	$t(nm)$	1^{st}	2^{nd}
1	Ta	140	0	0	0.7	7	0.5		
2	NiCr	140	0	0	0.8	6	5		
3	PtMn	200	0	0	0.8	1	7		
4	Co50Fe50	19	0.45	0.1	0.5	4	3	1	1
5	interf2	48	-0.2	0	0	3	1		
6	Ru	30	0	0	0	30	0.8		
7	interf2	48	-0.2	0	0	3	1		
8	Co50Fe50	19	0.45	0	0	4	0.8	0	0
9	inter	45	0.7	0	0	3	1	0	0
10	Cu	7	0	0	0	50	0.3		
11	inter	45	0.7	0	0	3	1	0	0
12	Co50Fe50	19	0.45	0	0	4	0.8	0	0
13	inter	45	0.7	0	0	3	1	0	0
14	Cu	7	0	0	0	50	0.3		
15	inter	45	0.7	0	0	3	1	0	0
16	Co50Fe50	19	0.45	0	0	4	0.8	0	0
17	inter	45	0.7	0	0	3	1	0	0
18	Cu	7	0	0	0	50	0.3		
19	inter	45	0.7	0	0	3	1	0	0
20	Co50Fe50	19	0.45	0	0	4	1.2	0	0
21	inter	45	0.7	0	0	3	1	0	0
22	Cu	7	0	0	0	50	3		
23	inter	45	0.7	0	0	3	1	0	1
24	Co50Fe50	19	0.45	0	0	4	1	0	1
25	inter	45	0.7	0	0	3	1	0	1
26	Cu	7	0	0	0	50	0.3		
27	inter	45	0.7	0	0	3	1	0	1
28	Co50Fe50	19	0.45	0	0	4	1	0	1
29	inter	45	0.7	0	0	3	1	0	1
30	Cu	7	0	0	0	50	0.3		
31	inter	45	0.7	0	0	3	1	0	1
32	Co50Fe50	19	0.45	0	0	4	1	0	1
33	inter	45	0.7	0	0	3	1	0	1
34	Cu	7	0	0	41	50	5		
35	Ru	30	0	0	0.45	30	1		
36	Au	10	0	0	0.1	1	10		

iii) Structure “c”

	Material	ρ	β	γ	r	$l_{sf}(nm)$	$t(nm)$	1^{st}	2^{nd}
1	Ta	140	0	0	0.7	7	0.5		
2	NiCr	140	0	0	0.8	6	5		
3	PtMn	200	0	0	0.8	1	7		
4	Co50Fe50	19	0.45	0.1	0.5	4	3	1	1
5	interf2	48	-0.2	0	0	3	1		
6	Ru	30	0	0	0	30	0.8		
7	interf2	48	-0.2	0	0	3	1		
8	Co50Fe50	19	0.45	0	0	4	0.8	0	0
9	inter	16	0.45	0	0	3	1	0	0
10	Ag	7	0	0	0	50	0.6		
11	inter	16	0.45	0	0	3	1	0	0
12	Co50Fe50	19	0.45	0	0	4	0.8	0	0
13	inter	16	0.45	0	0	3	1	0	0
14	Ag	7	0	0	0	50	0.6		
15	inter	16	0.45	0	0	3	1	0	0
16	Co50Fe50	19	0.45	0	0	4	0.8	0	0
17	inter	16	0.45	0	0	3	1	0	0
18	Ag	7	0	0	0	50	0.3		
19	inter	16	0.45	0	0	3	1	0	0
20	Co50Fe50	19	0.45	0	0	4	1.2	0	0
21	inter	45	0.7	0	0	3	1	0	0
22	Cu	7	0	0	0	50	3		
23	inter	45	0.7	0	0	3	1	0	1
24	Co50Fe50	19	0.45	0	0	4	1	0	1
25	inter	45	0.7	0	0	3	1	0	1
26	Cu	7	0	0	0	50	0.3		
27	inter	45	0.7	0	0	3	1	0	1
28	Co50Fe50	19	0.45	0	0	4	1	0	1
29	inter	45	0.7	0	0	3	1	0	1
30	Cu	7	0	0	0	50	0.3		
31	inter	45	0.7	0	0	3	1	0	1
32	Co50Fe50	19	0.45	0	0	4	1	0	1
33	inter	45	0.7	0	0	3	1	0	1
34	Cu	7	0	0	23	50	5		
35	Ru	30	0	0	0.45	30	1		
36	Au	10	0	0	0.1	1	10		

iv) Structure "d"

	Material	ρ	β	γ	r	$l_{sf}(nm)$	$t(nm)$	1^{st}	2^{nd}
1	Ta	140	0	0	0.7	7	0.5		
2	NiCr	140	0	0	0.8	6	5		
3	PtMn	200	0	0	0.8	1	7		
4	Co50Fe50	19	0.45	0.1	0.5	4	3	1	1
5	interf2	48	-0.2	0	0	3	1		
6	Ru	30	0	0	0	30	0.8		
7	interf2	48	-0.2	0	0	3	1		
8	Co50Fe50	19	0.45	0	0	4	0.8	0	0
9	inter	16	0.45	0	0	3	1	0	0
10	Ag	7	0	0	0	50	0.6		
11	inter	16	0.45	0	0	3	1	0	0
12	Co50Fe50	19	0.45	0	0	4	0.8	0	0
13	inter	16	0.45	0	0	3	1	0	0
14	Ag	7	0	0	0	50	0.6		
15	inter	16	0.45	0	0	3	1	0	0
16	Co50Fe50	19	0.45	0	0	4	0.8	0	0
17	inter	16	0.45	0	0	3	1	0	0
18	Ag	7	0	0	0	50	0.3		
19	inter	16	0.45	0	0	3	1	0	0
20	Co50Fe50	19	0.45	0	0	4	1.2	0	0
21	inter	45	0.7	0	0	3	1	0	0
22	Cu	7	0	0	0	50	3		
23	inter	45	0.7	0	0	3	1	0	1
24	Co50Fe50	19	0.45	0	0	4	1	0	1
25	inter	16	0.45	0	0	3	1	0	1
26	Ag	7	0	0	0	50	0.3		
27	inter	16	0.45	0	0	3	1	0	1
28	Co50Fe50	19	0.45	0	0	4	1	0	1
29	inter	16	0.45	0	0	3	1	0	1
30	Ag	7	0	0	0	50	0.3		
31	inter	16	0.45	0	0	3	1	0	1
32	Co50Fe50	19	0.45	0	0	4	1	0	1
33	inter	16	0.45	0	0	3	1	0	1
34	Cu	7	0	0	15	50	5		
35	Ru	30	0	0	0.45	30	10		
36	Au	10	0	0	0.1	1	10		

INDEX

Part A : Spin-transfer in CPP spin-valves: an introduction 11

Chapter 1. Current - perpendicular - to - plane giant magnetoresistance 13
A.1.1. Simple intuitive GMR model 13
A.1.2. CPP-GMR and Valet-Fert theory for metallic multilayers 17

Chapter 2. (Some) Spin-transfer theory 27
A.2.1. Model structure 28
A.2.2. Mechanisms of spin-transfer 29
A.2.3. Ballistic theory: Slonczewski's original model 30
A.2.4. Diffusive theory: the model of Zhang, Levy and Fert 34
A.2.5. Magnetic temperature model 39
A.2.6. Important parameters 40
A.2.6.a. The decay length 41
A.2.6.b. Sign of the torque 40
A.2.6.c. Switching currents 42
A.2.6.d. Amplification factor and non-magnetic lead influence 43
A.2.6.e. Effective field 43
A.2.6.f. Presence of a polarizing layer 43

Chapter 3. Current induced magnetization precession: numerical simulations ... 47
A.3.1. Switching dynamics with a spin-torque term 47
A.3.1.a. Time evolution of the magnetization during spin-current induced switching 48
A.3.1.b. Effect of a strong easy-plane anisotropy and high current, low field distortion of M(I) 49
A.3.1.c. High current, high field switching threshold 50
A.3.2. Micromagnetic study of magnetization dynamics with spin-torque 51
A.3.2.a. Hysteresis loops with spin torques 52
A.3.2.b. Magnetization-current loops 53
A.3.2.c. Out-of-plane stable states, precession and energy pumping 54
A.3.2.d. Switching speed and thermal effects 54
A.3.3. Influence of the Oersted field 56
A.3.4. Spin-transfer induced noise in CPP-GMR read heads 57
A.3.5. Conclusion 60

Chapter 4. Experimental state-of-the-art 65
A.4.1. Static measurements 66
A.4.1.a. First experiments on current induced magnetization switching 66
A.4.1.b. Stochastic nature of the switching currents and thermal activation 68
A.4.1.c. "Static" phase diagrams 69
A.4.1.d. Telegraph noise in the coercivity region of the phase diagram 72
A.4.1.e. "Instability" current versus switching current 74
A.4.1.f. GMR versus switching currents 75
A.4.2. Dynamic measurements 76
A.4.2.a. Switching probability 76

A.4.2.b. Frequency-dependent experiments and the dynamic phase diagram 79
A.4.2.c. High frequency telegraph noise in the precession region of the phase diagram....82
A.4.3. Conclusion....85

Part B : Spin-transfer effects in spin-valves developed for CPP-GMR heads 89

Chapter 1. Motivation....91

Chapter 2. Experimental details....97
B.2.1. Sample structure....97
B.2.2. Sample fabrication....99
B.2.3. Experimental setups for transport measurements....101
B.2.3.a. Experimental setup for static measurements....101
B.2.3.b. Experimental setup for frequency-dependent measurements....102

Chapter 3. Static experiments: phase diagrams....105
B.3.1. Current induced magnetization switching....106
B.3.2. Preliminaries: Influence of the NiFe electrode....108
B.3.2.a. Asymmetric heating....108
B.3.2.b. Noise in very low applied field and “inverse” coercivity....110

B.3.3. Phase diagram: general trends and macrospin modeling....112
B.3.3.a. Evolution of the resistance versus current curves with the applied magnetic field....113
B.3.3.b. Evolution of the magnetoresistance curves with the sense current.... 115
B.3.3.c. Static phase diagram....117
B.3.3.d. Switching current distribution....119
B.3.3.e. Macrospin modeling....120
B.3.3.f. Discussion....123
B.3.3.g. Telegraph noise....128
B.3.3.h. General trends: conclusion....131

B.3.4. Very low coercivity samples....131
B.3.4.a. Evolution of the resistance versus current characteristics with the applied field....132
B.3.4.b. Evolution of the magnetoresistance curves with the sense current 134
B.3.4.c. Phase diagram....136
B.3.4.d. Discussion....138
B.3.4.e. Low coercivity: conclusion....141
B.3.5. Static phase diagrams: conclusion....141

Chapter 4. Influence of the laminating material....145
B.4.1. Experimental results....145
B.4.1.a. Magnetoresistance change with the structure....146

B.4.1.b. Magnetoresistance versus switching currents values and asymmetry 149
B.4.2. Modeling: extension of the Valet-Fert theory 152
B.4.3. Method and discussion 152
B.4.3.a. Method 152
B.4.3.b. GMR versus average critical currents 153
B.4.3.c. Switching currents and their asymmetry versus polarization and $g(\theta)$ 156
B.4.4. Conclusions 160

Chapter 5. Frequency-dependent experiments 163
B.5.1. Precession states of the free layer: general trends 164
B.5.1.a. Static characterization 164
B.5.1.b. Positive currents & fields 168
B.5.1.c. Negative currents & fields 174
B.5.1.d. Dynamic versus static phase diagram 178
B.5.1.e. Micromagnetic simulations 180
B.5.1.f. Discussion 186
B.5.2. Very low coercivity samples 188
B.5.2.a. Static characterization 189
B.5.2.b. Dynamic results 192
B.5.2.c. Discussion 198
B.5.3. Precession states of the reference layer 200
B.5.4. Conclusion 205

Chapter 6. Conclusions and perspectives 209
B.6.1. Conclusions 209
B.6.2. Perspectives 211
B.6.2.a. Reducing spin-transfer effects in CPP-GMR heads 211
B.6.2.b. Spin-transfer for microwave oscillators 213